UNITED STATES

DEPARTMENT OF THE INTERIOR

GEOLOGICAL SURVEY

SUMMARY OF RESEARCH ON THE EFFECTS OF TOPOGRAPHIC AMPLIFICATION OF EARTHQUAKE SHAKING ON SLOPE STABILITY

by
Randall W. Jibson
U.S. Geological Survey
Reston, Virginia 22092

U.S. Geological Survey Open-File Report 87-268

Draft report of research conducted while a visiting
researcher at the Public Works Research Institute,
Ministry of Construction, Government of Japan

This report is preliminary and has not been edited
or reviewed for conformity with editorial standards
and nomenclature of the U.S. Geological Survey

Preface

This report summarizes my research activities conducted at the Public Works Research Institute (PWRI) of the Ministry of Construction, located in Tsukuba Science City, Japan. The research, carried out from January to March of 1987, was funded through the Science and Technology Agency of the Government of Japan. Dr. Yasushi Sasaki, Head of the Ground Vibration Division at PWRI, supervised the project. This report is a copy of the draft report submitted to PWRI at the conclusion of my stay in Japan and provides a record of my research activities there.

The objective of my research at PWRI was to determine the effects of topographic amplification of earthquake shaking on slope stability, particularly in the case of large, deep-seated landslides. The massive debris avalanche from the south flank of Mt. Ontake triggered by the 1984 Naganoken-Seibu earthquake was investigated as a possible case study of topographic amplification leading to slope failure. This study required synthesis of research on several subjects:

1. A method was developed to estimate the relative dynamic performances of slopes having different dynamic stabilities and experiencing different levels of seismic shaking.

2. Findings from other investigations of topographic amplification were analyzed for comparison with each other and with findings from the present research. Data from seismic site-response experiments in Chile and Japan were examined in detail.

3. Results of shaking-table tests on silicon slope models, conducted at PWRI in 1987, were analyzed and compared with the results of the field studies mentioned above and to the Mt. Ontake debris avalanche.

4. Findings from the research described above were synthesized and applied to the Mt. Ontake debris avalanche to determine the effects, if any, of topographic amplification on the formation of the avalanche.

The research activities outlined above are summarized in four reports included herein as Parts 1-4, respectively. The reports were written somewhat independently of each other as the research progressed and are presented sequentially as written. Therefore, some statements in later reports supersede those made in earlier reports, because new information became available. The reports do, however, reference each other where appropriate (for example, "see Part 3").

Page numbers are sequential from the beginning of Part 1 through the end of Part 4. Figures, tables, and equations, however, are numbered separately within each Part (for example, "figure 2.5" is figure 5 of Part 2); figures and tables for each Part are collected at the end of that Part. References from all Parts are combined in a reference section at the end of the report.

Several people provided valuable help and support throughout this project. Dr. Y. Sasaki and Dr. T. Iwasaki of PWRI arranged for my visit and directed the research; Mr. T. Kuwabara of PWRI provided the results of his slope model tests and aided in their interpretation; Mr. Tamura of PWRI provided data from the Matsuzaki dense seismic array; Dr. K. Ishihara of Tokyo University helped me reconstruct his slope-stability model and provided data on dynamic soil shear strengths; discussions with Dr. Y. Kobayashi of Kyoto University and Dr. E. Harp of the U.S. Geological Survey aided in the evaluation of dynamic slope performance.

CONTENTS

PREFACE ii

PART 1:
Use of the Newmark Analysis to Predict Dynamic Slope Performance

Introduction 2
Earthquake shaking intensity 3
Seismic slope stability 5
Evaluation of dynamic slope performance 8
Tables 1.1-1.3 12
Figures 1.1-1.3 15

PART 2:
Description and Analysis of Preliminary Results of Seismic Site-Response Experiment Following the March 3, 1985 Central Chile Earthquake

Introduction 19
Comparisons of seismic responses 20
    North-South versus East-West components 21
    Ridge B-C versus ridge E-F 22
    Station CBB versus station CBC 22
    Station CBE versus station CBF 23
    Comparison of all stations 23
    Low-frequency versus high-frequency peak responses 25
Analysis of peak amplification 25
Conclusions 28
Tables 2.1-2.4 30
Figures 2.1-2.12 34

PART 3:
Comparison of Results of Slope Model Tests with Field Studies of Topographic Amplification of Ground Shaking

Introduction 47
Description of model tests 47
Analysis of frequency-domain test results 48
Spatial variation in acceleration 52
    Variation along ridge crests 52
    Variation along the maximum vertical cross section 54
    Conclusions 55
Spatial variation in shear stress 56
    Variation along ridge crests 56
    Variation along the maximum vertical cross section 58
    Conclusions 58
Comparison with results of Chile earthquake experiment 59
Comparison with data from the Matsuzaki dense seismic array 62
Summary and conclusions 62
Tables 3.1-3.5 65
Figures 3.1-3.58 70

PART 4:
Did Topographic Amplification of Earthquake Shaking Play a Role in Triggering the Mount Ontake Debris Avalanche?

Introduction 129
Modeling slope stability 130
Comparison with similar slopes 132
Possible effects of topographic amplification 134
Summary and discussion 137
Tables 4.1-4.2 139
Figures 4.1-4.6 141

REFERENCES 147

APPENDIX: Activity Report submitted to the Public Works Research Institute 152

PART I

Use of the Newmark Analysis to Predict Dynamic Slope Performance

PART I

Use of the Newmark Analysis to Predict Dynamic Slope Performance

INTRODUCTION

A method for comparing the dynamic responses of slopes having different stabilities and in different levels of earthquake shaking would find wide application in regional seismic hazard analysis. The most recent and comprehensive study on this subject is that of Wilson and Keefer (1986), who developed a method for predicting the areal limits of earthquake-induced landsliding from a given design earthquake. They used a four-step approach. First, they showed how to determine a slope's seismic stability as measured by its critical acceleration, the threshold ground acceleration required to initiate landslide movement. Second, they introduced the use of Arias intensity as a measure of earthquake shaking intensity and developed an equation that relates Arias intensity to earthquake magnitude and source distance. Third, they used the landslide displacement analysis developed by Newmark (1965) to model dynamic slope response and estimated the amount of Newmark displacement necessary to cause failure. Fourth and finally, they determined the combination of critical acceleration and Arias intensity necessary to generate this amount of displacement and calculated the distance from the seismic source at which this Arias intensity would occur for their design earthquake.

The approach outlined above provides a valuable theoretical and practical framework for evaluation of seismic slope stability, but it suffers from two significant problems: it is somewhat unwieldy and difficult to apply, and its governing equations are based on several unjustified, though not unreasonable, assumptions. To overcome these problems, I use an approach similar to that of Wilson and Keefer (1986), but I derive the governing equations in a different manner and then develop a single equation easily applied to the evaluation of slope performance during earthquakes. This will involve (1) the development of a relationship relating earthquake shaking intensity to magnitude and source distance, and (2) the development of a relationship between seismic slope stability, earthquake shaking intensity, and dynamic slope performance.

EARTHQUAKE SHAKING INTENSITY

Earthquake shaking intensity as defined by Arias (1970) has been shown to correlate well with earthquake damage in general and landslides in particular (Wilson and Keefer, 1983, 1986; Jibson, 1985; Jibson and Keefer, in press). As defined by Arias (1970), this intensity (I_a) is directly proportional to the integral of the square of an acceleration time-history of an earthquake, which is simply the area enclosed by the time-domain strong-motion record. Note that an *earthquake* does not have an Arias intensity, but rather an *earthquake strong-motion record* has an Arias intensity, because I_a is measured directly from a given acceleration time-history. Because it is an integration of acceleration, Arias intensity has units of velocity and is normally expressed in meters per second. Arias intensity yields a reliable measure of the total shaking content of a strong-motion record and is thus appropriate for use in analysis of seismic slope stability. Use of Arias intensity as a measure of earthquake shaking is preferred over use of peak ground acceleration, typically used in slope-stability studies, because I_a depends not only on the ground acceleration, which may have a peak value of very high frequency and short duration that will not affect many slopes, but also on the duration of strong shaking.

From considerations of seismological theory, Wilson and Keefer (1986) suggested a relationship between Arias intensity, earthquake magnitude, and depth-corrected source distance having the following functional form for the mean data distribution:

$$\log(I_a) = a(\mathbf{M}) - b\log(R) + c, \qquad (1.1)$$

where I_a is the Arias intensity; **M** is the moment magnitude as defined by Hanks and Kanamori (1979); R is the source distance corrected for focal depth; and a, b, and c are constants. They then assumed that a = 1 and b = 2, which assumes that the shaking intensity decreases as the square of the source distance; they further assumed a log-linear relationship between magnitude and Arias intensity in order to convert all the input data to a single equivalent magnitude. Although these assumptions may be reasonable as such, none was rigorously justified either theoretically or empirically; they were made solely for the purpose of reducing the problem to a bivariate linear regression.

The functional form of equation 1.1 is well supported by theory (Wilson and Keefer, 1986). Therefore, to produce an equation relating Arias intensity to earthquake magnitude and source distance that does not depend on unjustified assumptions, I employ a multiple linear regression model that allows all of the constants (a, b, and c) in equation 1.1 to vary. This permits the input data to determine the final form of the magnitude-distance equation. I use the same data set as Wilson and Keefer (1986) with the addition of a strong-motion record from the 1978 Tabas, Iran earthquake (table 1.1), included to add a large value of Arias intensity to the data set. The multiple regression analysis yielded the following equation:

$$\log(I_a) = 0.98(\mathbf{M}) - 1.35\log(R) - 4.90, \qquad (1.2)$$

where I_a is in meters/second and R is in kilometers. The coefficient for **M** is nearly 1, which demonstrates that the data justify this assumption of Wilson and Keefer; the coefficient for log(R), however, differs significantly from 2 and thus indicates that the Arias intensity does not decrease as R^2. This model yields a correlation coefficient (r) of 0.84, and is thus well fitted to the data. A comparitive chi-square test shows that equation 1.2 is significantly better at predicting the observed values in the input data set than is the equation of Wilson and Keefer (1986). Thus, the theoretical justifications for the functional form presented by Wilson and Keefer have been preserved, but an equation better fit to the data that does not rely on unjustifed assumptions has been developed to predict the variation in earthquake shaking intensity as a function of magnitude and source distance.

SEISMIC SLOPE STABILITY

Seismic slope stability traditionally has been evaluated by pseudostatic analysis, in which earthquake acceleration in conjunction with the landslide mass is treated as an explicit body force. By iteratively employing different input accelerations, a yield acceleration is determined at which the static factor of safety is reduced to 1.0, and any exceedance of this yield acceleration is defined as slope failure. As Wilson and Keefer (1983) point out, this method is overconservative because it assumes that any exceedance of the yield acceleration results in failure. Experience shows, however, that earthquakes can produce transitory peaks of very high acceleration, sometimes exceeding 1 g, but that many slopes having yield accelerations much lower than the peak earthquake acceleration do not fail despite the fact that their yield accelerations have been exceeded by a considerable amount. Newmark (1965) realized that short-duration, large accelerations can induce minor amounts of displacement in a landslide block without causing general failure; therefore, he developed a method for calculating the displacement of a landslide block of known yield acceleration (or critical acceleration, as expressed by Newmark) when subjected to shaking represented by a given strong-motion record. Newmark (1965) showed that for a homogeneous slope, the critical acceleration can be expressed as

$$A_c = (FS - 1) g \sin(\alpha), \tag{1.3}$$

where A_c is the critical acceleration in terms of g, the acceleration of gravity; FS is the static factor of safety, and α is the angle from the horizontal that the center of mass of the potential landslide block first moves. (For failure parallel to an infinite slope, α is the slope angle; for circular failure surfaces, α is the angle between a vertical line and a line connecting the center of mass of the landslide block and the center of the slip circle.) For nonhomogeneous slopes, yield acceleration may provide a more accurate index of a slope's dynamic stability.

As shown in figure 1.1, integration of those portions of a strong-motion record that exceed the critical acceleration of a potential landslide block produces a velocity profile of the block; a second integration produces a cumulative displacement profile of the landslide block. In this manner, a cumulative landslide displacement can be determined from a strong-motion record if the critical acceleration of the potential landslide block is known. Experience has shown that Newmark's method commonly underestimates the amount of actual landslide displacement, because in many slope materials, shear strength decreases during shearing, and thus the critical acceleration is continually decreasing as the slide block translates. Therefore, the results of Newmark's analysis do not necessarily predict the actual landslide displacement, but rather are a relative index of dynamic slope performance. Wilson and Keefer (1983), however, did document an instance where the Newmark analysis very accurately predicted the actual measured displacement of a landslide triggered by an earthquake.

Because it is seldom possible to find a strong-motion record having the exact shaking intensity of interest to a particular problem, it is desirable to develop a general relationship between Newmark displacement (D_n), critical acceleration, and Arias intensity. To do this, I calculated Newmark displacements from a wide variety of strong-motion records and for a similar variety of critical accelerations. For the 10 strong-motion records listed in table 1.2, which have Arias intensitites between 0.2 and 10 m/s, I conducted Newmark analyses for critical accelerations of 0.02, 0.05, 0.1, 0.2, 0.3, 0.4, and 0.5 g, the range of interest for most slope-stability problems. Figure 1.2 shows the results; critical acceleration is plotted as a function of Arias intensity and Newmark displacement, and best-fit lines are drawn through those data points corresponding to a given value of critical acceleration. The lines are nearly parallel as well as being fairly evenly spaced, and the best-fit lines for each critical acceleration have very high correlation coefficients (between 0.79 and 0.99), with the sole exception of A_c = 0.2 g (r = 0.46). This indicates a linear distribution of critical acceleration in relation to log (I_a) and log (D_n). To quantify this multivariate relationship, a multiple regression analysis using the following functional form was conducted:

$$\log (D_n) = a\log (I_a) + b(A_c) + c, \tag{1.4}$$

where D_n is the Newmark displacement; I_a is the Arias intensity; A_c is the critical acceleration; and a, b, and c are constants to be determined by the regression. The model produced by the regression analysis has a correlation coefficient (r) of 0.90, and the resulting equation is

$$\log (D_n) = 1.37\log (I_a) - 6.36(A_c) + 1.57, \tag{1.5}$$

where D_n is in centimeters, I_a is in meters/second, and A_c is in g's. The high correlation coefficient indicates that this model accurately predicts the Newmark displacement from the input data. Figure 1.3 shows the contours of critical acceleration predicted by equation 1.5 and plotted as a function of log (I_a) and log (D_n). The upper dashed line represents A_c = 0, the theoretical and practical upper bound to the data; the lower dashed line represents A_c = 0.5 g, for which only two data points exist, and which thus provides a practical lower bound for this analysis. Using this model, any combination of critical acceleration and Arias intenstiy can be combined to estimate Newmark displacement, which thus eliminates the need to locate a strong-motion record that has the exact Arias intensity desired.

EVALUATION OF DYNAMIC SLOPE PERFORMANCE

When analyzing dynamic slope performance, we seldom know the exact shaking intensity of interest; rather, we normally model the effects of some actual or postulated earthquake of known magnitude and location. Therefore, an equation directly relating Newmark displacement to earthquake magnitude and source distance, as well as to the critical acceleration of the slope, is most useful. Such an equation can be produced by substituting the right side of equation 1. 2 for I_a in equation 1. 5, which yields the following:

$$\log(D_n) = 1.37\,(0.98\,(\mathbf{M}) - 1.35\log(R) - 4.90) - 6.36\,(A_c) + 1.57, \qquad (1.6)$$

and thus

$$\log(D_n) = 1.34\,(\mathbf{M}) - 1.85\log(R) - 6.36\,(A_c) - 5.14, \qquad (1.7)$$

where D_n is in centimeters, **M** is the moment magnitude, R is in kilometers, and A_c is in g's. The signs of the coefficients in this equation are intuitively consistent, in that they indicate that increasing magnitude produces increased landslide displacement, and that increasing source distance or critical acceleration results in decreased landslide displacement. This equation is very versatile, and can be solved for any of the four variables if the other three are known or postulated, as follows:

$$\log(R) = 0.72(\mathrm{M}) - 0.54\log(D_n) - 3.44(A_c) - 2.78 \qquad (1.8)$$

$$\mathrm{M} = 1.38\log(R) + 0.75(D_n) + 4.75(A_c) + 3.84 \qquad (1.9)$$

$$A_c = 0.21(\mathrm{M}) - 0.29\log(R) - 0.16\log(D_n) - 0.81 \qquad (1.10)$$

In the case of Mt. Ontake (see Part 4), the magnitude and hypocenter of the earthquake are known, the critical accelerations of various slopes on the mountain can be calculated from the estimated static safety factors and the slope angles, and thus the Newmark displacement can be estimated for comparison of the dynamic performances of these slopes. Equations 1.7-1.10 can also be applied in any number of ways to problems of regional hazard analysis as well as to individual sites.

For some applications, it is more useful to have an equation in terms of peak ground acceleration (*PGA*) than earthquake magnitude and distance. Wilson (in press) developed a well constrained relationship between I_a, *PGA*, and the duration of strong ground shaking, T_d (defined by Dobry and others (1978) as the time required to build up the central 90 percent of the Arias intensity of an earthquake record):

$$I_a = 0.90\ (PGA^2)\ (T_d), \qquad (1.11)$$

where I_a is in meters/second, *PGA* is in g's, and T_d is in seconds. Substituting the right side of equation 1.11 for I_a in equation 1.5 yields the following:

$$\log(D_n) = 2.74\log\ (PGA) + 1.37\log\ (T_d) - 6.36\ (A_c) + 1.51. \qquad (1.12)$$

Thus, equation 1.12 can be used to estimate the Newmark displacement if the peak ground acceleration, shaking duration, and critical acceleration of the landslide are known or estimated.

Appraisal of dynamic slope performance from the Newmark displacement requires considerable judgment, however. Wilson and Keefer (1986) suggested using 10 cm of Newmark displacement as the threshold for failure (macroscopic cracking and damage to overlying structures) for coherent slides, and 2 cm for rock falls and other disrupted slides. The amount of actual landslide displacement, however, will depend on the properties of the landslide material. For slopes that will fail in tension and for slopes composed of very brittle materials or highly sensitive soils--those whose shear strength decreases by a large amount during shearing--a Newmark displacement of about 2 cm will probably result in catastrophic failure (infinite displacement). For moderately sensitive soils, large displacements will probably occur for Newmark displacements of about 5 cm. For nonsensitive or only slightly sensitive soils, the Newmark displacement probably corresponds approximately to the actual displacement, and, as Wilson and Keefer (1986) note, displacements of about 10 cm generally cause ground cracking and damage to overlying structures. Regardless of the relationship of the actual landslide displacement and that predicted by the Newmark analysis, for a given type of slope material, the Newmark displacement provides a valuable index to the relative dynamic performance of slopes having any range of static slope stabilities and in any level of earthquake shaking.

The amount of Newmark displacement required to cause catastrophic failure for a given type of sope material can be estimated by examining case studies of historical landslides triggered by earthquakes. If Newmark displacements for several such landslides can be calculated, they may indicate a minimum amount of Newmark displacement necessary to cause failure in a given type of slope material. Ishihara and Hsu (1986) compiled data on several landslides triggered by the 1980 Irpinia, Italy and the 1984 Naganoken-seibu, Japan earthquakes. Table 1.3 lists the critical acceleration of each of the landslides and the magnitude and source distance of the triggering earthquake. The Newmark displacement, D_n, was calculated using equation 1.7.

The landslides triggered by the Naganoken-seibu earthquake all formed in pumice, and 3 cm appears to be a reasonable lower bound of Newmark displacement required to cause catastrophic failure. The landslides triggered by the Irpinia earthquake all were reactivated slides in variegated clay; for these slides, 2 cm of Newmark displacement is a reasonable lower bound leading to general failure. These amounts of Newmark displacement agree well with the estimated critical displacements discussed previously.

Equations 1.7-1.10 and 1.12 reflect the well supported theoretical basis established by Wilson and Keefer (1986) for the relationship between earthquake magnitude, source distance, seismic slope stability, and dynamic slope response. These equations also are extremely easy to use, are rigorously constrained by empirical data, and are not based on unsupported assumptions.

Table 1.1 — Magnitude - distance - Arias intensity data (from Wilson and Keefer, 1986).

Earthquake/station	Moment magnitude (M)	Source distance (r), in km	Acceleration (A)	Arias intensity (I_a), in m/s
Kern County/Taft	7.4	43	0.179	0.59
Parkfield/Station 2	6.1	6.6[1]	.498	1.71
Parkfield/Station 5	6.1	9.3[1]	.434	.85
Lower California/El Centro	6.5	53	.182	.62
Imperial/El Centro	7.0	12	.348	1.93
San Fernando/Castaic	6.6	21	.271	.99
Eureka/Federal Building	6.5	25	.257	.710
San Fernando/Orion	6.6	20	.255	1.28
Lytle Creek/Wrightwood	5.3	14	.198	.14
Parkfield/Temblor	6.1	16[1]	.347	.45
Ferndale/City Hall	5.6	25	.237	.105
San Fernando/Palmdale	6.6	34	.113	.334
Kern County/Pasadena	7.4	130	.053	.114
Hollister/City Hall	5.6	40	.065	.135
San Francisco/Golden Gate	5.3	11	.105	.05
San Francisco/State Bldg.	5.3	17	.085	.052
San Francisco/Alex. Bldg.	5.3	16	.043	.016
San Francisco/Oakland	5.3	26	.04	.010
Borrego/San Onofre	6.6	122	.046	.035
Kern County/(A005)	7.4	85	.131	.29
Kern County/(A006)	7.4	109	.053	.11
Borrego/(A020)	6.6	96	.029	.03
Long Beach/Vernon	6.3	53	.133	.23
San Jose/(A010)	5.8	10	.102	.075
Southern California/(B023)	5.4	38	.033	.010
Tabas, Iran	7.4	37	.705	9.926
Wheeler Ridge/(B031)	5.9	43	.068	.042
Central California/(U307)	5.0	6	.057	.05
Northern California/(U308)	5.7	59	.075	.04
Torrance-Gardena/(V316)	5.4	6	.055	.04
Southern California/(V329)	5.0	6	.167	.100

Table 1.2. — STRONG MOTION RECORDS FOR NEWMARK ANALYSIS

Number	File Name	Earthquake Information	Duration (sec)	Time Increment (sec)	Arias Intensity (m/sec)	PGA (g)
1	PARKFL_2	1966 Parkfield, station 2	12	0.05	1.636	0.485
2	PARKFL_5	1966 Parkfield, station 5	11	0.05	0.953	0.447
3	ELCENTRO	1940 Imperial Valley El Centro station	34	0.05	1.722	0.293
4	TAFT	1952 Tehachapi Taft School	29	0.05	0.461	0.144
5	GOLETA	1978 Santa Barbara Goleta station	30	0.05	0.928	0.338
6	HILO_75	1975 Hilo	12	0.05	0.200	0.205
7	GLRY6_NE	1979 Coyote Lake Gilroy station 6 (050)	12	0.05	0.710	0.360
8	GLYCC250	1979 Coyote Lake Coyote Creek station (250)	11	0.05	0.245	0.206
9	PACO_SE	1971 San Fernando Pacoima Dam S16E	21	0.01	9.069	1.22
10	IRAN2	1978 Tabas, Iran	34	0.01	9.926	0.705

Table 1. 3. Newmark displacements of landslides triggered by the 1980 Irpinia, Italy and 1984 Naganoken-Seibu, Japan earthquakes. Data on earthquake magnitudes and distances and on critical accelerations from Ishihara and Hsu (1986).

LANDSLIDE	EARTHQUAKE MAGNITUDE	SOURCE DISTANCE (km)	CRITICAL ACCELERATION (g)	NEWMARK DISPLACEMENT (cm)
1980 Irpini, Italy Earthquake				
Buoninventre	6. 5	8	0. 210	3. 66
Serra dell' Acquara	6. 5	10	0. 135	7. 27
Pergola	6. 5	10	0. 170	4. 35
Grassano	6. 5	80	0. 155	1. 83
Andretta	6. 5	18	0. 095	4. 40
1984 Naganoken-seibu, Japan Earthquake				
Ontake Headwall	6. 8	10	0. 27	2. 54
Matsukoshi	6. 8	1	0. 32	86. 46
Ontake Highland 1	6. 8	3	0. 30-0. 32	11. 33-15. 18
Ontake Highland 2	6. 8	3	0. 27-0. 34	8. 45-23. 56
Ontake Highland 3	6. 8	3	0. 40	3. 51
Ontake Highland 4	6. 8	3	0. 40	3. 51

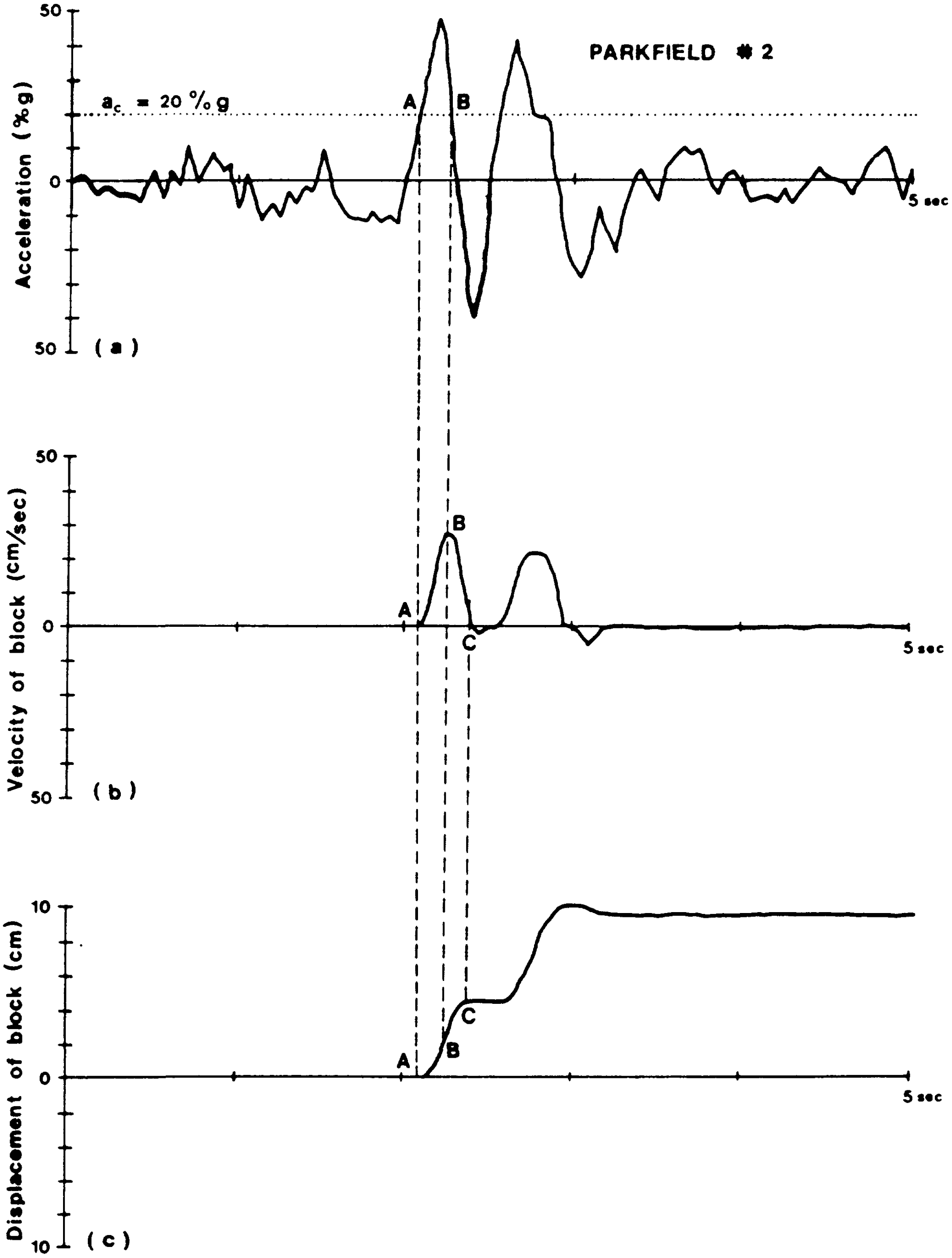

Figure 1.1 Demonstration of the Newmark-analysis algorithm: (a) strong-motion record with critical acceleration (dotted line) superimposed; (b) velocity of block versus time; and (c) displacement of block versus time. (from Wilson and Keefer, 1983)

Figure 1.2 — Best-fit lines of critical acceleration as a function of Newmark displacement and Arias intensity.

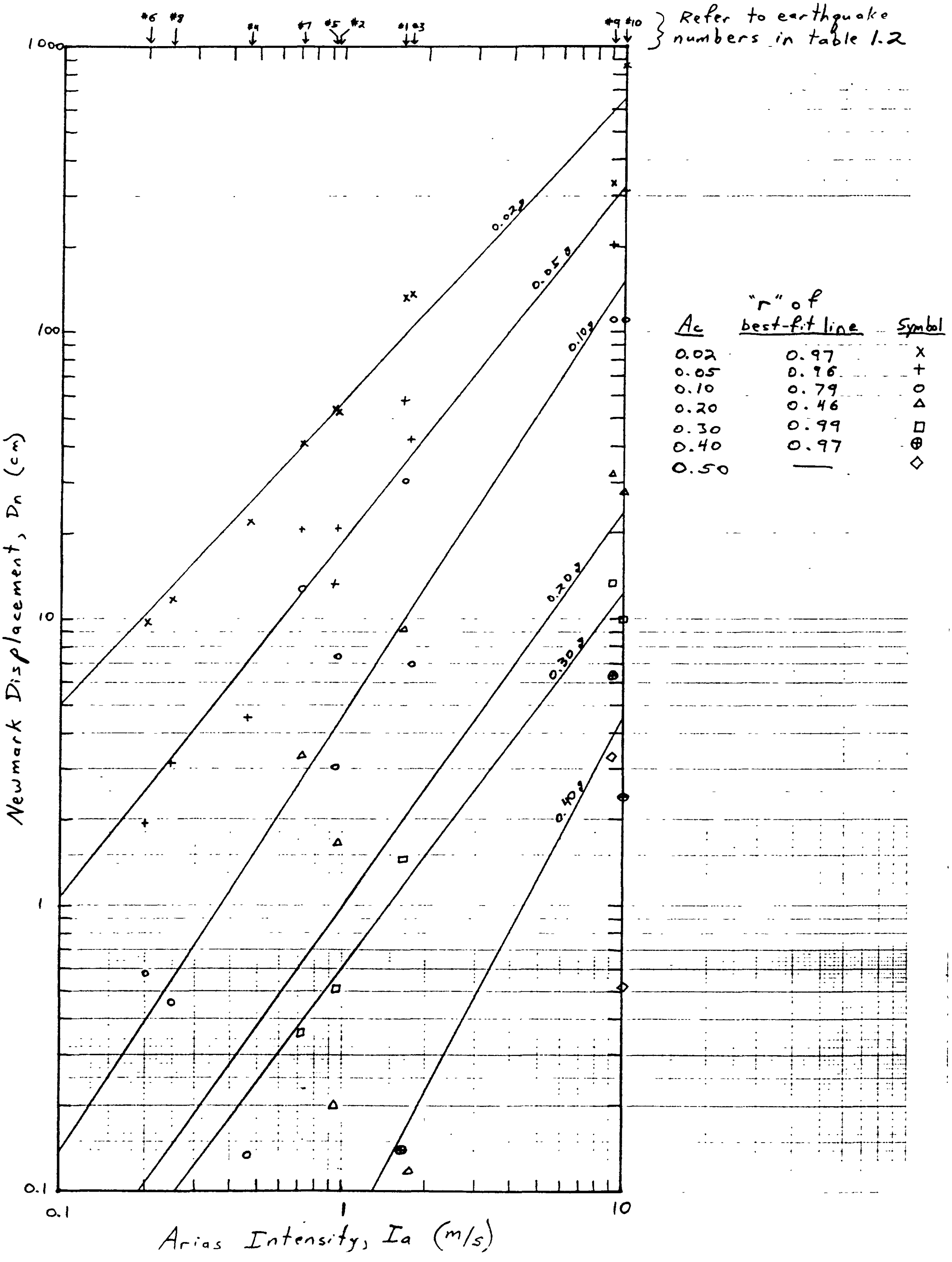

Ac	"r" of best-fit line	Symbol
0.02	0.97	x
0.05	0.96	+
0.10	0.79	o
0.20	0.46	△
0.30	0.99	□
0.40	0.97	⊕
0.50	—	◇

Figure 1.3 – Lines of critical acceleration predicted by equation 1.5.

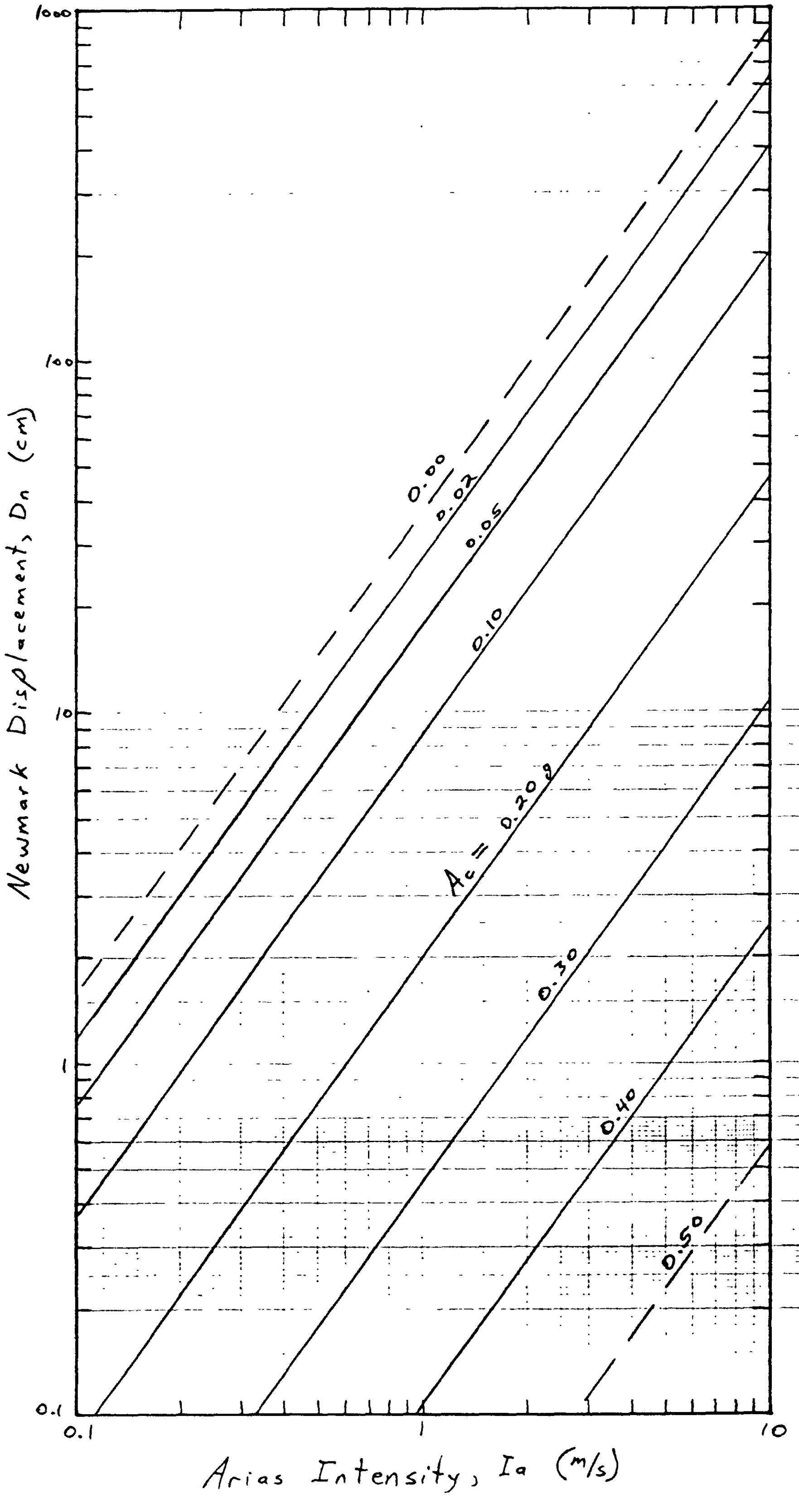

PART 2

Description and Analysis of Preliminary Results of Seismic Site-Response Experiment Following the March 3, 1985 Central Chile Earthquake

PART 2

Description and Analysis of Preliminary Results of Seismic Site-Response Experiment Following the March 3, 1985 Central Chile Earthquake

INTRODUCTION

Following the 3 March 1985 Central Chile earthquake (M_S=7.8), personnel from the United States Geological Survey (USGS) deployed seismic instruments in the Canal Beagle subdivision of Vina del Mar, about 10 km east of Valparaiso (figure 2.1). The instruments were deployed along ridge crests and intervening valley bottoms to observe possible effects of topographic amplification of seismic shaking during aftershocks of the main earthquake (Celebi, 1986, in press).

Earthquake motions were recorded by eight portable General Earthquake Observation Systems (GEOS), which used two sets of three-component sensors consisting of force-balance accelerometers and velocity transducers. The only results available at present are from the velocity recordings (Celebi, 1986). Ground motions were recorded at several sites in Canal Beagle (figure 2.2), which rests on Pleistocene sediments and decomposed granite. Ground motions at station CBA (figure 2.2), located in a valley bottom in Canal Beagle, were first compared with those recorded at a flat, hard-rock site (VAL in figure 2.1) near Valparaiso to determine the amplification effects owing to geology. All ground motions recorded at other stations in Canal Beagle were referenced to the motions at station CBA, and any differences in ground-motion reponse were attributed to the effects of topography. Stations CBB and CBC were located on one ridge (ridge B-C), stations CBE and CBF were located on a second ridge (ridge E-F), and station CBD was located on the hilltop from which both ridges emerge. All instruments were located on the ground floors of 1-5 story structures (table 2. 1).

All graphical representations of amplification ratios contained in the present paper were drawn by visually averaging the amplification ratios of at least two seismic events as shown by Celebi (1986). With one exception, ratios plotted for the same stations from different events showed similar responses, so the averaging process should introduce minimal error into the description and analysis of the test results. The single exception is station CBD, which showed responses having considerable variation; results for station CBD are thus uncertain.

COMPARISONS OF SEISMIC RESPONSES

Figure 2. 3 shows the amplification ratio of station CBA relative to the flat, hard-rock site at station VAL. Celebi (1986) assumed that all variations in ground-motion response between these stations are due to geological conditions because the seismic source parameters and source distances for the two stations are about the same. Figure 2. 3 indicates that the geological conditions at Canal Beagle cause amplification of frequencies from about 4-8 Hz and 9-10 Hz; no amplification or some deamplification occurs below 4 Hz and from 8-9 Hz.

Figures 2. 4-2. 8 show the responses of the two horizontal components of ground motion at each of the five stations located on ridges; all plots show the amplification ratio of the named station to station CBA. Figures 2. 9 and 2. 10 show the responses of all stations for the E-W and N-S components, respectively. All the responses are somewhat similar and display two major amplification peaks, one around 4 Hz, the other around 8 Hz. Table 2. 2 summarizes the characteristics of these two dominant response peaks in the data, hereafter referred to as the low-frequency peak and the high-frequency peak. Table 2. 2 lists the upper and lower frequency limits of the peaks (defined as the points between which the amplification ratio exceeds 2. 0), the widths and center points of the peaks, the frequencies at which the greatest amplification occurs, and the peak amplification ratios.

Despite the overall similarity in the responses of all stations, some differences, mostly minor, are present. The following sections compare the spectral responses from the Canal Beagle experiment with respect to the following parameters: (1) north-south (N-S) versus east-west (E-W) components of ground motion at each site; (2) response on ridge B-C versus ridge E-F (figure 2.2); (3) response of station CBB versus CBC, and of station CBE versus CBF; (4) overall responses of stations CBB, CBC, CBD, CBE, and CBF; and (5) characteristics of the low-frequency response peaks compared to those of the high-frequency response peaks.

North-South Versus East-West Components

The ridges at Canal Beagle are aligned nearly east-west, so we might expect to see a systematic difference in the seismic responses between the two horizontal components of ground motion. Table 2.2 shows that few differences exist between the responses of the two horizontal components of ground motion. The following observations can be made:

1. For stations CBB and CBC, the low-frequency peak appears to be sharper and more well defined for the E-W component than for the N-S component, but this does not hold true for the other stations.

2. The center points of the response peaks for the E-W components at all stations are located at slightly lower frequencies than those for the N-S components. The offset is no greater than 0.8 Hz but is systematic throughout the data.

3. At the high-frequency peak, the amplification ratios for the N-S components are all greater than for the E-W components. At the low-frequency peak, variations in amplification ratios are inconsistent.

The systematic differences in the the locations (in the frequency domain) and amplification ratios between N-S and E-W components suggests that these two components may respond somewhat differently to different aspects of the ridge geometries. However, the differences are small enough that little error is introduced by combining the horizontal ground-motion response into a single, average response (figure 2. 11).

Ridge B-C Versus Ridge E-F

Two observations can be made regarding the response differences between ridge B-C and ridge E-F. First, the low-frequency peak of ridge B-C is located at a higher frequency than that of ridge E-F; the difference ranges from 0. 2 to 1. 6 Hz. Second, the low-frequency response peaks for the stations on ridge E-F are wider and not as well defined as those for ridge B-C. This may be due to geometrical differences between the ridges, as discussed subsequently.

Station CBB Versus Station CBC

Comparison of stations CBB and CBC will give insight into the the variations of ground shaking on different portions of the same ridge. Station CBC is located along the ridge crest about halfway from the top to the base of the ridge; station CBB is located on the ridge crest about midway between station CBC and the base of the ridge. The following observations can be made (figures 2.9-2.10):

1. Station CBC has much higher amplification ratios (15-24) than station CBB (8-9) at the low-frequency peak. At the high-frequency peak, amplification ratios are comparable.

2. At the low-frequency peak, station CBC has slightly broader response centered at slightly lower frequency than station CBB. At the high-frequency peak, the responses are similar, though that of CBC is very slightly broader.

3. Overall, the amplification of station CBC is generally greater than that of CBB. This observation is similar to that for the PWRI model tests that indicate that amplification is greatest near the midpoints of ridge crests (see Part 3).

Station CBE Versus Station CBF

Station CBE is located about where ridge E-F emerges from the main hill and is relatively higher on the ridge crest than is station CBC on ridge B-C. Station CBF is located farther down the ridge crest, downslope from the midpoint, at a point relatively higher on the crest than is station CBB on ridge B-C. The following observations can be made (figures 2.9-2.10):

1. Both high- and low-frequency response peaks for station CBF are broader than those for CBE, but peaks for both stations are centered at the same frequencies.

2. Amplification ratios for station CBF at both high- and low-frequency response peaks are significantly greater than those for CBE: ratios of 13-16 versus 3-6 for the low-frequency peak, and ratios of 8-12 versus 3-5 for the high-frequency peak. This may occur because station CBF is closer to the midpoint of the ridge line than is station CBE, and because station CBE is located on the emerging portion of the ridge and is therefore more firmly anchored or buttressed to the main hill than is CBF.

Comparison of All Stations

If the two ridges are assumed to have identical ideal responses, then it is possible to compare all stations as if they were aligned progressively down a single ridge crest. In this case, station CBD would be at the top of the crest line, and, moving progressively downslope, would be stations CBE, CBC, CBF, and CBB. The ridges at Canal Beagle differ from those modeled at PWRI (see Part 3) in that they do not have a uniformly sloping crest line, but rather have relatively gently sloping upper surfaces and a steeply sloping nose or ridge front. Stations CBB and CBF are located on the noses or fronts of their respective ridges and therefore may experience similar amplifications at a level greater than might be expected from the model tests conducted on ridges having uniformly sloping crest lines.

The average horizontal responses of all stations (figure 2.11) show that at the high-frequency peak, stations CBB, CBC, and CBF all have peaks centered at the same frequency and having about the same amplitude. Each of these three stations is located either near the midpoint of the ridge crest or on the nose or front of the ridge, where amplification is expected to be greatest. Stations CBD and CBE have significantly lower amplitude responses, and, perhaps surprisingly, the response of CBE is lower than that of CBD. This may be because station CBD is actually located on the midpoint of the much larger ridge from which the smaller ridges emerge (this ridge peaks at the closed 150-m contour and slopes downward to the northwest), so CBD may be responding to the effects of the larger ridge, rather than responding as if it were at the peak of one of the smaller ridges (fig. 2.2).

At the low-frequency peak, the responses are less uniform. Stations CBC and CBF have peak responses of similar amplitude, but they are centered at different frequencies (3.7 and 2.3 Hz, respectively). Stations CBB and CBC have a similar peak response, but the other stations appear to have either a very broad peak response or, more likely, two closely spaced peak responses at about 2 and 4 Hz. This significant difference in the nature of the low-frequency response may relate to differences in ridge geometries, as discussed subsequently. As with the high-frequency peaks, station CBE has the lowest amplitude response, CBD the next lowest.

Comparison of all stations indicates the following:

1. The stations distant from the point where the ridges connect to the main hill experience the greatest amplification, whether they be at the midpoint of the crest line or on the exposed fronts of the ridges.

2. Station CBD may be responding to the effects of the geometry of the larger ridge on which it is located.

3. Station CBE, located where ridge E-F connects with the main hill, had the lowest amplification ratios in all cases.

Low-Frequency Versus High-Frequency Peak Responses

The most notable difference between the high- and low-frequency response peaks is that the high-frequency peaks are invariably narrower and more well defined than the low-frequency peaks. This holds true for all stations; the mean width of the high-frequency peaks is 1.6 Hz, and the mean width of the low-frequency peaks is 3.0 Hz, almost twice as wide. The peak amplifications, however, are very similar for the two peaks; the mean peak amplification ratio for the high-frequency response is about 9, and for the low-frequency response it is about 11. The high-frequency peaks are all centered at about the same frequency, 8.3 Hz, and have a standard deviation about this mean of only 0.23. The low-frequency peaks are not centered so uniformly: the mean center frequency is 3.2 Hz, and the standard deviation is 0.42, nearly twice as great as for high-frequency peaks (table 2.2).

Some of the low-frequency peaks, particularly those from stations CBD, CBE, and CBF, may actually contain two peaks, one at about 2.5 Hz and another at about 4.0 to 4.5 Hz. The broad, double-peaked shape of these responses, with a significant low point between peaks, suggests the possibility of two closely spaced but distinct peaks. This could account for the relatively broader, less consistently centered nature of the low-frequency response for these stations.

ANALYSIS OF PEAK AMPLIFICATION

Several researchers have modeled or documented topographic amplification of seismic waves (Boore, 1972, 1973; Bouchon, 1973; Davis and West, 1973; Rogers and others, 1974; Wong and Jennings, 1975; Griffiths and Bollinger, 1979; Brune, 1984; Sasaki and Kuwabara, 1986), but none have been able to provide quantitative conclusions regarding how to predict which frequencies will be either amplified or deamplified. Davis and West (1973) stated that "the amount of amplification and periods at which it occurs vary with the size of the mountain and are probably a function of the relationship between the wavelengths of the incoming signal and the dimensions of the mountain." A similar observation was made by Bouchon (1973), who stated that "the effect of topography on surface motion appears to be very important when the wavelength is of the order of the dimension of the anomally..." Brune (1984) reported on model tests of seismic amplification and showed that amplification is maximum at ridge crests, for vertically incident shear waves, and that it varies according to the ratio of the incoming wavelength and the width of the ridge. Sasaki and Kuwabara (1986) introduced a factor "*I*" to predict the resonant period of ridges:

$$I = HL/W(V_S), \tag{2.1}$$

where H, L, and W are the ridge height, length, and width, respectively, and V_S is the shear-wave velocity of the ridge material. They postulated that this factor I is about equal to the fundamental resonance period of ridges; any relationship of I to higher resonance modes is unclear.

Figure 2.12 shows a topographic map of the Canal Beagle area, and geometric constructions as recommended by Sasaki and Kuwabara (1986) to determine the dimensions of the ridges are shown. Dimensions are recorded in table 2.3, along with values of factor I for each ridge, for a shear-wave velocity of 700 m/s for the Pleistocene sediments composing the ridges at Canal Beagle. For ridge B-C, $I = 0.29$ s, which corresponds to a resonance frequency of 3.5 Hz; for ridge E-F, $I = 0.25$ s, which corresponds to a resonance frequency of 4.1 Hz. Figure 2.11 and table 2.2 indicate that stations CBB and CBC, located on ridge B-C, have low-frequency amplification peaks centered at 3.6 Hz, which corresponds closely to the value predicted by factor I. Stations CBE and CBF, located on ridge E-F have low-frequency peaks centered near 3.0 Hz, but as explained above, this broad low-frequency peak may in reality be two closely spaced but distinct peaks (see figure 2.11). If this is the case, the higher frequency of these two minor peaks is centered near 4.1 Hz, again the frequency predicted by factor I. These results suggest that the fundamental resonance frequencies of ridges B-C and E-F are 3.5 and 4.1 Hz, respectively.

The other peak responses cannot easily be explained by factor *I*, which is an aggregate measure of the total ridge geometry and accounts for all the dimensions of the ridges simultaneously. If we examine single dimensions of the ridges individually as they relate to the incident seismic wavelength, however, we may be able to better understand the locations of the other response peaks. Bouchon (1973) and Davis and West (1973) suggested that amplification probably occurs at wavelengths corresponding to the widths, heights, or lengths of topographic features. This hypothesis can be tested by setting the incident shear-wave length equal to each of these three dimensions for the two ridges and using the simple relationship

$$f = V_S / \lambda \qquad (2.2)$$

where f is the frequency, V_S is the shear-wave velocity, and λ is the wavelength. The computed frequency can then be located on figure 2.11 to determine if it coincides with an amplification peak. Assuming a shear-wave velocity of 700 m/s for the Pleistocene sediments, frequencies corresponding to wavelengths equal to the ridge dimensions are shown in table 2.4. For ridge B-C, the height corresponds to a frequency of 8.2 Hz, very near the center of the high-frequency peaks of stations CBB and CBC (figure 2.11, table 2.2). The width of ridge B-C corresponds to a frequency of 3.5 Hz, which coincides with the centers of the low-frequency peaks for stations CBB and CBC; this frequency also coincides with the resonance frequency of ridge B-C as estimated by *I*. For ridge E-F, the height corresponds to a frequency of 7.8 Hz, close to the center of the high-frequency peaks of stations CBE and CBF; the ridge width corresponds to a frequency of 2.0 Hz, near the centers of the lower of the two low-frequency peaks of CBE and CBF.

These results appear to explain the difference in the nature of the low-frequency peaks of ridges B-C and E-F. Stations CBB and CBC have relatively narrow, well defined low-frequency response peaks, presumably because the overall resonance frequency of the ridge, predicted by factor *I*, coincides with the frequency of the wavelength-matching effect of the ridge width. Stations CBE and CBF have broader, more diffuse low-frequency peaks that appear to be the merging of two closely spaced but distinct peaks. This is explained by the overall resonance frequency from factor *I*, 4. 1 Hz, being significantly different from the frequency of the matching wavelength of the ridge width, 2. 0 Hz. These two frequencies correspond to the two minor peaks within the broad low-frequency peak for these two stations.

The frequencies corresponding to the lengths of both ridges do not coincide with amplification peaks from any of the stations (figure 2. 11, table 2. 2). This may be because the data are highly variable and not well constrained at such low frequencies for this experiment, or it could indicate that the long dimensions of topographic features are not as greatly affected by wavelength-matching as are the two shorter dimensions.

CONCLUSIONS

All of the stations show approximately similar amplification responses in that they have two frequency ranges where the amplification ratios exceed 2. 0, one peak being centered around 3-4 Hz, the other around 8-9 Hz. Many of the minor differences discussed herein may be insignificant or at least unexplainable at present. The most significant difference in the amplification responses is that stations on ridge E-F have a broad, two-peaked response in the 3-4 Hz range, whereas stations on ridge B-C have narrower peaks in that range. The effects of resonance of the entire ridges, having frequencies predicted by factor *I* of Sasaki and Kuwabara (1986), together with wavelength matching at frequencies corresponding to the heights and widths of the ridges, appear to explain the amplification responses of stations on both ridges.

The greatest amplification ratios were recorded at stations located near the midpoints of the ridge crest lines and on the exposed fronts of ridges. Amplification ratios exceeding 20 were computed for some stations at some frequencies, and peak ratios exceeding 10 were common. Results of this experiment reported by Celebi (1986) show that ground motions on topographic ridges can be amplified by a large amount in frequency ranges related to the ridge geometry.

TABLE 2.1
Canal Beagle Experiment Stations

(from Celebi, 1986).

Station	Description
Site Stations:	
CBA	At ground floor (no basement) of Type B* structure founded on a clear cut at canyon between two ridges. The structure and its twin next to it were not damaged. Geologic formation: sedimentary. (Building #1)
CBB	At ground floor of a Type B* structure on top of ridge where there is extensive damage. Geologic formation: Sedimentary and decomposed granite. (Building #7)
CBC	(Same as above, CBB.) (Building #12)
CBD	At ground floor of a Type A* (single story) structure. This part of Canal Beagle is on the main body of the hill crowned by the ridges. (699 Ventisquero Street - at corner of Canal Kivke Street)
CBE	At ground floor (no basement) of Type C* (all 5 stories) structure located on top of emerging portion of the ridge. (Building #4 - Edificio Thomson)
CBF	At ground floor (no basement) of Type C* (all 5 stories) structure located at the top of the ridge. (Building #15 - Edificio Hyatt)
Reference Stations:	
VAL	On a concrete pedestal at the University of Santa Maria. Same location as the SMA station of the Chilean strong motion network. The site is amphibolite and granite gneiss formation.

---

* There are three types of structures in Canal Beagle. Type A structures are single and two-story buildings on top of the hill, whereas Type B structures are four-story buildings on one ridge and Type C structures are five-story buildings on another ridge. Two of the Type B structures are in a canyon at the entrance to the subdivision.

Table 2. 2. Characteristics of amplification peaks.

LOW-FREQUENCY PEAK							HIGH-FREQUENCY PEAK						
STATION⁄ COMP.	LOWER LIMIT (Hz)	UPPER LIMIT (Hz)	WIDTH (Hz)	CENTER POINT (Hz)	PEAK POINT (Hz)	AMPLIFICATION RATIO	STATION⁄ COMP.	LOWER LIMIT (Hz)	UPPER LIMIT (Hz)	WIDTH (Hz)	CENTER POINT (Hz)	PEAK POINT (Hz)	AMPLIFICATION RATIO
CBB⁄E-W	2. 9	4. 4	1. 5	3. 7	3. 8	9x	CBB⁄E-W	7. 5	8. 8	1. 3	8. 2	8. 2	8x
CBB⁄N-S	2. 3	5. 5	3. 2	3. 9	4. 1	9x	CBB⁄N-S	7. 4	9. 1	1. 7	8. 3	8. 3	18x
CBB⁄AVE.	2. 5	4. 8	2. 3	3. 7	3. 9	8x	CBB⁄AVE.	7. 4	9. 1	1. 7	8. 3	8. 3	11x
CBC⁄E-W	1. 9	4. 6	2. 7	3. 3	3. 7	24x	CBC⁄E-W	6. 8	9. 0	2. 2	7. 9	8. 2	10x
CBC⁄N-S	1. 8	4. 8	3. 0	3. 3	4. 3	15x	CBC⁄N-S	7. 4	9. 3	1. 9	8. 4	8. 2	15x
CBC⁄AVE.	2. 0	4. 8	2. 8	3. 4	3. 7	15x	CBC⁄AVE.	7. 2	9. 1	1. 9	8. 2	8. 2	11x
CBD⁄E-W	1. 3	4. 1	2. 8	2. 7	3. 4	6x	CBD⁄E-W	7. 7	8. 8	1. 1	8. 3	8. 2	6x
CBD⁄N-S	1. 4	5. 1	3. 7	3. 3	2. 4	10x	CBD⁄N-S	7. 8	9. 5	1. 7	8. 7	8. 4	8x
CBD⁄AVE.	1. 4	4. 3	2. 9	2. 9	1. 9	6x	CBD⁄AVE.	7. 8	9. 6	1. 8	8. 7	8. 4	5x
CBE⁄E-W	1. 3	4. 1	2. 8	2. 7	2. 3	4x	CBE⁄E-W	7. 7	8. 3	0. 6	8. 0	8. 1	3x
CBE⁄N-S	2. 0	4. 6	2. 6	3. 3	4. 4	6x	CBE⁄N-S	7. 6	9. 1	1. 5	8. 4	8. 4	5x
CBE⁄AVE.	1. 9	4. 5	2. 6	3. 2	2. 6	3x	CBE⁄AVE.	7. 6	8. 9	1. 3	8. 3	8. 0	4x
CBF⁄E-W	1. 0	4. 4	3. 4	2. 7	2. 2	16x	CBF⁄E-W	7. 2	9. 0	1. 8	8. 1	7. 8	8x
CBF⁄N-S	1. 3	5. 6	4. 3	3. 5	2. 4	14x	CBF⁄N-S	7. 5	9. 2	1. 7	8. 4	8. 3	12x
CBF⁄AVE.	1. 3	4. 6	3. 3	3. 0	2. 3	13x	CBF⁄AVE.	7. 4	9. 1	1. 7	8. 3	7. 9	9x

Table 2. 3. Ridge dimensions and "*I*" values (shear-wave velocity 700 m/s).

RIDGE	HEIGHT (m)	WIDTH (m)	LENGTH (m)	FACTOR *I* (sec)	FREQUENCY (Hz)
B-C	85	200	475	0. 29	3. 5
E-F	90	345	660	0. 25	4. 1

Table 2.4. Frequencies corresponding to wavelengths equal to ridge dimensions (shear-wave velocity 700 m/s).

RIDGE	DIMENSION	VALUE (m)	FREQUENCY (Hz)
Ridge B-C			
	Height	85	8.2
	Width	200	3.5
	Length	475	1.5
Ridge E-F			
	Height	90	7.8
	Width	345	2.0
	Length	660	1.1

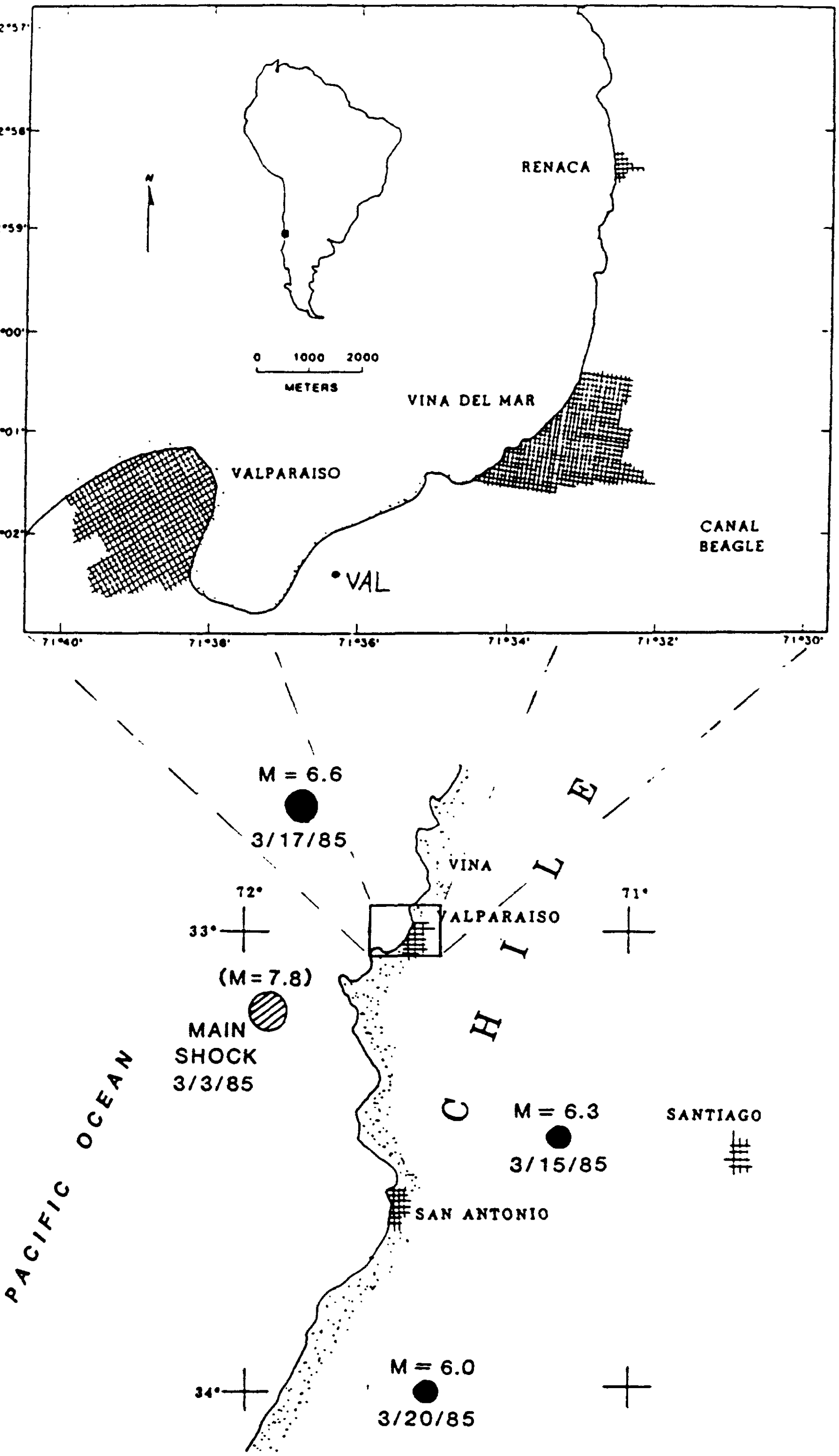

Figure 2.1 Location map showing main shock and largest aftershocks. (adapted from Celebi, 1986)

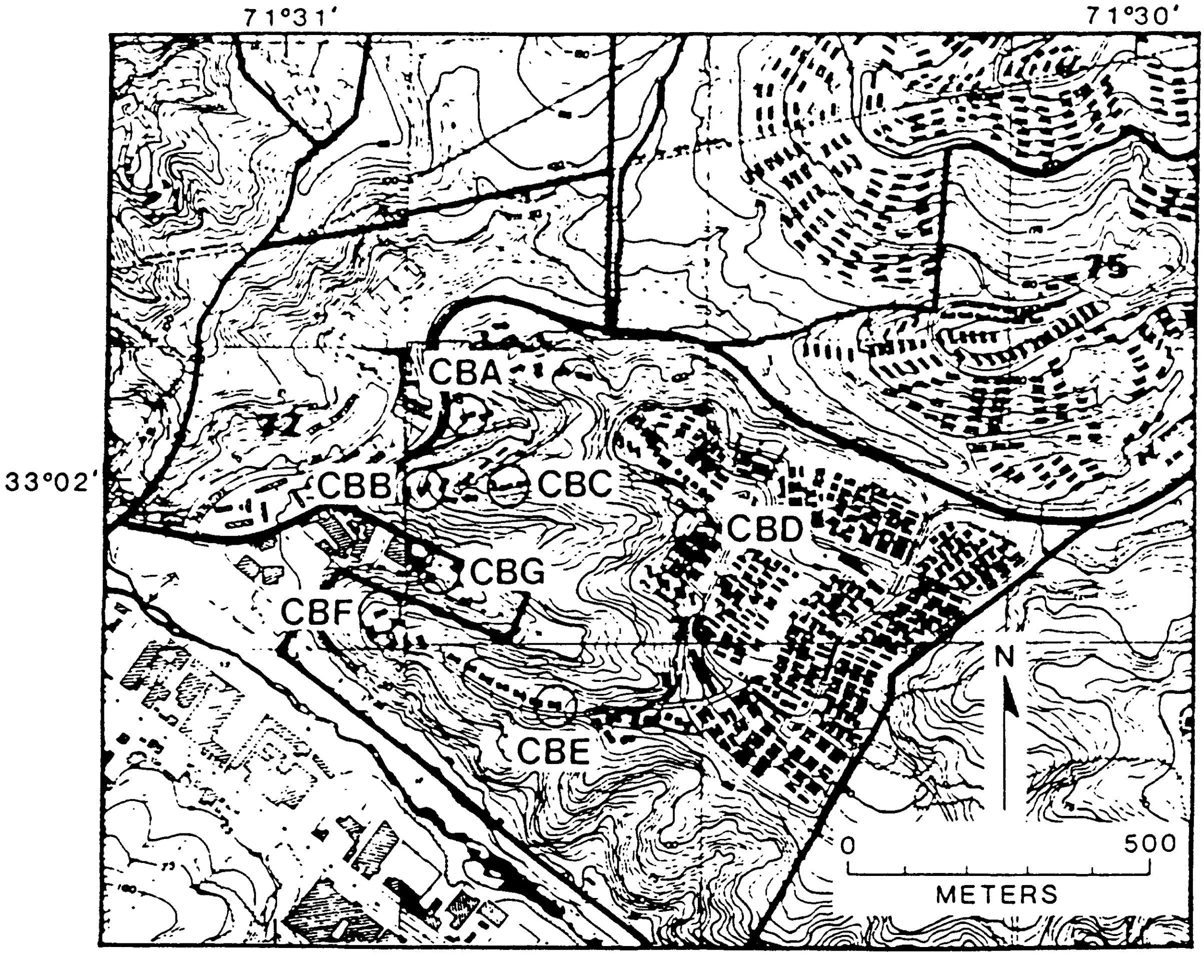

Contour interval 5 m

Figure 2.2 Detailed topography of Canal Beagle. The stations of the Canal Beagle site are indicated. Also a general scale and the latitudes and longitudes are shown. (from Celebi, 1986)

Figure 2.3

CBA/VAL

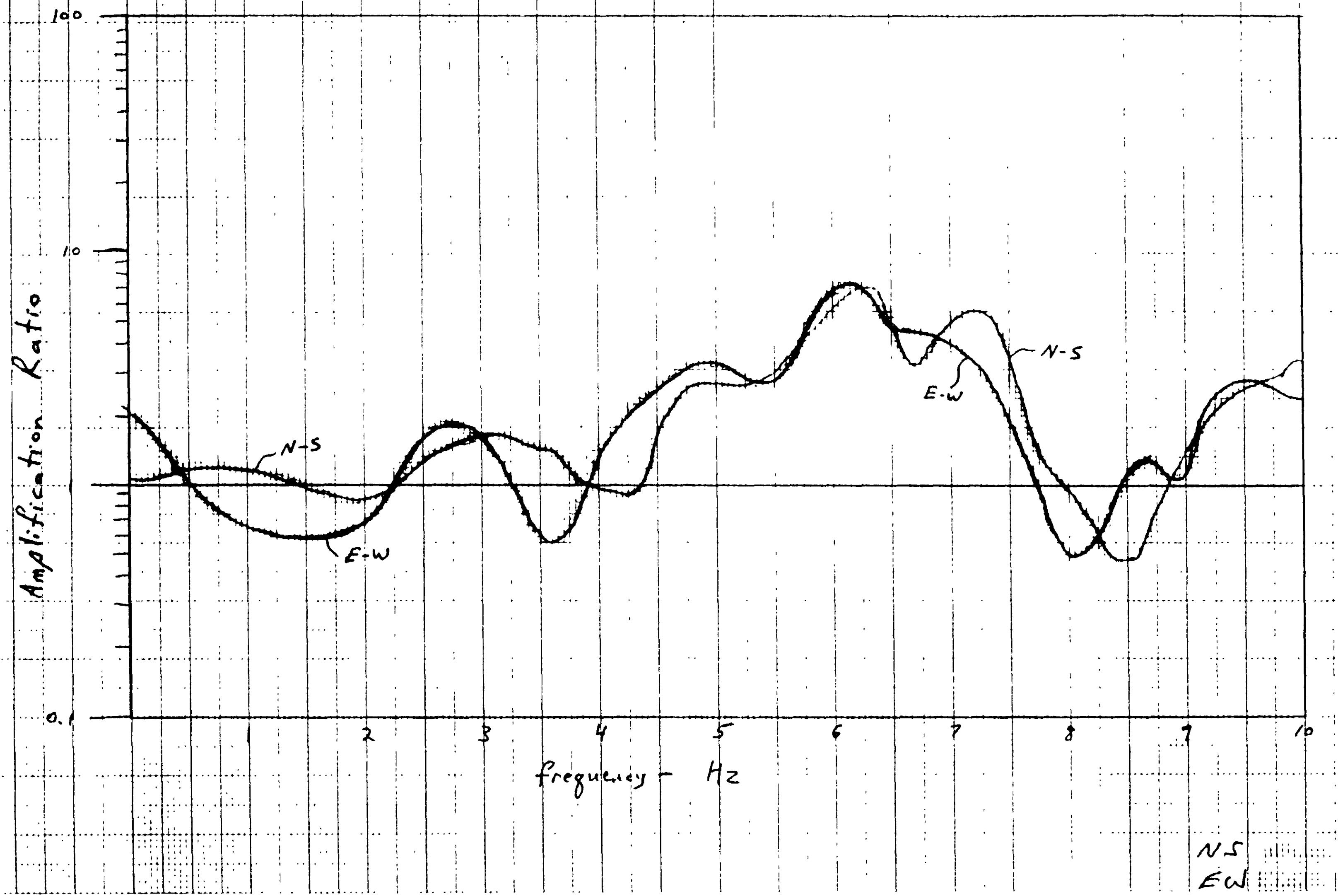

Figure 2.4

CBB/CBA

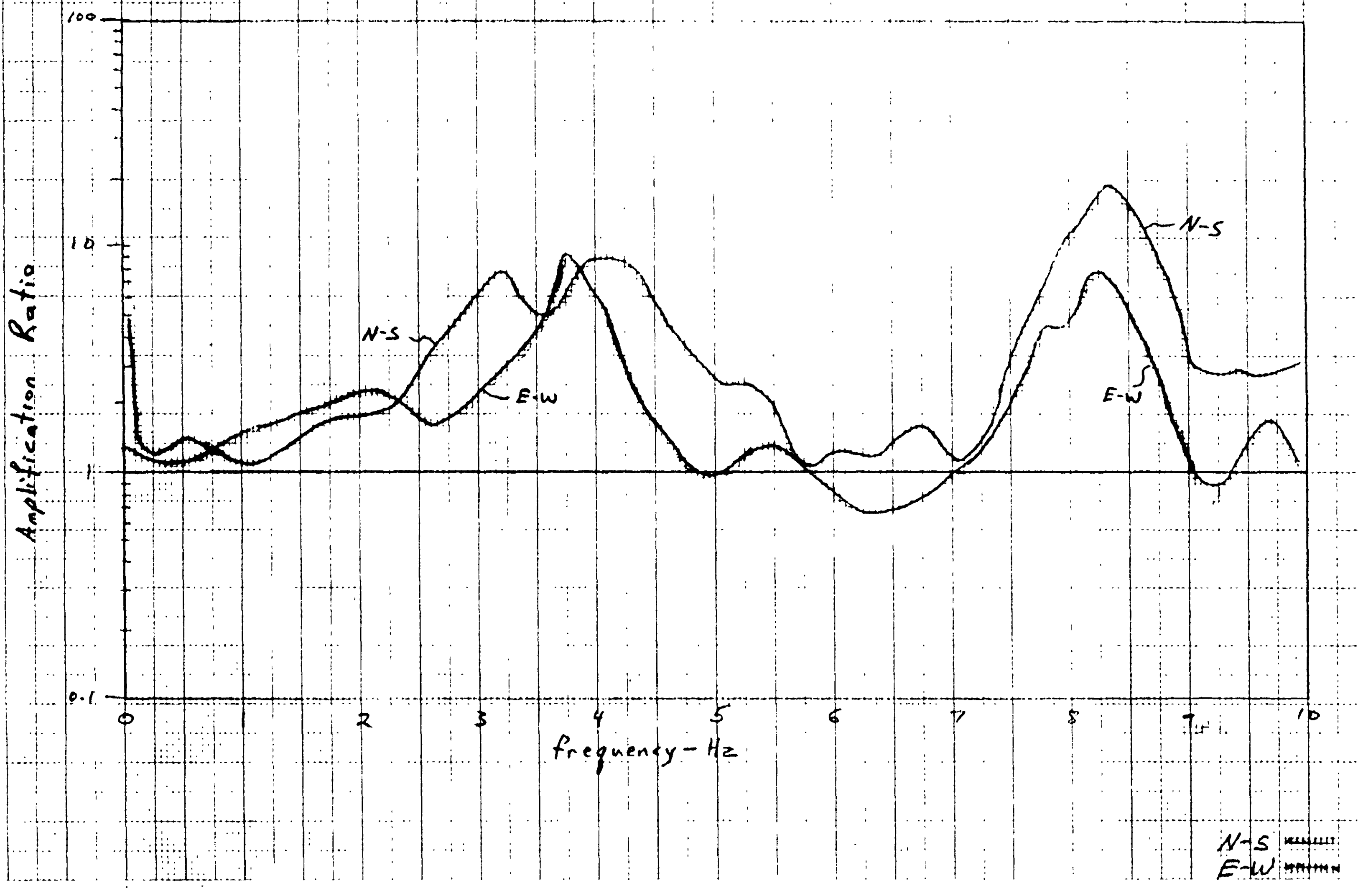

Figure 2.5

CBC/CBA

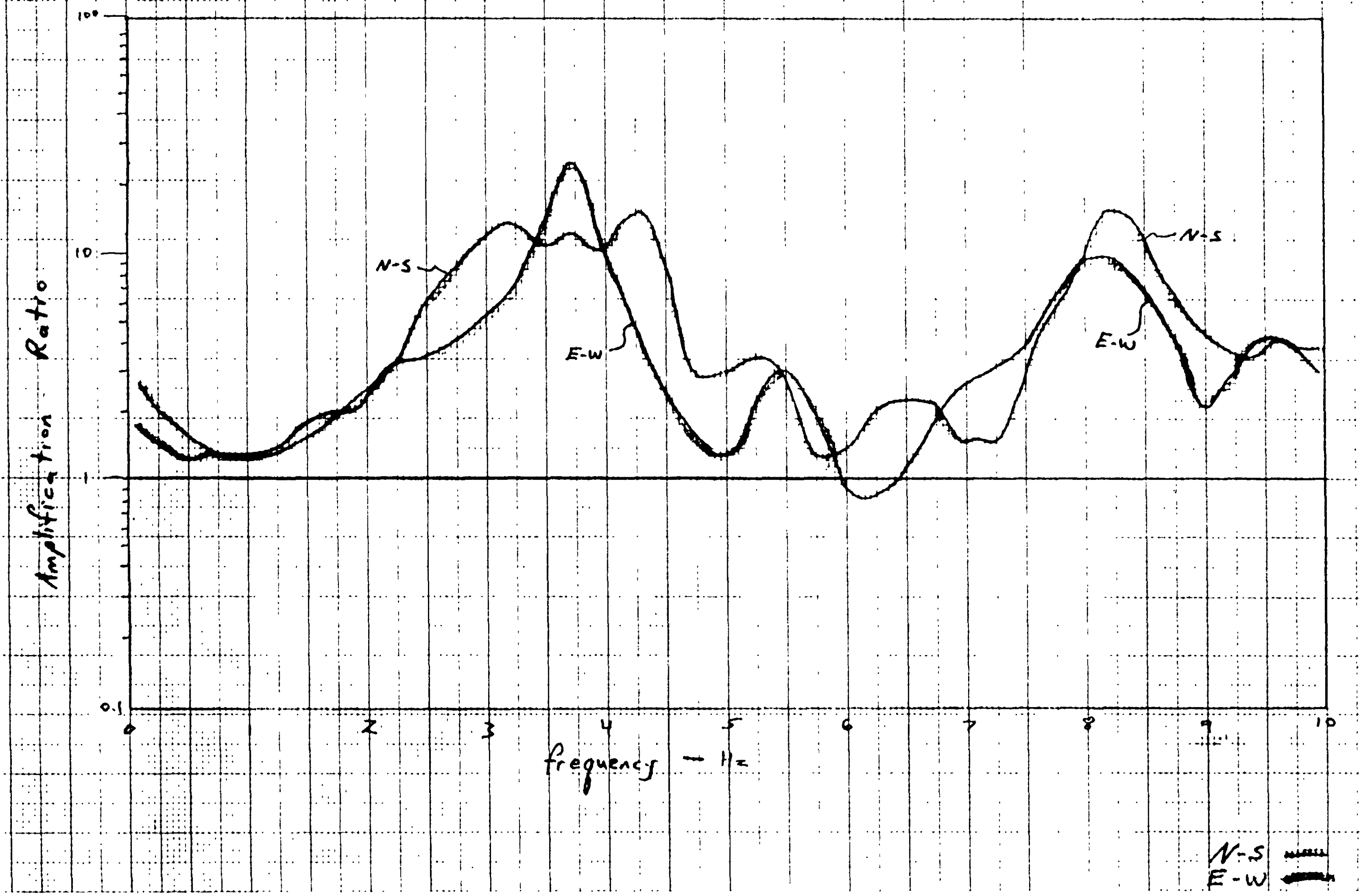

Figure 2.6

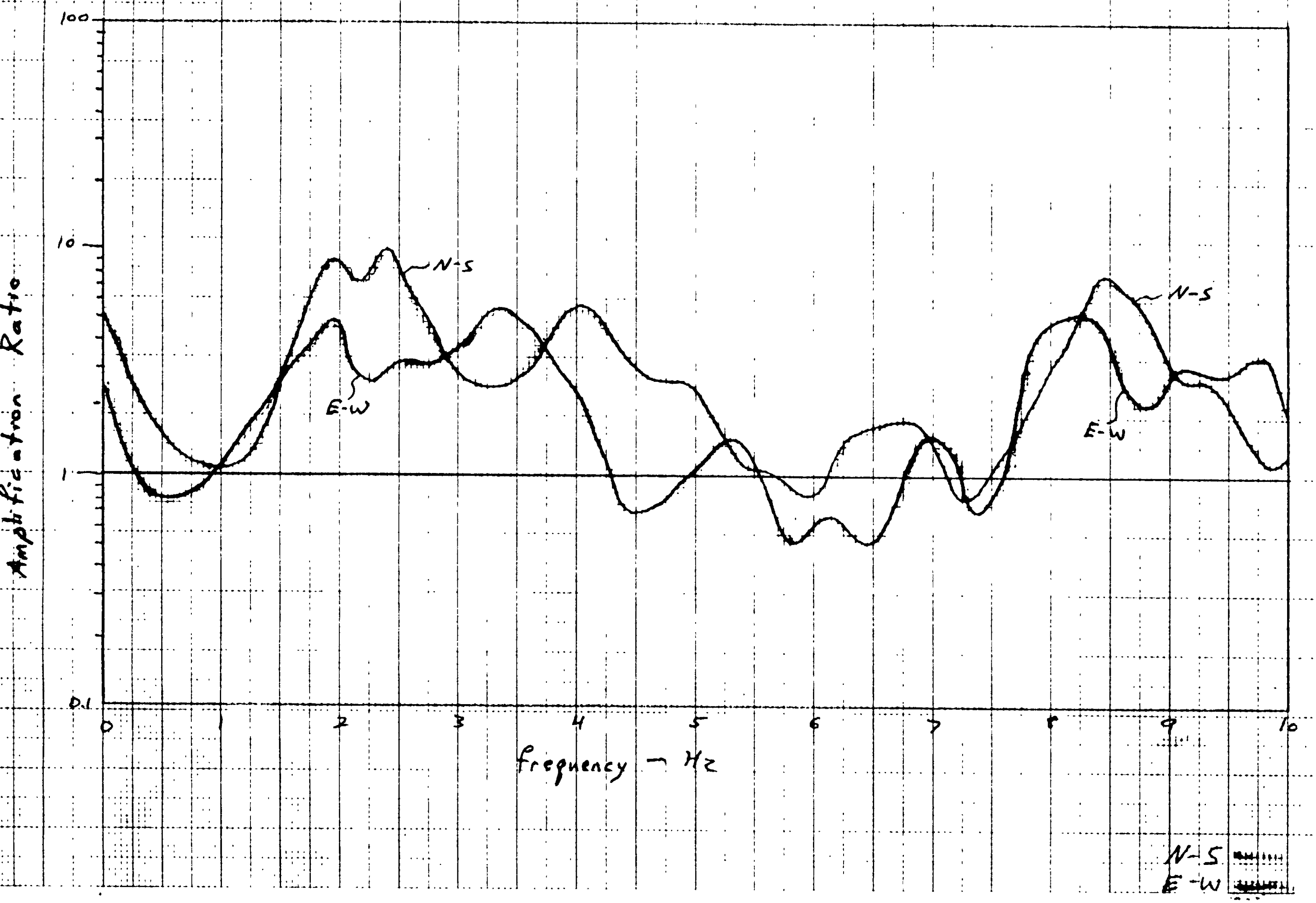

CBD/CBA

Figure 2.7

CBE/CBA

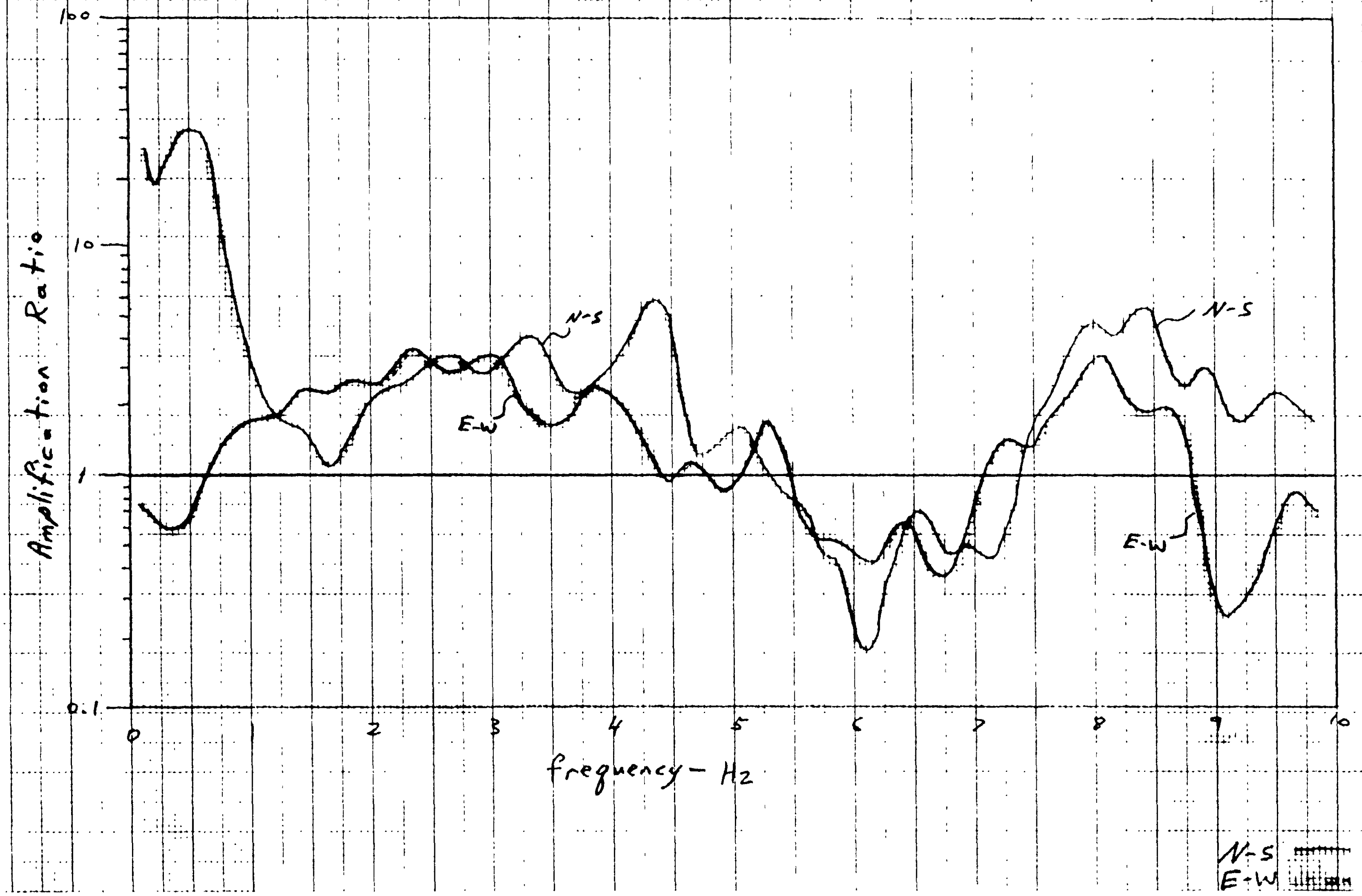

Figure 2.8

CBF/CBA

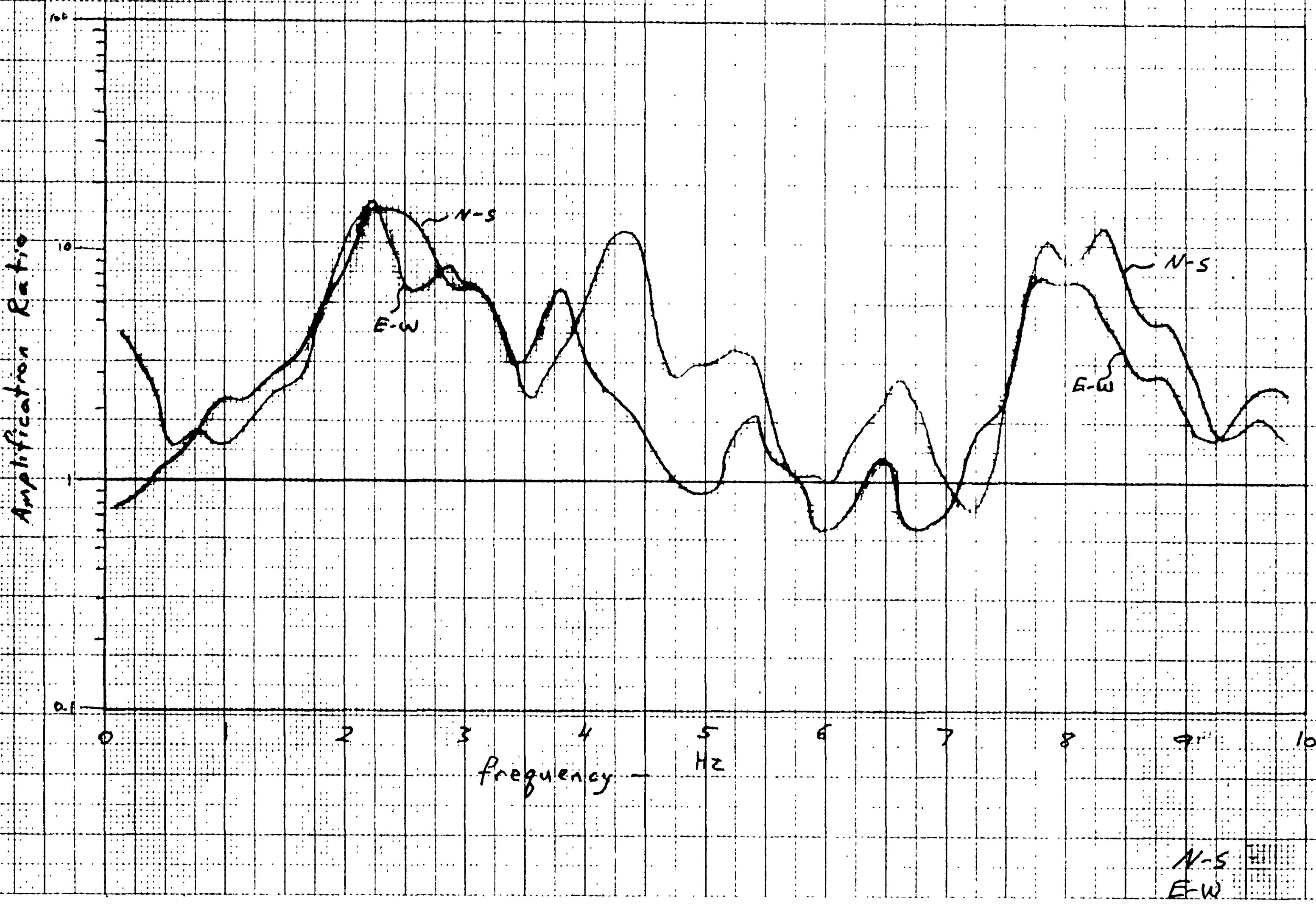

Figure 2.9

East-West components

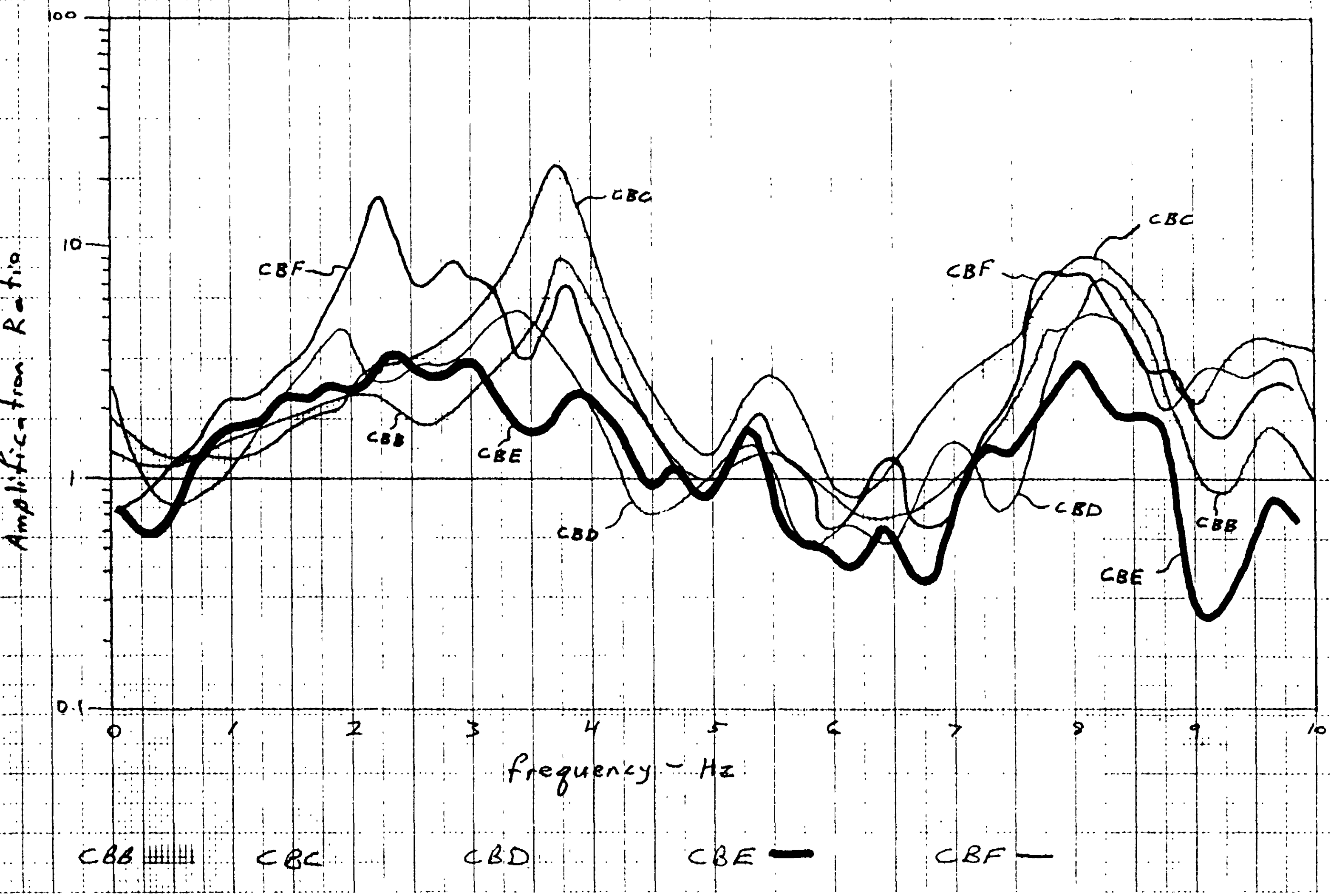

Figure 2.10

North-South components

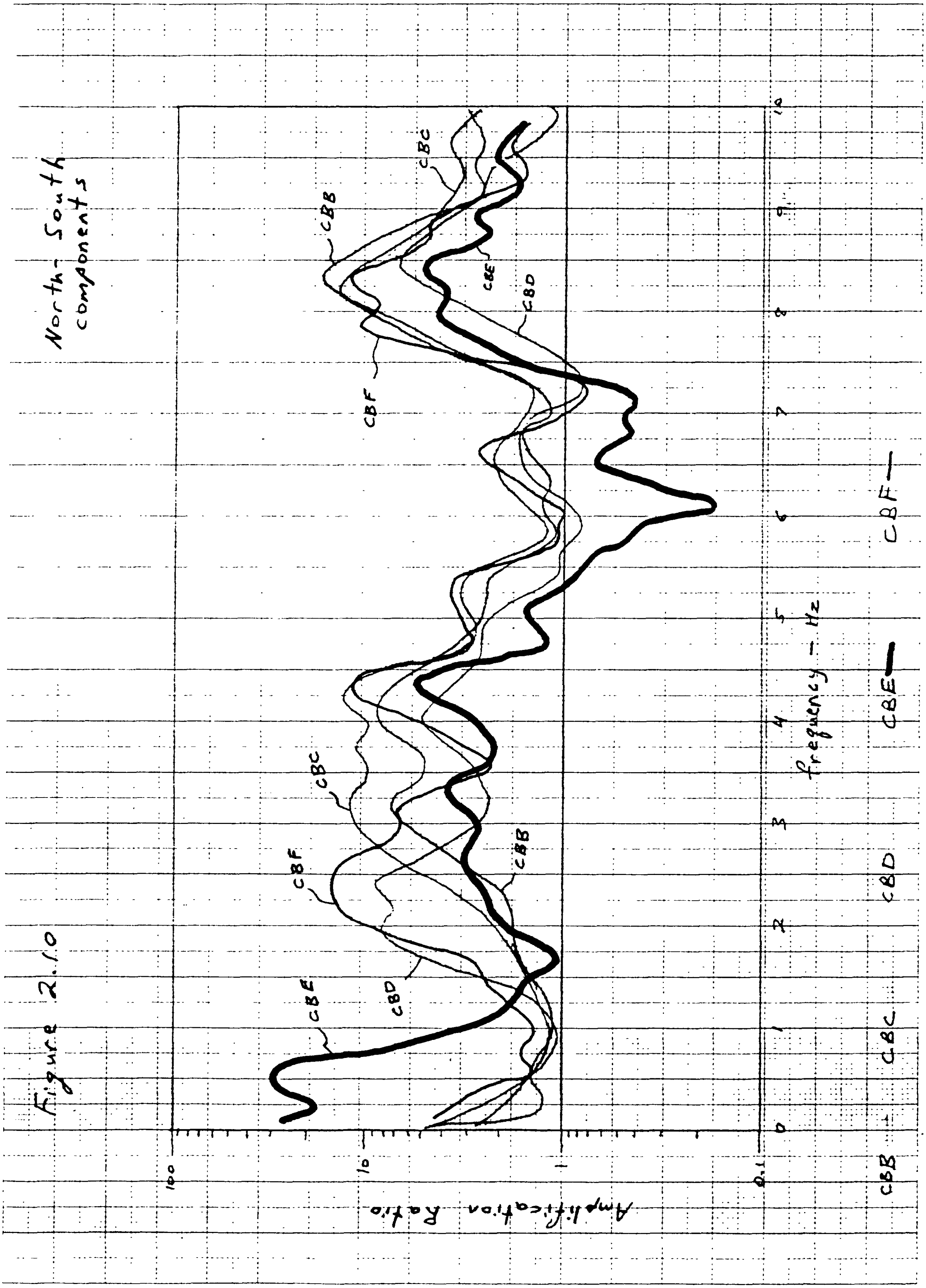

Figure 2.11

Average Horizontal

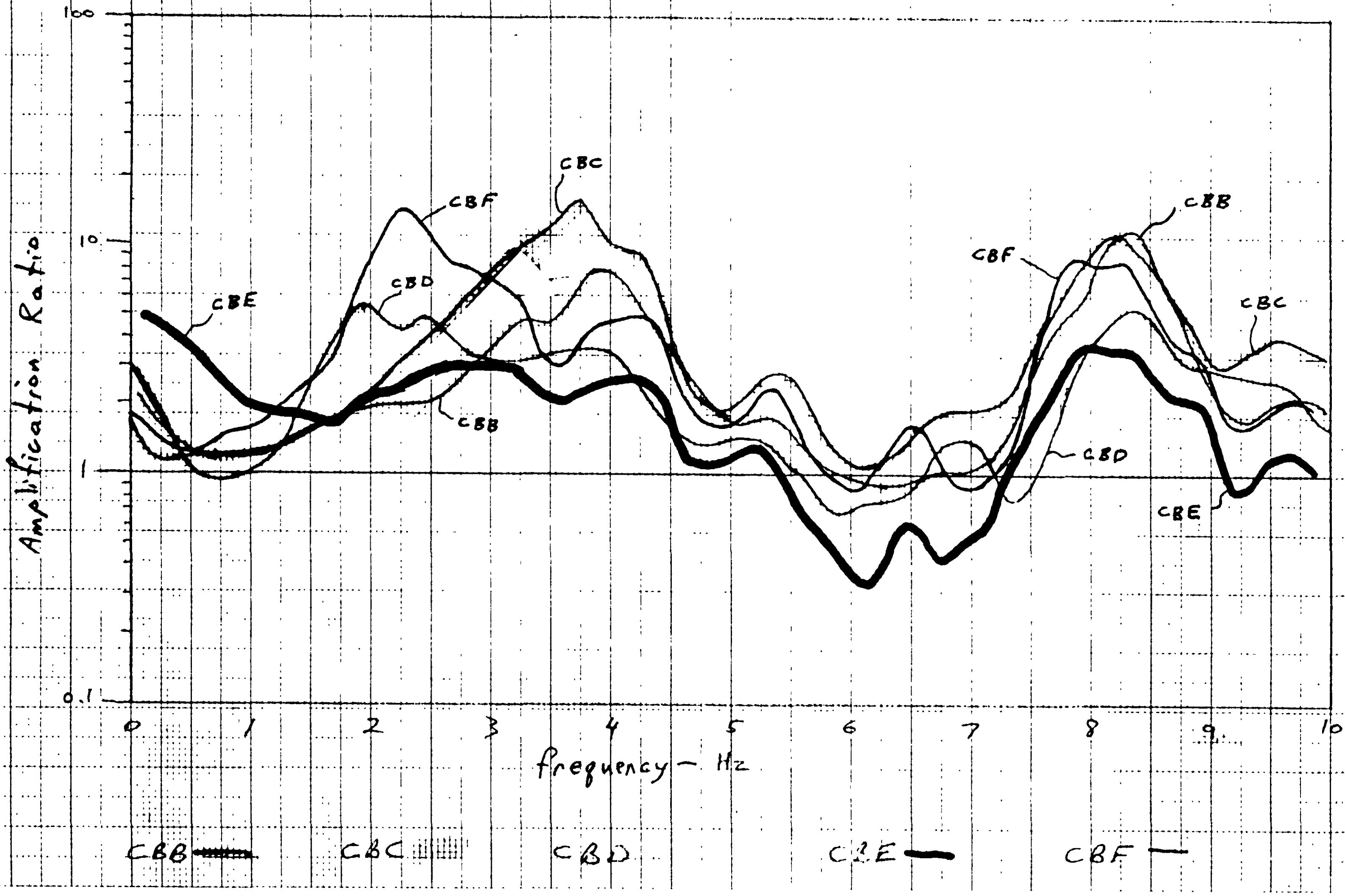

Figure 2.12. Geometric constructions to measure ridge dimensions.

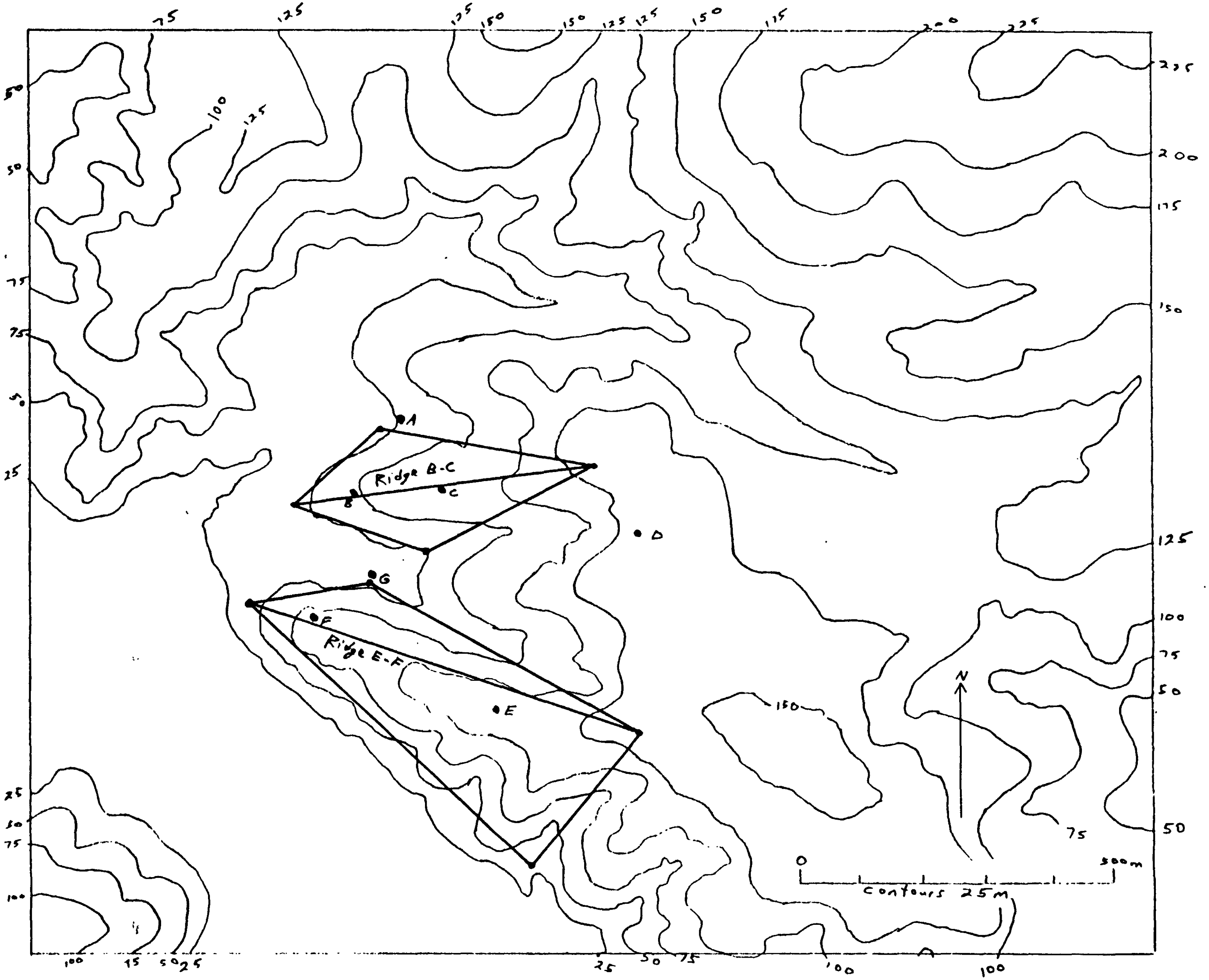

PART 3

Comparison of Results of Slope Model Tests with Field Studies of Topographic Amplification of Ground Shaking

PART 3

Comparison of Results of Slope Model Tests with Field Studies of Topographic Amplification of Ground Shaking

INTRODUCTION

In January and February 1987, a series of model tests were designed and conducted by personnel in the Ground Vibration Division of the Public Works Research Institute (PWRI), Tsukuba Science City, Japan, to observe the effects of topography on the amplification of earthquake ground motion. The present paper (Part 3) compares the results of the model tests with results from the seismic site-response experiment conducted after the 1984 Central Chile earthquake (Celebi, 1986, in press; Part 3) and with data from the dense seismic array at Matsuzaki, Japan. What follows is not a rigorous analysis of the model-test results but rather a summary for comparison with the field-study results.

DESCRIPTION OF MODEL TESTS

Six slope models having different geometries were manufactured for testing on the 6x8-m shaking table at PWRI. The models were constructed of transparent silicon having a shear-wave velocity of approximately 1237 mm/s, and 12 miniature accelerometers were placed on the outer surfaces or within each of the silicon models. Figure 3. 1 shows the generalized geometry of all the models and the nomenclature for measuring their geometries, and figures 3. 2-3. 7 show scaled drawings of models 1-6, respectively, including the locations and channel numbers of the accelerometers mounted on each model. Table 3. 1 lists the overall dimensions of each of the models.

The models were exposed to one horizontal component of ground shaking at a time and were shaken in directions perpendicular to the long dimensions of the models (transverse shaking) and parallel to the long dimensions of the models (longitudinal shaking). Tests were conducted at frequencies ranging from 3-60 Hz and having constant zero-to-peak acceleration of about 200 gal. A sinusoidal waveform was used. Two types of tests were conducted: (1) sweeping-frequency tests where the frequency of the ground motion increased 1 Hz/s from 3-60 Hz, and (2) constant-frequency tests conducted at 0.5-Hz intervals from 3-60 Hz. Test results were summarized in the frequency domain by plotting the ratio of the recorded acceleration for each channel to the input acceleration measured on the rigid base of the shaking table.

ANALYSIS OF FREQUENCY-DOMAIN TEST RESULTS

Figures 3.8-3.13 show the frequency-domain acceleration ratios for transverse shaking recorded on all accelerometers for models 1-6, respectively. All models displayed similar responses: the fundamental resonance frequency is about 14-15 Hz, and the response peaks for this resonance mode differ by no more than 1.5 Hz between models. Second-mode peaks of smaller amplitude are less consistently located, but are generally between 20-25 Hz. Figures 3.14-3.18 show frequency-domain acceleration ratios for longitudinal shaking for models 1-5, respectively. The models all had fundamental resonance frequencies of about 16-17 Hz and secondary peaks centered between 30-35 Hz.

The similarity of the responses of model slopes having significantly different geometries indicates that the fundamental resonance frequency is controlled by one or more of the inter-related geometric parameters held constant for all models. These parameters include the maximum vertical cross-sectional height or thickness (figure 3.1, dimension *T*); the 45° angle of the rigid backslope to which the model is attached; and, more approximately, the slope length measured along the crestline (figure 3.1, dimension *S*). Thus, overall slope height, width, and horizontal length (figure 3. 1, dimensions *H*, *W*, and *L*, respectively), the dimensions related by Sasaki and Kuwabara (1986) (see Part 2) through a factor "*I*" to predict the fundamental resonance frequency, appear unrelated to the fundamental resonance frequency in the model tests. This observation is confirmed by calculating values of factor *I* for each of the models. Table 3. 2 shows *I*-values calculated in several different ways for each of the models. The fundamental resonance period of the models as measured by the shaking-table tests ranges from 0. 067 to 0. 071 s. None of the values listed in table 3. 2 are close to this range, and most differ by a large amount.

To detect any minor response differences between slope models, I compared the responses of the six models channel by channel for the case of transverse shaking. Figures 3. 19-3. 30 show the responses for channels 3-14, respectively, as located on model 1 (different, but analogous, channels were plotted in some cases for models 3 and 6 because transducers on these models were arranged somewhat differently). Two types of systematic response differences were investigated: (1) differences in responses between models having different crestline slope angles (figure 3. 1, angle α) when the angle of the side slopes (figure 3. 1, angle β) is constant, which requires comparison of models 1, 2, 3, and 6; and (2) differences in responses between models having different side-slope angles when the crestline angle is constant, which requires comparison of models 1, 4, and 5.

To document any systematic effects of increasing crestline angle on the fundamental resonance frequency, I examined figures 3. 19-3. 30 and recorded those instances where the model peak responses increased or decreased in frequency consistently with increasing crestline angle (crestline angle increases in the model sequence 3-2-1-6). Observations are summarized in table 3. 3. Channels 6, 12, 13, and 14 (figures 3. 22, 3. 28-3. 30) showed slight but systematic decreases in the fundamental resonance frequency with increasing crestline angle; channels 9 and 10 (figures 3. 25, 3. 26) showed slight increases in the fundamental resonance frequency with increasing crestline angle. The remaining channels showed no systematic response differences. For the secondary response peaks, only channels 10 and 11 showed systematic differences: the peak frequency increased slightly with increasing crestline angle. Thus, even these minor response differences vary inconsistently.

Examination of the effects of increasing the side-slope angle (model sequence 5-1-4) shows that channels 6, 7, and 9 (figures 3. 22, 3. 23, 3. 25) all display slight systematic decreases in the fundamental resonance frequency with increasing side-slope angle. The other channels show no systematic differences. For the secondary response peak, channels 6, 7, and 9 show decreases, and channel 4 (figure 3. 20) shows an increase in the resonance frequency with increasing side-slope angle. Thus, in the majority of cases where systematic differences are present, increasing either crestline angle or side-slope angle results in very slight decreases in the fundamental and secondary resonance frequencies. It must be remembered, however, that most channels showed no systematic differences between the models, and that those differences that do exist are slight and not entirely consistent. One reason for this inconsistency is that each accelerometer is measuring the response of a different part of the resonating model.

Systematic variations in the amplification ratio were also investigated (table 3. 3). For the case of increasing crestline angle, channels 9, 10, 12, 13, and 14 (figures 3. 25, 3. 26, 3. 28-3. 30) all showed systematic increases in the amplification ratio; channel 6 (figure 3. 22) showed a systematic decrease in the ratio. For the secondary response peaks, channel 10 showed an increase, and channel 11 (figure 3. 27) showed a decrease in amplification ratio with increasing crestline angle. Other channels showed no systematic variations in either response peak.

For the case of increasing side-slope angle, channel 6 (figure 3. 22) showed a increase and channels 7 and 9 (figures 3. 23, 3. 25) decreases in amplification ratio. For the secondary response peaks, channels 4, 6, 7, 9, and 11 (figures

3.20, 3.22, 3.23, 3.25, 3.27) all showed systematic increases in amplification ratio with increasing side-slope angle.

The variations in amplification ratio with changing slope geometry are of much more significant magnitude than the variations in frequency. Whereas peak response frequencies vary by no more than 1.5 Hz between models, amplification ratios for a given channel location vary between models by factors as great as 2. The majority of the data suggest that increasing the crestline angle tends to increase the amplification ratio for the fundamental resonance mode; increasing the side-slope angle tends to decrease the amplification ratio for the fundamental resonance peak, but it tends to increase the ratio for the secondary response peak. The data, however, are not entirely consistent.

The most significant and consistent factor affecting the magnitude of the amplification ratio is the vertical distance from the rigid model base to the accelerometer. Figure 3.31 shows amplification ratio plotted against accelerometer height for all channels having a response peak at the fundamental resonance frequency (14-15 Hz). The solid line is the "best-fit" from a standard linear regression; it has a correlation coefficient (r) of 0.93 and is thus well fitted to the data. The amplification ratio for an accelerometer height equal to zero is 0.64, which is reasonably close to the value of 1.0 intuitively expected at the rigid base of the model. The dashed line in figure 3.31 is constrained to have an amplification ratio of 1.0 at zero accelerometer height and was visually fitted to the data. Thus, the model tests confirm theory and intuition that amplification of ground motion is maximum at the highest points of ridges. These results also agree with results from Brune (1984) that showed a consistent increase in the amplification ratio from the base to the apex of a ridge model similar in shape to those tested at PWRI.

In most cases, for a given accelerometer height, accelerometers located along the longitudinal axis of the models displayed greater amplifications than accelerometers located along the flanks of the ridges. This phenomenon was not consistent throughout the data, however.

SPATIAL VARIATION IN ACCELERATION

One way in which topographic amplification of ground motion can lead to ground failure is by increasing the inertial forces acting to drive potential landslide blocks downslope. This effect can be examined by plotting the spatial variation in acceleration for each of the models. This section discusses the variation in acceleration ratios between (1) accelerometers located along the model ridge crests and (2) accelerometers aligned vertically along the centerlines of the maximum vertical cross-sections.

Variation Along Ridge Crests

For each of the model cases (1-6), I plotted the acceleration ratio for each accelerometer located on the crestline as a function of its proportional distance along the crestline from the base to the top of the ridge. Data are plotted for each frequency at which any of the accelerometers along the crestline had peak responses. Data from transverse as well as from longitudinal ground vibration are plotted as figures 3. 32-3. 37 and 3. 38-3. 42, respectively. No data from case 6 for longitudinal shaking is available. Figures 3. 43 and 3. 44 summarize the data for transverse and longitudinal ground shaking, respectively, by showing acceleration-ratio plots for the three major response peaks (peak1, peak 2, peak 3) for each of the six cases. The frequency ranges of these peaks is indicated on the figures.

Figure 3. 43 shows that the peak-1 reponses of each of the models subjected to transverse ground shaking are essentially identical: a single acceleration-ratio maximum of 5-7 centered between 0. 4 and 0. 6 of the way from the base to the top of the crestline. This shows that the maximum acceleration in the fundamental resonance mode is at the center of the crestline. Examining cases 3-2-1-6 shows the effects of increasing the crestline angle, which appears to

cause the acceleration maximum to be centered successively lower along the crestline. Increasing the side slope angle (cases 5-1-4) has no discernable effect.

The peak-2 responses are less consistent. Cases 3 and 6, at the extremes of the range of crestline angle, show a distinctive two-peaked response centered near the one-third points along the crestline. Case 2 has a broad, single-peaked response centered at 0. 5. Cases 1, 4, and 5 have responses intermediate between those previously described, but are similar to each other in that the peak response is at about 0. 3. These latter three cases have the same crestline angle but differing side-slope angles, and the plots suggest that increasing the side-slope angle increases the peak acceleration ratio from about 3. 8 to about 5. 4. On average, acceleration ratios for peak 2 are less than those for peak 1.

All of the plots for peak 3 show similar two-peaked shapes centered close to the one-third points. No systematic variations in the responses with differing crestline angle or side slope-angle are evident. Acceleration ratios, on average, are roughly the same as those for peak 2.

Figure 3. 44 shows peak responses from longitudinal ground shaking for cases 1-5. The peak-1 plots are very similar to those of figure 3. 43: single-peak responses centered near the midpoint of the crestline. As is the case for transverse ground shaking, increasing the crestline angle (cases 3-2-1) moves the peak response lower along the crestline. Peak acceleration ratios range from about 4. 5 to 6. 5.

The peak-2 plots in figure 3. 44 show two-peaked responses that are asymmetrical, the peak lower along the crestline generally having the greatest acceleration ratio. Maximum acceleration ratios range from about 2 to 4, and increasing the crestline angle appears to cause a decrease in the peak response.

Only cases 1, 4, and 5 yielded valid data in the frequency range of peak 3. All cases show two-peaked responses having very low (less than 2) acceleration ratios.

These data for both transverse and longitudinal ground shaking show that the maximum acceleration ratios occur between about 0.2 and 0.8 of the way from the base to the top of the crestline. Between these points, however, locations of acceleration maxima vary considerably. In the fundamental mode (peak 1) the maxima are near the crestline midpoint; in higher frequency modes (peaks 2 and 3) the maxima are located near the one-third points, but locations can vary significantly. Acceleration ratios for peak 1 tend to be the greatest. In the case transverse ground shaking, acceleration ratios for peaks 2 and 3 are slightly less than those for peak 1; in the case of longitudinal shaking, they are much less than those for peak 1.

Variations Along the Maximum Vertical Cross Section

Acceleration ratios for accelerometers located along the vertical line bisecting the maximum vertical cross section were plotted in a manner similar to that explained in the previous section. Only data for transverse ground shaking was recorded. Figures 3.45-3.50 show plots for cases 1-6, respectively; data were plotted from frequencies at which any of the accelerometers along the vertical section had peak responses. Figure 3.51 summarizes these data by showing plots of the three major response peaks for each of the six cases.

The peak-1 acceleration ratios range from 4-7, and in all cases the acceleration increases from the base to the top of the ridge, though not linearly. No significant differences attributable to changing ridge geometry are evident.

The peak-2 acceleration ratios, ranging from about 1.5 to 4, are generally less than those for peak 1. The response shape is distinct from that of peak 1 but is similar for each of the six cases. As in the previous case, maximum accelerations are at the ridge top. Increasing the crestline angle appears to decrease the maximum acceleration response; while increasing the side-slope angle tends to increase the maximum acceleration response.

The peak-3 acceleration ratios are much lower than those of peaks 1 and 2; ratios are all less than 2.5, and most are less than 2.0.

Conclusions

The model-test results summarized in this section indicate that inertial forces within a ridge are greatest along the crestline near its midpoint. Significant amplification of ground shaking occurs along the central 60 percent of ridge crests, but response peaks in different frequencies and from ridges having different geometries are located in different places within this region. Amplificaton of ground motion is invariably greatest at the ridge crest as compared to points within the ridge vertically below the crest. These findings suggest that inertial forces will have the greatest effect on potential landslides near the surface (shallow landslides) on the central parts of ridge crests. This conclusion is substantiated by my observations, as well as those in several reports, that topographic amplification of earthquake shaking commonly results in (1) shattered ridge crests covered by churned surficial soils and (2) shallow, disrupted landsides in surficial material.

SPATIAL VARIATION IN SHEAR STRESS

In addition to increasing inertial forces, differential amplification of ground shaking induces increased shear stresses within a ridge. The greater the difference in acceleration between adjacent elements of soil, the greater the induced shear stress. Thus, spatial differences in the amplification ratio are an index of induced shear stress. To measure this effect, I calculated and plotted the absolute value of the first derivative of the acceleration-ratio plots shown in figures 3. 43, 3. 44, and 3. 51. The derivative was calculated as the ratio of the difference in acceleration ratio between two adjacent points to the proportional distance separting those two points. This point-to-point calculation eliminates the bias in the approximated curves drawn in the figures. The derivative is the ratio of two dimensionless numbers and is referred to herein as the "Shear-Stress Index" because it is a semiquantitative index of the induced shear stress within the ridge.

Variations Along Ridge Crests

Figure 3. 52 shows the distribution of relative induced shear stress along the crestlines of the six models for each of the three major response peaks in the case of transverse ground shaking. For peak 1, shear stress is least at the extremeties of the crestlines and is greatest in the central portion. In the case of increasing crestline angle (cases 3-2-1-6), the maximum shear stress tends to decrease, but its location varies within the central 60 percent of the crestline. The shear-stress distribution for cases 5, 1, and 4, which have identical crestline angles and increasing side-slope angles, have similar shapes, but the magnitude of the Shear-Stress Index varies inconsistently with the differing geometries. The maximum values of the Shear-Stress Index range from about 15 to 23.

The plots for peak 2 mostly show shear-stress maxima near the extremeties of the crestlines and minima in the central portions. Case 3 is a notable exception, which shows a constant induced shear stress across the entire central part of the crestline. Maximum values of the Shear-Stress Index for peak 2 range from about 9 to 18, somewhat lower than those for peak 1. Increasing the side-slope angle tends to increase the shear stress, but the spatial distribution remains unchanged. Increasing the crestline angle has no systematic effect.

Plots for peak 3 show inconsistent shear-stress distributions: some are shaped similarly to those from peak 1, others to those from peak 2. The maximum values of the Shear-Stress Index range from about 12 to 29, the latter being the greatest value calculated for transverse shaking. No consistent variations in the shear-stress distribution can be correlated with changing crestline or side-slope angle.

The induced shear stress is of similar magnitude for each of the three peaks even though the acceleration ratios for peaks 2 and 3 were much lower than those for peak 1. Thus, the higher frequency response peaks are as significant as the fundamental response peak in inducing shear stress along the ridge crest in the case of transverse ground shaking.

Figure 3.53 shows the induced shear-stress distribution for the case of longitudinal ground shaking. The distributions for peak 1 are similar to those in figure 3.52 in that the ridge extremeties have shear-stress minima. All of the plots also show a local shear-stress minimum near the ridge-crest centers between two maxima. Maximum values of the Shear-Stress Index range from 13-17, lower than those for transverse shaking. No systematic differences related to ridge geometry are evident.

For the peak-2 data, the induced shear stress tends to be concentrated in the central portion of the crestlines. Maximum values of the Shear-Stress Index range from about 5 to 20, and most of the values are much lower than are those for peak 1. No differences related to ridge geometry are evident.

For peak 3, only cases 1, 4, and 5 produced valid data. The Index for case 1, having a maximum value of about 20, is the greatest calculated for longitudinal shaking and is located at the center of the crestline. The shear stresses induced for cases 4 and 5 are minimal.

The distribution of induced shear stress for longitudinal shaking shows that shear stress tends to be concentrated in the central parts of the ridges, but not in a unique area. The induced shear stresses decrease from peak 1 through peak 2 to peak 3, such that for peak 1, the stresses are similar to those induced from transverse shaking, but for peak 3, the stresses are insignificant in most cases.

Variation Along the Maximum Vertical Cross Section

Figure 3. 54 shows the distribution of induced shear stress along the vertical line bisecting the maximum vertical cross section of the models. The scale of the plotted Shear-Stress Index is 40 percent of that in figures 3. 52 and 3. 53, so the magnitude of induced shear sress in the vertical section is much smaller than it is along the ridge crest. The maximum Shear-Stress Index in the vertical section is about 8, compared to a maximum of about 30 along the ridge crest.

The data for peak 1 indicate that, except for case 4, the shear stress is maximum near the center of the ridge. The effects of increasing crestline angle (cases 3-2-1-6) are a systematic increase in maximum induced shear stress. Maximum values range from about 5 to 8.

The peak-2 data generally show shear-stress minima in the ridge centers and maxima at the ridge base or top. Increasing crestline angle appears to correlate with decreasing shear stress. Maximum values of Shear-Stress Index range from about 1. 5 to 6.

The data for peak 3 show very small induced shear stress, Index values ranging from about 1 to 4. No systematic pattern in shear-stress distribution is discernable.

Conclusions

Figure 3. 55 shows the sum of the Shear-Stress Index for the three major response peaks depicted in all cases shown in figures 3. 52-3. 54. This summation

shows the overall distribution of induced shear stress over all frequency ranges tested. For transverse shaking, figure 3. 55 shows that the shear stress is least at the extremeties of the crestline, but that no unique area within the central 60-80 percent of the ridge crest consistently displays a shear-stress maximum. For longitudinal shaking, the overall shear stress is less than that for transverse shaking, and is similarly randomly distributed within the central parts of the ridge crest. The shear stresses in the maximum vertical cross section are of much lower magnitude than those along the crestline, and no significant variation along the vertical cross section is evident.

The preceding evidence indicates that shear stresses induced from all three response peaks, both individually and collectively, are distributed more or less randomly along the entire central portion of the ridge crest and along the entire vertical cross section; no single part of the ridge can be identified as consistently having anomalously high induced shear stress. Shear stresses induced along the ridge crest are much greater than those induced along the maximum vertical cross section, which agrees with findings from the previous section on spatial variation in acceleration that deformation and consequent ground failure induced by topographic amplification will tend to be concentrated near the ground surface.

COMPARISON WITH RESULTS OF CHILE EARTHQUAKE EXPERIMENT

The resonance frequencies observed in the results of the Chile earthquake experiment (Celebi, 1986, in press; Part 2) appeared to relate consistently both to the frequency predicted by factor *I* of Sasaki and Kuwabara (1986) and to frequencies corresponding to wavelengths equal to the height and width of the ridges. As discussed previously, the model responses do not occur at the frequencies predicted by factor *I* (table 3. 2), and table 3. 4 shows that frequencies corresponding to wavelengths equal to the dimensions of the models as listed in table 3. 1 likewise do not correlate with the observed resonance frequency (14-15 Hz) of the models.

Two general reasons for the lack of agreement between the Chile earthquake experiment results and the results of the PWRI model tests are possible. First, differences between the natural ridges in Chile and the model ridges tested may be so pronounced that they behave in fundamentally different ways and thus respond to incident ground motion differently. Such differences might include (1) geometric differences between the models and the Chile ridges, (2) the properties and behavior of the ridge materials, (3) possible complex subsurface geologic structure in the Chilean ridges, (4) effects of three components of random ground shaking versus one component of steady-state shaking, or (5) scale effects in the model tests.

The second possible reason for the lack of agreement is misinterpretation of one or both of the data sets. The model tests indicate that the fundamental resonance frequency is probably related to slope length (measured parallel to the crestline), maximum vertical ridge thickness, and (or) the geometry of the rigid base to which the model is attached. Examination of these factors for the Chilean ridges, which had responses similar to one another, shows that (1) the "rigid base geometry" of the two ridges is probably similar because they lie adjacent to one another in an area of relatively uniform geology, so it is reasonable to assume that the subsurface geologic structure within and beneath the two ridges is similar; (2) the maximum height or thickness of the ridges is similar; and (3) the slope lengths differ somewhat, but, as with all such measurements, the beginning and ending points of the slopes are somewhat arbitrarily determined. Also, for the Chile ridges, the ridge height and ridge thickness as measured in the models (figure 3. 1) are identical because the "rigid base" on which the ridges rest is probably nearly horizontal. Thus, the Chilean ridges and the PWRI model ridges may be responding to similar parameters, and the resonant frequencies predicted by factor *I* and by wavelength-matching effects may have been coincidental in the case the Chile data.

The effects of scale must be accounted for in the model tests for appropriate comparison of results with actual ridges. Sasaki and Kuwabara (1986) suggest using a scaling relationship based on a model of shearing in a vertical plane. Using their relationship, I plotted (figure 3. 56) model frequency as a function of a scaling ratio, *K*, and the frequency of an actual ridge. For the most likely range of shear-wave velocities of the Chile ridge material (500-700 m/s), the two main resonance frequencies for the model tests (14 and 22 Hz) are plotted as a function of *K*, the ratio of the ridge thickness to the model thickness, and the frequency of the ridge. The resonance peaks of the Chile ridges predicted by the model tests using this scaling relationship are 13-19 Hz and 22-30 Hz. The observed resonance peaks in the Chile data were centered at about 4 and 8 Hz. This indicates that (1) the scaling relationship used is inappropriate for the type of deformation experienced in the models or the Chile ridges, (2) the models and the Chile ridges deformed in significantly different ways, or (3) the differences in the geometries of the models and the Chile ridges are so great that they behave fundamentally differently.

Overall trends in the amplification ratios for the Chile data and the PWRI model tests are quite similar. Accelerometers located nearest to the crestline midpoints and the points of maximum ridge thickness on the models uniformly recorded the greatest accelerations (figures 3. 8-3. 18). This result is similar to the results from the Chile experiment, which showed that stations near the crestline midpoints and on exposed ridge faces recorded the greatest accelerations. The magnitudes of the acceleration ratios are also similar for the two data sets. Ratios from the Chile experiment, though reaching peak values between 20 and 30, typically ranged from about 2 to 8. Amplification ratios from the PWRI model tests were as great as 6. 8 and generally ranged from about 2 to 5. The two ridges instrumented in Chile had fairly similar geometries, so it is impossible to observe any effects of changing ridge geometry on amplification of ground shaking.

COMPARISON WITH DATA FROM MATSUZAKI DENSE SEISMIC ARRAY

PWRI has deployed several seismometers in a dense array in Matsuzaki on the western Izu Peninsula, as shown in figure 3. 57. The array is located on a long ridge having a gently sloping (less than 10°) upper part and a steeply sloping (15-25°) face. Station 1 is located where the ridge abruptly steepens and is thus on the thickest portion of the ridge on an exposed promontory. Stations 2-5 are spaced along the steep lower part of the ridge face to the base of the ridge. Peak ground accelerations (*PGA*) from strong motion records from five earthquakes are recorded in table 3. 5 for stations 1-5. Figure 3. 58 shows the ratio of the *PGA* recorded at each station to the *PGA* recorded at station 1 plotted versus the elevations of the stations above the ground surface at station 5. The ratios decrease significantly from the maximum ratio of 1. 0 for station 1 on the ridge crest to a minimum mean ratio of 0. 36 for station 5 at the base of the ridge. Thus, the Matsuzaki data agree with observations from the Chile data and from the model tests that amplification is maximum on the thickest parts of ridges and on exposed ridge faces. Amplification ratios as great as about 3 (1/0. 36) at station 1 compared to station 5 at Matsuzaki are in the same range as amplifications from the other data sets.

SUMMARY AND CONCLUSIONS

The PWRI slope models all displayed similar resonance responses when vibrated in the 3-60 Hz frequency range. For ground shaking transverse to the length of the ridges, the fundamental resonance frequency is 14-15 Hz, and secondary resonance peaks are centered between 20 and 25 Hz. For ground shaking longitudinal to the ridge length, the fundamental resonance frequency is 16-17 Hz, and the secondary resonance peak is centered between 30 and 35 Hz. The models had differing overall heights, widths, and horizontal lengths; maximum vertical thicknesses (maximum vertical cross-sectional heights), slope lengths measured parallel to the crestline, and rigid model-base geometries were the same for all models. The similarity of responses between models indicates that these latter factors that were held constant govern the fundamental resonance frequency of the models and that the factors that varied between models do not significantly affect the fundamental resonance frequency. This finding differs markedly from the findings of previous studies that used a factor *I*, related to overall slope height, width, and horizontal length, to predict the fundamental resonance frequency. This contradiction may be due to fundamental differences in the behaviors of the model ridges and the natural ridges studied previously, or possibly to misinterpretation of one or more of the data sets.

Plots of the spatial variation of acceleration along the ridge crestlines and along the maximum vertical cross section indicate that accelerations are greatest along the central 60-80 percent of the crestline, but that no unique part of the crestline experiences anomalously high accelerations. A similar result is obtained from plots of the induced shear-stress distribution: maximum shear stress is distributed somewhat randomly along the central 80 percent of the crestline. No particular part of the ridge could be identified as being especially susceptible to deformation or ground failure as a result of inertial forces related to amplification of acceleration or to induced shear stress related to differential amplification. Plotting the distribution of acceleration ratio and induced shear stress over the entire range of frequencies tested (at 1-2 Hz intervals) would more completely illustrate space- and frequency-dependent variations in these parameters.

The magnitude of the amplification ratios in the model tests agree well with data from the Chile earthquake experiment and from the Matsuzaki dense seismic array. Amplification in all cases is greatest along ridge crests and on exposed ridge faces and decreases towards the bases of slopes and the on anchored or buttressed portions of slopes. Maximum amplification ratios along ridge crests generally range from about 2-8. Amplification ratios at points lower on the ridge crest or flanks--or deeper within the ridges--are much lower and appear to decrease as a linear function of height above the base of the ridge.

These findings are in general agreement with my experience and with documented field observations of apparent topographic amplification effects along ridges in past earthquakes. The commonest reported observation is that of surficial material along ridge crests being highly disrupted and churned or of boulders and other objects resting on the ground surface having been overturned or otherwised disturbed. Rock falls, debris slides, and other shallow, disrupted landslides have likewise been reported along ridges that may have experienced topographic amplification. For the most part, observations of the effects of topographic amplification of earthquake shaking are of near-surface effects. Topographic amplification decreases rapidly toward the bases of ridges; therefore, the effects of such amplification on deep-seated landslides having failure surfaces near the bases of ridges is probably much smaller than the maximum effects present along the ridge crests.

Table 3. 1. Dimensions of slope models as defined in figure 3. 1 (*L*, *H*, *W*, *S*, and *T* in mm; α and β in degrees).

CASE	*L*	*H*	*W*	*S*	*T*	α	β
1	852	397	424	940	212	25	45
2	915	333	424	974	212	20	45
3	1,081	290	424	1,119	212	15	45
4	852	397	244	940	212	25	60
5	852	397	734	940	212	25	30
6	866	500	424	1,000	212	30	45

Table 3.2. Values of factor I computed in various ways (H, L, W, T, and S as defined in figure 3.1; V is the shear-wave velocity of ridge material, 1237 mm/s).

	Case 1	Case 2	Case 3	Case 4	Case 5	Case 6
$I_a = HL/VW$	0.645	0.581	0.598	1.121	0.373	0.826
$I_b = HS/VW$	0.712	0.618	0.619	1.236	0.411	0.953
$I_c = TL/VW$	0.344	0.370	0.437	0.598	0.199	0.350
$I_d = TS/VW$	0.380	0.394	0.452	0.660	0.219	0.404
$I_e = H^2/VW$	0.301	0.211	0.160	0.522	0.174	0.477
$I_f = T^2/VW$	0.086	0.086	0.086	0.149	0.050	0.086

	Resonance Frequency				Amplification Ratio				
	Channel	Figure 3.—	1st Peak	2nd Peak	Channel	Figure 3.—	1st Peak	2nd Peak	
Increasing crestline slope angle	3	14			3	14			Model sequence 3→2→1→6
	4	15			4	15			
	5	16			5	16			
	6	17	—		6	17	—		
	7	18			7	18			
	8	19			8	19			
	9	20	+		9	20	+		
	10	21	+	+	10	21	+	+	
	11	22		+	11	22		—	
	12	23	—		12	23	+		
	13	24	—		13	24	+		
	14	25	—		14	25	+		
	Channel	Figure 3.—	1st Peak	2nd Peak	Channel	Figure 3.—	1st Peak	2nd Peak	
Increasing side-slope angle	3	14			3	14			Model sequence 5→1→4
	4	15		+	4	15		+	
	5	16			5	16			
	6	17	—	—	6	17	+	+	
	7	18	—	—	7	18	—	+	
	8	19			8	19			
	9	20	—	—	9	20	—	+	
	10	21			10	21			
	11	22			11	22		+	
	12	23			12	23			
	13	24			13	24			
	14	25			14	25			

Table 3.3—Systematic acceleration responses. A "+" indicates a systematic increase in resonance frequency or amplification ratio; a "—" indicates a systematic decrease. No symbol is shown where no systematic increase or decrease is present.

コクヨ コヒ-115D (52×36)

Table 3.4. Frequencies corresponding to wavelengths equal to the ridge dimensions listed in table 3.1 (values in Hz; shear-wave velocity is 1237 mm/s).

DIMENSION	Case 1	Case 2	Case 3	Case 4	Case 5	Case 6
L	1.45	1.35	1.14	1.45	1.45	1.43
H	3.12	3.71	4.27	3.12	3.12	2.47
W	2.92	2.92	2.92	5.07	1.69	2.92
S	1.32	1.27	1.11	1.32	1.32	1.24
T	5.83	5.83	5.83	5.83	5.83	5.83

Table 3.5. Peak ground accelerations (PGA), amplification ratios, and station elevations (relative to ground surface at station 5) for five earthquakes recorded at the Matsuzaki dense seismic array.

STATION	COMPONENT	ELEVATION (m)	PGA (gal)	RATIO
Earthquake of 9/13/85				
1	N-S	167	106.4	1.0
2	N-S	148	86.0	0.808
4	N-S	48	78.4	0.737
5	N-S	0	77.9	0.732
5	N-S	-5	32.1	0.302
1	E-W	167	101.4	1.0
2	E-W	148	70.0	0.690
4	E-W	48	47.1	0.464
5	E-W	0	87.1	0.859
5	E-W	-5	26.3	0.259
1	U-D	167	65.8	1.0
2	U-D	148	26.4	0.401
4	U-D	48	23.9	0.363
5	U-D	0	24.8	0.377
5	U-D	-5	18.2	0.277
Earthquake of 10/4/85				
1	N-S	167	21.8	1.0
2	N-S	148	12.8	0.587
4	N-S	48	5.9	0.271
1	E-W	167	20.6	1.0
2	E-W	148	9.7	0.471
4	E-W	48	8.1	0.393
1	U-D	167	8.1	1.0
2	U-D	148	4.9	0.605
4	U-D	48	2.4	0.296
Earthquake of 10/18/85				
1	N-S	167	43.2	1.0
2	N-S	148	21.1	0.488
4	N-S	48	29.3	0.678
5	N-S	-5	15.9	0.368
1	E-W	167	34.7	1.0
2	E-W	148	22.4	0.646
4	E-W	48	14.3	0.412
5	E-W	-5	10.8	0.311
1	U-D	167	26.5	1.0
2	U-D	148	14.3	0.540
4	U-D	48	8.0	0.302
5	U-D	-5	6.7	0.253
Earthquake of 6/24/86				
1	N-S	167	22.3	1.0
2	N-S	148	10.5	0.471
3	N-S	98	8.8	0.395
4	N-S	48	6.9	0.309
5	N-S	-5	2.9	0.130
1	E-W	167	18.6	1.0
2	E-W	148	10.9	0.586
3	E-W	98	9.8	0.527
4	E-W	48	6.7	0.360
5	E-W	-5	3.5	0.188
1	U-D	167	11.5	1.0
2	U-D	148	9.9	0.861
3	U-D	98	5.5	0.478
4	U-D	48	6.1	0.530
5	U-D	-5	3.4	0.296
Earthquake of 11/22/86				
1	N-S	167	49.6	1.0
2	N-S	148	30.6	0.617
5	N-S	0	18.1	0.365
5	N-S	-5	11.3	0.228
1	E-W	167	32.2	1.0
2	E-W	148	24.4	0.758
5	E-W	0	16.9	0.525
5	E-W	-5	9.3	0.289
1	U-D	167	19.7	1.0
2	U-D	148	12.3	0.624
5	U-D	0	7.8	0.396
5	U-D	-5	5.4	0.274

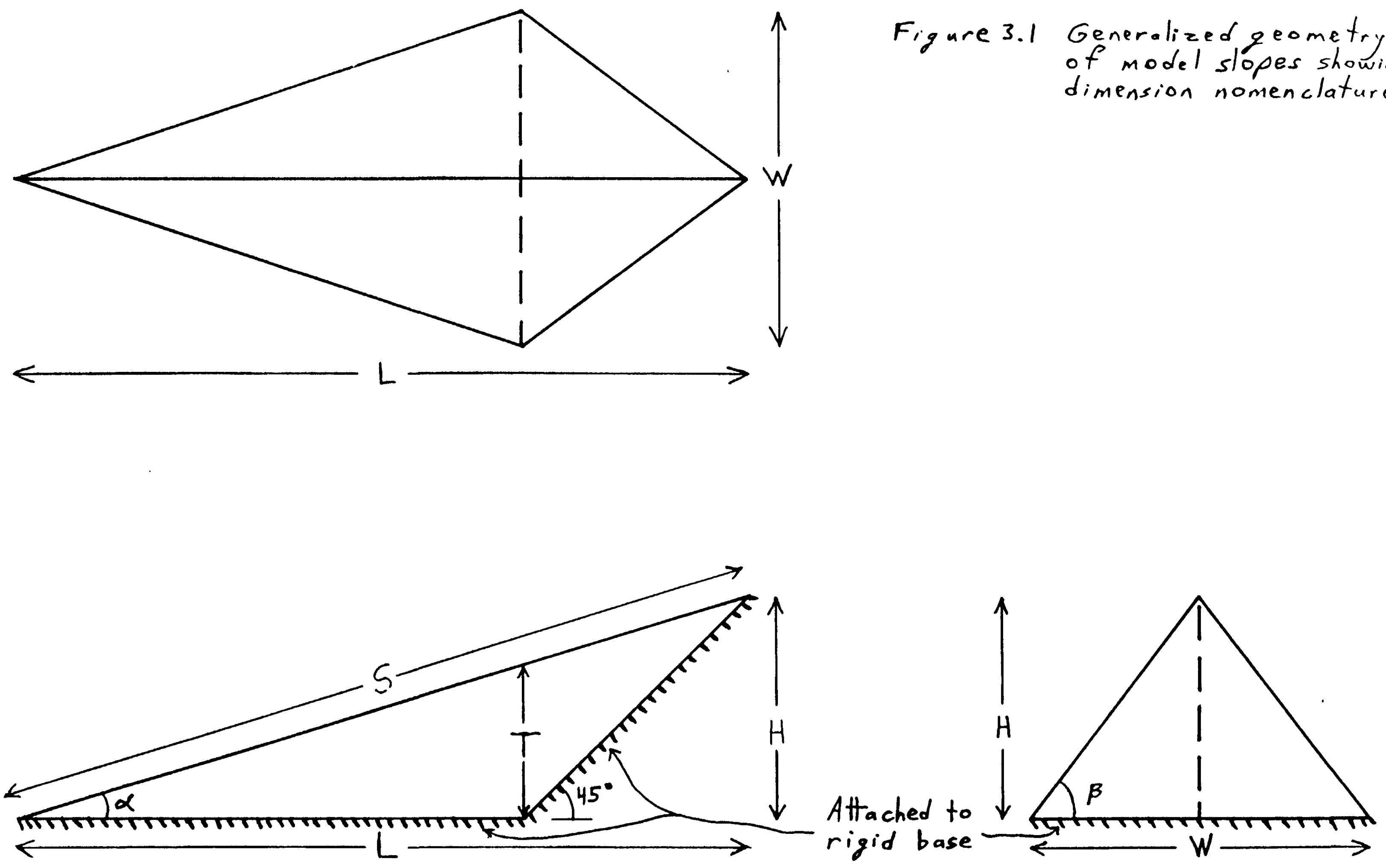

Figure 3.1 Generalized geometry of model slopes showing dimension nomenclature.

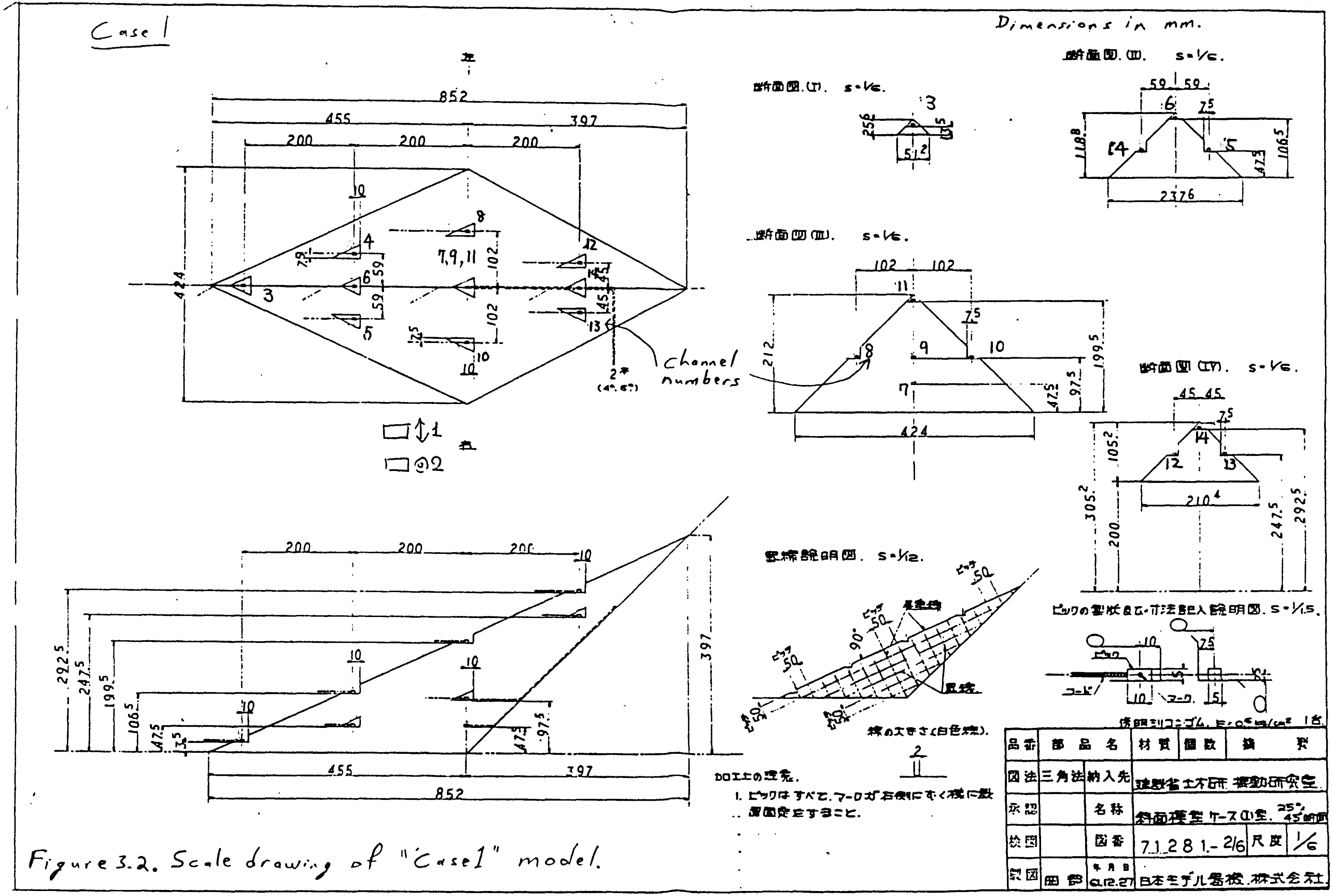

Figure 3.2. Scale drawing of "Case1" model.

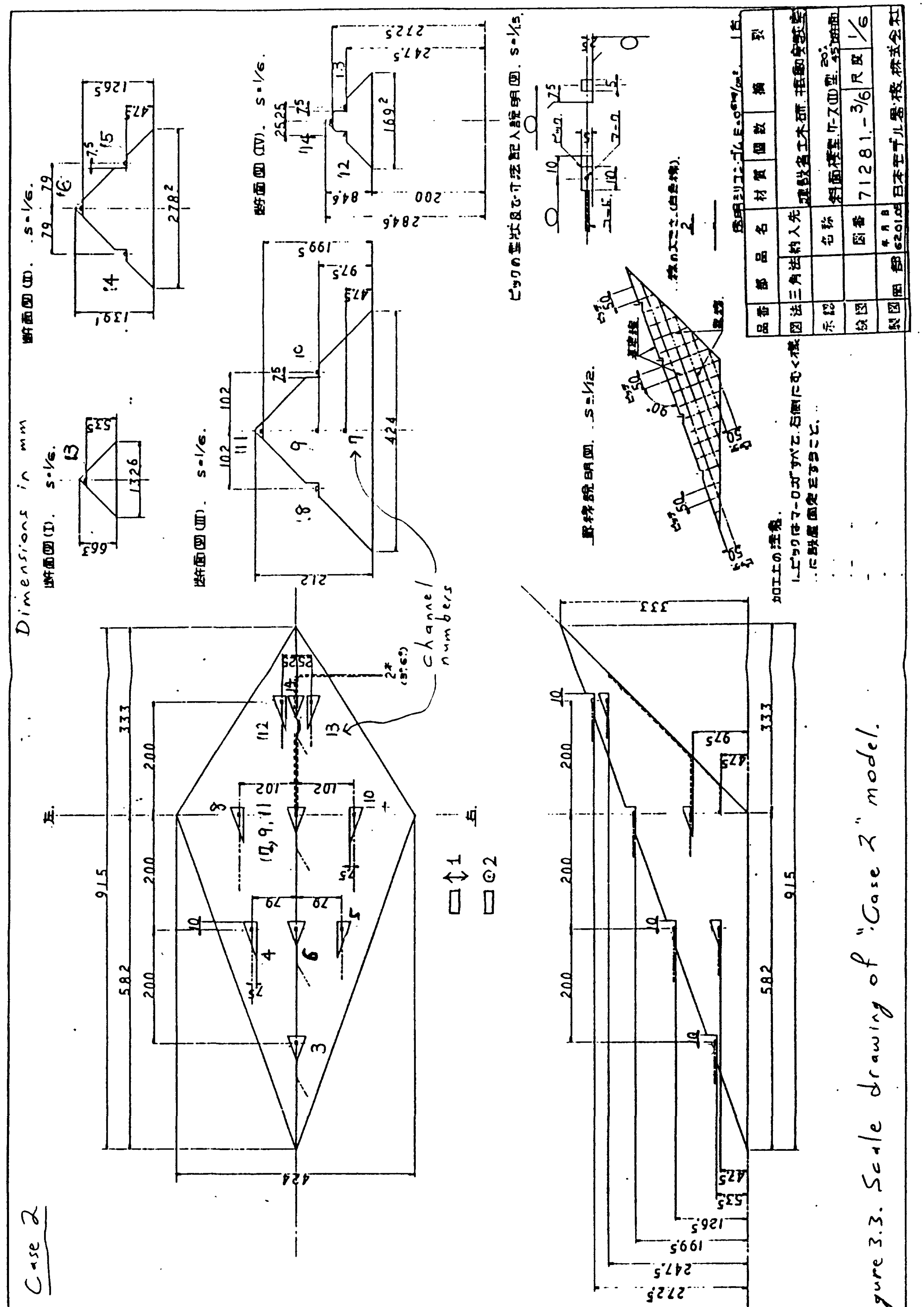

Figure 3.3. Scale drawing of "Case 2" model.

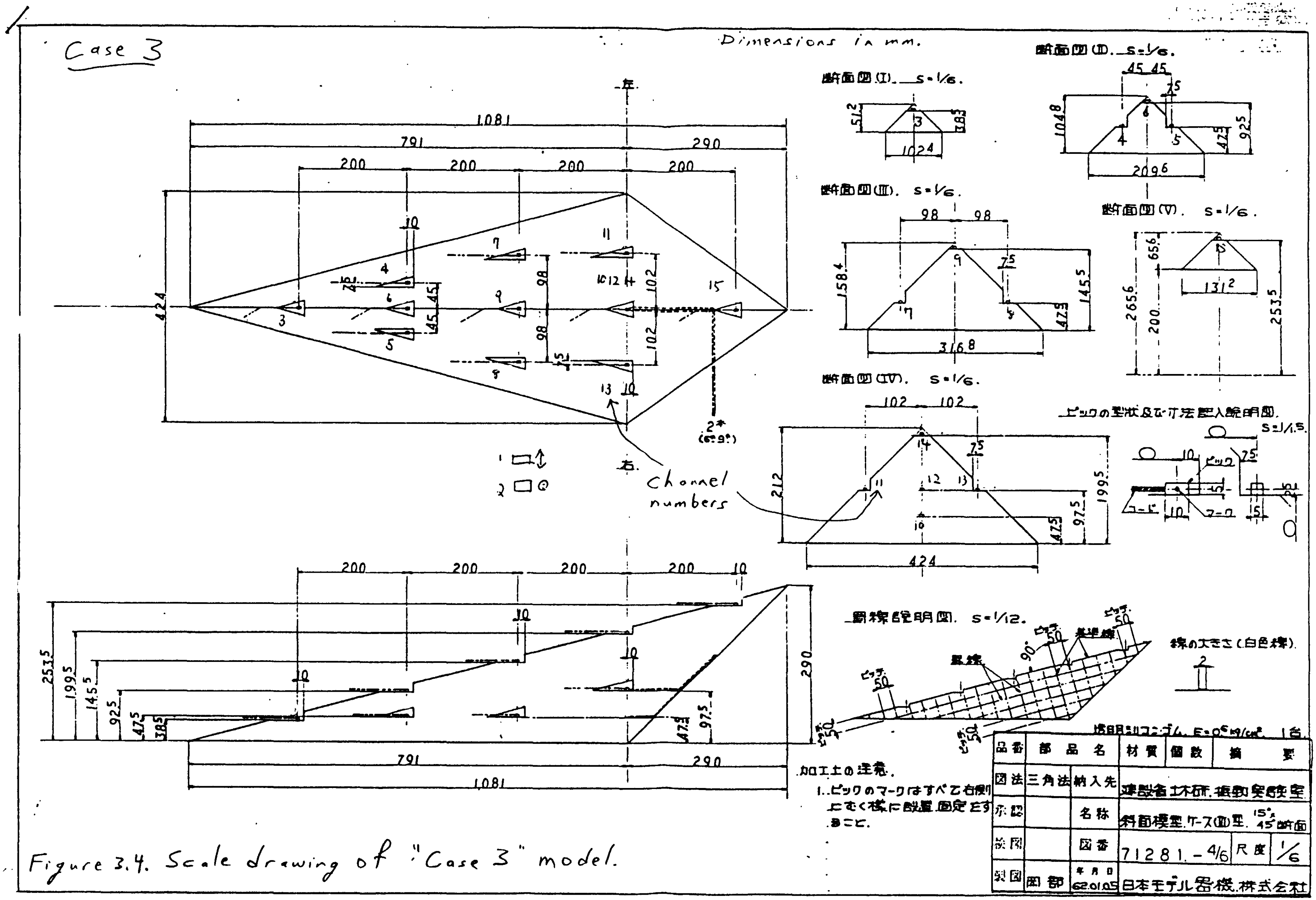

Figure 3.4. Scale drawing of "Case 3" model.

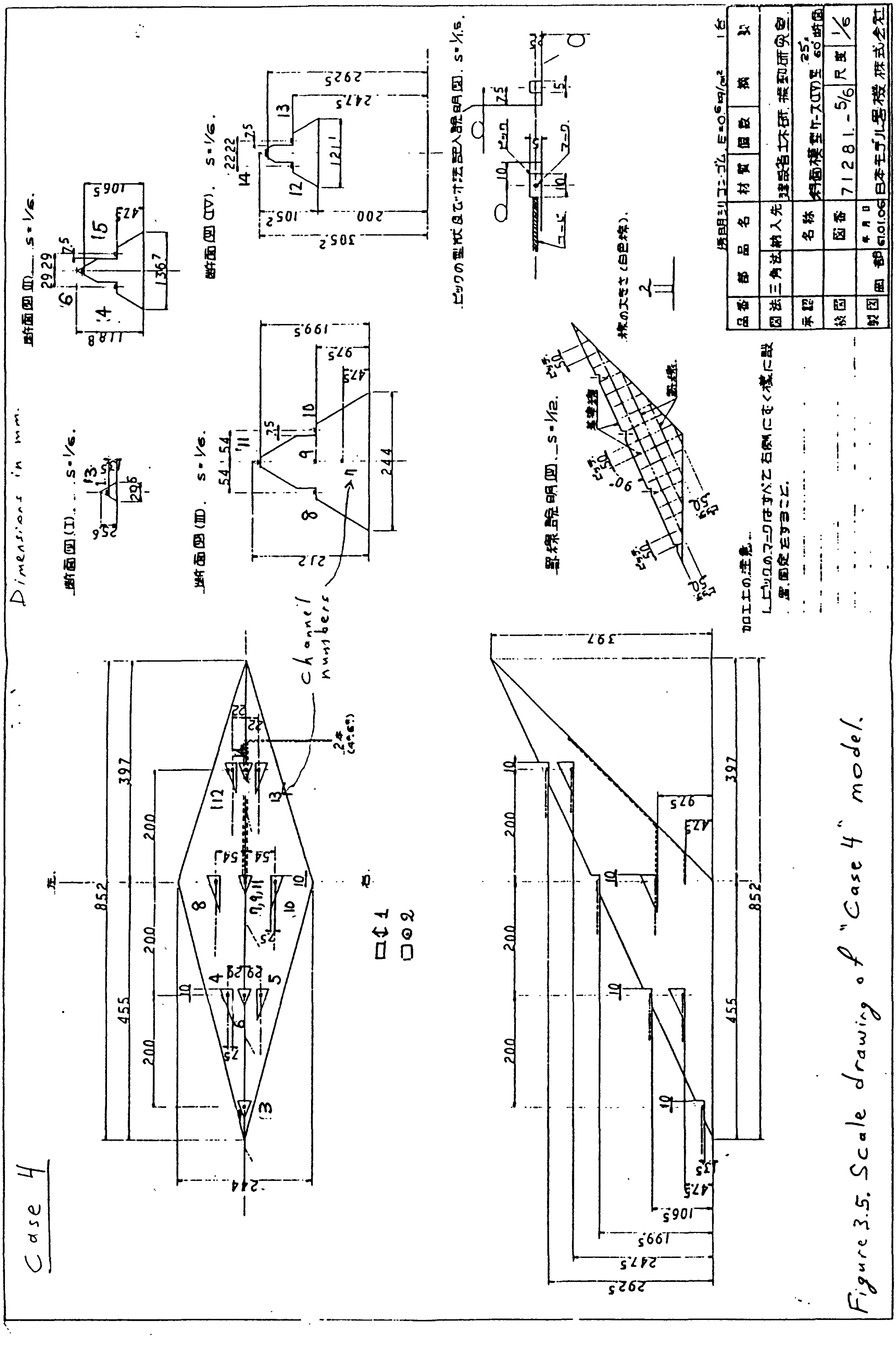

Figure 3.5. Scale drawing of "Case 4" model.

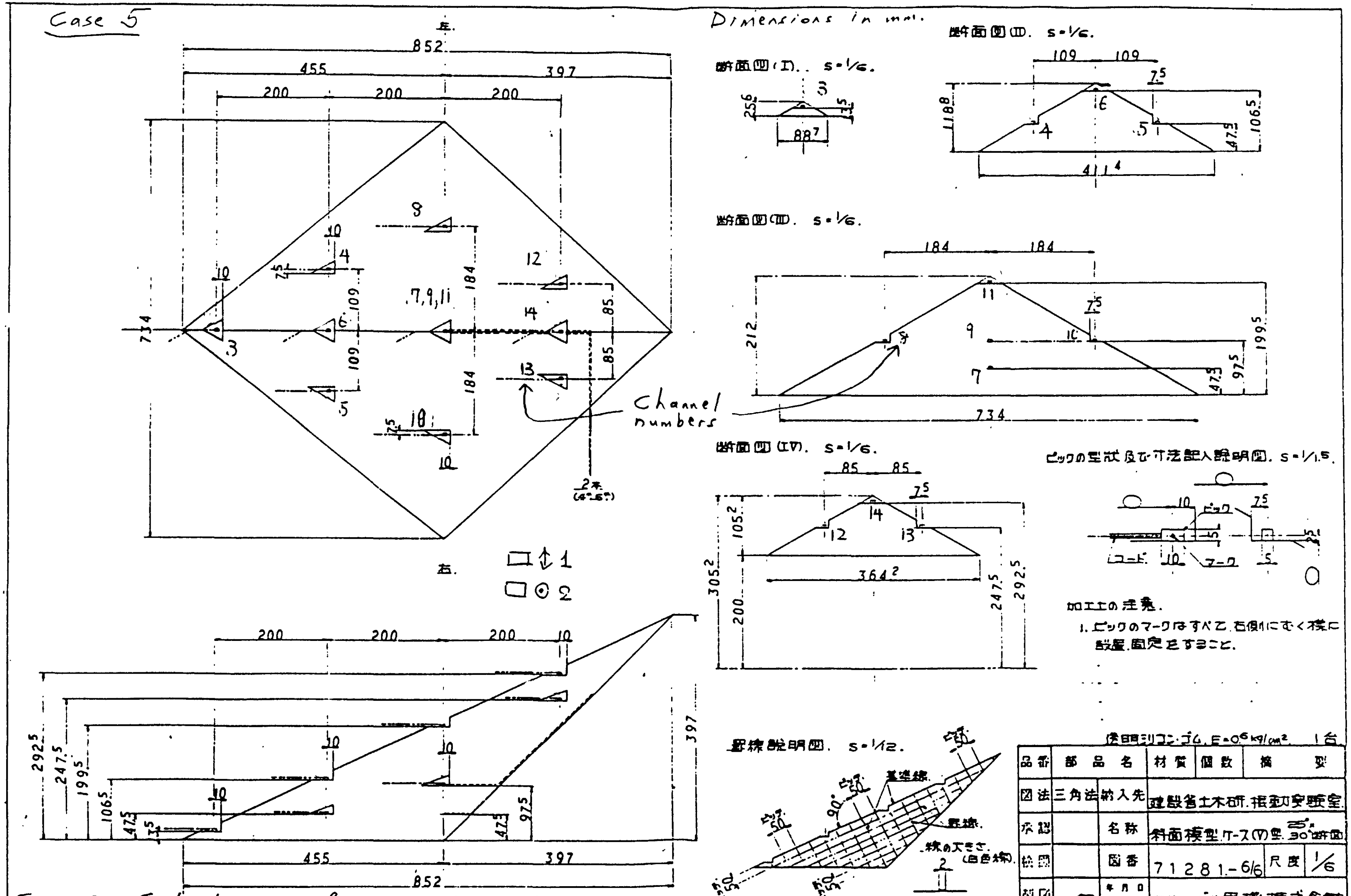

Figure 3.6 Scale drawing of "Case 5" model.

23

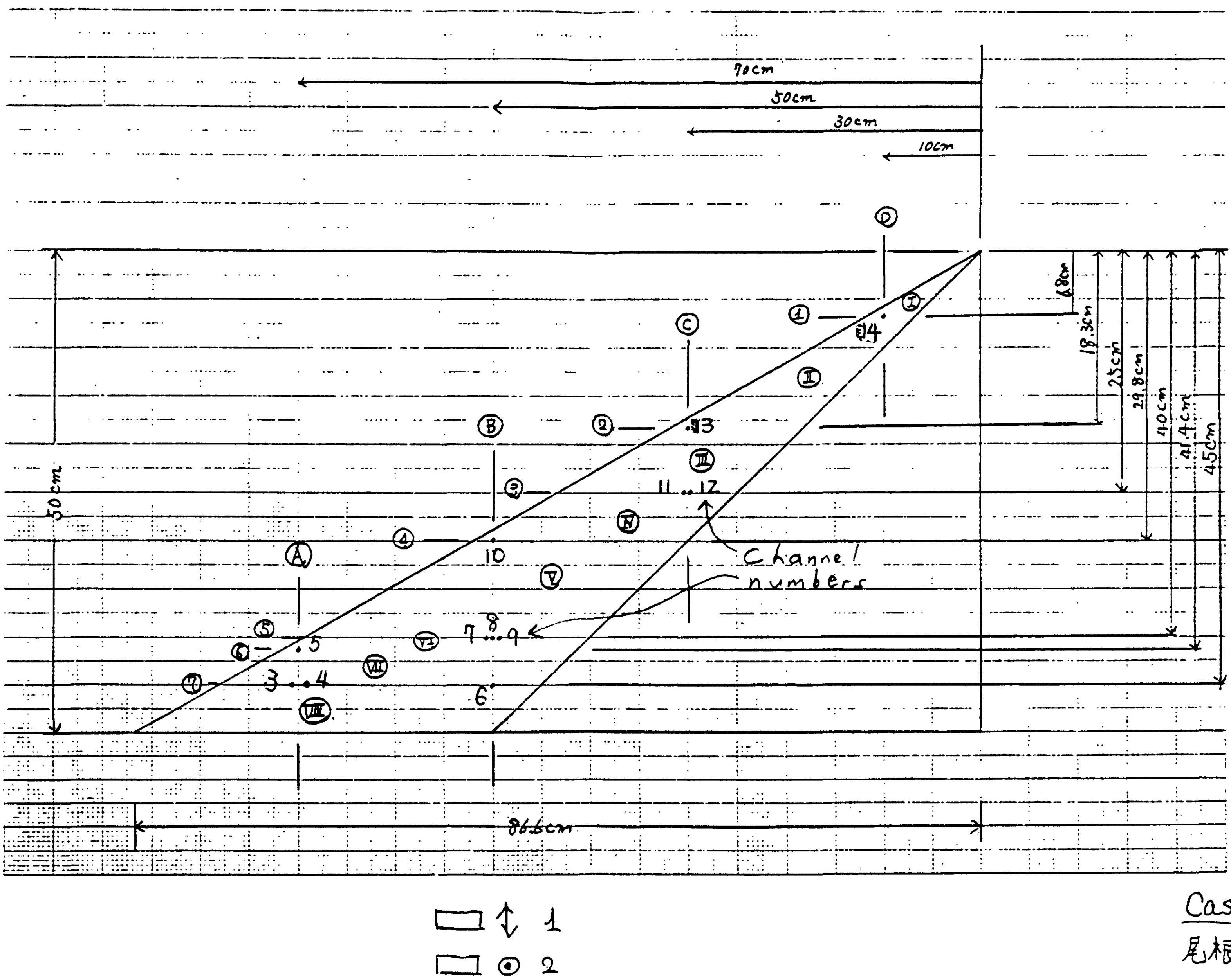

Case - 6

尾根角度 30°

斜面角度 45°

Figure 3.7. Diagram of "Case 6" model.

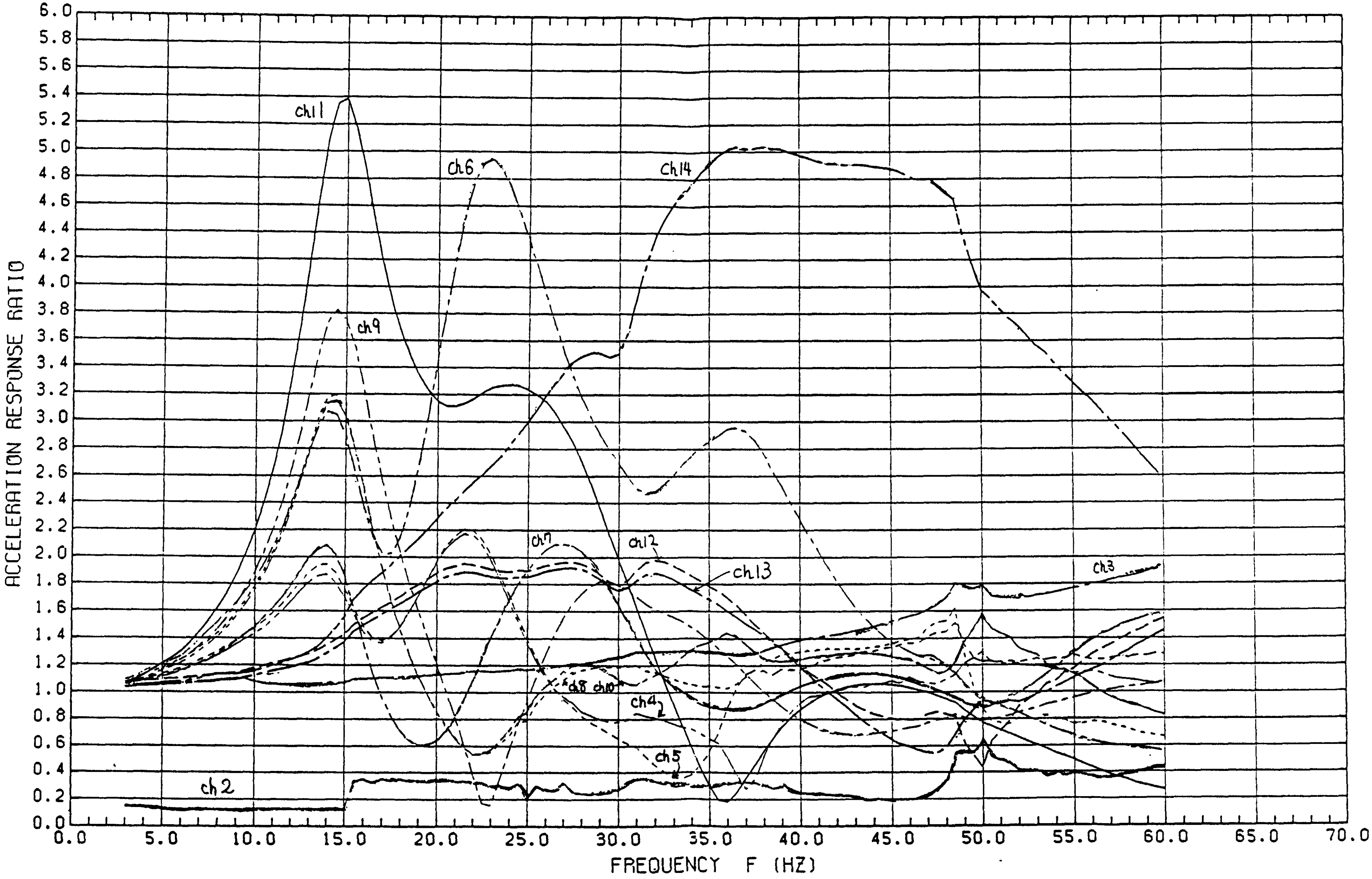

Figure 3.8 Acceleration response for case-1 model, transverse shaking.

SLOPE RESONANCE TEST CASE-1 FEB.10,1987

: 87-02-10 / 19:10:17.26 > PAGE NO 1

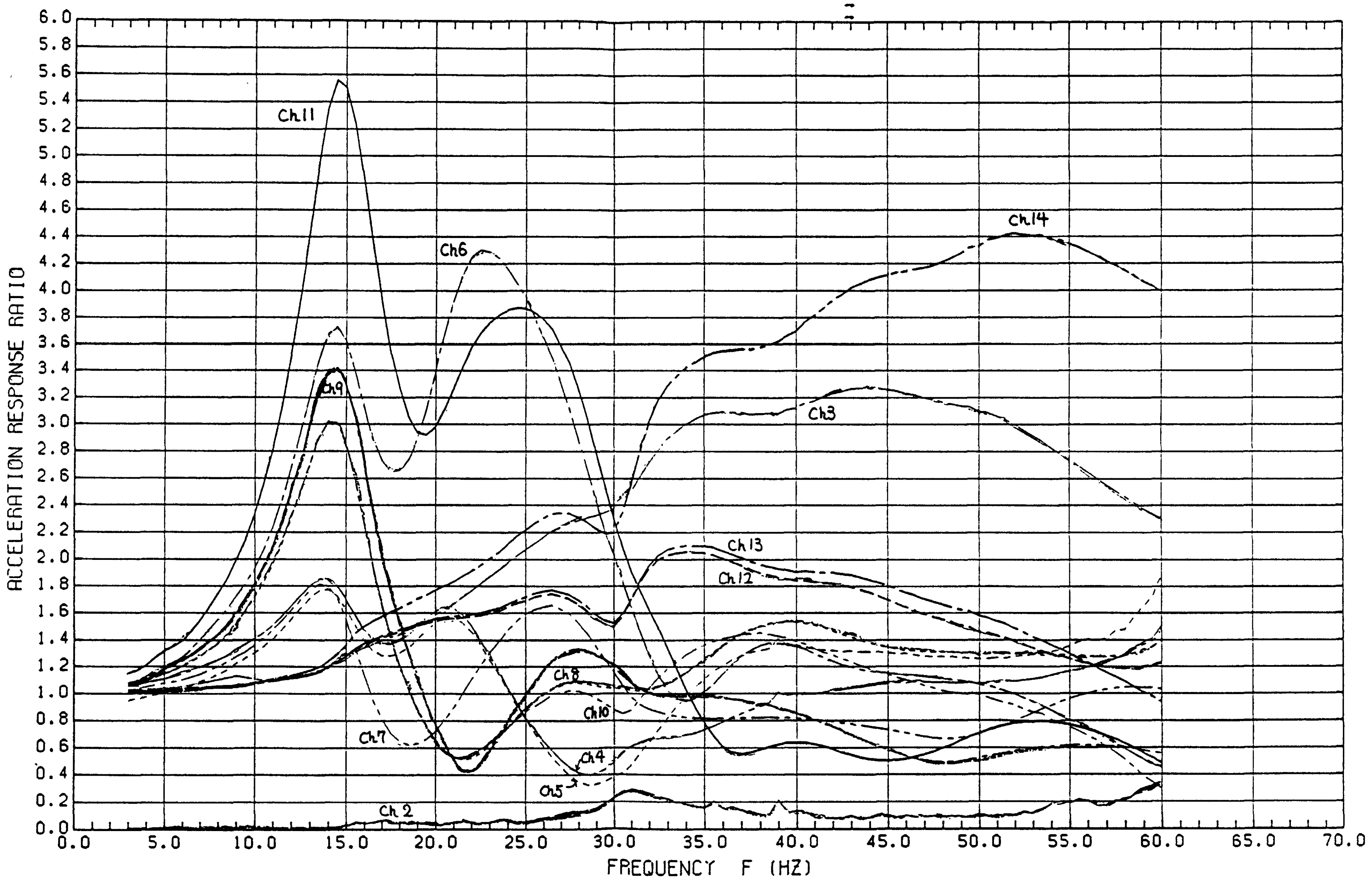

Figure 3.9 Acceleration response for case-2 model, transverse shaking.

SLOPE RESONANCE TEST CASE-2 FEB.06.1987

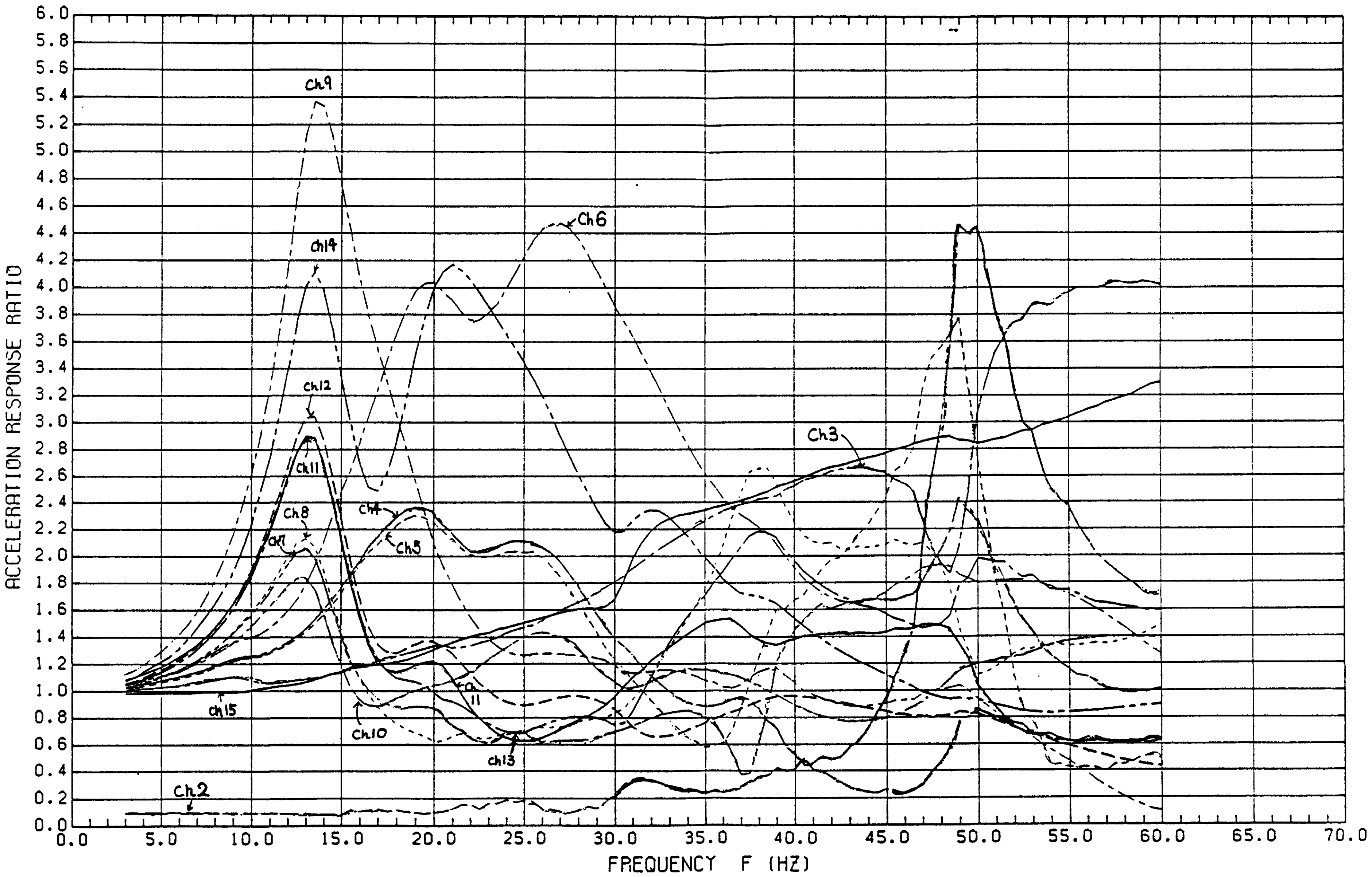

Figure 3.10. Acceleration response for case-3 model, transverse shaking.

SLOPE RESONANCE TEST CASE-3 JAN.30,1987

87-02-05 / 11:53:01.30 > PAGE NO.1

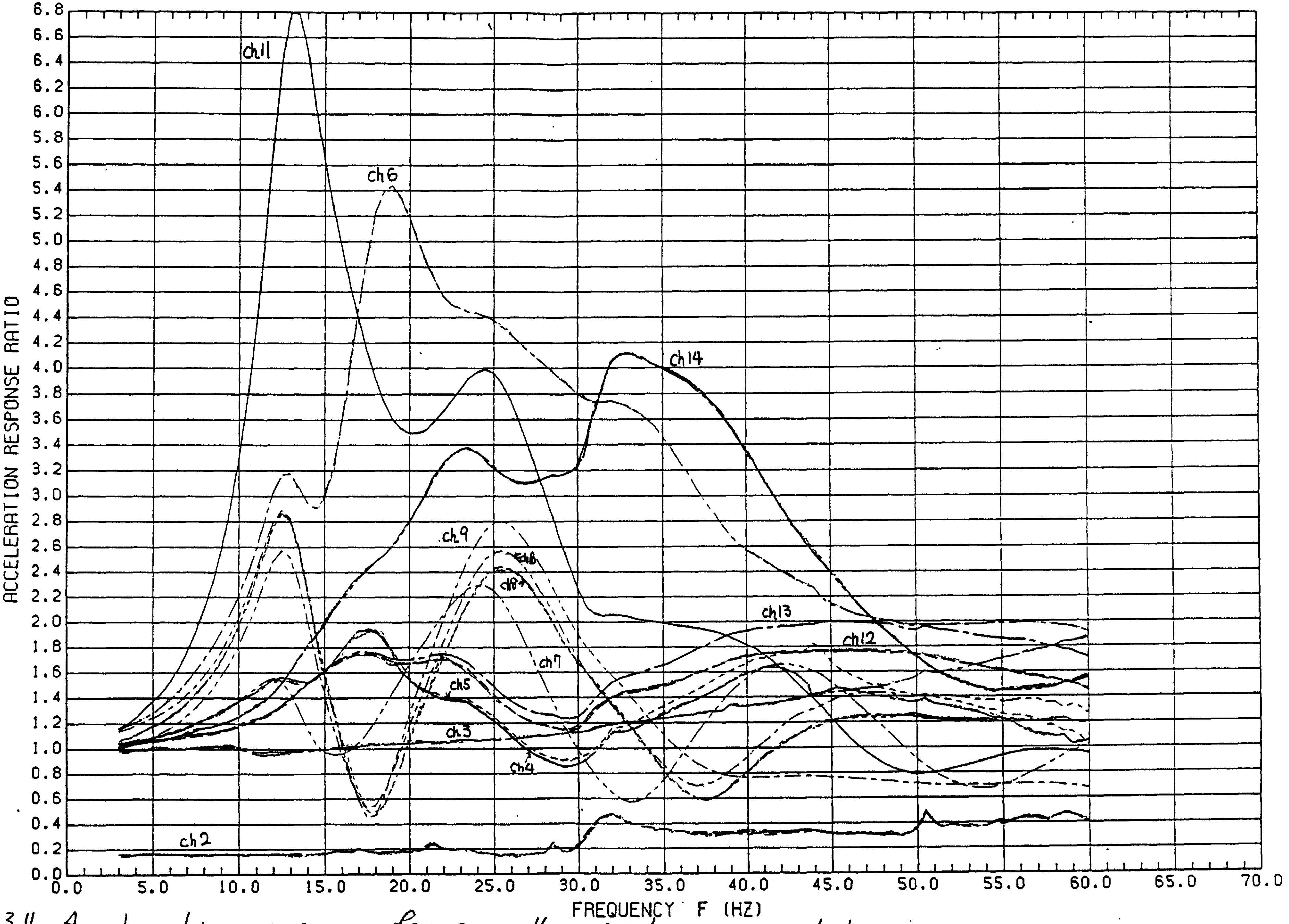

Figure 3.11. Acceleration response for case-4 model, transverse shaking.

SLOPE RESONANCE TEST CASE-4 FEB. 12, 1987

TE : 87-02-12 / 21:30:35.28 > PAGE NO.1

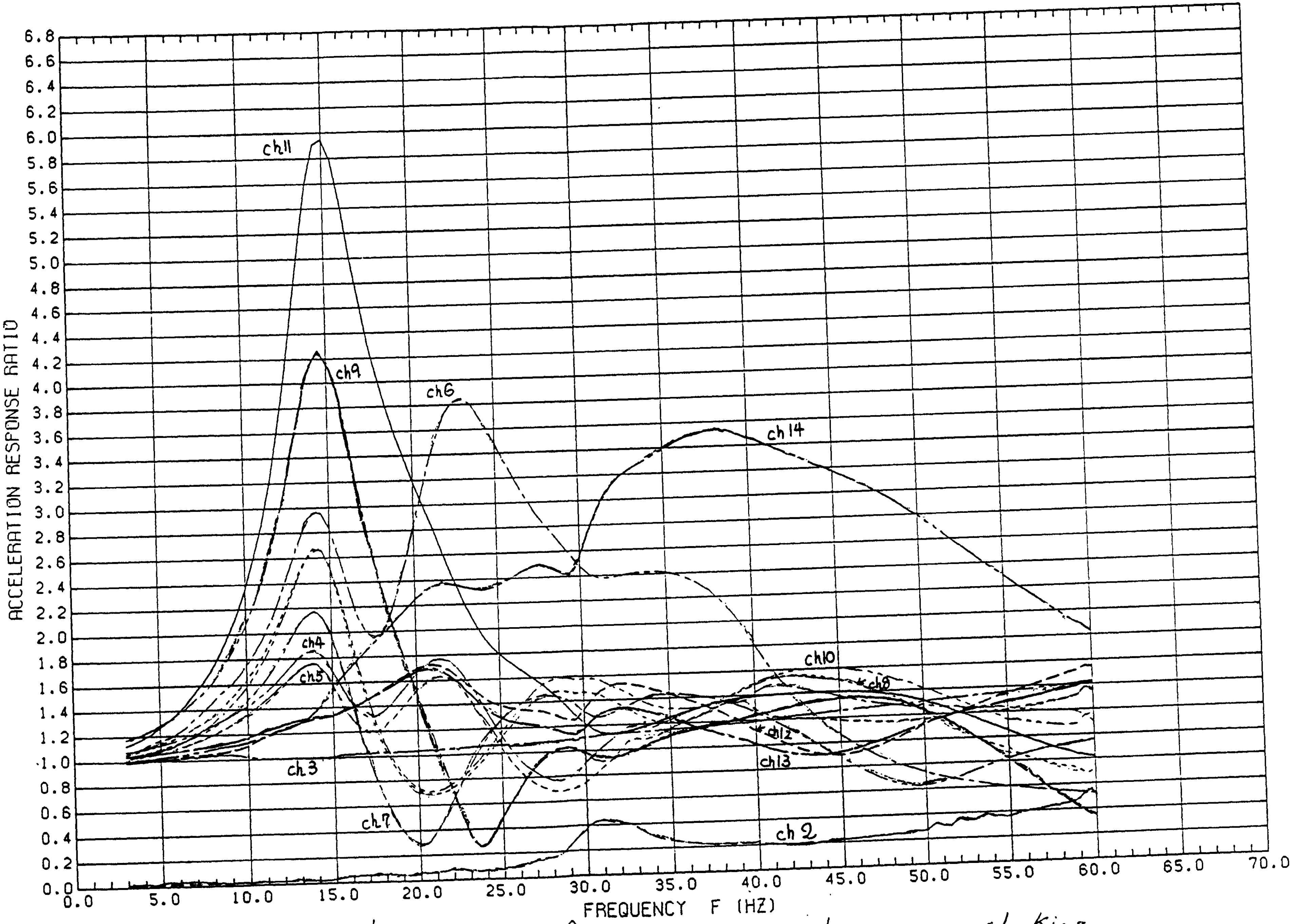

Figure 3.12. Acceleration response for case-5 model, transverse shaking

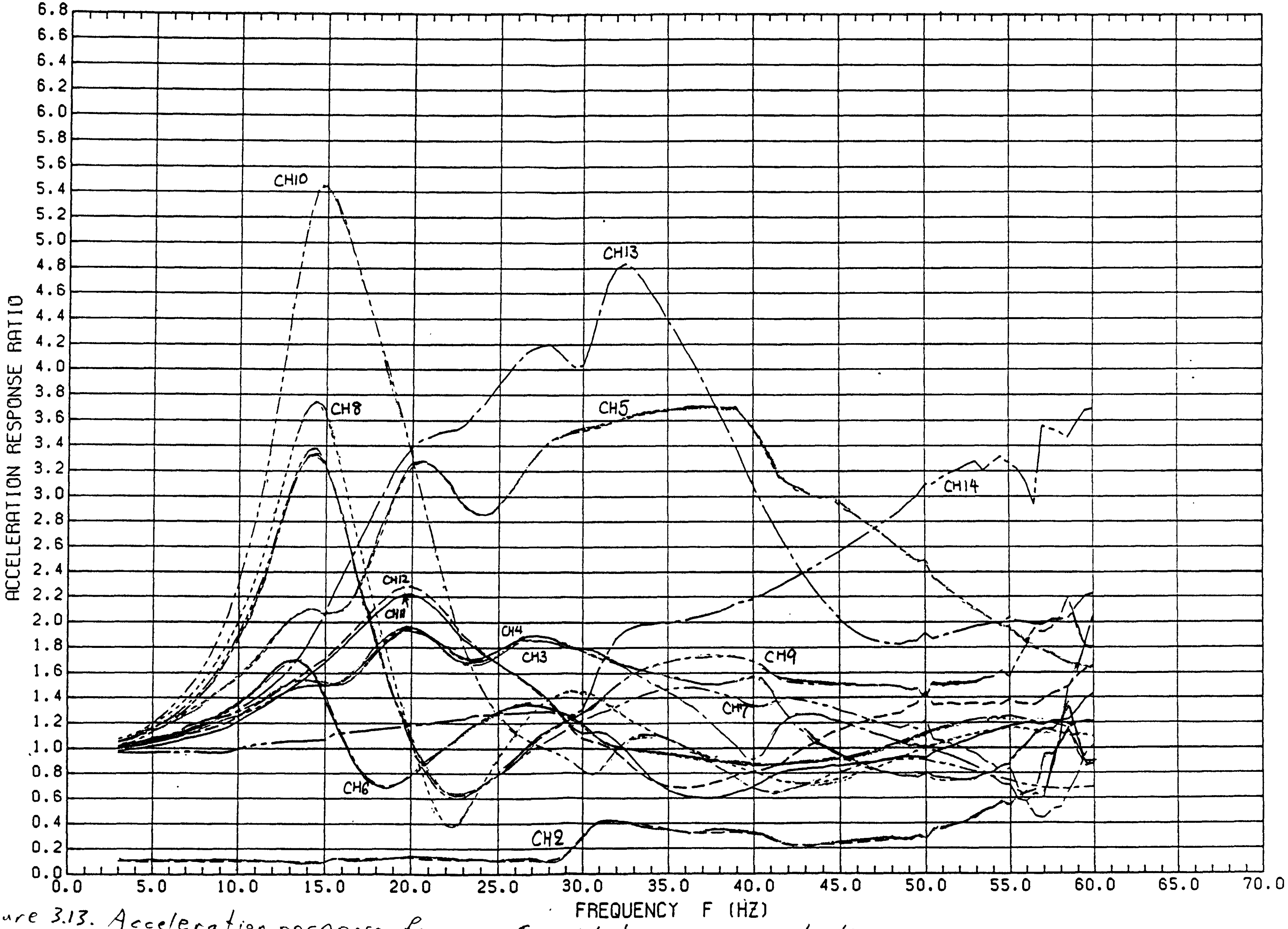

Figure 3.13. Acceleration response for case-6 model, transverse shaking.

SLOPE RESONANCE TEST CASE-6 FEB.19.1987

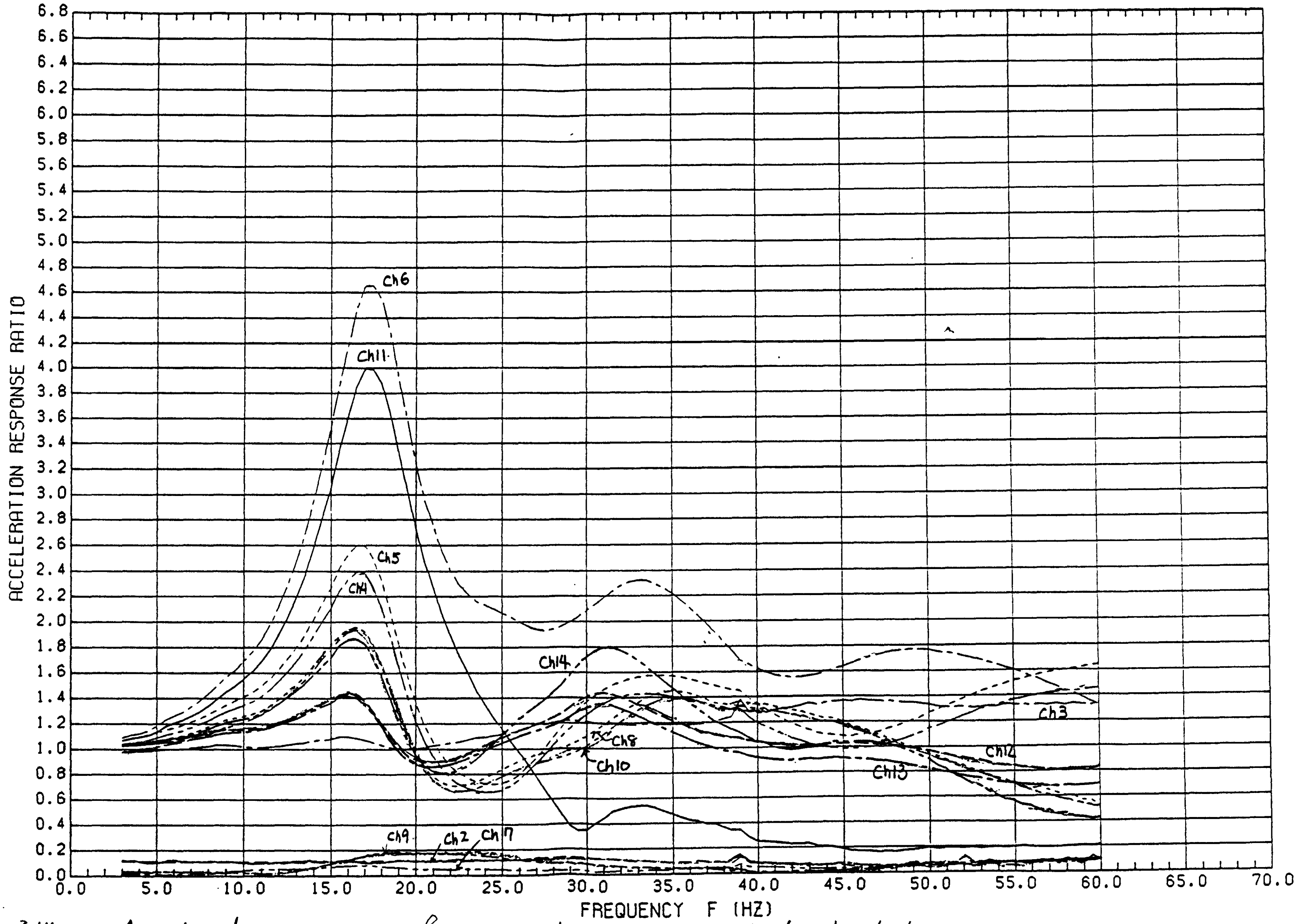

Figure 3.14. Acceleration response for case-1 model, longitudinal shaking

SLOPE RESONANCE TEST CASE-1V FEB.24.1987

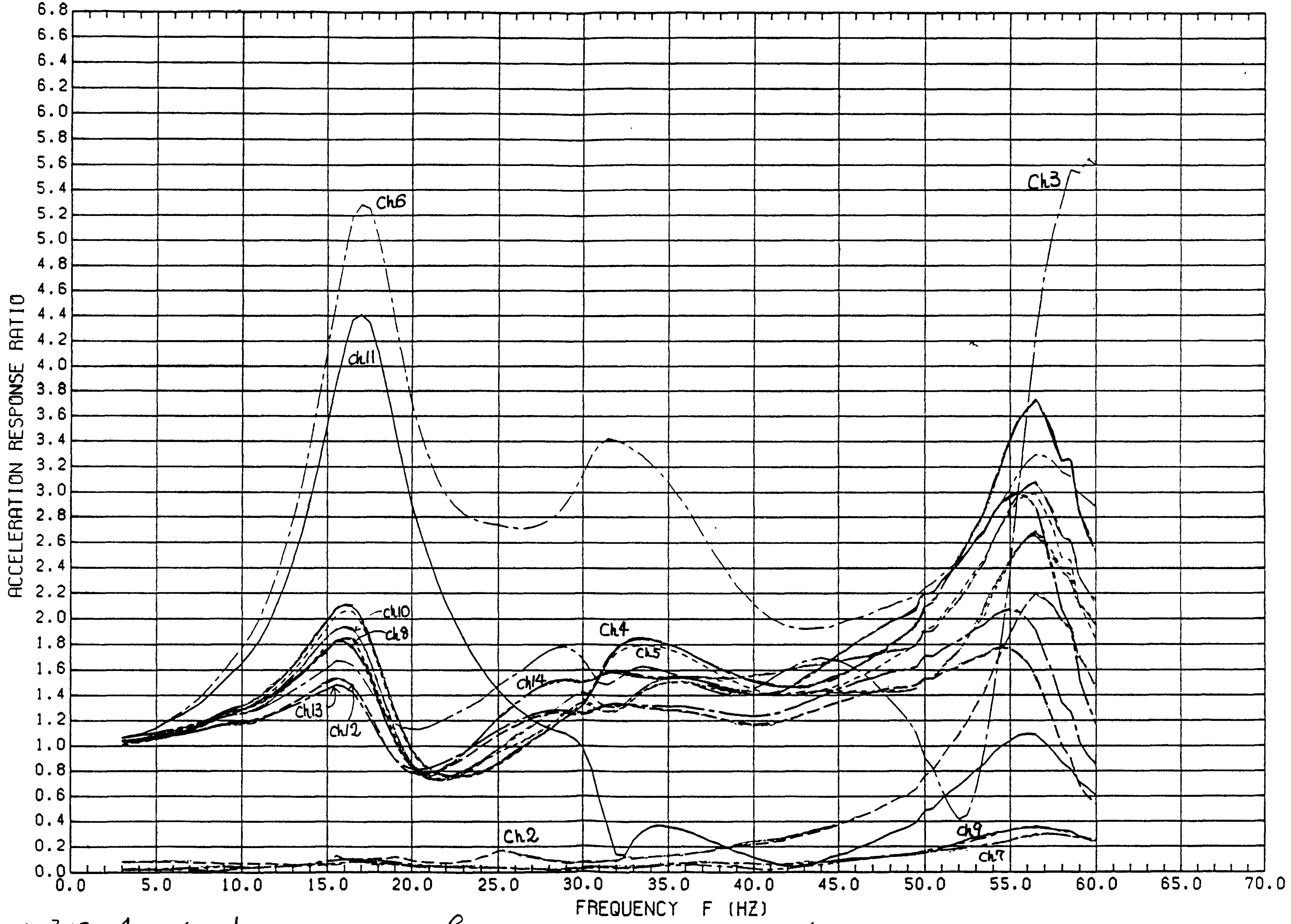

Figure 3.15. Acceleration response for case-2 model, longitudinal shaking.

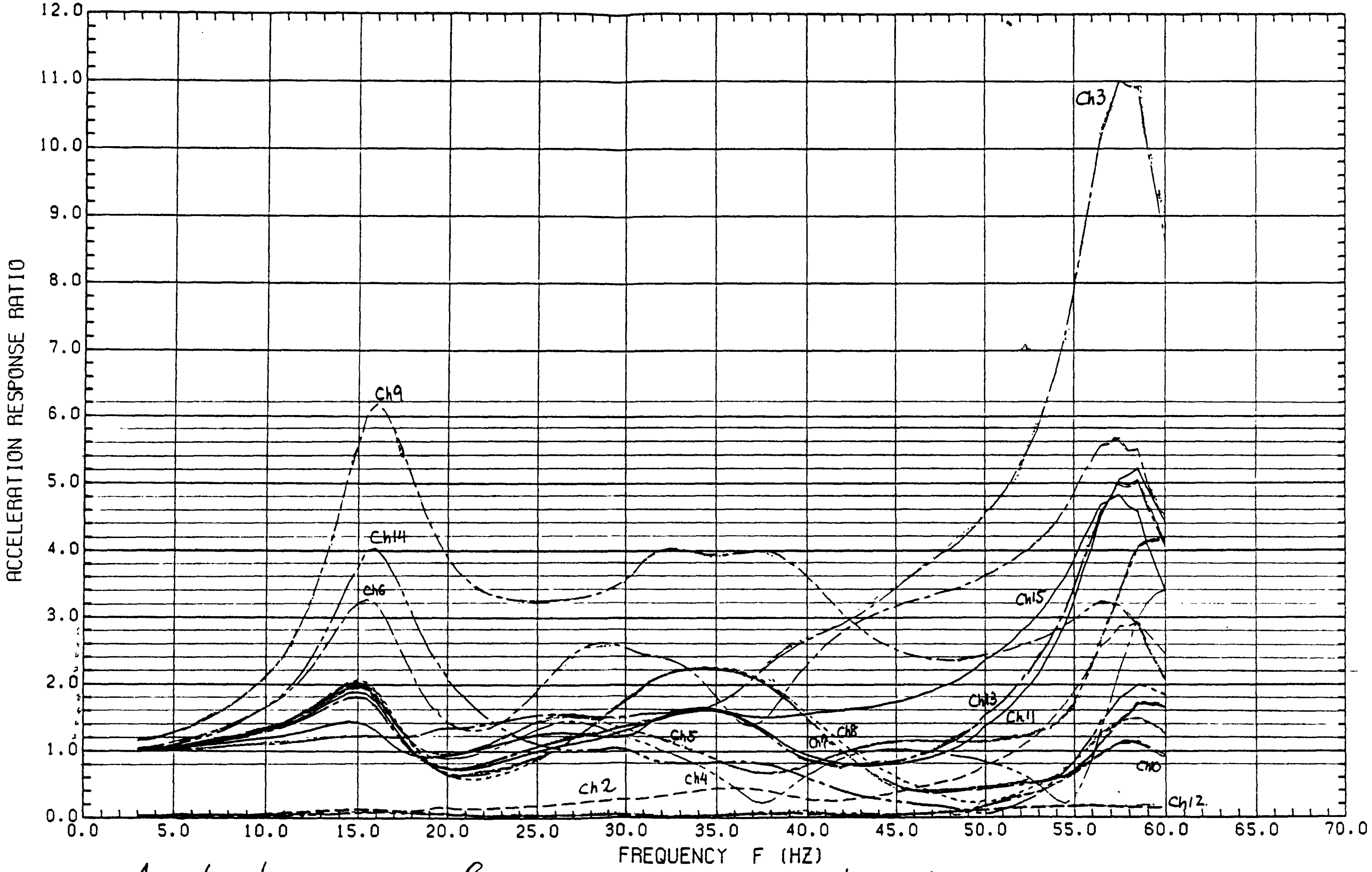

Figure 3.16. Acceleration response for case-3 model, longitudinal shaking.

SLOPE RESONANCE TEST CASE-3V FEB.23,1987

: 87-02-23 / 14:09:43.38 > PAGE NO.1

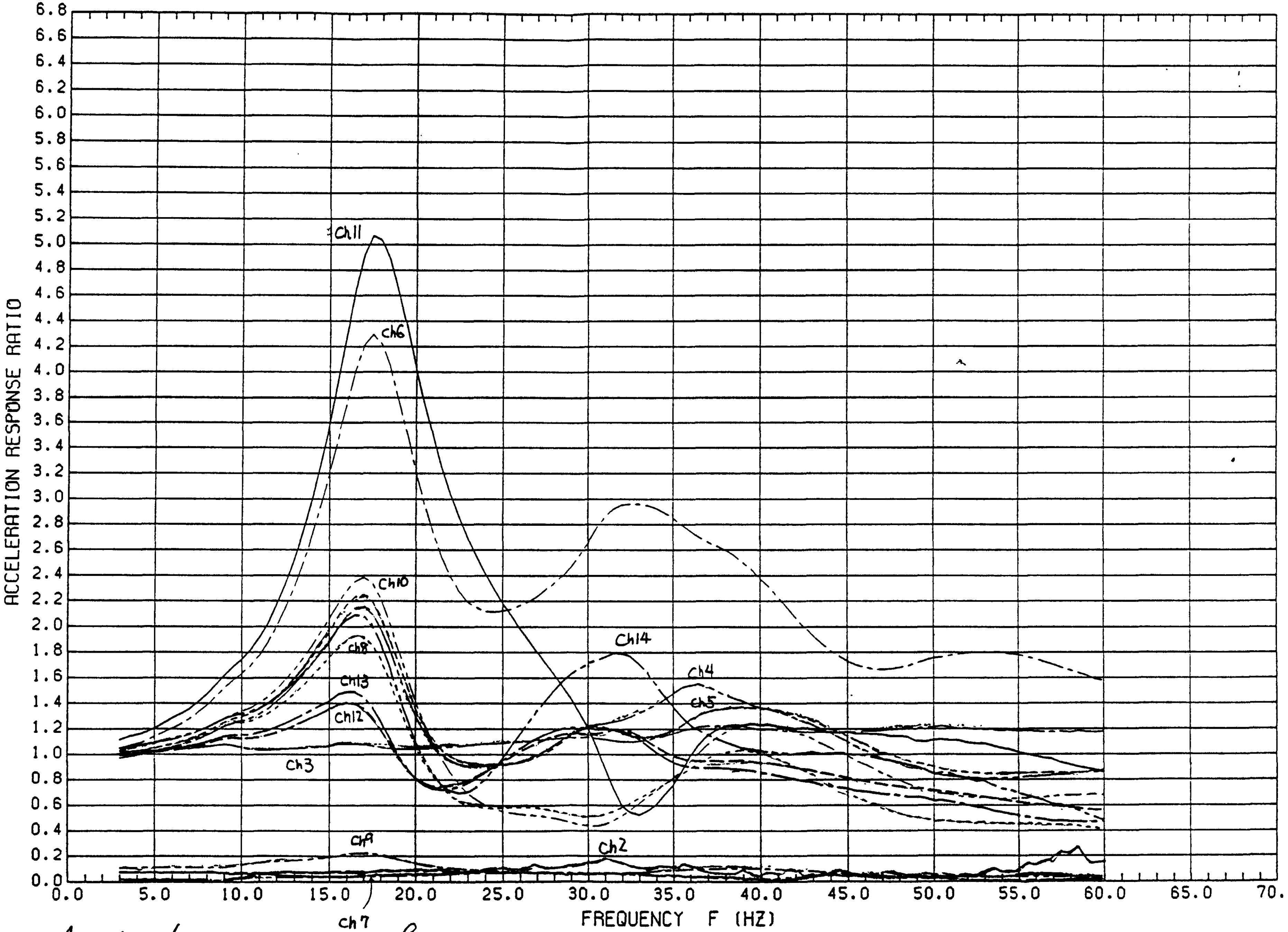

Figure 3.17. Acceleration response of case-4 model, longitudinal shaking.

SLOPE RESONANCE TEST CASE-4V MAR.03.1987

DATE : 87-03-03 / 13:10:13.25 > PAGE NO.1

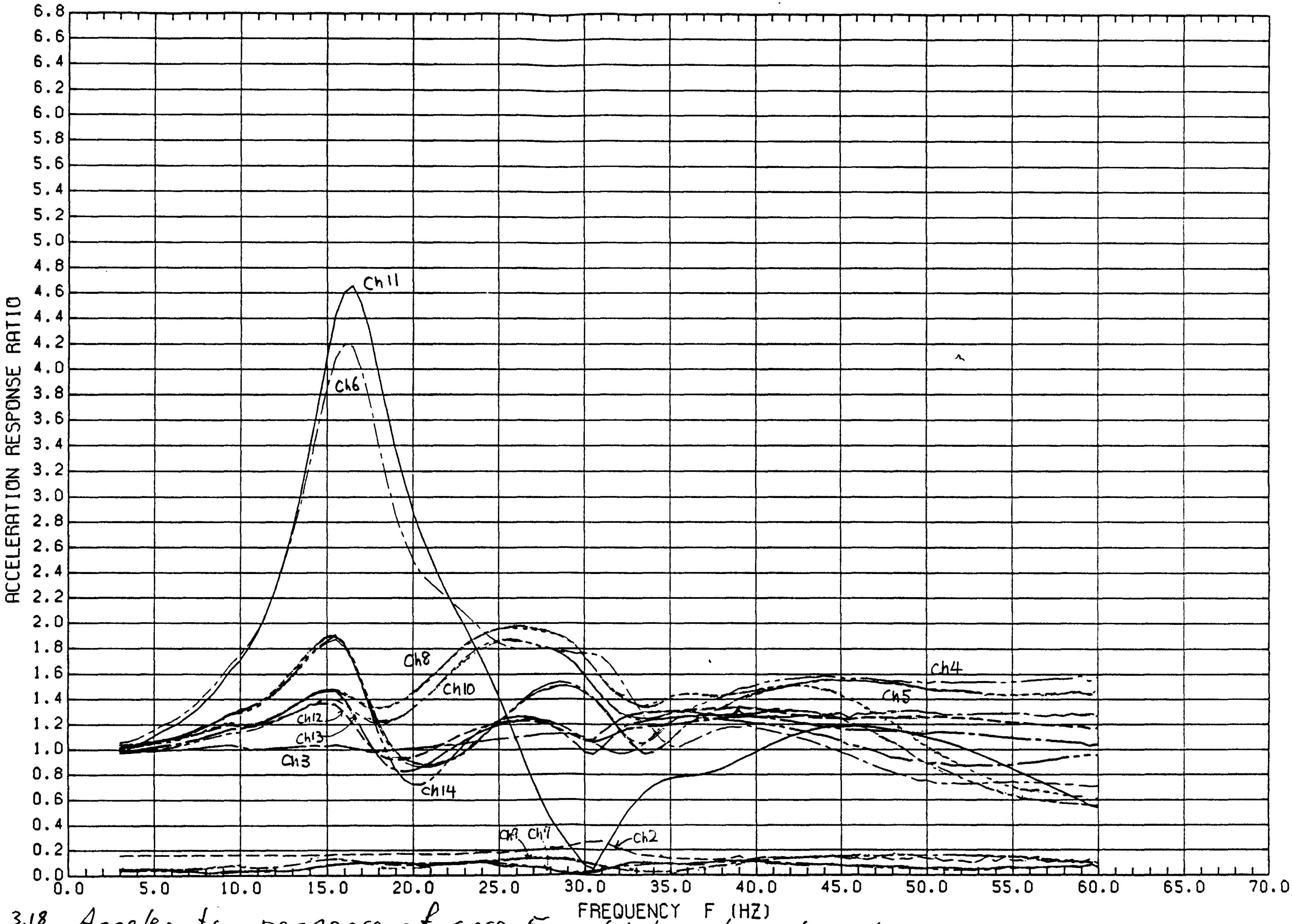

Figure 3.18. Acceleration response of case-5 model, longitudinal shaking.

SLOPE RESONANCE TEST CASE-5V FEB.25.1987

ATE : 87-02-25 / 17:00:11.70 > PAGE NO.1

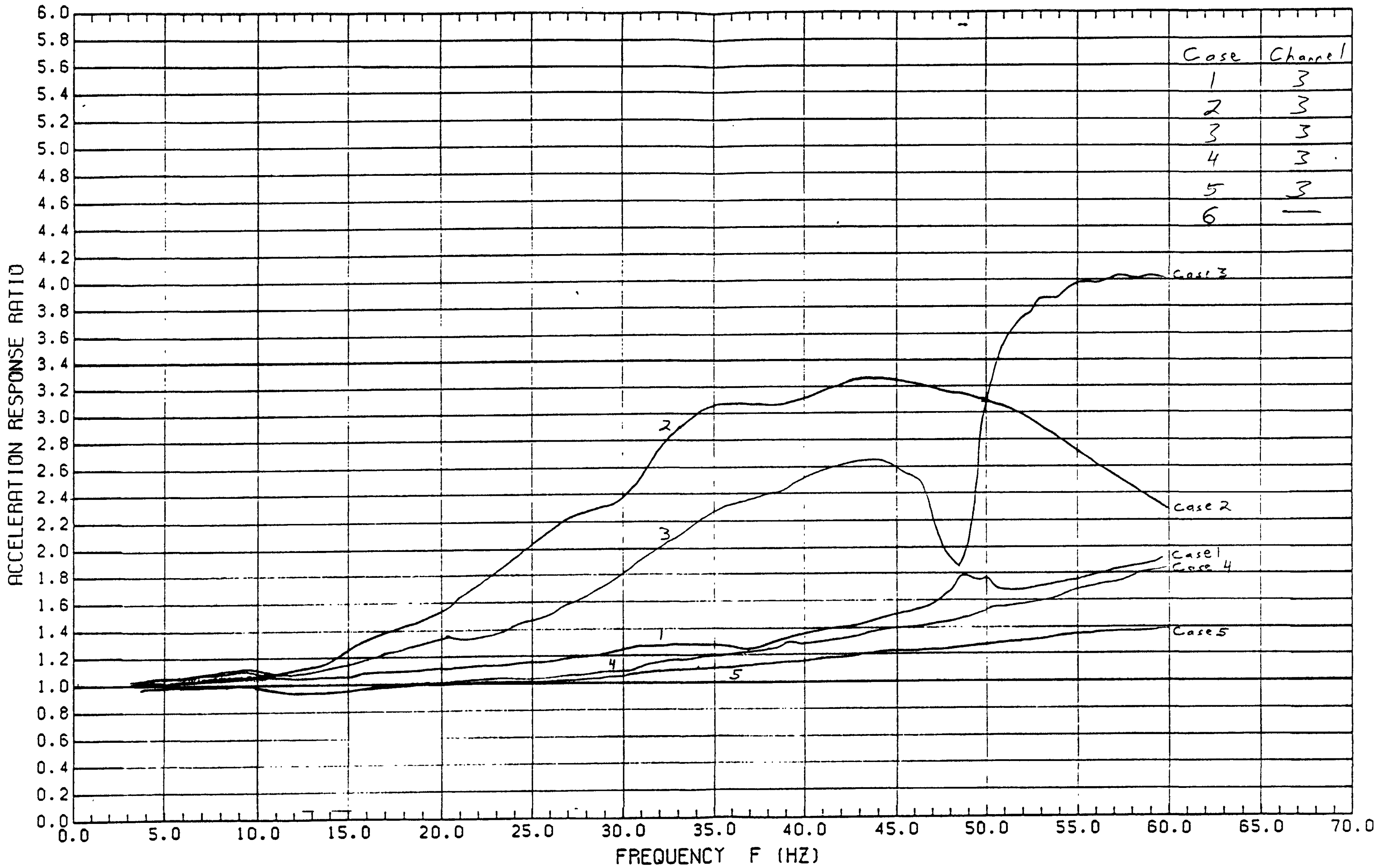

Figure 3.19. Acceleration response of channel 3, transverse shaking.

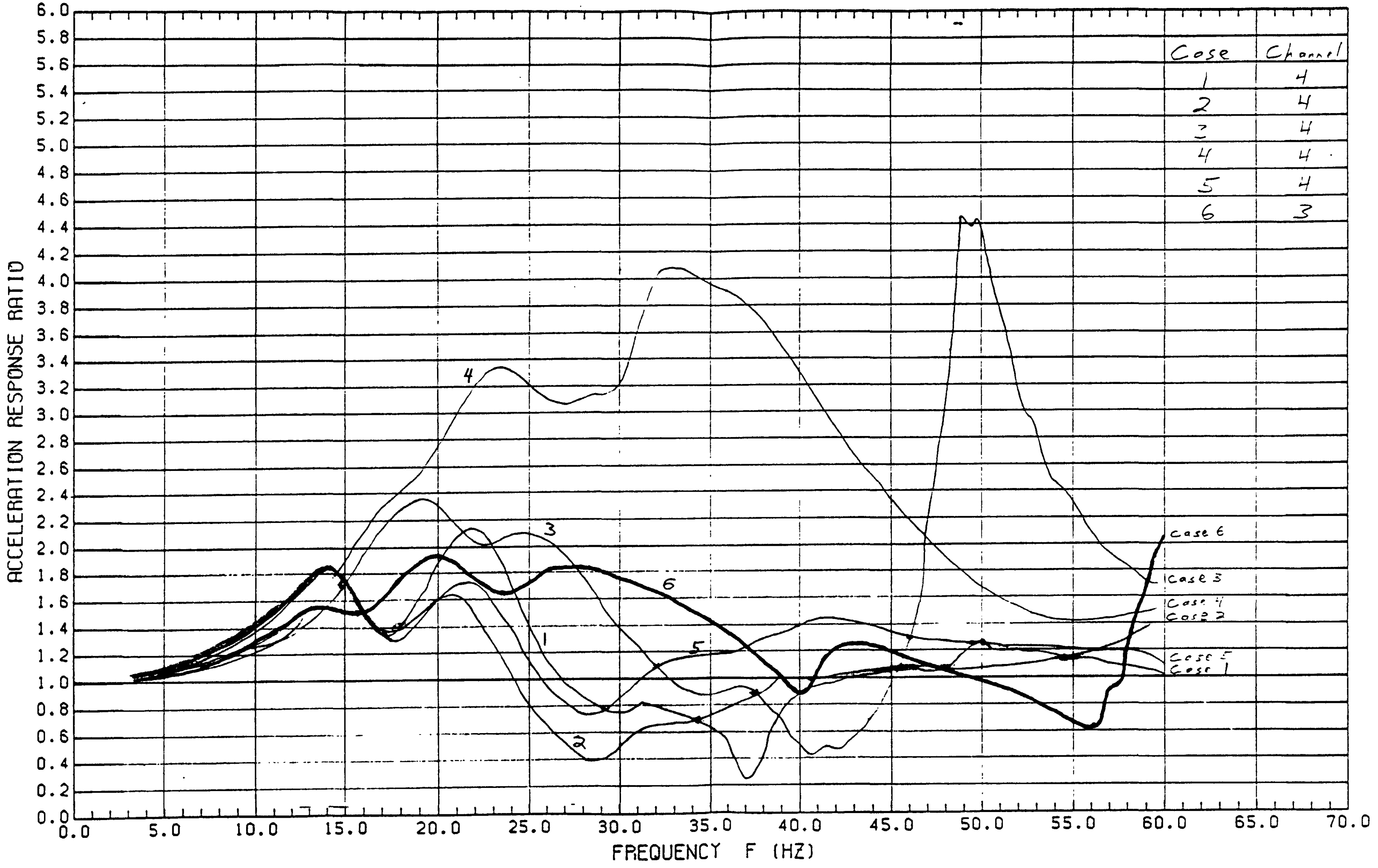

Figure 3.20. Acceleration response of channel 4 (ch. 3, case 6), transverse shaking.

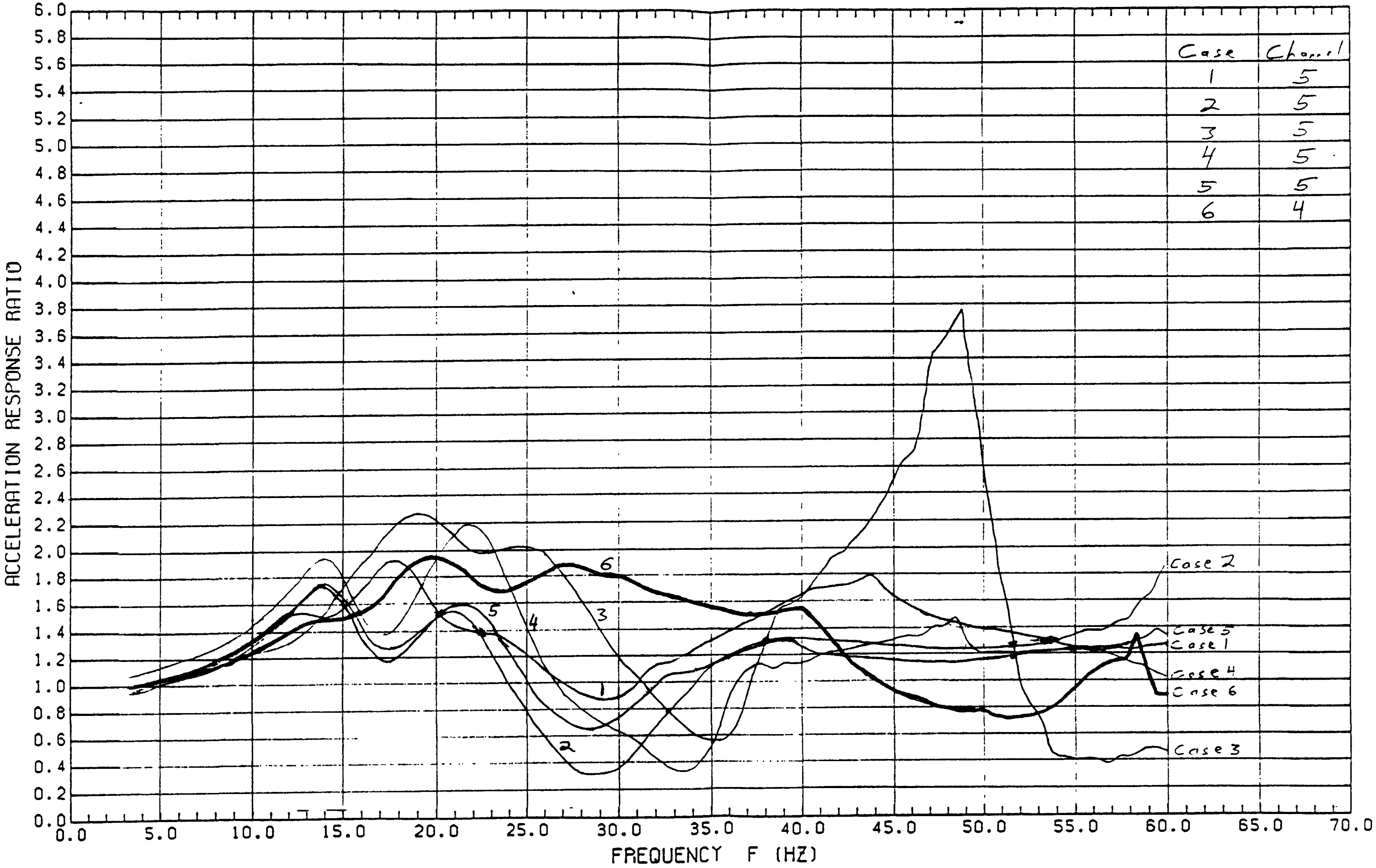

Figure 3.21. Acceleration response of channel 5 (ch. 4, case 6), transverse shaking.

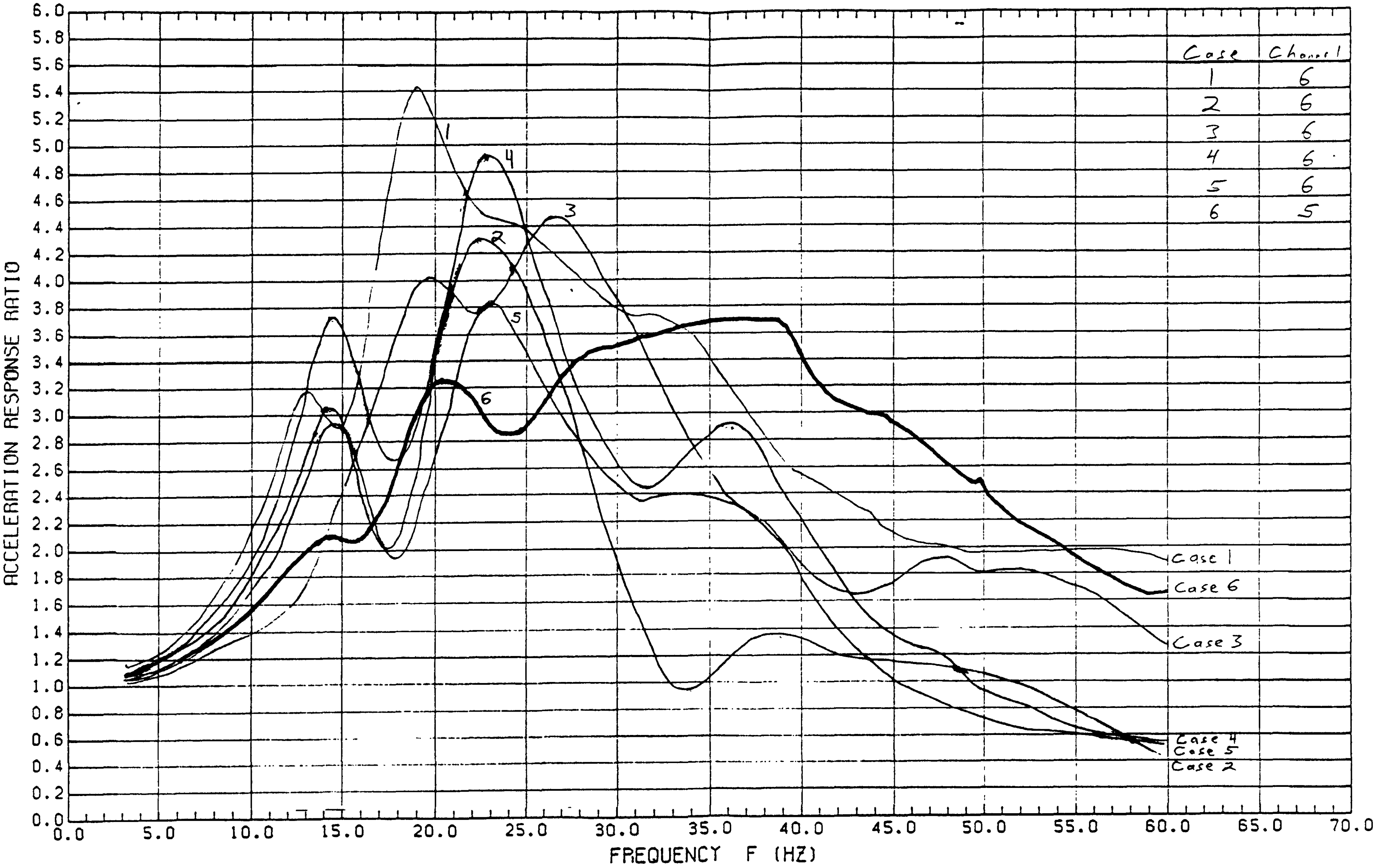

Figure 3.22. Acceleration response of channel 6 (ch. 5, case 6), transverse shaking.

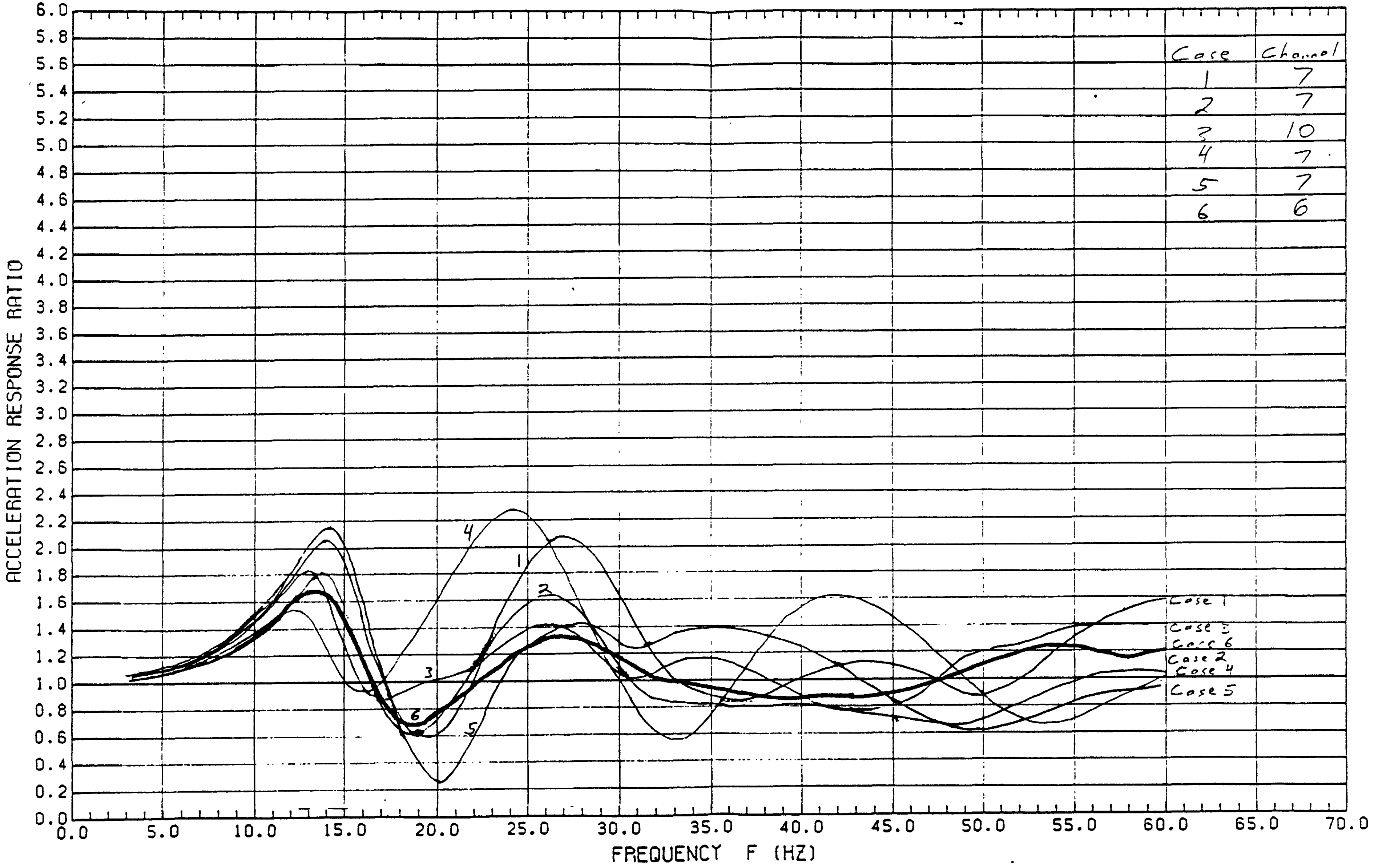

Figure 3.23. Acceleration response of channel 7 (ch. 10, case 3; ch. 6, case 6), transverse shaking.

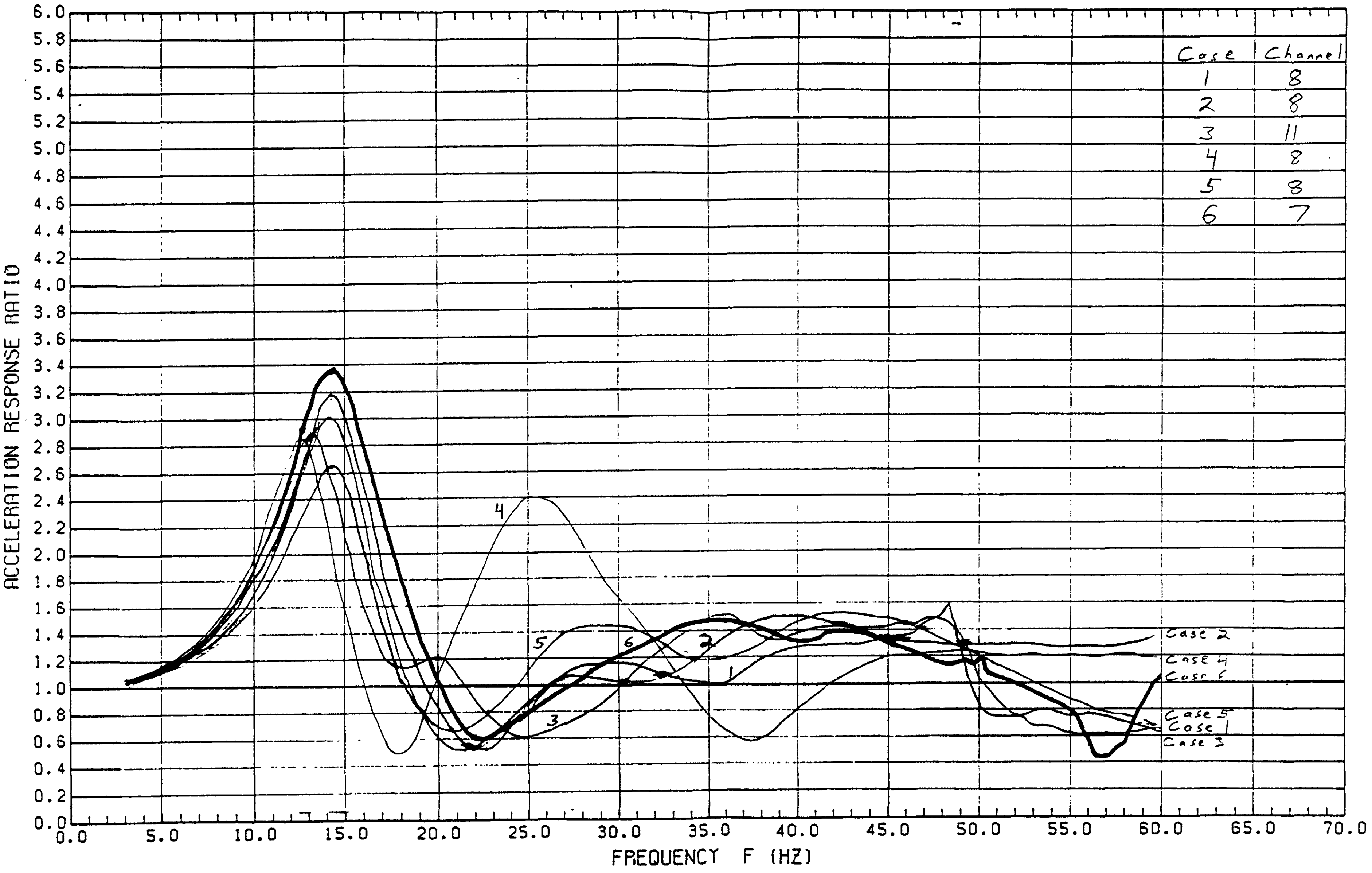

Figure 3.24. Acceleration response of channel 8 (ch. 11, case 3; channel 7, case 6), transverse shaking

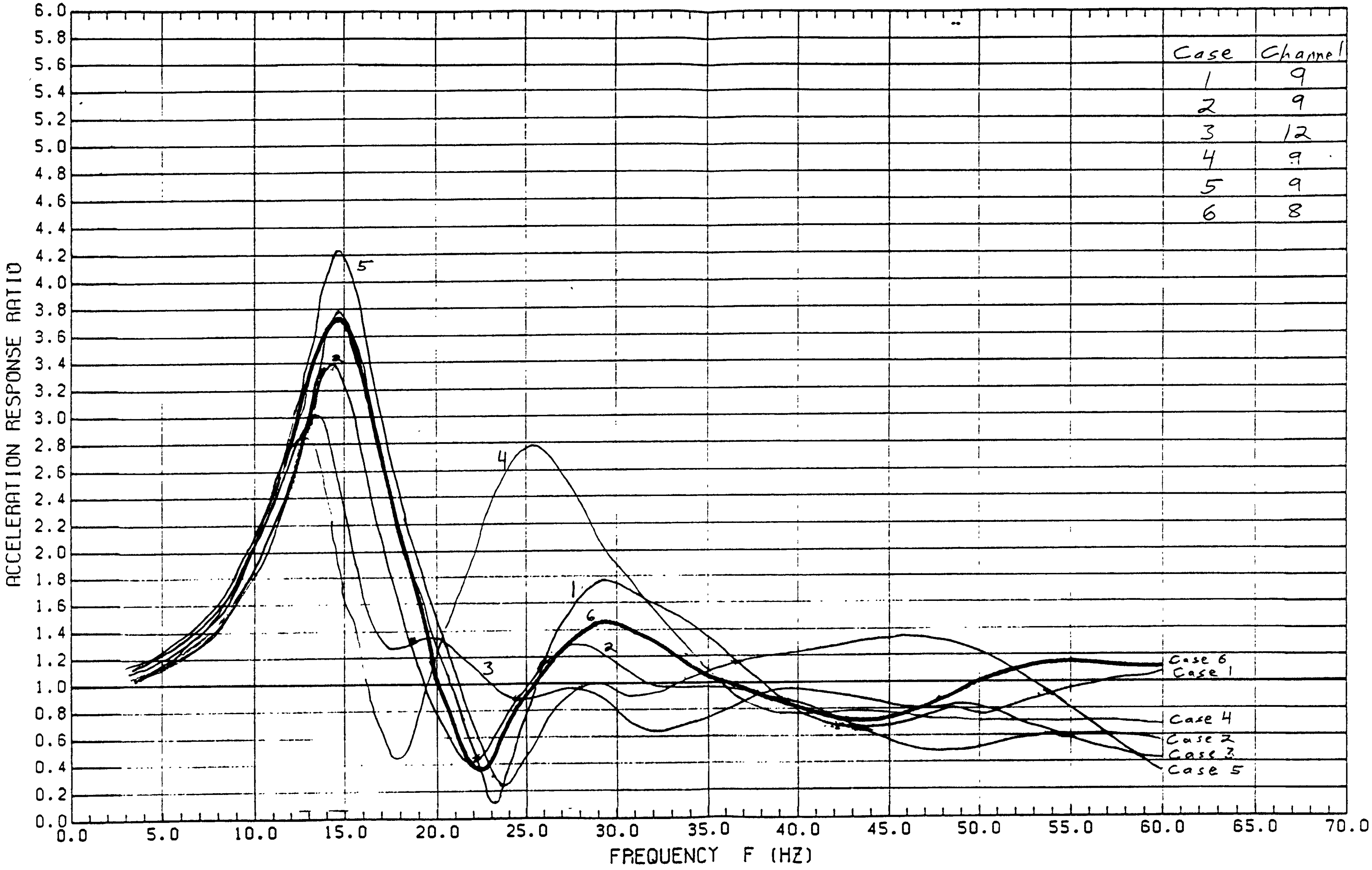

Figure 3.25. Acceleration response of channel 9 (ch. 12, case 3; ch. 8, case 6), transverse shaking.

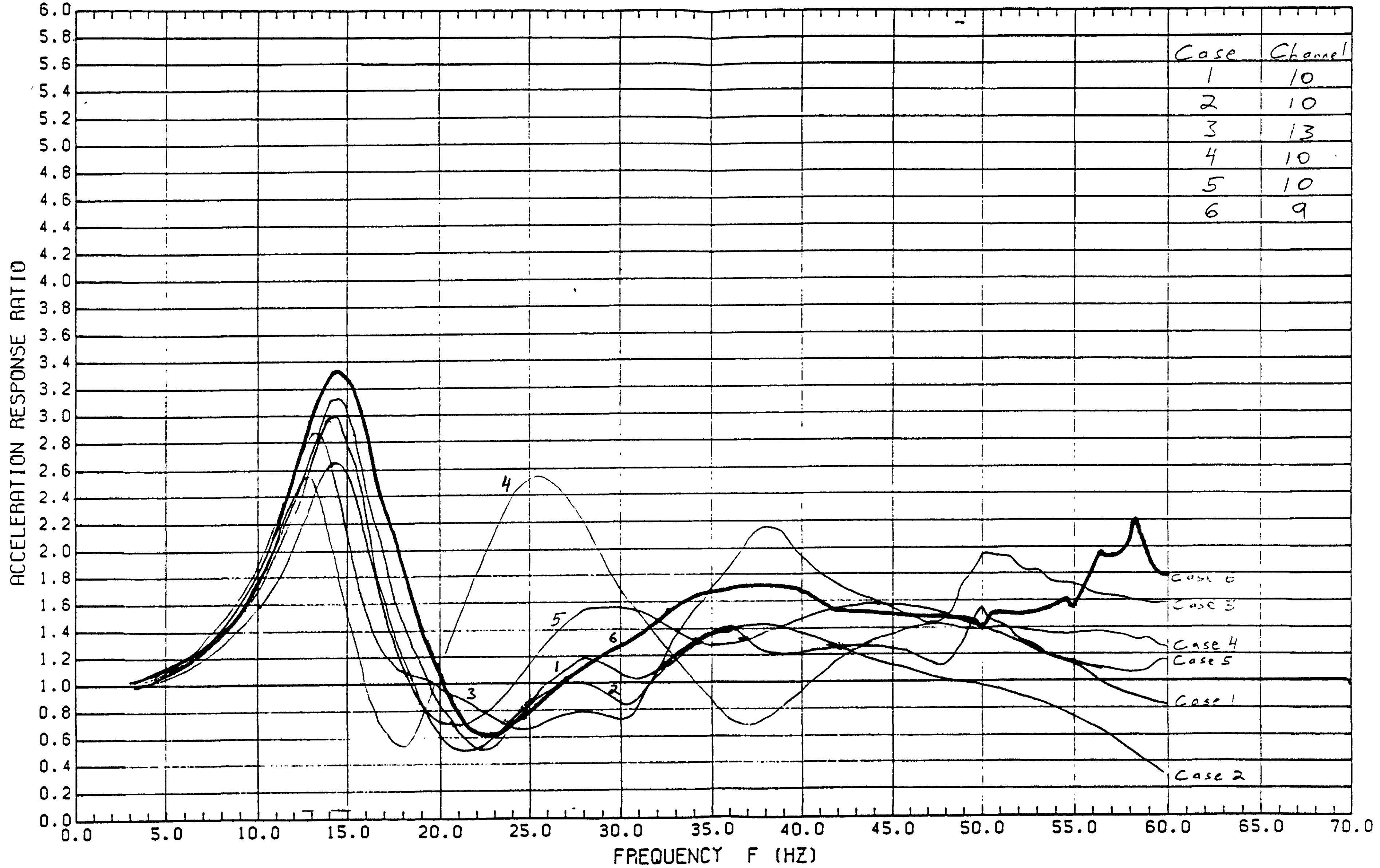

Figure 3.26. Acceleration response of channel 10 (ch. 13, case 3; ch. 9, case 6), transverse shaking.

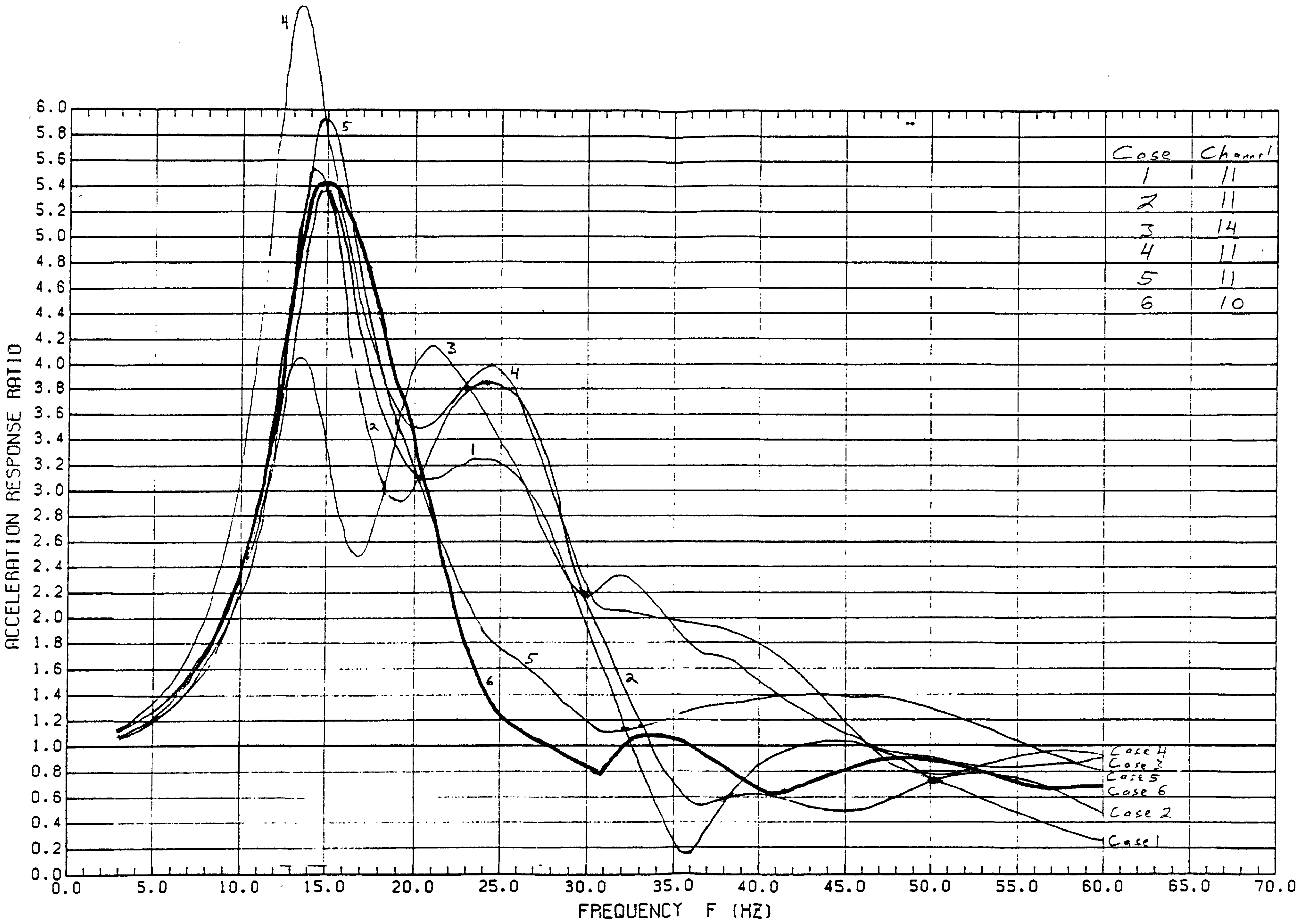

Figure 3.27. Acceleration response of channel 11 (ch. 14, case 3; ch. 10, case 6), transverse shaking.

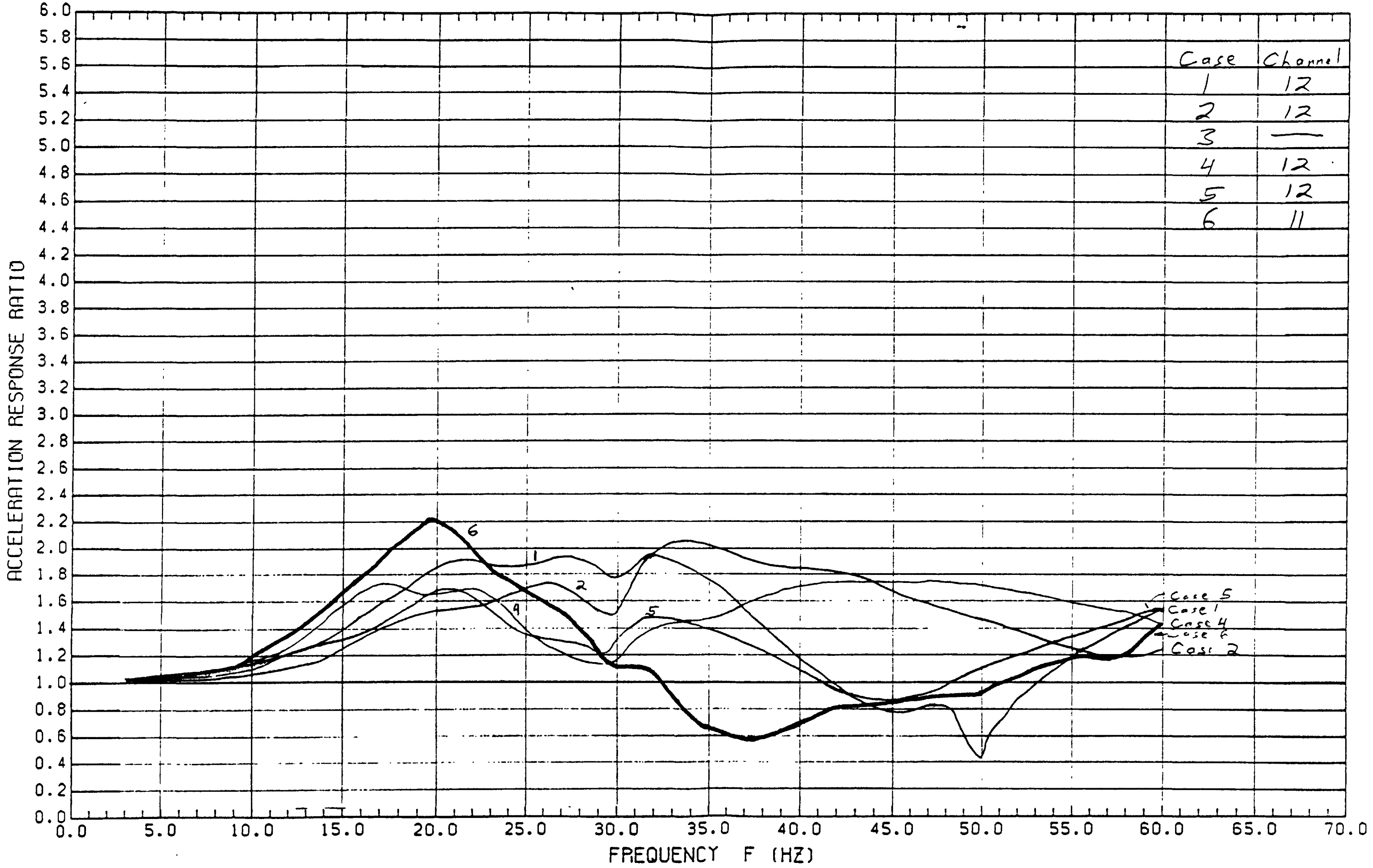

Figure 3.28. Acceleration response of channel 12 (ch. 11, case 6), transverse shaking.

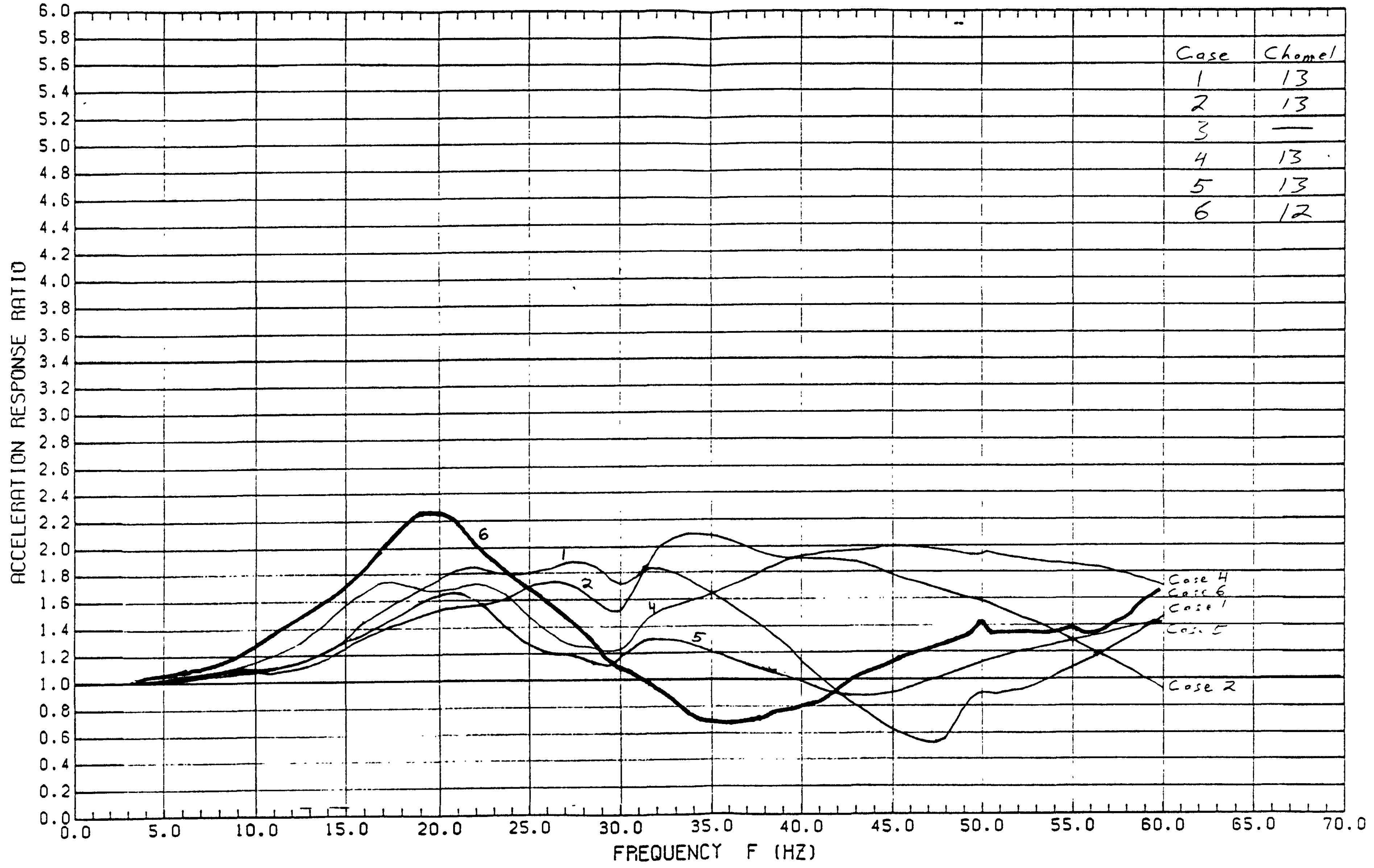

Figure 3.29. Acceleration response of channel 13 (ch. 12, case 6), transverse shaking.

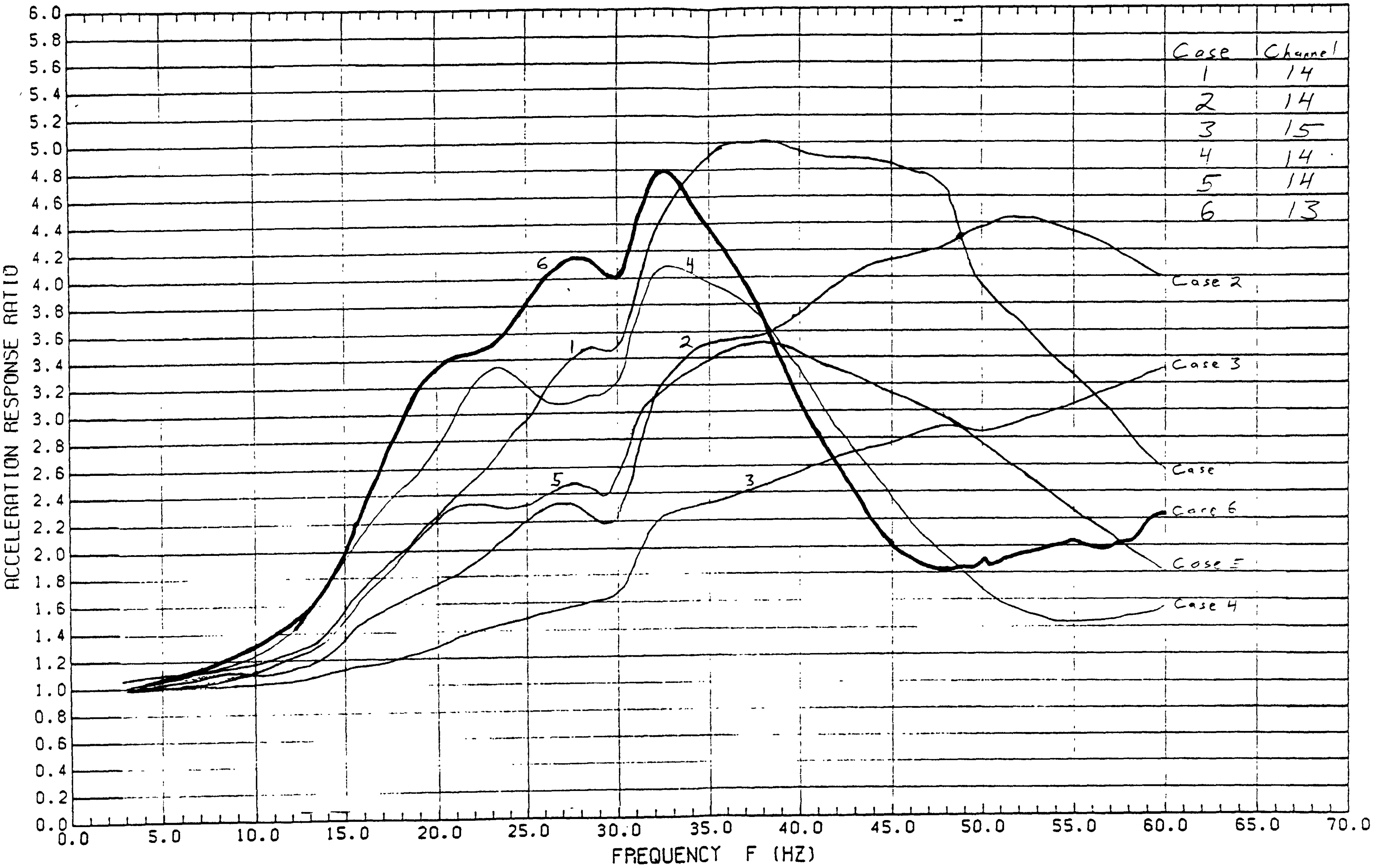

Figure 3.30. Acceleration response of channel 14 (ch. 15, case 3; channel 13, case 6), transverse shaking.

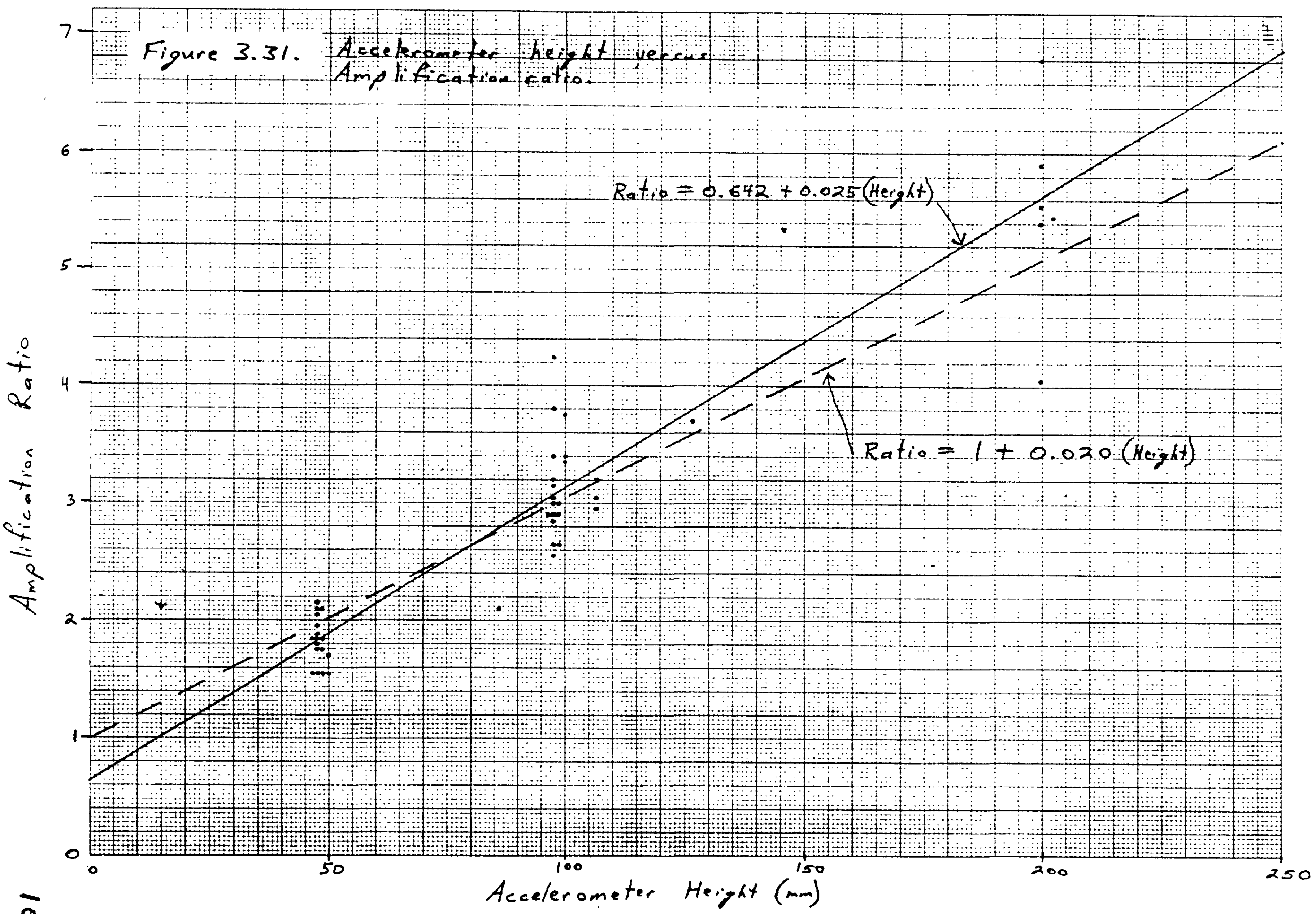

Figure 3.31. Accelerometer height versus Amplification ratio.

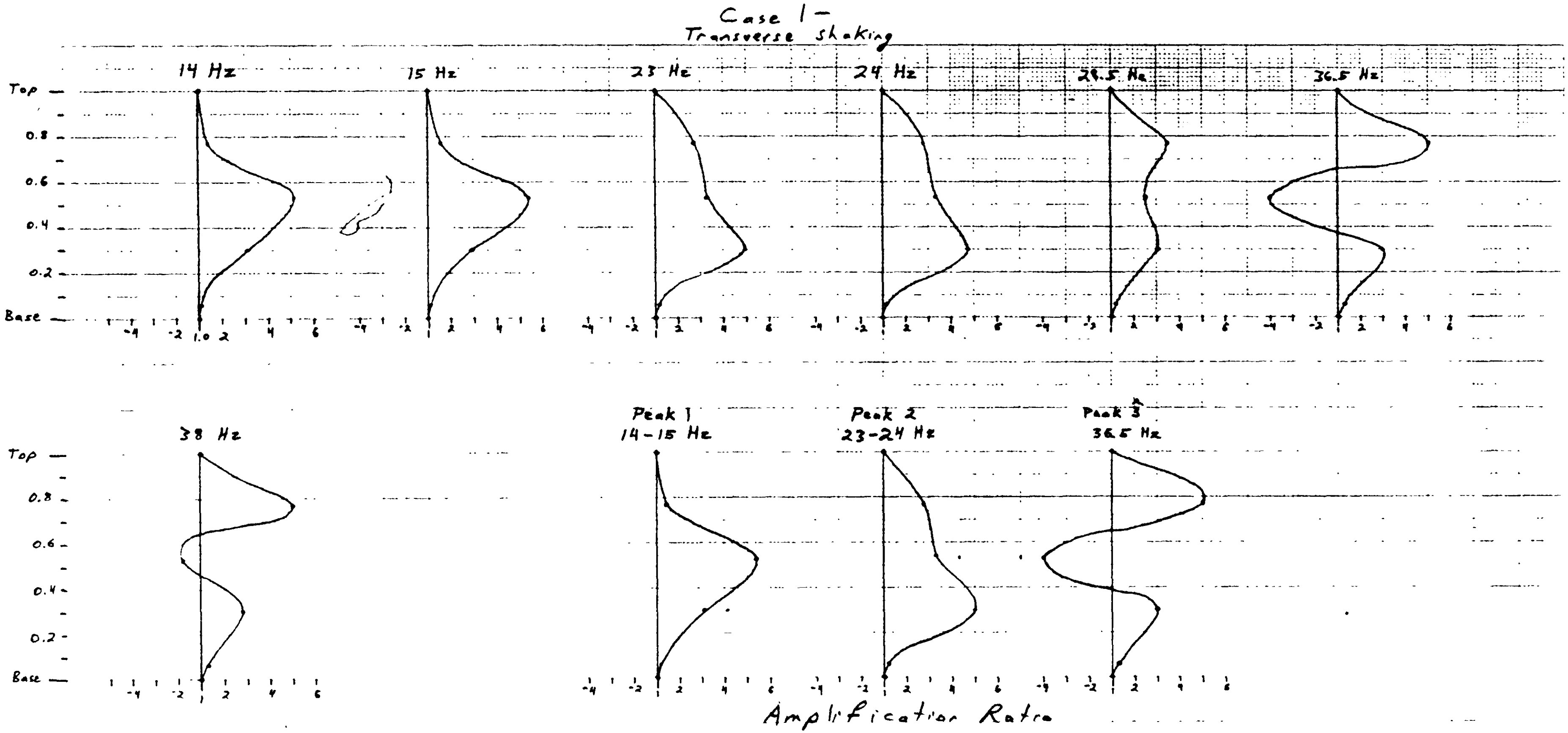

Figure 3.32. Acceleration ratio plotted along ridge crestline, case 1, transverse shaking.

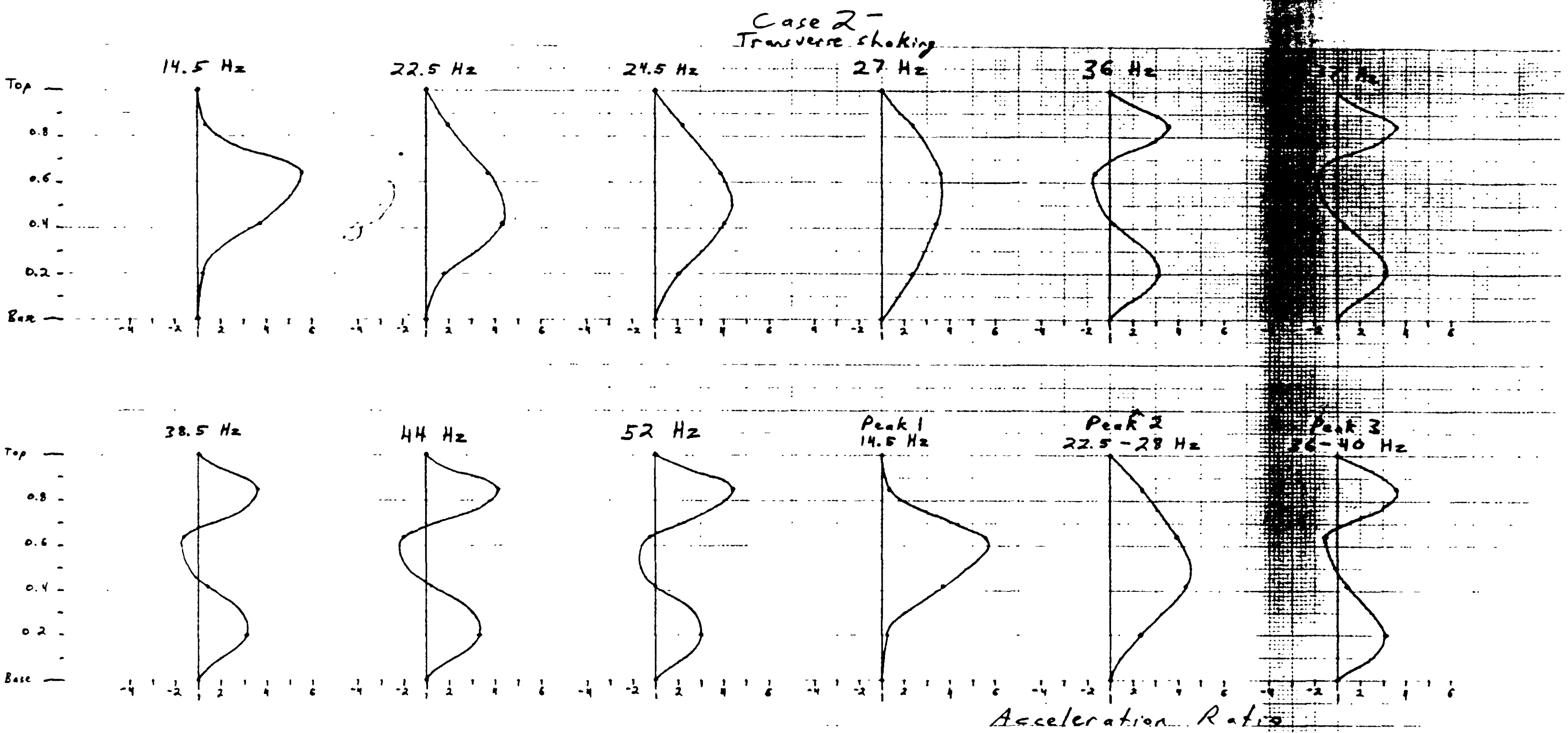

Figure 3.33 Acceleration ratio plotted along ridge crestline, case 2, transverse shaking.

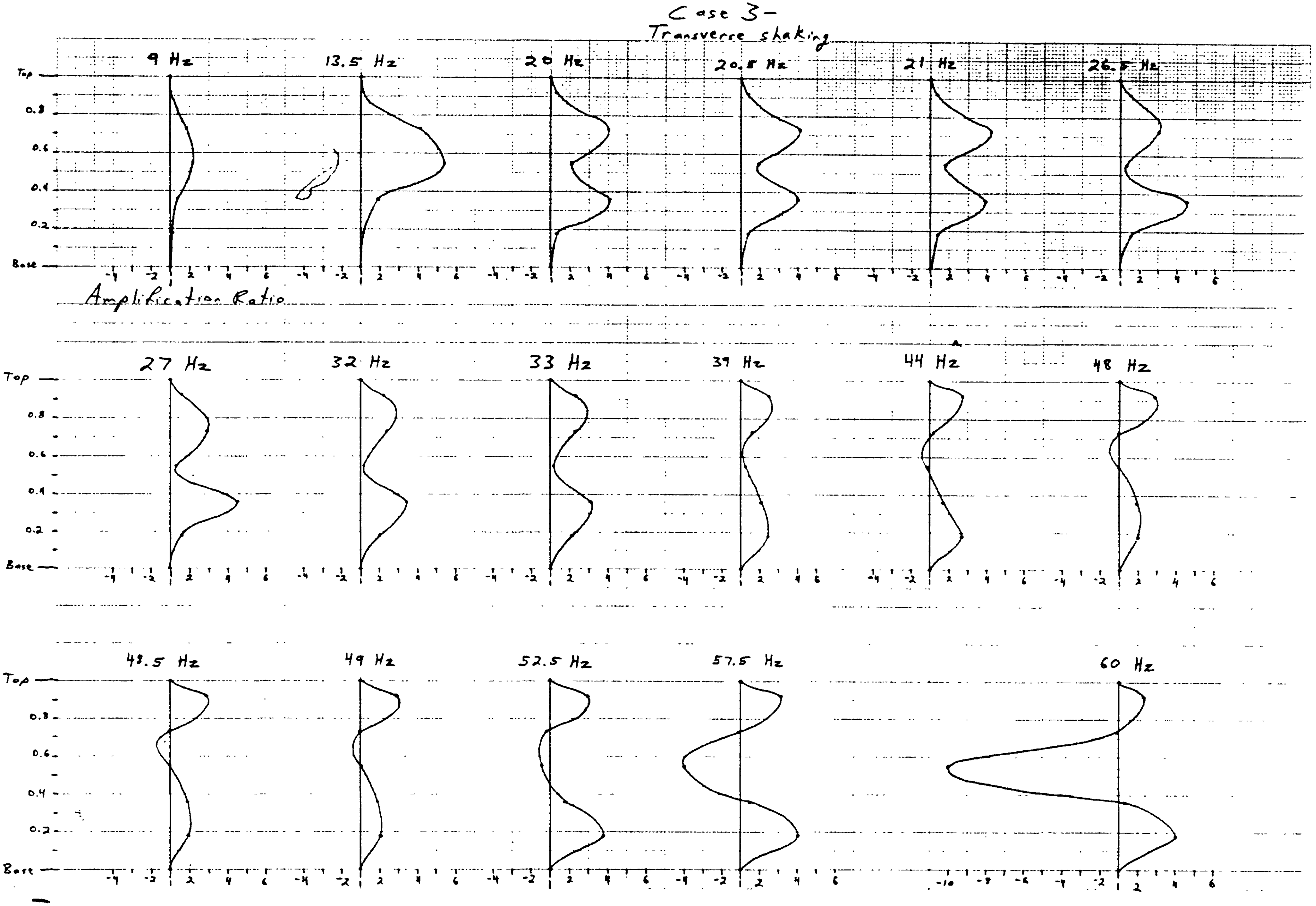

Figure 3.34. Acceleration ratio plotted along ridge crestline, case 3, transverse shaking.

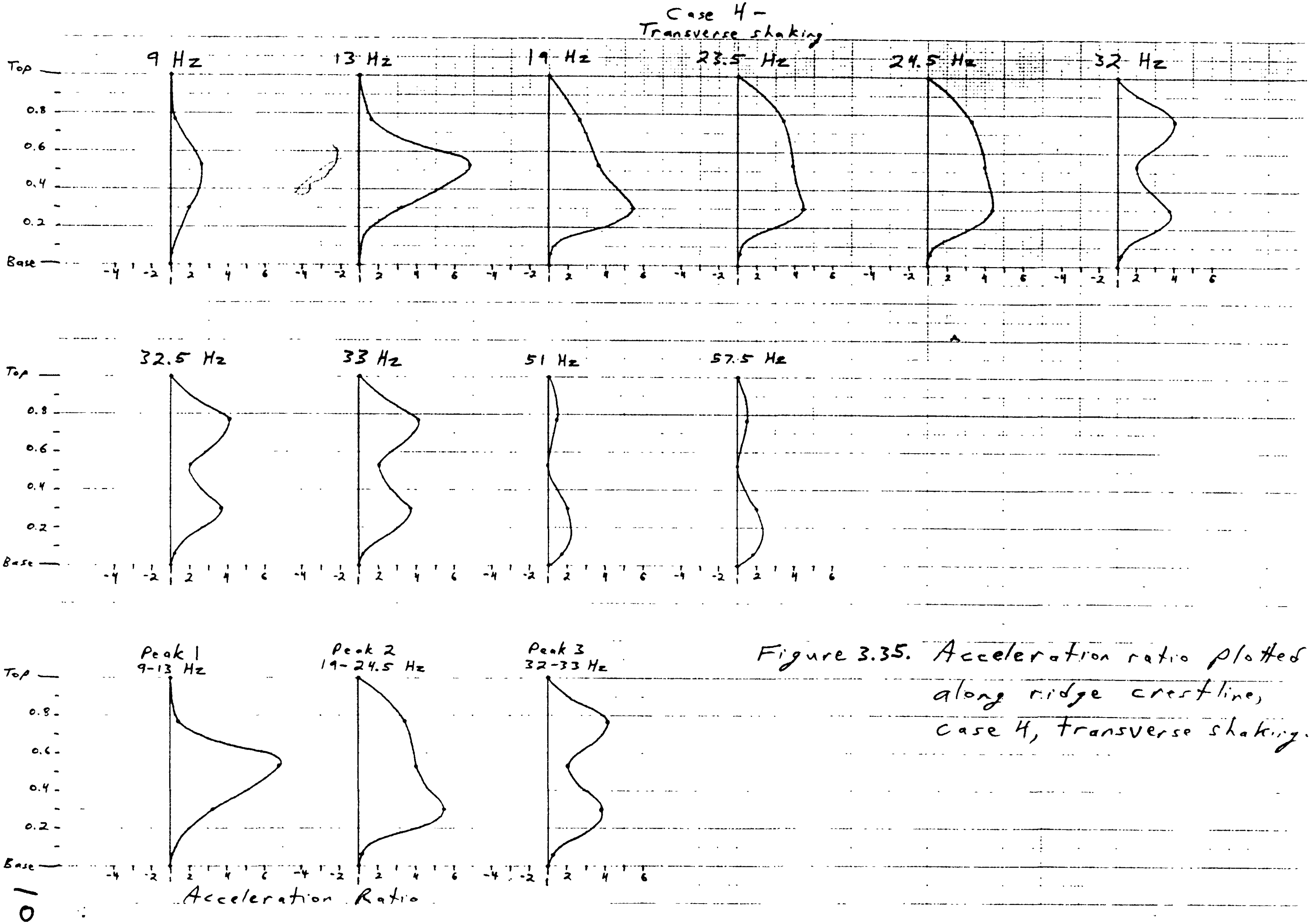

Figure 3.35. Acceleration ratio plotted along ridge crestline, case 4, transverse shaking.

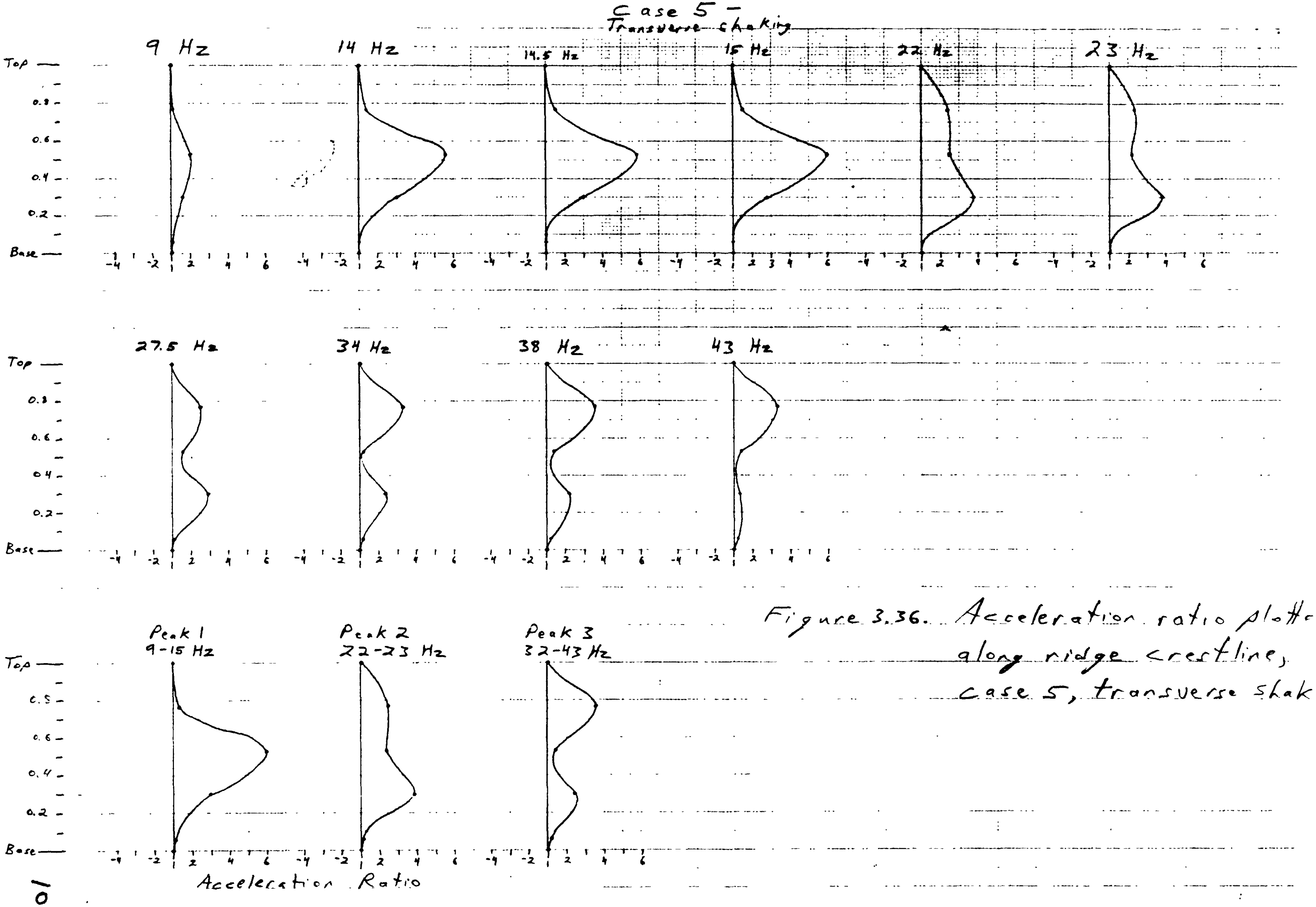

Figure 3.36. Acceleration ratio plotted along ridge crestline, case 5, transverse shaking.

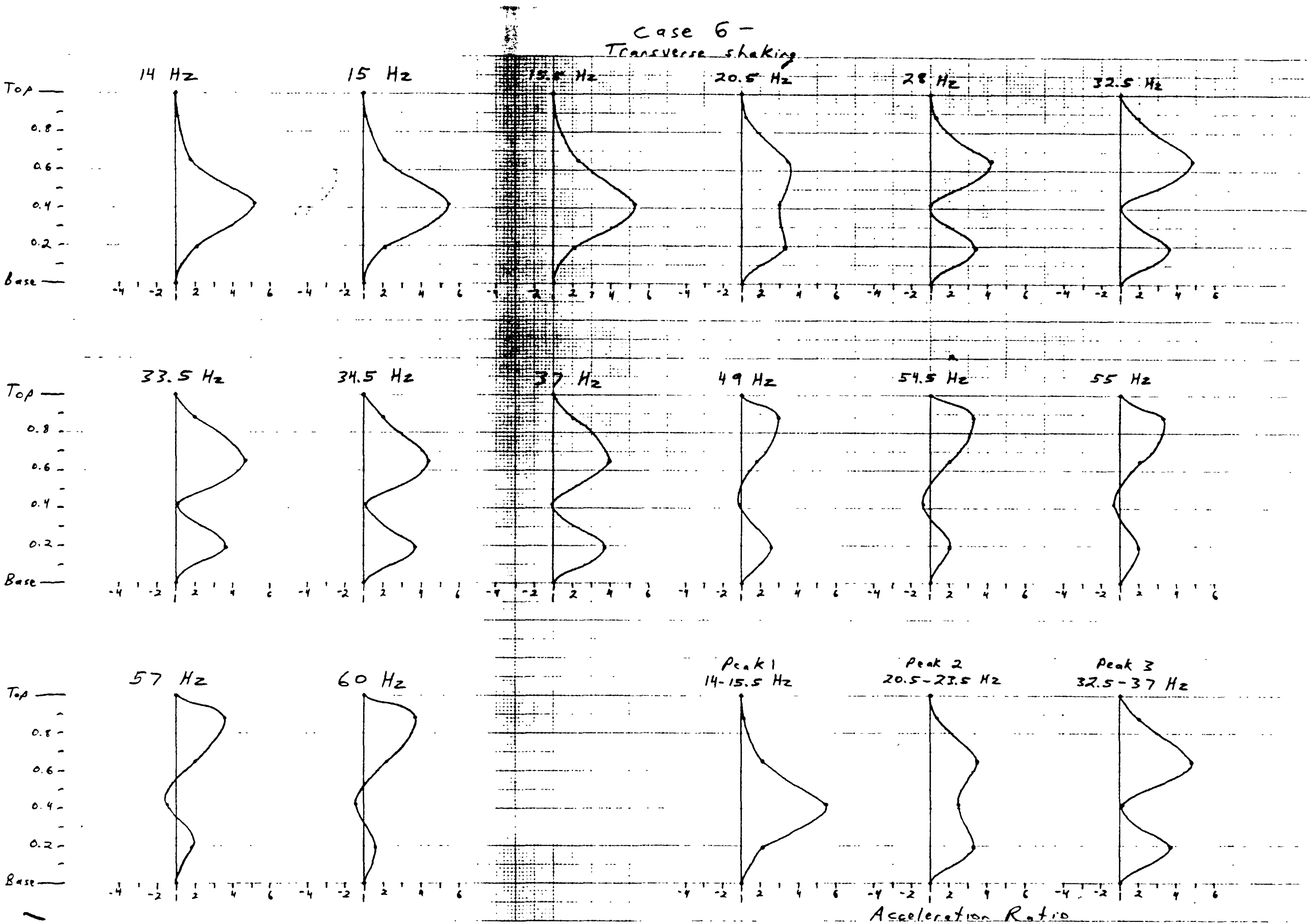

Figure 3.37. Acceleration ratio plotted along ridge crestline, case 6, transverse shaking.

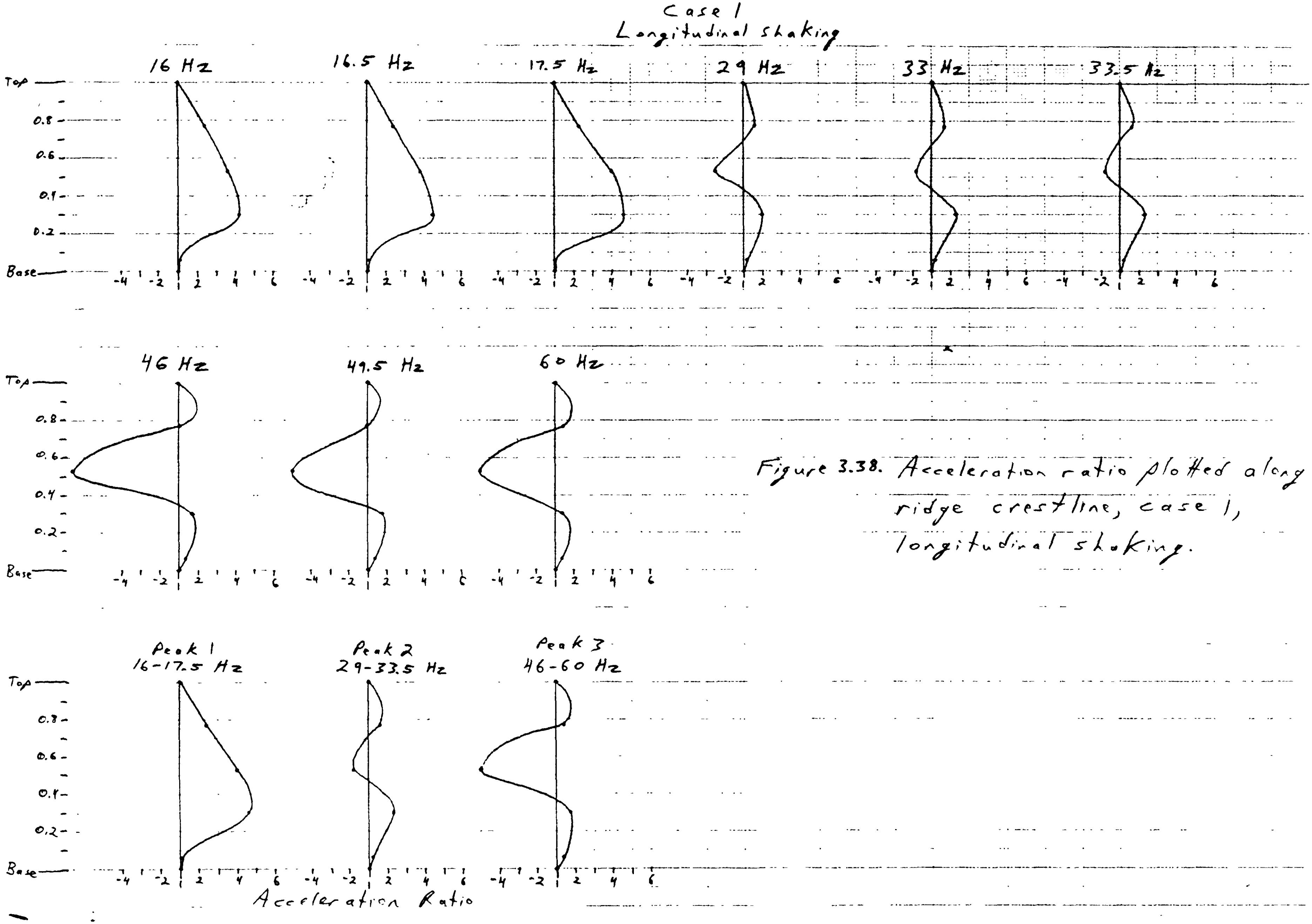

Figure 3.38. Acceleration ratio plotted along ridge crestline, case 1, longitudinal shaking.

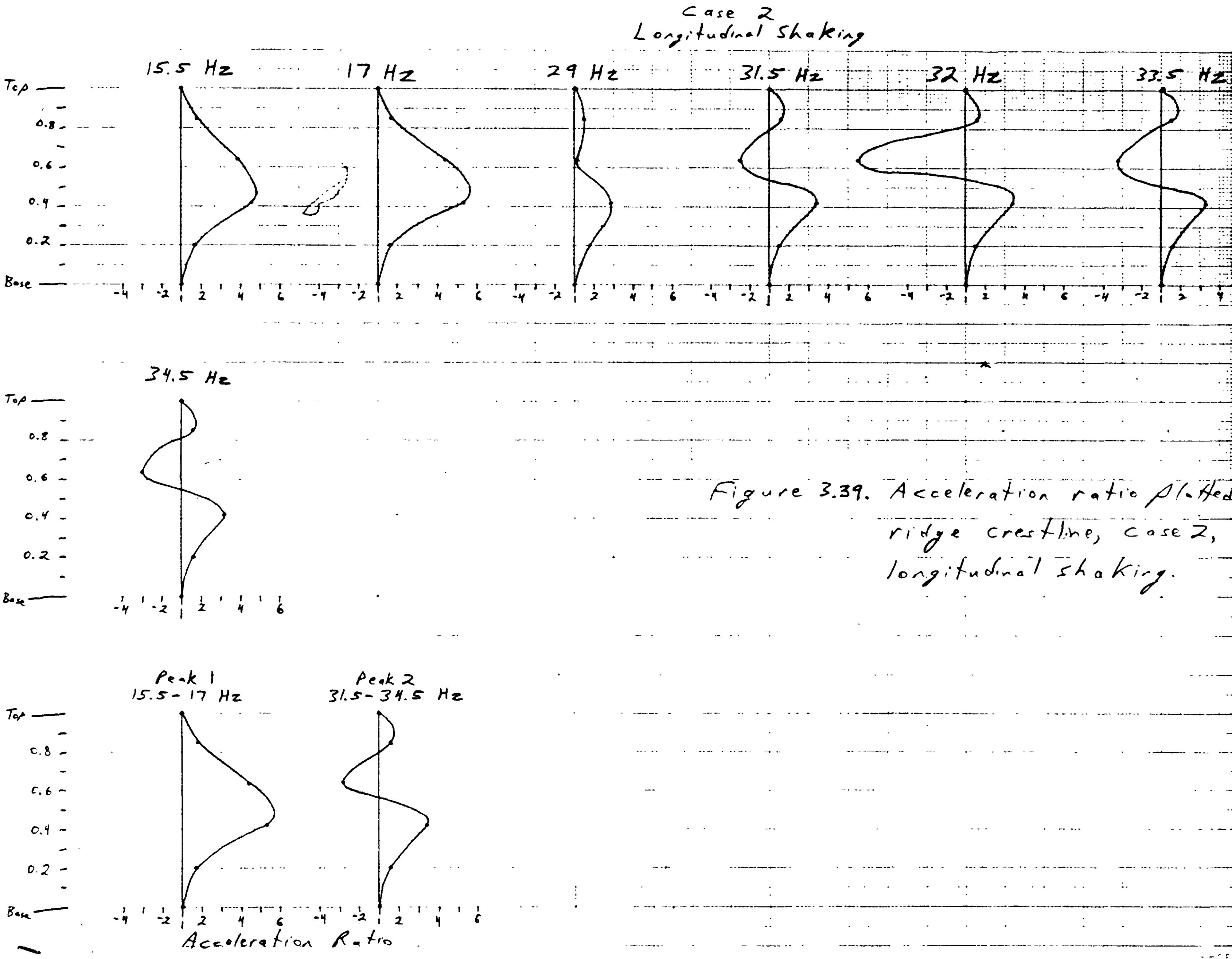

Figure 3.39. Acceleration ratio plotted along ridge crestline, case 2, longitudinal shaking.

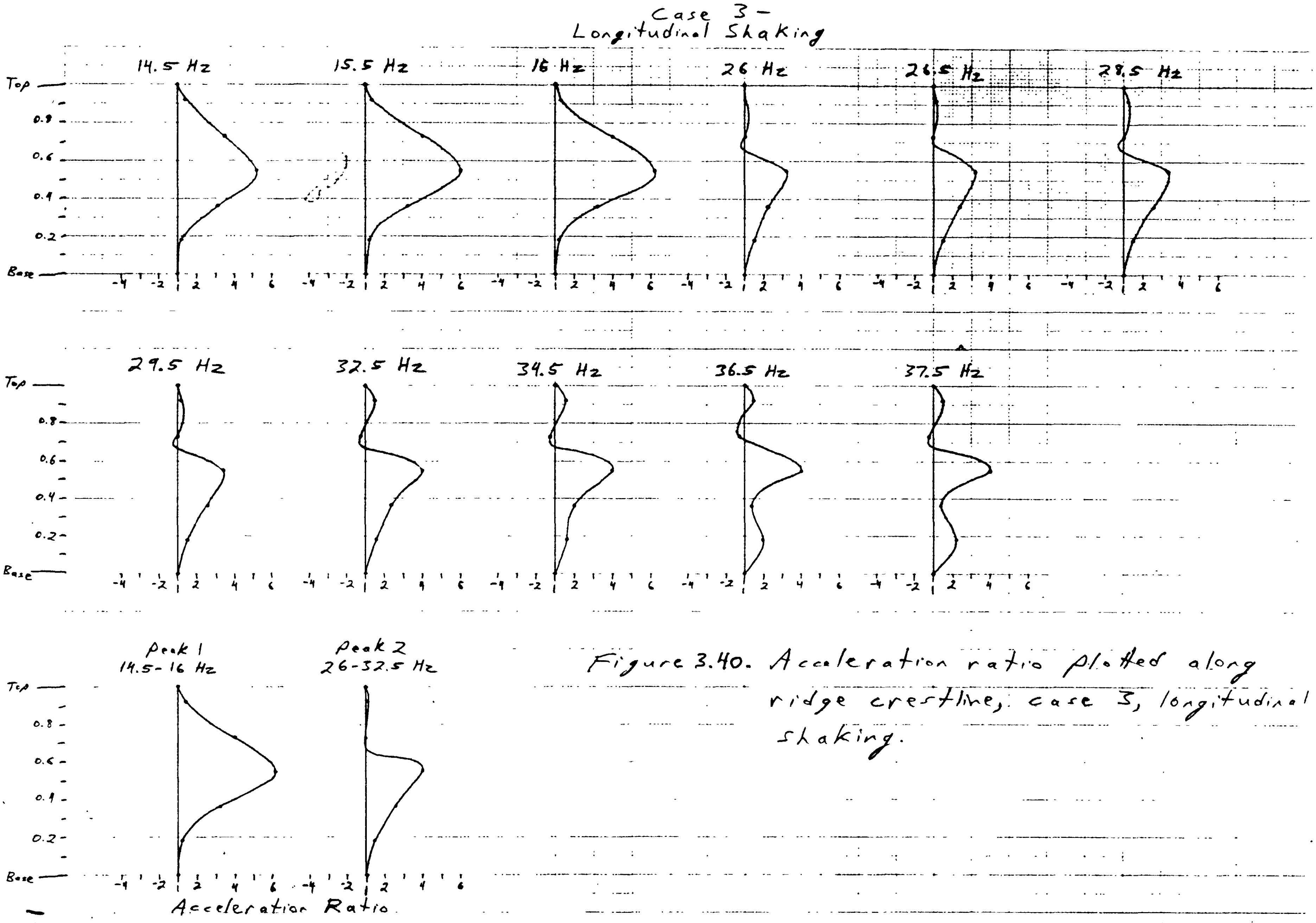

Figure 3.40. Acceleration ratio plotted along ridge crestline, case 3, longitudinal shaking.

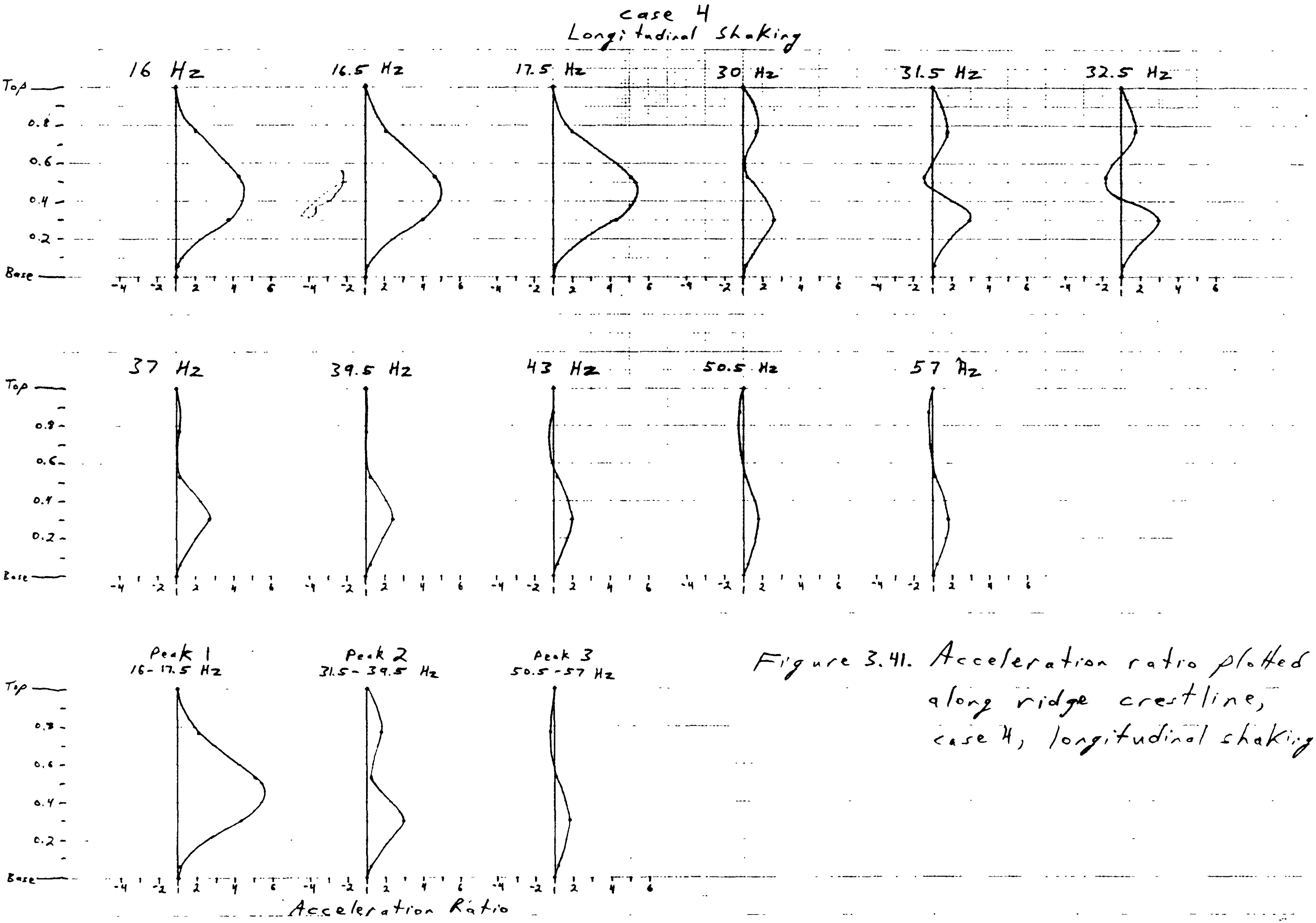

Figure 3.41. Acceleration ratio plotted along ridge crestline, case 4, longitudinal shaking.

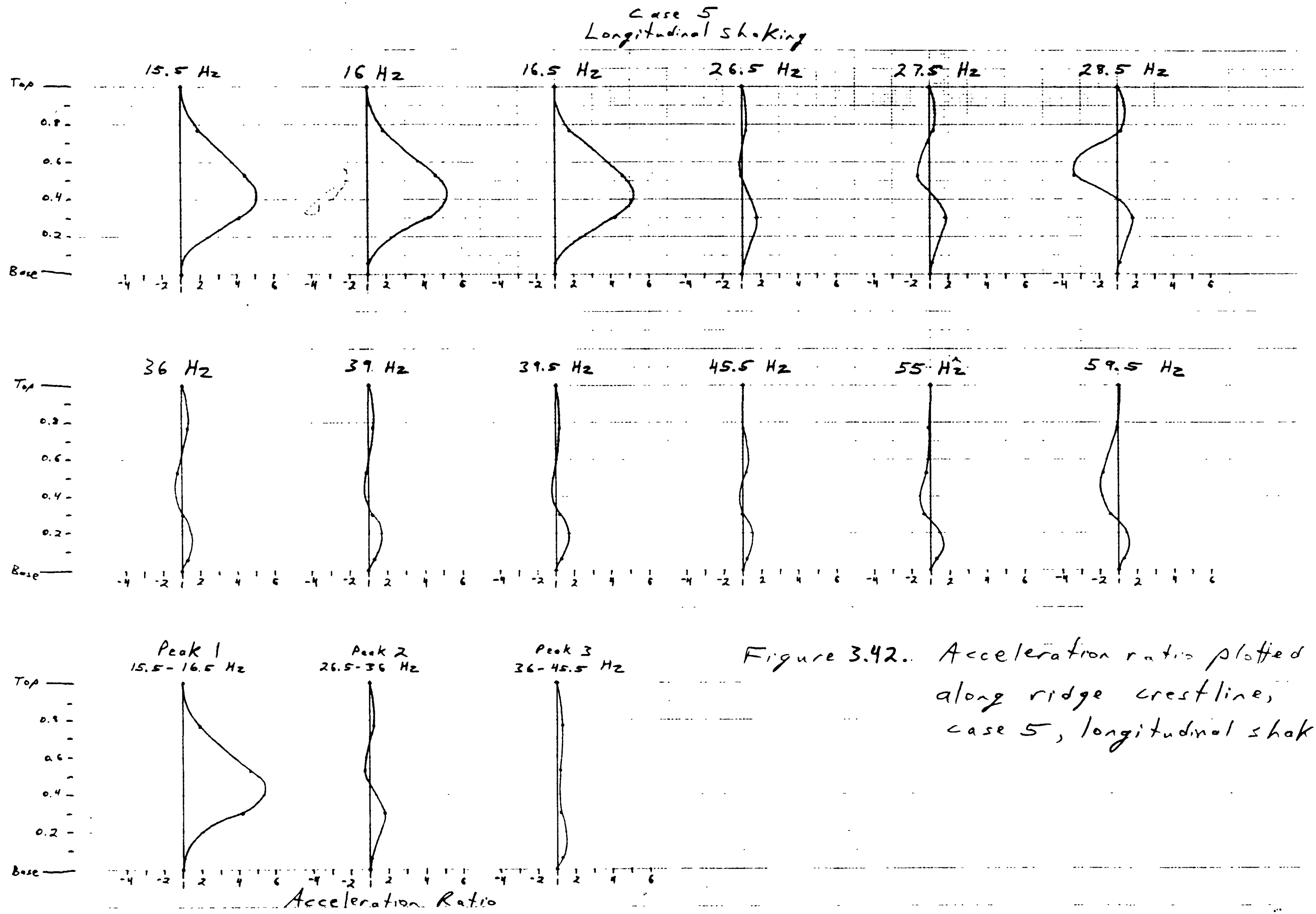

Figure 3.42. Acceleration ratio plotted along ridge crestline, case 5, longitudinal shaking.

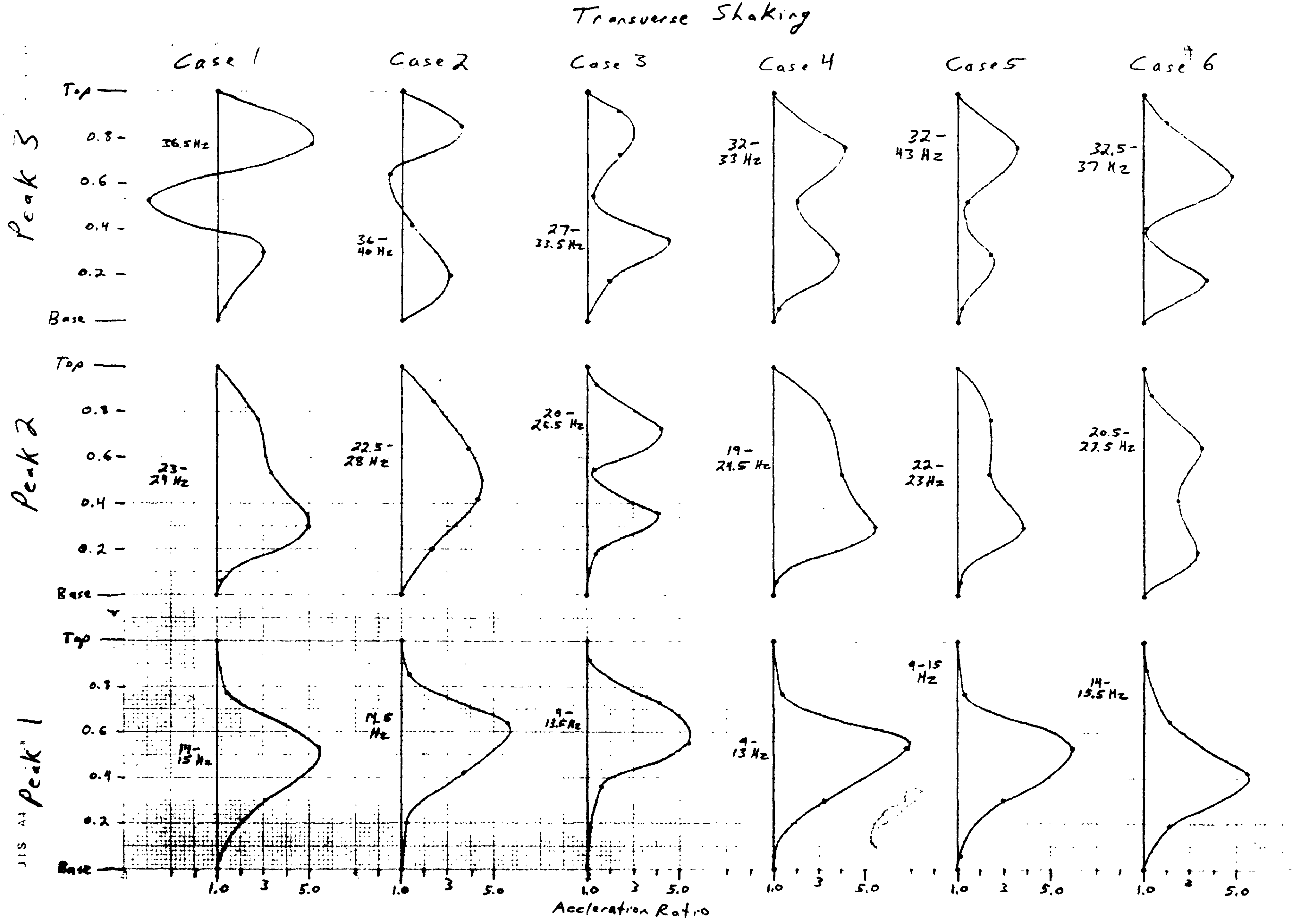

Figure 3.43. Acceleration ratio plotted along ridge crestline for three major response peaks, transverse shaking.

Longitudinal Shaking

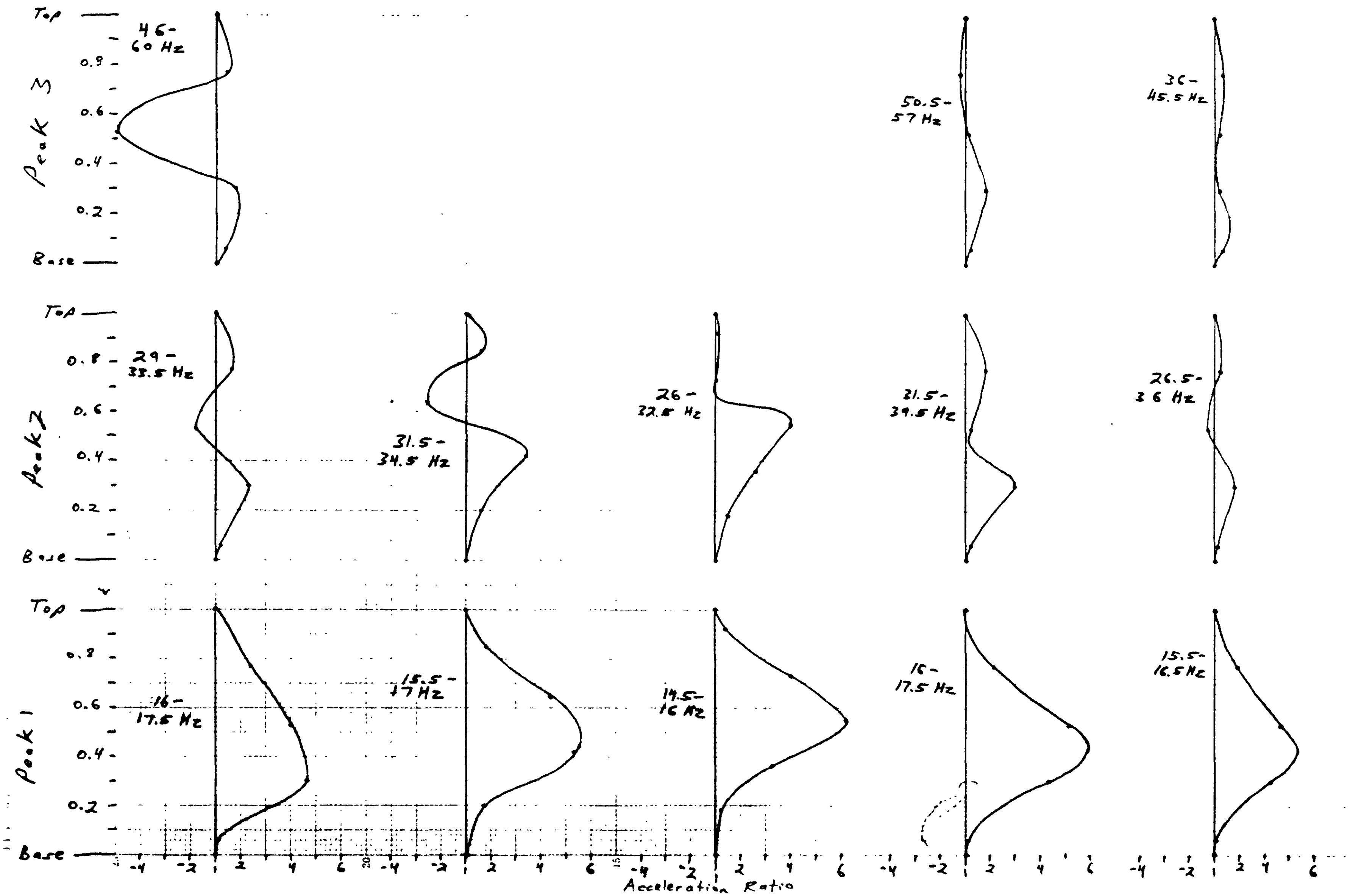

Figure 3.44. Acceleration ratio plotted along ridge crestline for three major response peaks, longitudinal shaking.

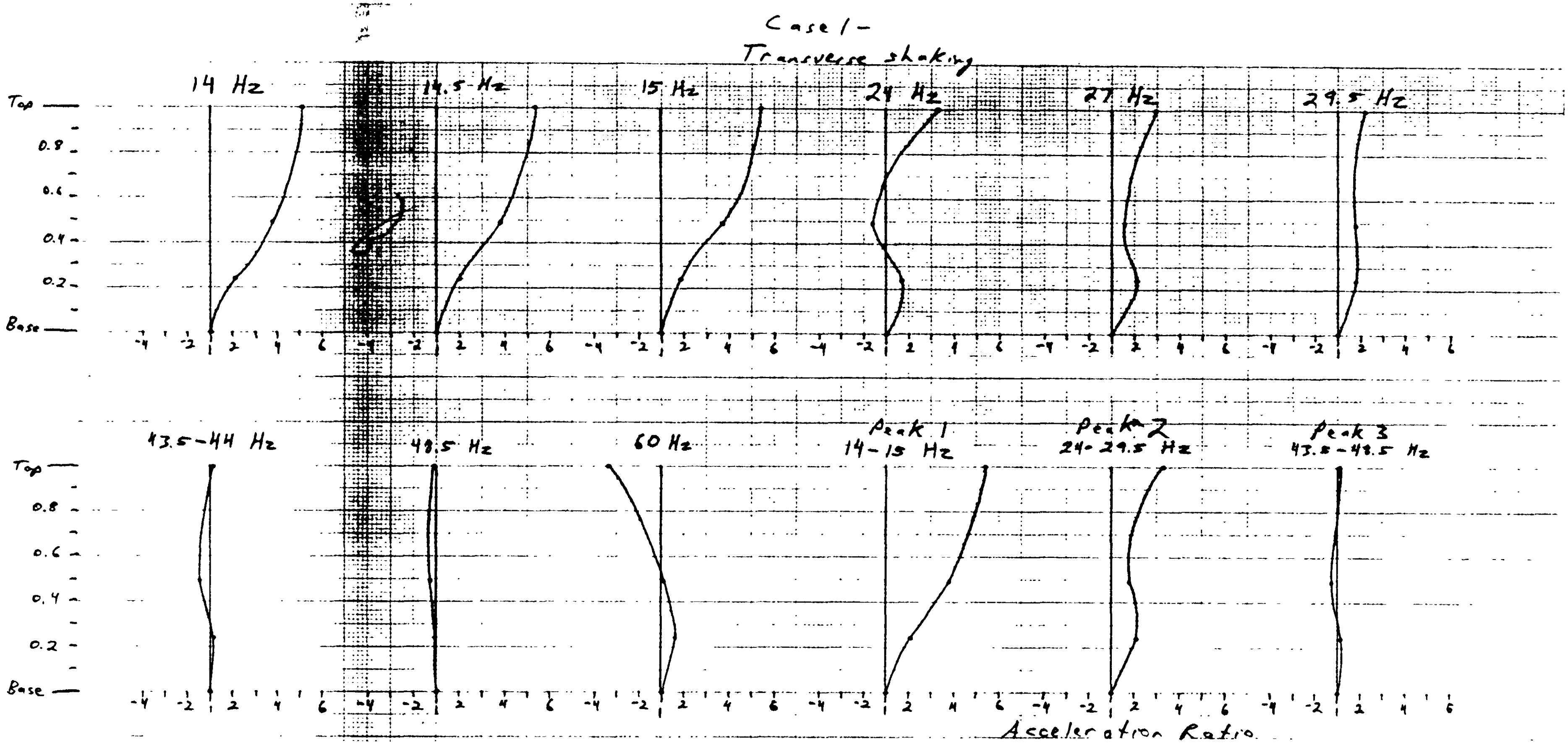

Figure 3.45. Acceleration ratio plotted along maximum vertical cross section, Case 1, transverse shaking.

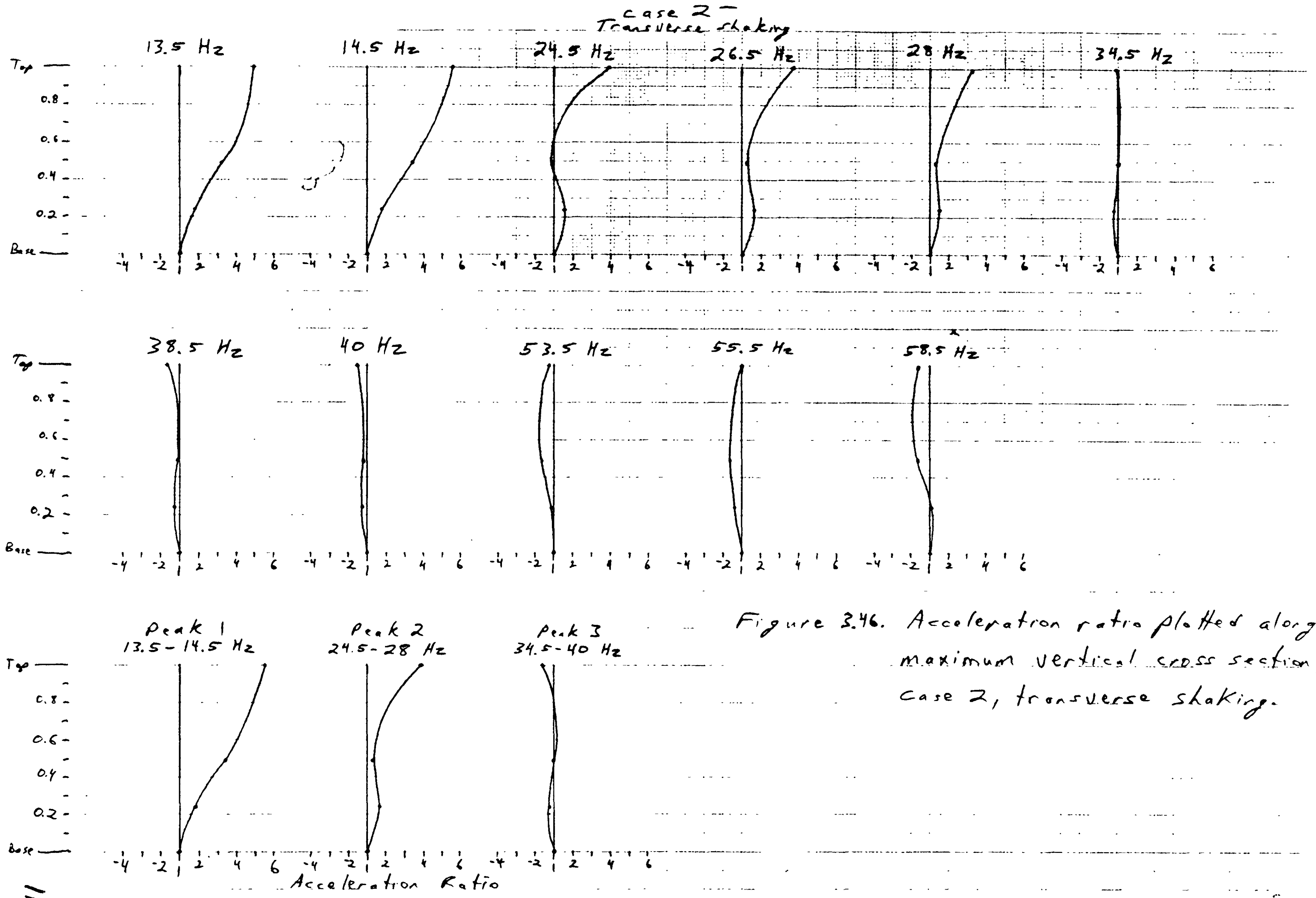

Figure 3.46. Acceleration ratio plotted along maximum vertical cross section, case 2, transverse shaking.

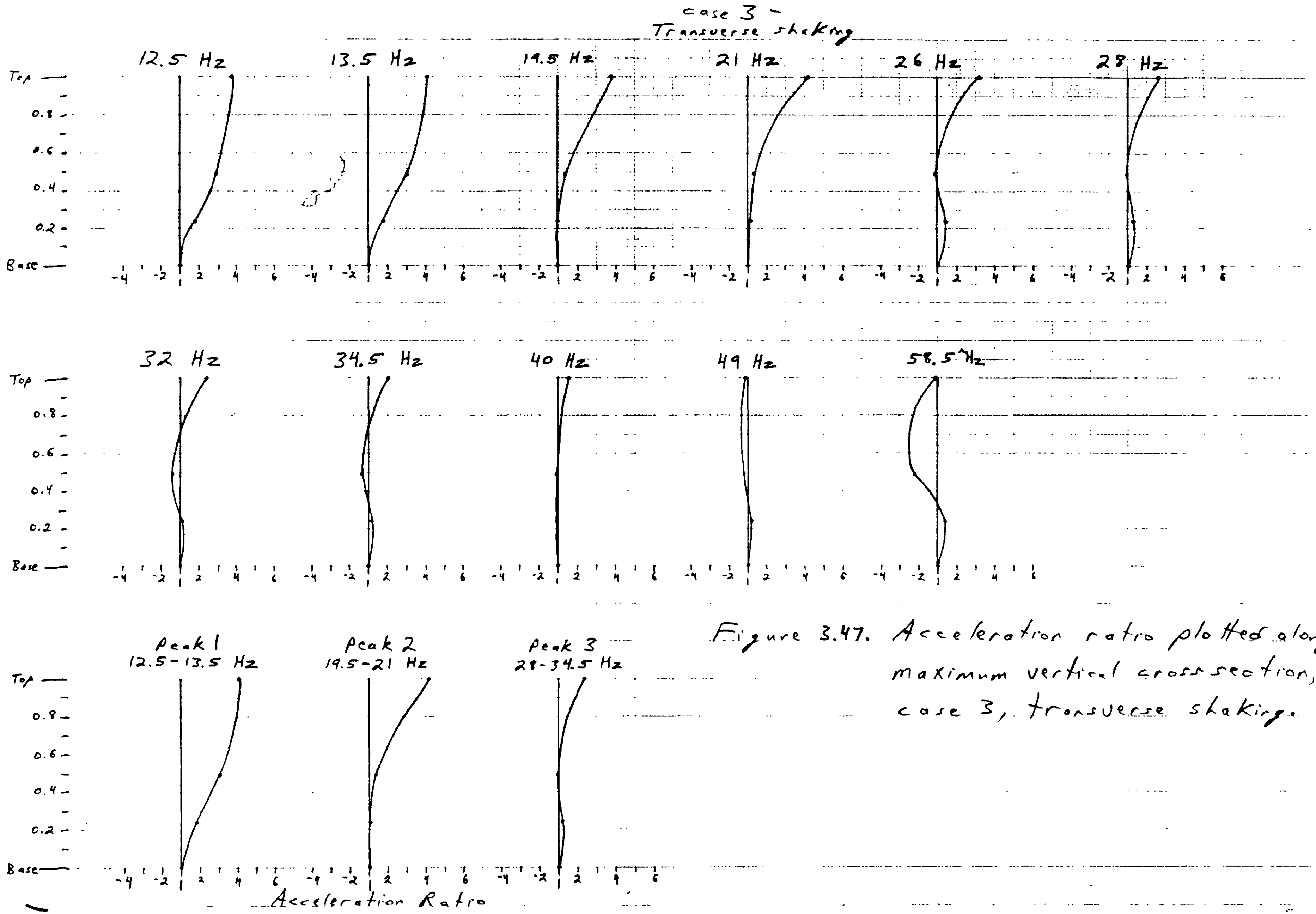

Figure 3.47. Acceleration ratio plotted along maximum vertical cross section, case 3, transverse shaking.

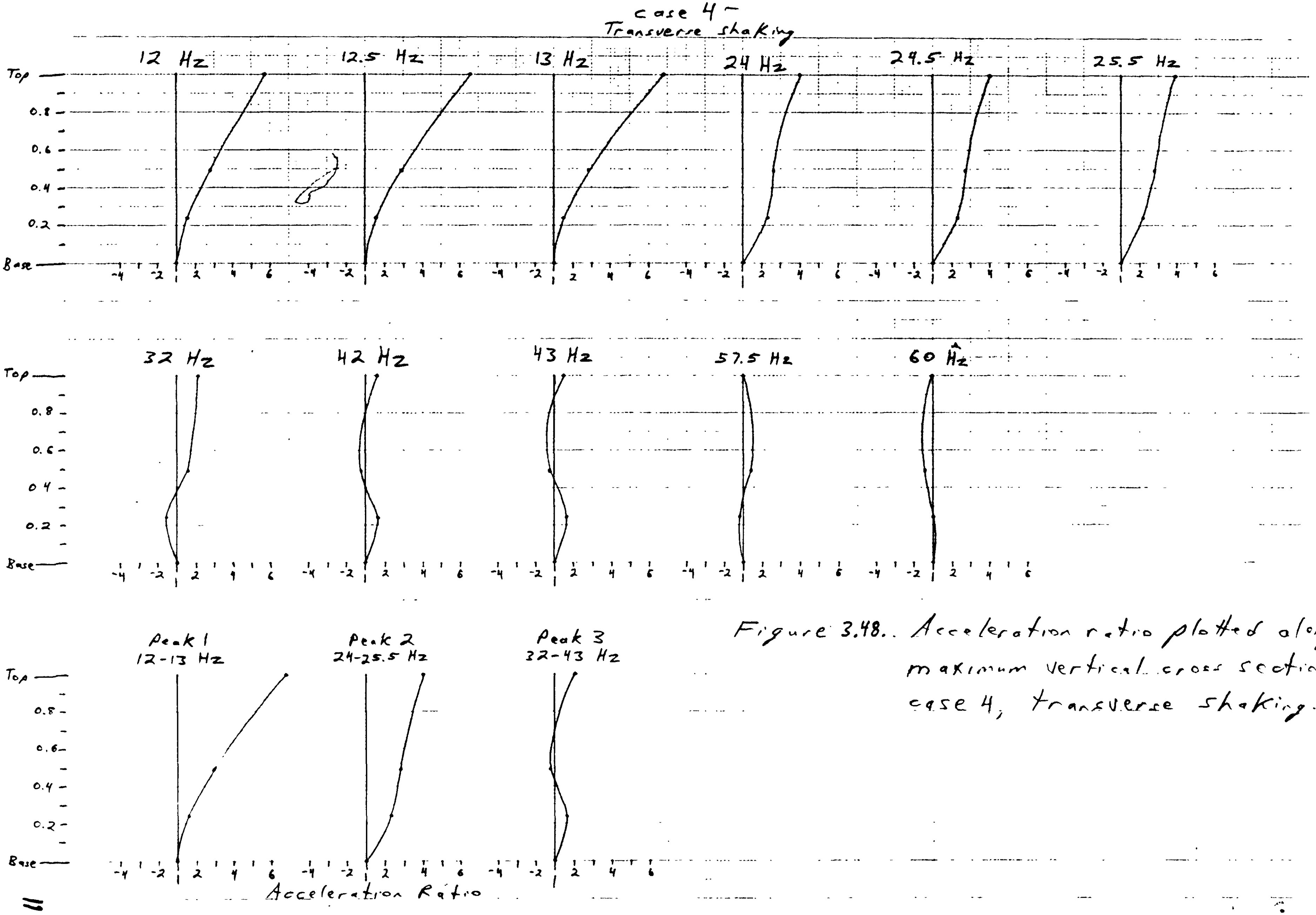

Figure 3.48. Acceleration ratio plotted along maximum vertical cross section, case 4, transverse shaking.

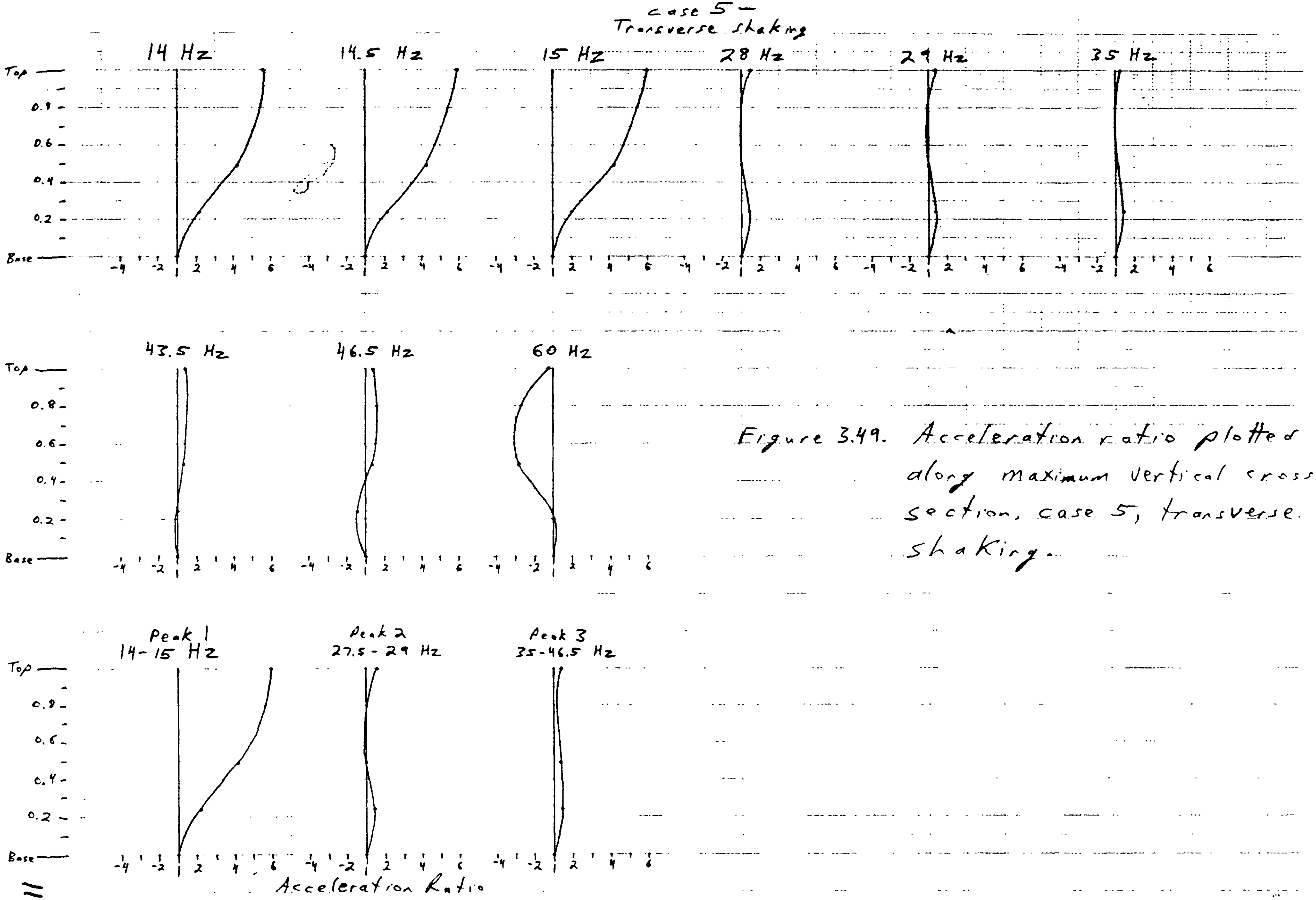

Figure 3.49. Acceleration ratio plotted along maximum vertical cross section, case 5, transverse shaking.

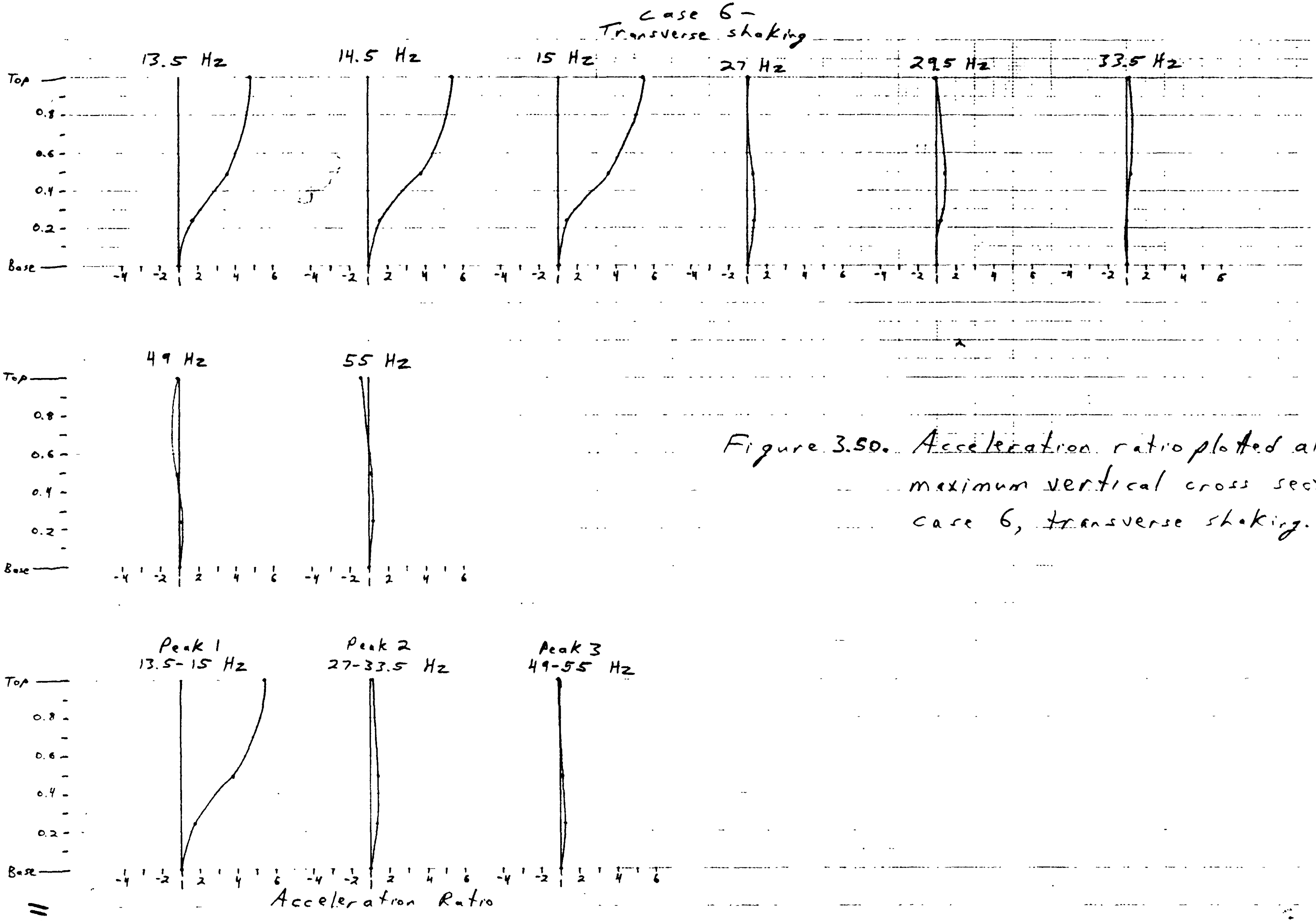

Figure 3.50. Acceleration ratio plotted along maximum vertical cross section, case 6, transverse shaking.

Transverse Shaking

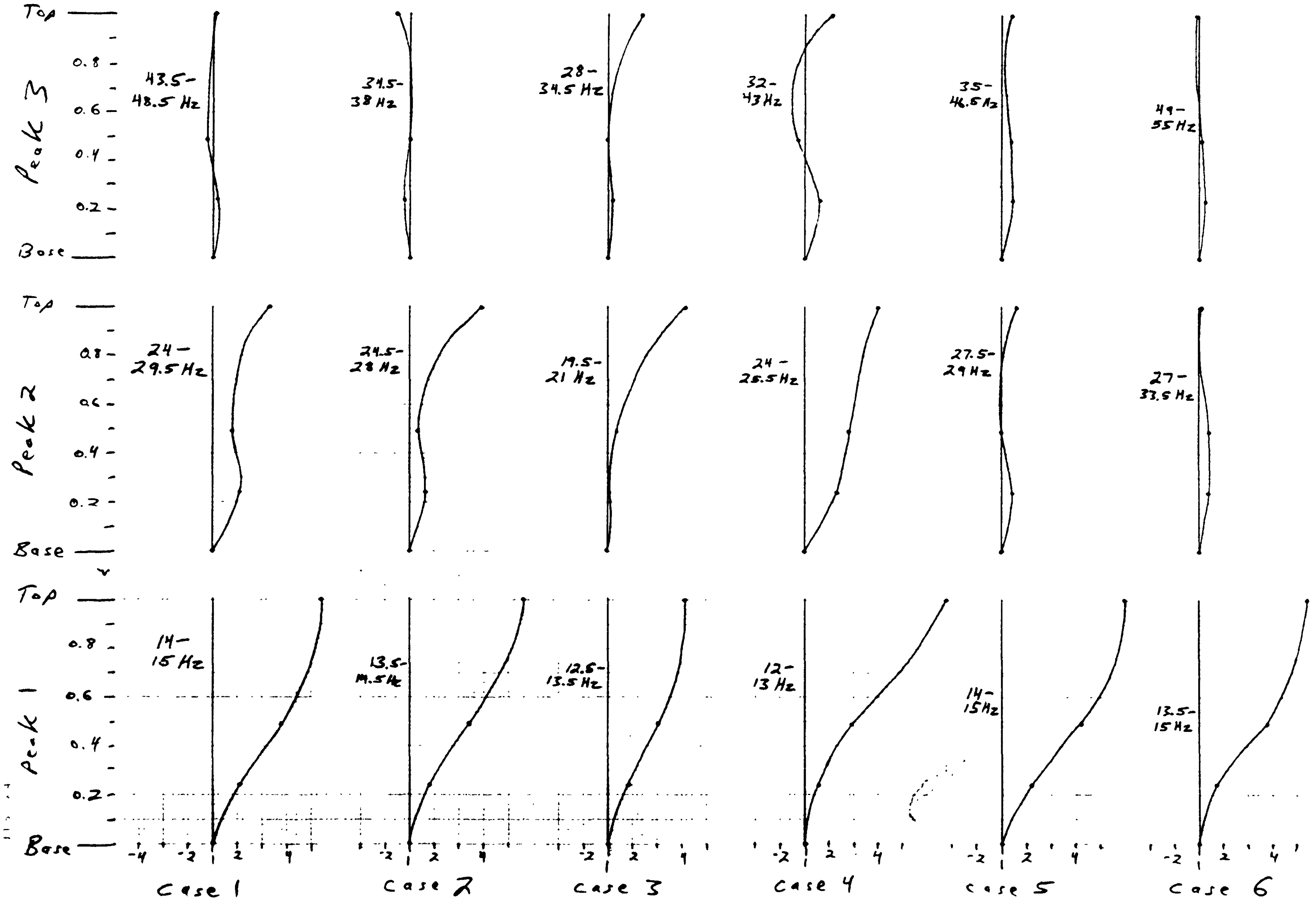

Figure 3.51. Acceleration ratio plotted along maximum vertical cross section for three major response peaks, transverse shaking.

Transverse Shaking

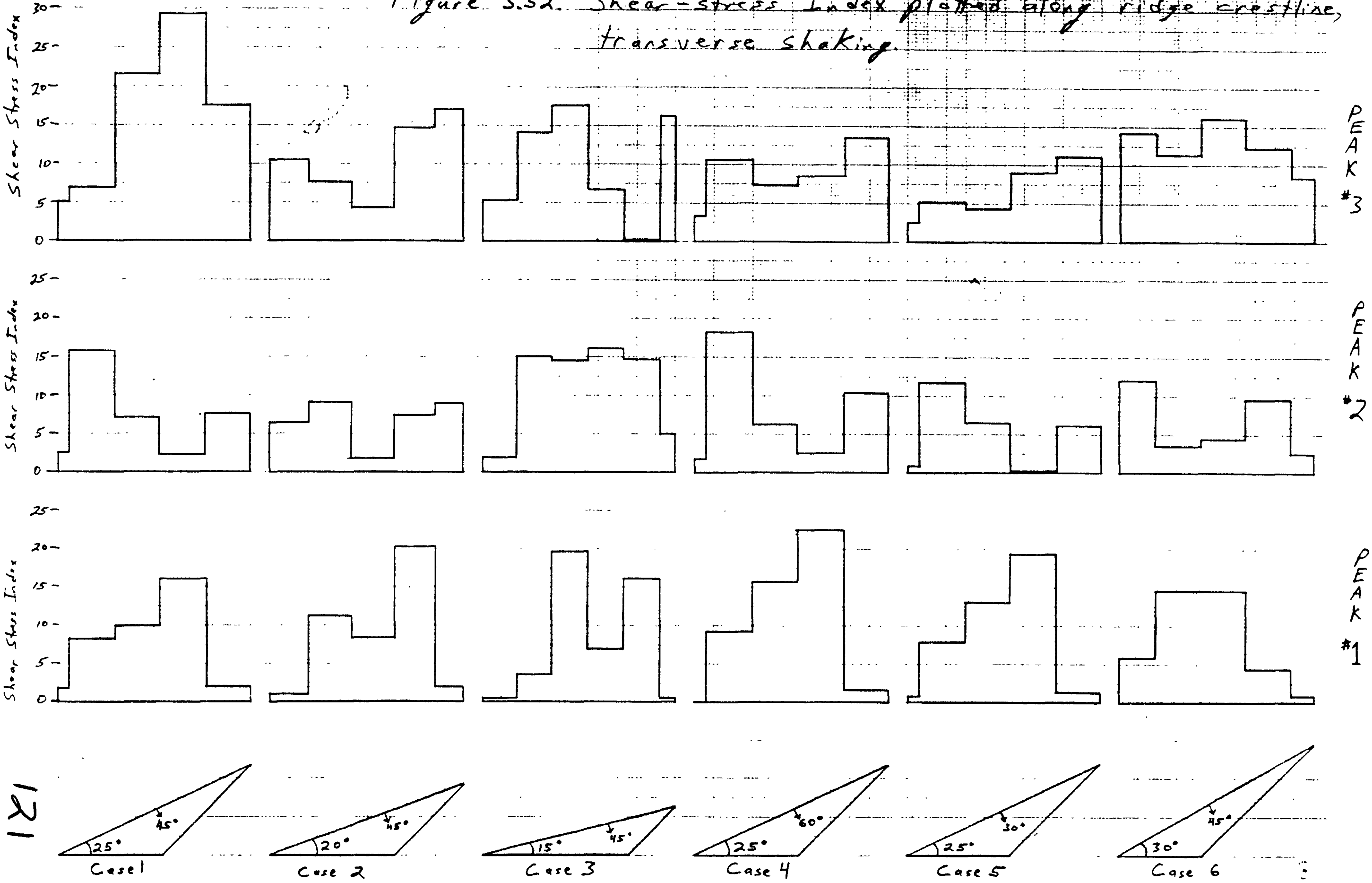

Figure 3.52. Shear-stress Index plotted along ridge crestline, transverse shaking.

Longitudinal Shaking

Figure 3.53. Shear-Stress Index plotted along ridge crestline, longitudinal shaking.

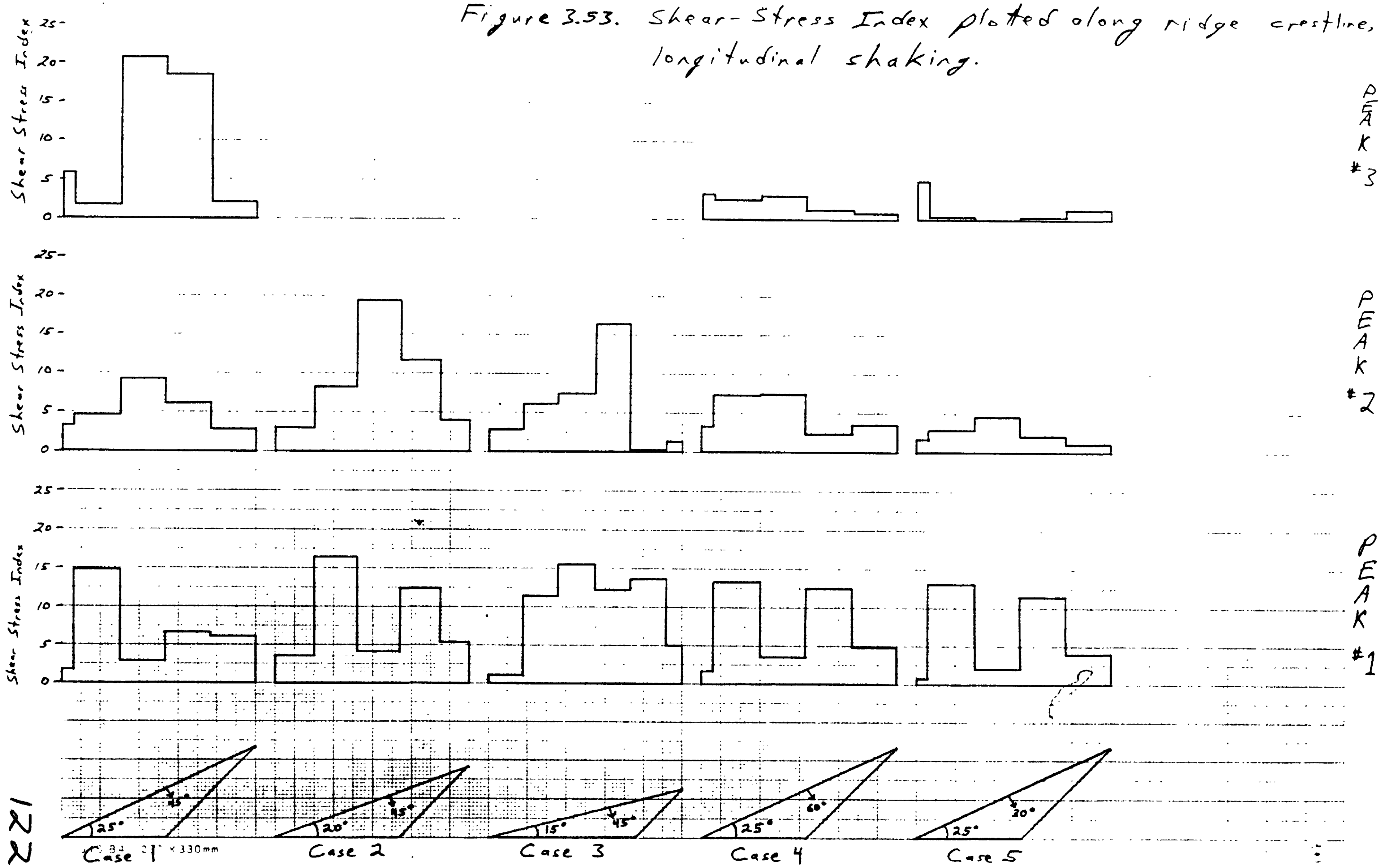

Figure 3.54. Shear-Stress Index plotted along the maximum vertical cross section, transverse shaking.

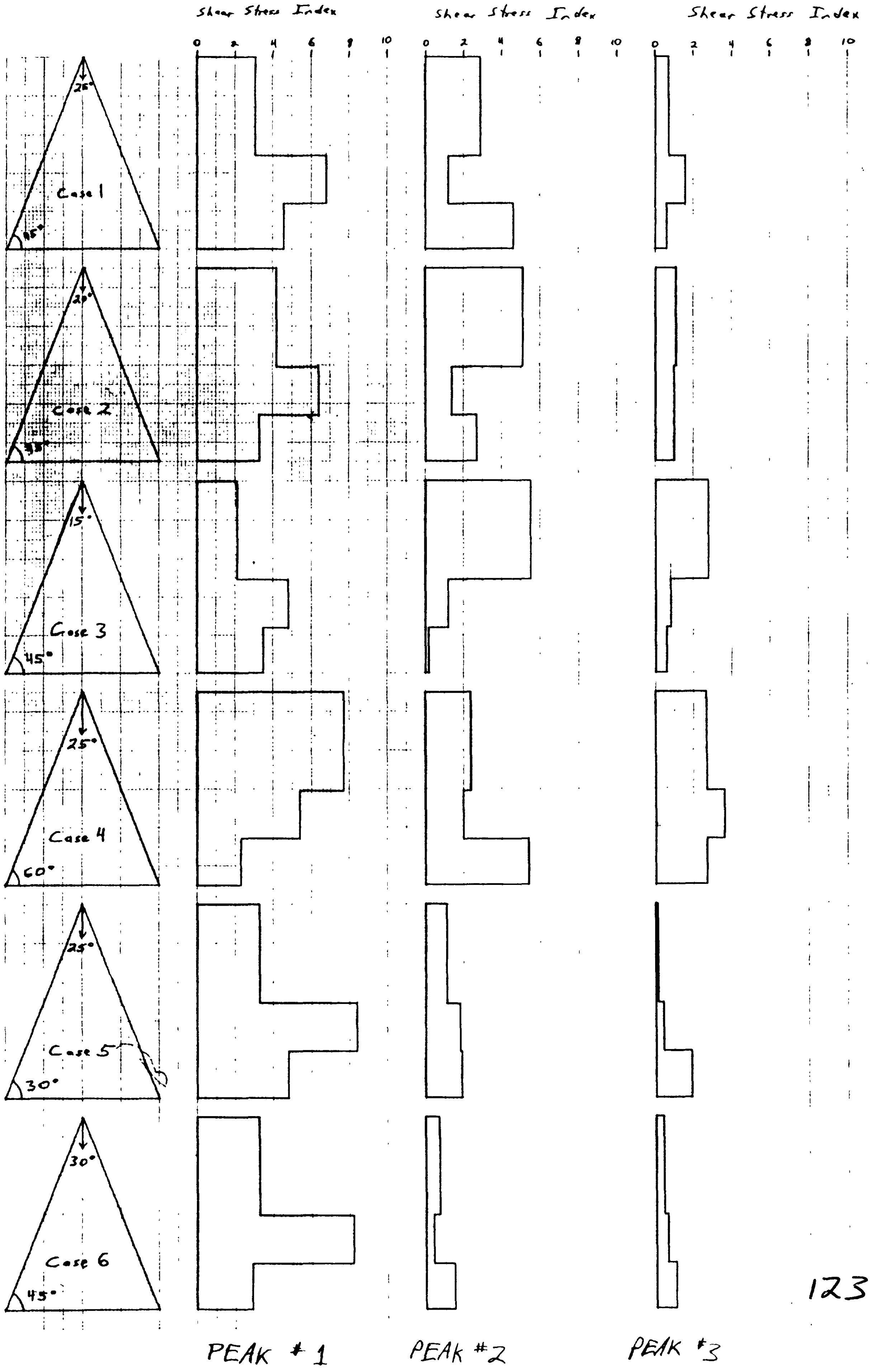

Figure 3.55. Sum of Shear-Stress Index for three major response peaks shown in figures 52-54.

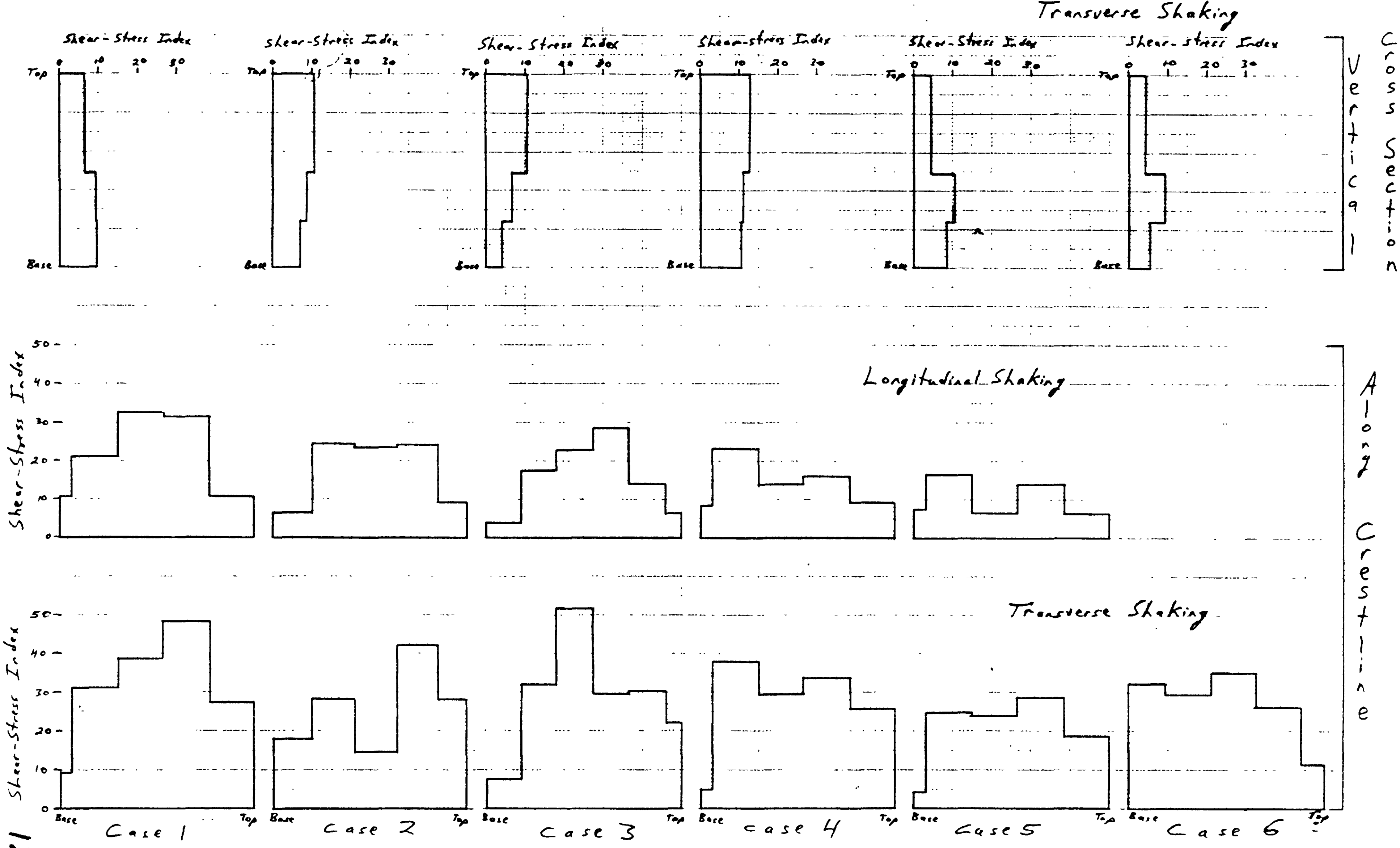

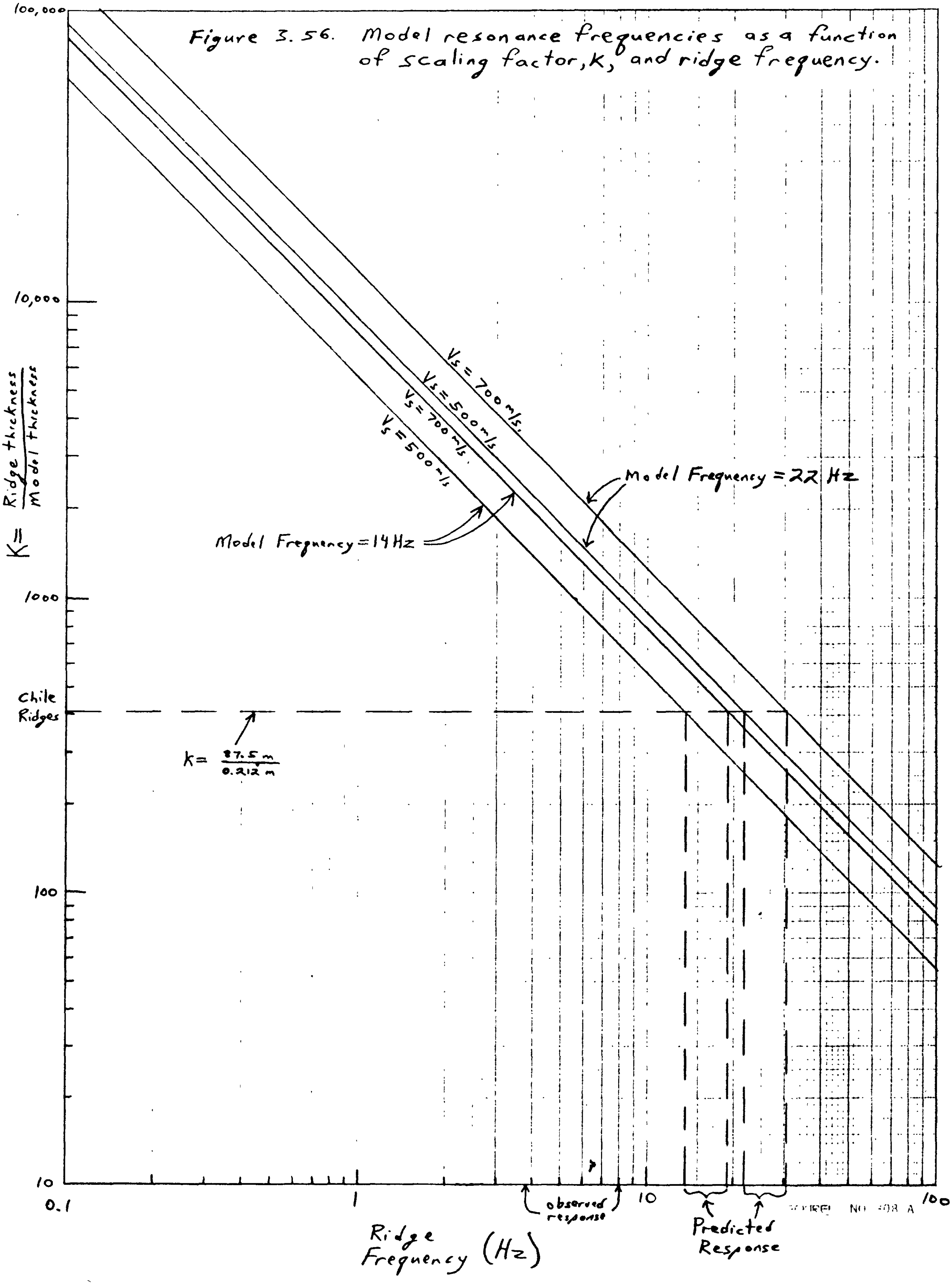

Figure 3.56. Model resonance frequencies as a function of scaling factor, k, and ridge frequency.

Figure 3.57. Matsuzaki dense seismic array.

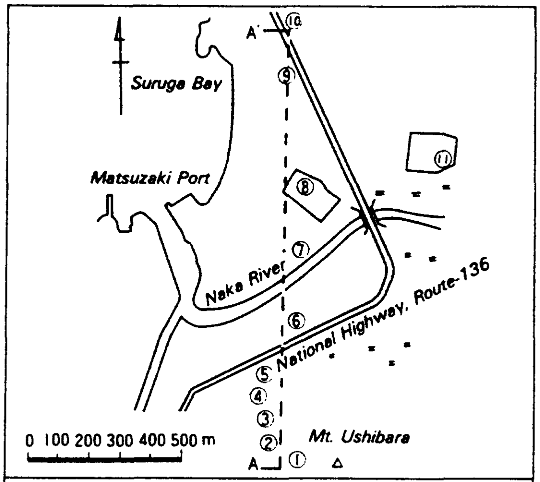

Map Showing Deployment of Accelerographs at Matsuzaki Site

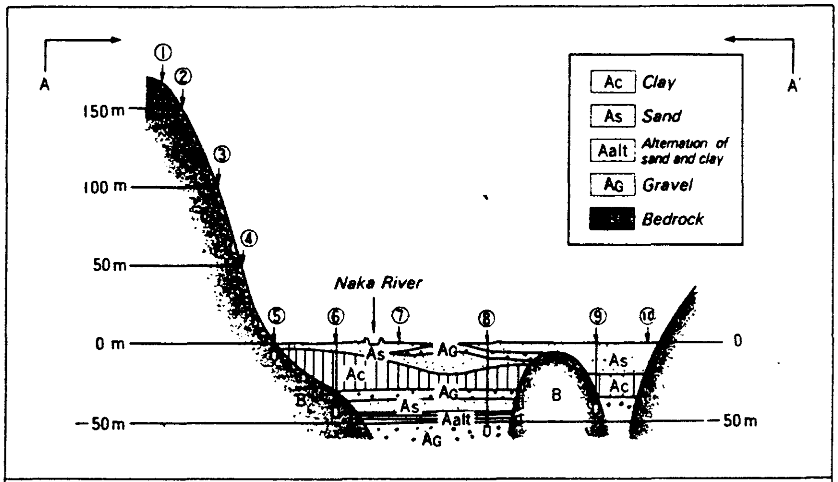

Longitudinal Section of A-A′ Traverse Line

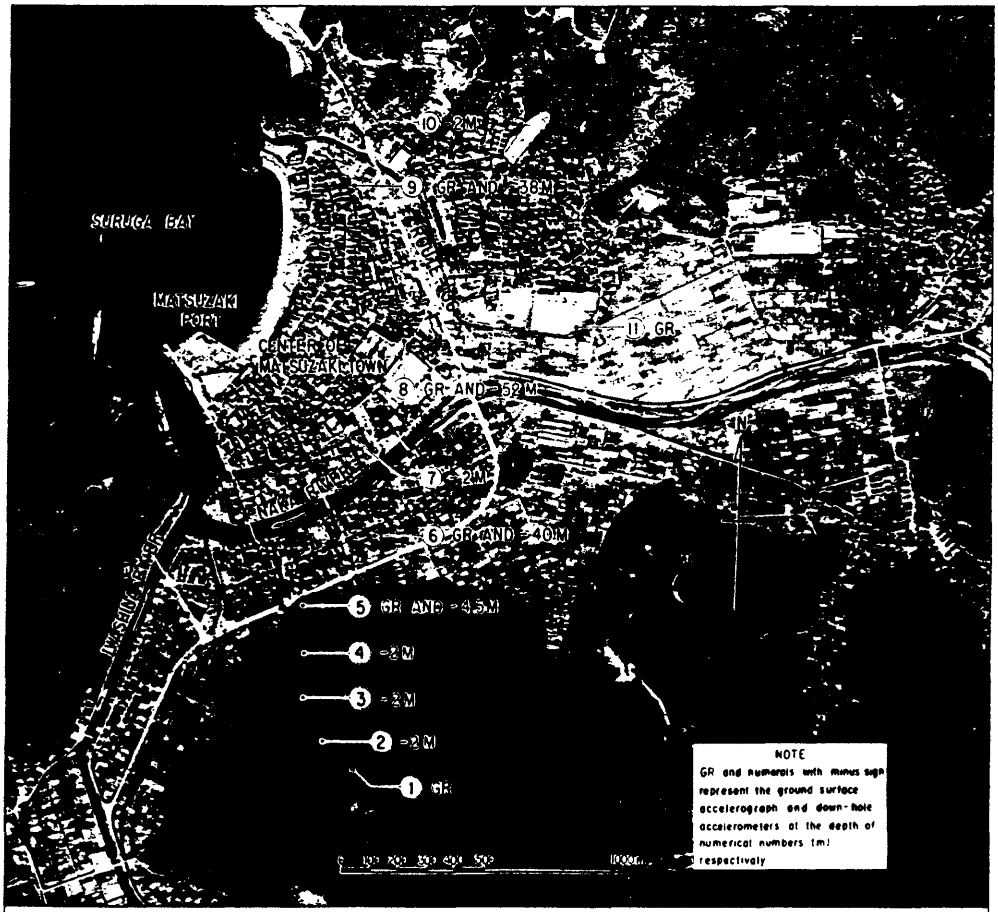

NOTE
GR and numerals with minus sign represent the ground surface accelerograph and down-hole accelerometers at the depth of numerical numbers (m) respectively

Array at Matsuzaki Site

List of Locations of Accelerographs Installed

Point	Locations installed
①	Ground surface
②	Ground surface (−2m)
③	Ground surface (−2m)
④	Ground surface (−2m)
⑤	Ground surface, −5m
⑥	Ground surface, −40m
⑦	Ground surface (−2m)
⑧	Ground surface, −52m
⑨	Ground surface, −38m
⑩	Ground surface (−2m)
⑪	Ground surface

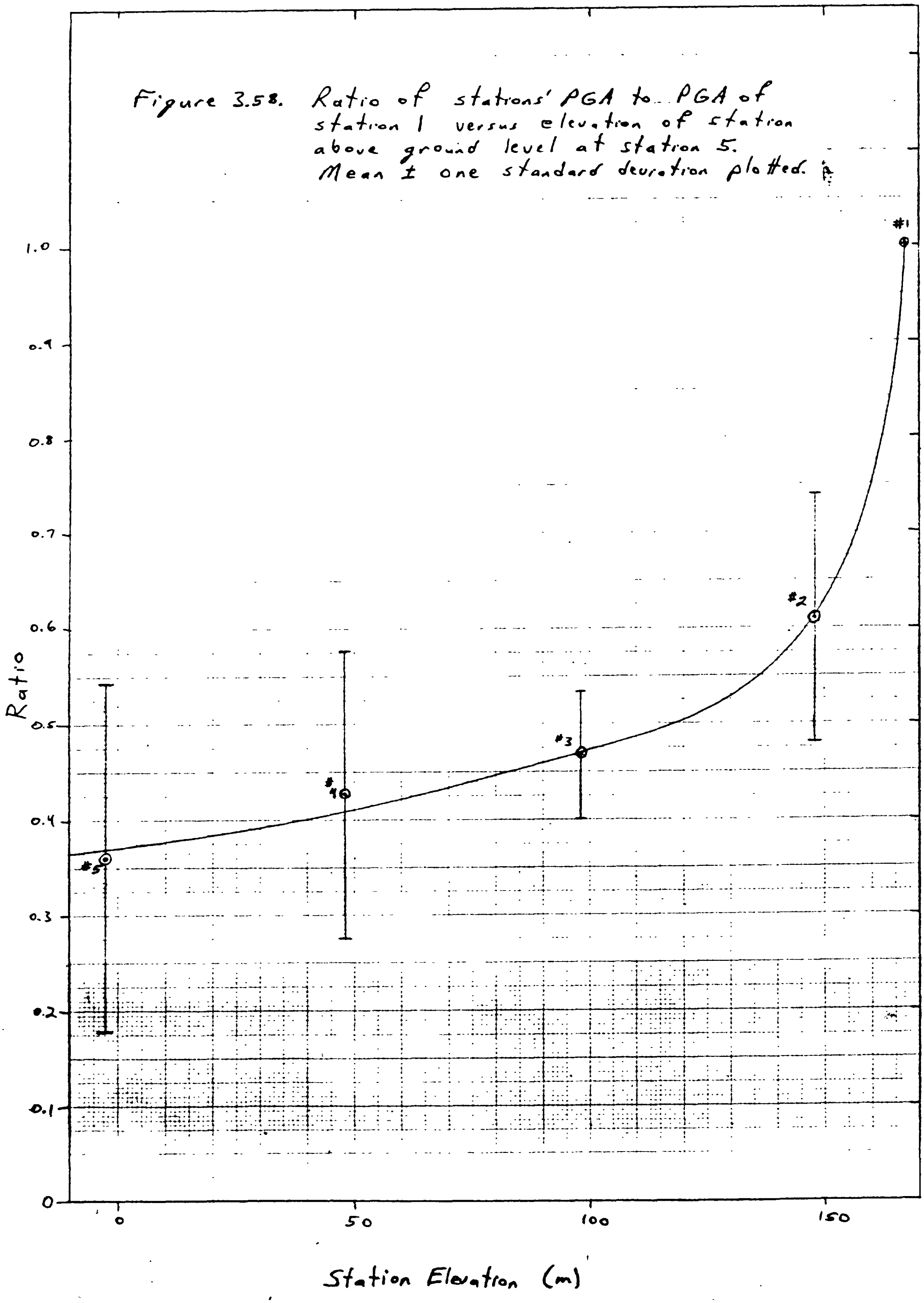

Figure 3.58. Ratio of stations' PGA to PGA of station 1 versus elevation of station above ground level at station 5. Mean ± one standard deviation plotted.

PART 4

Did Topographic Amplification of Earthquake Shaking Play a Role in Triggering the Mount Ontake Debris Avalanche?

PART 4

Did Topographic Amplification of Earthquake Shaking Play a Role in Triggering the Mount Ontake Debris Avalanche?

INTRODUCTION

On September 14, 1984, a large (M=6.8) earthquake struck the Nagano Prefecture in central Japan. Several landslides were triggered by the quake, the largest of which was a debris avalanche consisting of about 35 million m^3 of volcanic soil and rock, which initiated at an elevation of 2550 m on the south flank of Mt. Ontake. The debris traveled a total distance of about 12 km and caused at least 15 fatalities. The Mt. Ontake debris avalanche (hereafter referred to as the Ontake slide) has been described and analyzed by Okusa and others (1985), Tanaka and others (1985), Ishihara and others (1986), and Ishihara and Hsu (1986).

The mass that slid had formed a prominent ridge before the earthquake triggered its failure; the ridge had an average slope of about 25°. Reports of historical earthquakes indicate that such ridges in the epicentral areas of earthquakes have experienced topographic amplification of ground shaking resulting in anomalously large ground motions and consequent secondary ground failure. The discussion that follows centers on the estimated dynamic response of the mass that failed, both with and without the possible effects of topographic amplification, as well as the responses of nearby ridges having similar morphologies. Findings of research on (1) use of the Newmark displacement analysis to evaluate dynamic slope performance, (2) documented topographic amplification during other earthquakes, and (3) shaking-table tests on model slopes, summarized in Parts 1-3 of the present report, are used to address the question of whether or not topographic amplification of earthquake shaking played a significant role in the formation of the Mt. Ontake debris avalanche.

MODELING SLOPE STABILITY

Ishihara and others (1986) conducted static and pseudostatic stability analyses of the Ontake slide. Figure 4. 1 shows their geometric model (hereafter referred to as Ishihara's model) analyzed using an equilibrium equation similar to that proposed by Janbu (1955). I constructed an identical slope-stability model using Ishihara's geometric construction and material properties in order to observe the sensitivity of the model to changes in certain parameters, as discussed below.

Ishihara's equilibrium equation ignores interslice forces; in my model I added the empirical factor, related to the curvature of the slip surface, suggested by Janbu (1973) to account for the interslice forces. Addition of this factor increases the static factor of safety slightly.

No water table is assumed in Ishsihara's model, and thus no effects of pore pressure on the failure surface are present. In the week preceding the earthquake, however, 165 mm of rain fell in the epicentral area (Ishihara and others, 1986; Tanaka and others, 1985). The material overlying the slip surface of the Ontake slide was highly fractured and permeable andesite lava, and the slip surface consisted of relatively impermeable pumice predominantly composed of silt-sized particles. Thus, much of the antecendent rainfall probably percolated through the fractured andesite and formed a perched water table on the less permeable pumice. The pumice that failed had water contents greater than 100 percent, well above the liquid limit of the material, and Ishihara and others (1986) reported springs in the lower part of the failure surface. Tanaka and others (1985) state that concentration of ground water on the pumice layer probably contributed to failure. Therefore, it appears likely that the pumice layer that failed was saturated, or nearly so, and that a water table at least 1-2 meters above the slip surface was present in the slide mass at the time of the earthquake.

Static factors of safety using dynamic strength parameters (indicated in figure 4. 1) were calculated for a potential slide mass having a water table parallel to the failure surface for a variety of water-table heights. Dynamic strengths were employed because the stability models will be used to determine the critical acceleration of the potential slide mass--that earthquake ground acceleration required to initiate movement of the potential slide block. Figure 4. 2 shows that the static factor of safety (for dynamic strength conditions) is 1. 90 in the absence of a water table; a water table perched just 7. 3 m above the failure surface, however, reduces the static factor of safety to 1. 00. If static soil strengths are used, an even lower water table reduces factor of safety to 1. 00, because dynamic shaking increases the cohesion of the material and does not affect on the friction angle. A concentration of a few meters of ground water on the relatively impermeable pumice as a result of very heavy antecedent rainfall is not an unlikely occurrence; therefore, the static safety factor of 1.90 must be considered an upper bound, and the factor of safety may have been only slightly greater than 1. 00 immediately before the earthquake. Lack of quantitative information regarding the ground-water conditions in the slope before the earthquake makes it impossible to more accurately establish the static factor of safety for the Ontake slide.

To estimate the dynamic response of the Ontake slide, we must determine the critical acceleration of the slide mass. For the range of water-table levels of interest, horizontal ground accelerations required to reduce the factor of safety to 1. 0 were determined using a standard pseudostatic approach on the model in figure 4. 1. Figure 4. 3 shows the relationship of critical acceleration to water-table level. Where the water table is below the slip surface, the critical acceleration is about 0. 32 g; a water table of about 7. 3 m reduces the critical acceleration to zero, the case of static slope failure.

COMPARISON WITH SIMILAR SLOPES

Only one of several morphologically similar ridges on Mt. Ontake failed during the 1984 earthquake; therefore, some unique combination of factors must have led to failure of the Ontake slide. Several factors could have contributed to failure:

1. The geometry and location of the Ontake slide were controlled by the presence of a relatively weak pumice layer. The extent of this pumice layer beneath other ridges in the area is unknown.

2. Smaller scale landsliding had been occurring at the toe of the Ontake slide for some time, primarily as a result of stream erosion and ground-water seepage. This condition probably reduced the stability of the Ontake slide relative to other ridges in the area.

3. The ridge that failed in the Ontake slide may have been particularly susceptible to amplification of ground shaking because of some unique geometric properties or azimuthal alignment.

4. The ridge that failed was on the flank of Mt. Ontake nearest to the fault rupture surface and thus probably experienced the strongest ground shaking.

The pumice layer that failed in the Ontake slide has been mapped in many locations on and around Mt. Ontake (Ishihara and others, 1986). For the purpose of comparison of the stability of adjacent ridges, it may be reasonable to assume that the pumice blankets the area and is present beneath all the ridges in the vicinity of the Ontake slide. This assumption is undoubtedly inaccurate in many instances, but the lack of detailed subsurface geologic information in the area precludes analysis of geologic variation between ridges.

Several ridges in the vicinity of the Ontake slide were identified and measured for comparison of dynamic slope performance during the 1984 earthquake. Ridge geometries were measured as recommended by Sasaki and Kuwabara (1986). Also, several linear profiles along the steepest parts of these ridges were analyzed. Table 4.1 lists the geometric properties of the ridges and profiles.

Also listed in table 4.1 are the distances from the ridges and profiles to the fault rupture surface of the 1984 Naganoken-seibu earthquake. The extent of the fault rupture surface was determined by the locations of aftershocks, and the rupture surface was assumed to extend to the ground surface owing to the very shallow (1-2 km) focal depth of the main shock and reports of possible minor fault rupture at the surface.

If a potential failure mechanism identical to that of the Ontake slide is assumed for the other ridges and profiles analyzed, the critical acceleration of each slope becomes a multivariate function of slope angle and water-table level. Pseudo-static stability calculations of critical acceleration for a variety of slope angles and water-table levels (using the model geometry in figure 4.1) are summarized in figure 4.4. The relationships shown can be expressed as

$$A_c = 0.822 - 0.020(\alpha) - 0.044(h) \qquad (4.1)$$

where A_c is the critical acceleration of the potential landslide block in g's, α is the slope angle in degrees, and h is the height of the water table above the potential slip surface in meters. This model is nearly perfectly fit to the data: the correlation coefficient is 1.00. Equation 4.1 is not a general relationship between A_c, α, and h but applies only to the model geometry in figure 4.1.

Critical accelerations were calculated using equation 4.1 for the slope angles listed for each of the ridges and profiles in table 4.1. Values of h equal to zero (no water table) and 2 m were employed to yield a range of critical accelerations encompassing the most likely situation. The relative dynamic performance of these slopes was estimated using Newmark displacement as follows:

$$\log(D_n) = 1.34(\mathbf{M}) - 1.85\log(R) - 6.36(A_c) - 5.14 \qquad (4.2)$$

where D_n is the Newmark displacement in centimeters, $\mathbf{M}$ is the moment magnitude of the earthquake, R is the earthquake source distance in kilometers, and A_c is the critical acceleration of the landslide in g's (this is equation 1. 7, Part 1)

Table 4. 2 lists the critical accelerations and Newmark displacements for the slopes on Mt. Ontake that were analyzed as well as for the Ontake slide, and figure 4. 5 plots the displacements as a histogram. The ridge that failed as the Ontake slide has the greatest Newmark displacement, 2. 23 to 8. 11 cm, of all the ridges (A-O) analyzed; the greatest Newmark displacement calculated for ridges A-O is 1. 14 to 4. 15 cm (ridge G), only half as great as that for the Ontake slide. For the profiles (1-23), only two had Newmark displacements greater the the Ontake slide; profile 4 (2. 82 to 10. 22 cm) and profile 7 (4. 86 to 17. 62 cm). Thus, even if the unfavorable geologic conditions leading to the Ontake slide are assumed to exist beneath all the ridges in the area, the ridge that failed is among the most susceptible to dynamic slope failure as estimated by the Newmark analysis (figure 4. 5). The close proximity of the Ontake slide to the fault rupture and the relatively steep ridge on which it formed rendered this slope highly susceptible to dynamic slope failure.

POSSIBLE EFFECTS OF TOPOGRAPHIC AMPLIFICATION

Results of the Newmark analysis described above indicate that the ridge that failed as the Ontake slide had Newmark displacements between 2. 23 and 8. 11 cm, for water tables below, and 2 m above, the slip surface, respectively. Findings from Part I indicate that, for the slope materials at Mt. Ontake, about 3 cm of Newmark displacement is the approximate threshold above which slope failure occurs. Therefore, if the water table was below the slip surface, the Newmark displacement of about 2 cm is somewhat below the estimated threshold for slope failure; any significant level of ground water above the slip surface would result in Newmark displacements above this threshold for failure. Therefore, some amount of topographic amplification of ground shaking may have occurred and contributed to the failure of the Ontake slide.

The effects of amplification of ground shaking can be observed through the application of the following equation:

$$\log(D_n) = 2.74\log(PGA) + 1.37\log(T_d) - 6.36(A_c) + 1.51, \qquad (4.3)$$

where D_n is the Newmark displacement in centimeters, PGA is the peak ground acceleration in g's, T_d is the duration of strong ground shaking (defined by Dobry and others (1978) as the time required to build up the central 90 percent of the Arias intensity) in seconds, and A_c is the critical acceleration of the landslide in g's (this is equation 1.12, Part 1). T_d can be estimated using a three-step approach:

1. Calculate the Arias intensity at the site using the following relationship:

$$\log(I_a) = 0.98(\mathbf{M}) - 1.35\log(R) - 4.90, \qquad (4.4)$$

where I_a is the Arias intensity in meters/second, **M** is the moment magnitude, and R is the earthquake source distance in kilometers (this is equation 1.2, Part 1). At the Ontake slide, the Arias intensity calculated using equation 4.4 is 4.12 m/s.

2. Estimate the PGA at the site using the attenuation relationship for medium ground proposed by Kawashima and others (1984):

$$PGA = 232.5\times10^{0.216m}/(\Delta + 30)^{1.218}, \qquad (4.5)$$

where PGA is the peak ground acceleration in gals, m is the earthquake magnitude, and Δ is the epicentral distance in kilometers. The PGA calculated using equation 4.5 for the 1984 earthquake at the Ontake slide is about 0.39 g.

3. Calculate the duration from the following equation proposed by Wilson (in press):

$$I_a \quad 0.90\,(PGA^2)\,(T_d), \qquad (4.6)$$

where I_a is the Arias intensity in meters/second, PGA is the peak ground acceleration in g's, and T_d is the duration in seconds (this is equation 1.11, Part I). Such a calculation yields a T_d of about 30 seconds, a reasonable duration.

By holding the duration constant, Newmark displacements for a range of peak ground accelerations and critical accelerations can be calculated using equation 4.3. Figure 4.6 shows contours of critical acceleration plotted as a function of Newmark displacement and peak ground acceleration for a T_d of 30 seconds. The maximum critical acceleration for no water table, 0.322 g, and the critical acceleration for a water table 2 m above the slip surface, 0.234 g, for the Ontake slide are shown. Amplification ratios for a PGA of 0.39 g are shown along the upper horizontal axis. For the case where A_c is 0.322 g and PGA is 0.39 g, the Newmark displacement is about 2.2 cm, which agrees with that previously calculated using equation 4.2. To have a Newmark displacement of 3 cm, the threshold for slope failure, at a critical acceleration of 0.322 g requires a peak ground acceleration of about 0.43 g, which corresponds to an amplification ratio of only 1.1. Thus, even in the most stable possible slope conditions, when no water table is present, only a very minor amount of topographic amplification of ground shaking would have been necessary to trigger failure. Indeed, the uncertainty inherent in this procedure because of model assumptions and approximations suggests that the role of topographic amplification in the failure of the Ontake slide is doubtful at best and probably was not required to cause failure.

SUMMARY AND DISCUSSION

Comparison of the dynamic performances of several ridges on Mt. Ontake similar to the one that failed suggest that, even if the unfavorable geologic conditions at the Ontake slide were present everywhere, the Ontake slide was more susceptible to failure than almost any other slope on the mountain: only two of the 38 ridges and profiles analyzed yielded greater Newmark displacements. This indicates that the ridge that failed did so because it was most susceptible to failure in the conditions present during the 1984 earthquake. Had many or most of the other ridges yielded greater Newmark displacements than the Ontake slide, this could have provided evidence that extraordinary conditions such as amplified ground shaking had occurred.

At present, there is no way to determine if the ridge that failed was uniquely susceptible to topographic amplification because of its geometry, azimuthal alignment, internal structure, or material properties. Results of the PWRI model tests, in their current form (see Part 3), cannot be used for such an analysis; further analysis of the model-test results may make such a determination possible in the future.

The amount of Newmark displacement calculated for the Ontake slide in the most stable slope condition, when no water table is present, is only slightly below the threshold or critical displacement necessary to cause failure; in the presence of even a few decimeters of hydrostatic head on the slip surface, this critical displacement is exceeded. Thus, results from the Newmark analysis indicate that the maximum amplification of ground shaking required to cause failure in the most stable slope condition is only 1. 1, an amount probably much less than the uncertainty introduced in the analysis by model assumptions and approximations.

The Ontake slide had a maximum thickness of about 150 m, and the slip surface formed along a weak pumice layer deep within the ridge near its base. The results of the PWRI model tests (Part 3) indicate that amplification of ground shaking deep within a ridge ranges from 1. 0 (no amplification) at the base of the ridge to no more than about 2.0 in the center of the maximum vertical cross section. Shear stresses induced by differential accelerations within a ridge are greatest along the ridge crest and are minimal deep within a ridge. These results suggest that possible amplification that may have affected the slip surface of the Ontake slide was no greater than about 1.5 and probably was less than 1.2.

Did topographic amplification of ground shaking contribute to the failure of the Mt. Ontake debris avalanche? Probably not. None of the evidence indicates that amplification was necessary to cause failure, that the ridge that failed was uniquely susceptible to amplification, or that significant amplification would have occurred. Evidence from the model tests suggests that any effects of amplification near the base of such a ridge would have been minimal.

The location and geometry of the Ontake slide were entirely controlled by the geologic structure within the ridge, and the critical acceleration of the slide block cannot be determined uniquely without knowing the ground-water conditions at the site. Also, no strong-motion records were written near the site, so estimates of the shaking are necessarily crude. These observations, in concert with the findings summarized above, indicate that the Ontake slide is not a valid case study of topographic amplification of ground shaking. Seismically induced slope failures in homogeneous slopes--such as earth dams, natural or man-made levees, or natural soil slopes--may better illustrate the effects of topographic amplification of earthquake shaking on slope stability.

Table 4. 1. Characteristics of ridges and profiles on Mt. Ontake.

RIDGE OR PROFILE	LENGTH (m)	HEIGHT (m)	WIDTH (m)	SLOPE ANGLE (°)	FOCAL DISTANCE (km)
		Ridges			
A	2690	920	1625	19	6.7
B	3050	1280	800	23	7.3
C	2075	750	550	20	8.0
D	1650	650	600	22	8.5
E	1225	270	650	12	8.8
F	1950	650	1100	18	10.2
G	1500	690	875	25	10.2
H	1900	670	1475	19	11.8
I	3060	1170	750	21	7.9
J	2610	610	2265	14	7.8
K	1675	600	625	20	9.4
L	1975	700	475	20	10.4
M	1975	460	625	13	12.9
N	2775	1010	1150	20	11.8
O	2050	820	400	22	11.5
		Profiles			
1	1265	450		20	7.1
2	1475	600		20	7.3
3	1250	500		22	8.2
4	800	400		27	8.6
5	675	250		20	8.8
6	1065	350		18	10.5
7	515	300		30	10.3
8	675	350		27	11.9
9	1000	400		22	11.7
10	975	400		22	12.0
11	890	300		19	13.7
12	800	400		27	11.8
13	650	350		28	11.8
14	1425	450		18	12.0
15	1315	400		17	12.1
16	690	250		20	12.5
17	575	250		24	12.5
18	915	350		21	11.8
19	1125	550		26	11.1
20	1065	450		23	10.4
21	850	350		22	9.4
22	1425	350		14	9.0
23	1465	600		22	7.9

Table 4.2. Critical accelerations and Newmark displacements for ridges and profiles on Mt. Ontake.

	NO WATER TABLE		WATER TABLE 2 M ABOVE BASE	
RIDGE OR PROFILE	CRITICAL ACCELERATION (g)	NEWMARK DISPLACEMENT (cm)	CRITICAL ACCELERATION (g)	NEWMARK DISPLACEMENT (cm)
Ontake Slide	0.322	2.23	0.234	8.11
Ridges				
A	0.442	0.43	0.354	1.56
B	0.362	1.18	0.274	4.29
C	0.422	0.41	0.334	1.50
D	0.382	0.67	0.294	2.41
E	0.582	0.03	0.494	0.12
F	0.462	0.15	0.374	0.53
G	0.322	1.14	0.234	4.15
H	0.442	0.15	0.354	0.55
I	0.402	0.57	0.314	2.06
J	0.542	0.07	0.454	0.27
K	0.422	0.31	0.334	1.12
L	0.422	0.26	0.334	0.93
M	0.562	0.02	0.474	0.08
N	0.422	0.20	0.334	0.73
O	0.382	0.38	0.294	1.38
Profiles				
1	0.422	0.52	0.334	1.87
2	0.422	0.49	0.334	1.78
3	0.382	0.71	0.294	2.58
4	0.282	2.82	0.194	10.22
5	0.422	0.35	0.334	1.26
6	0.462	0.14	0.374	0.51
7	0.222	4.86	0.134	17.62
8	0.282	1.54	0.194	5.60
9	0.382	0.37	0.294	1.34
10	0.382	0.35	0.294	1.28
11	0.442	0.14	0.354	0.51
12	0.282	1.57	0.194	5.69
13	0.262	2.10	0.174	7.63
14	0.462	0.11	0.374	0.40
15	0.482	0.08	0.394	0.29
16	0.422	0.18	0.334	0.66
17	0.342	0.59	0.254	2.12
18	0.402	0.27	0.314	0.98
19	0.302	1.31	0.214	4.75
20	0.362	0.61	0.274	2.23
21	0.382	0.55	0.294	2.00
22	0.542	0.06	0.454	0.21
23	0.382	0.76	0.294	2.76

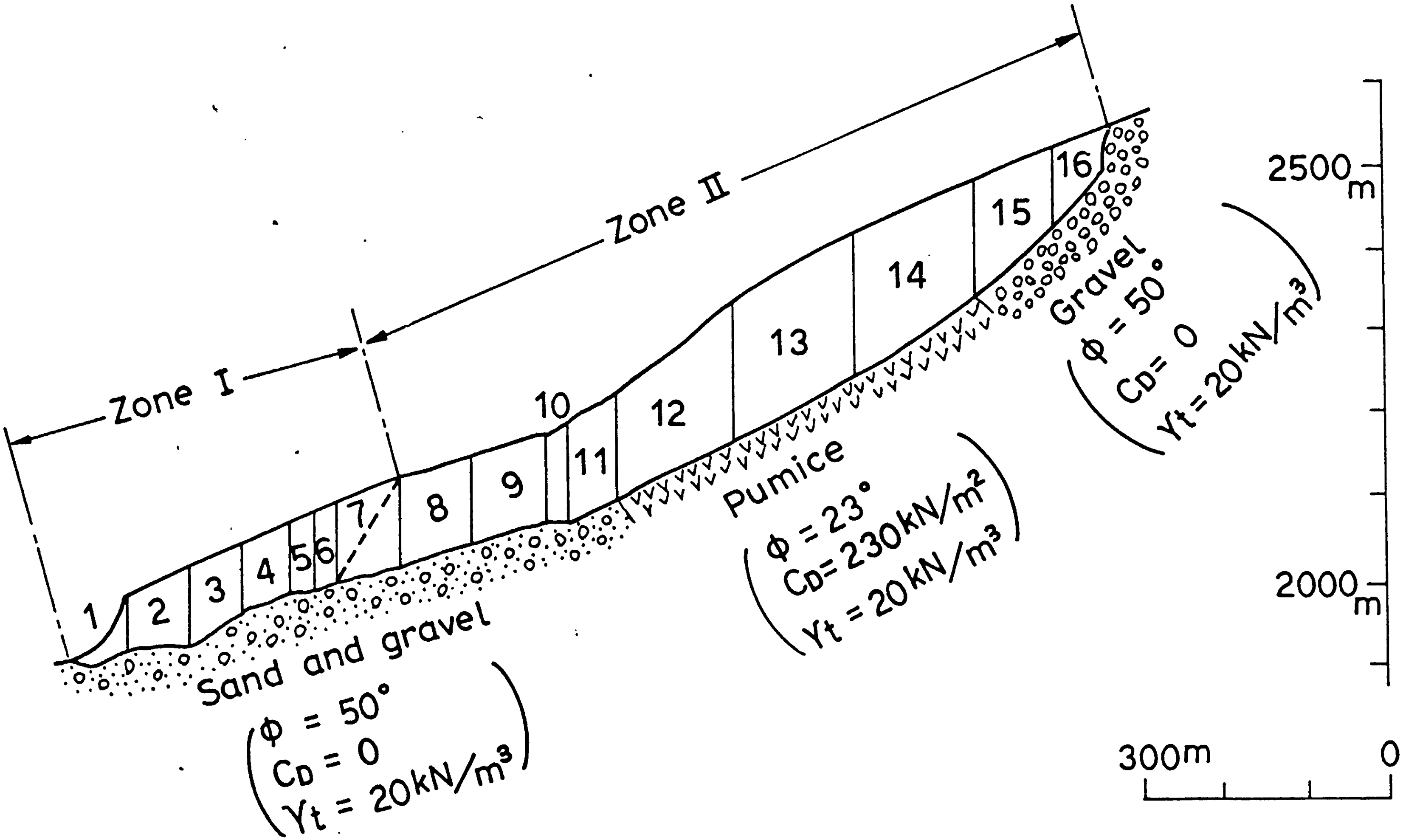

Figure 4.1. Slope-Stability model proposed by Ishihara and others (1986) for the Mt. Ontake debris avalanche.

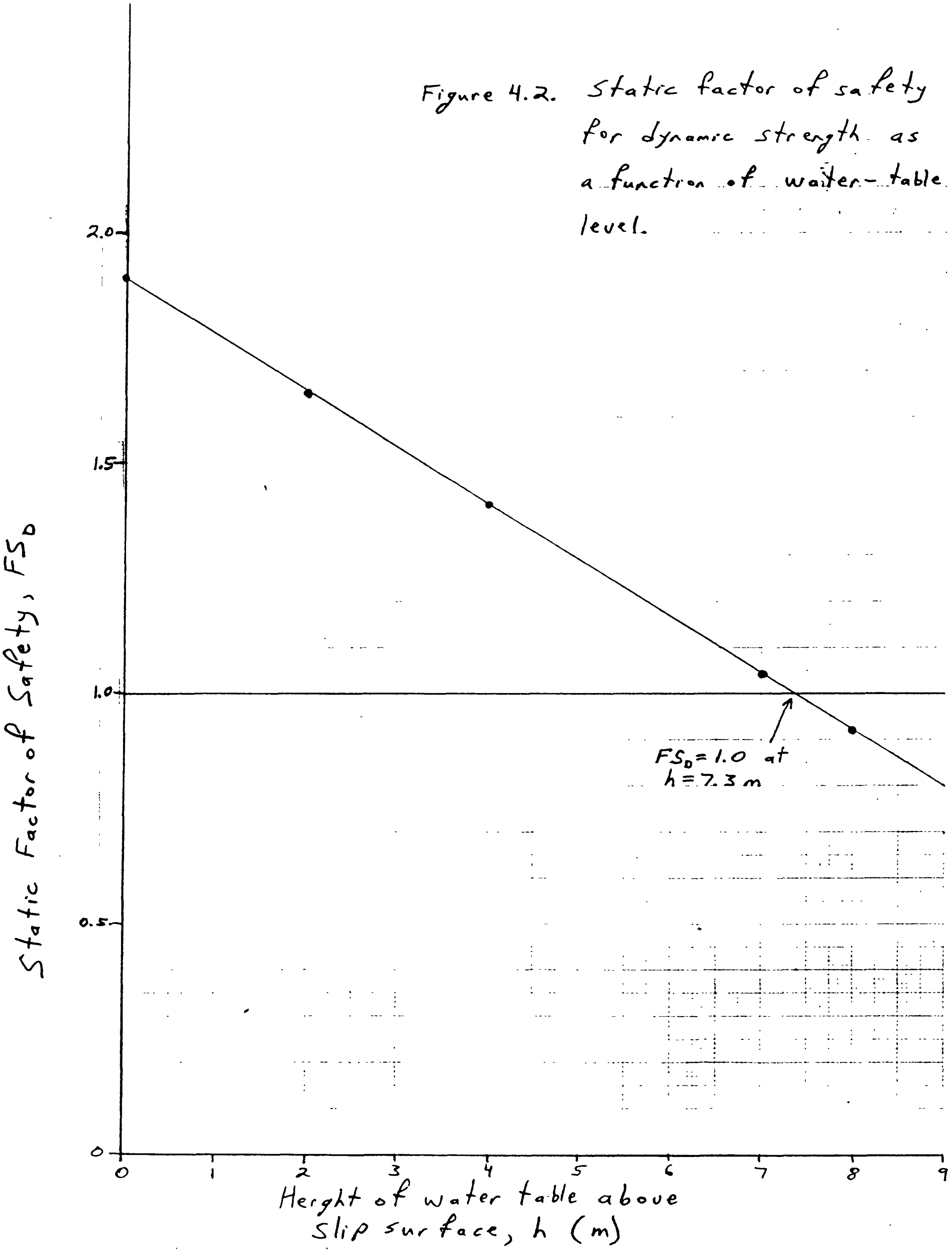

Figure 4.2. Static factor of safety for dynamic strength as a function of water-table level.

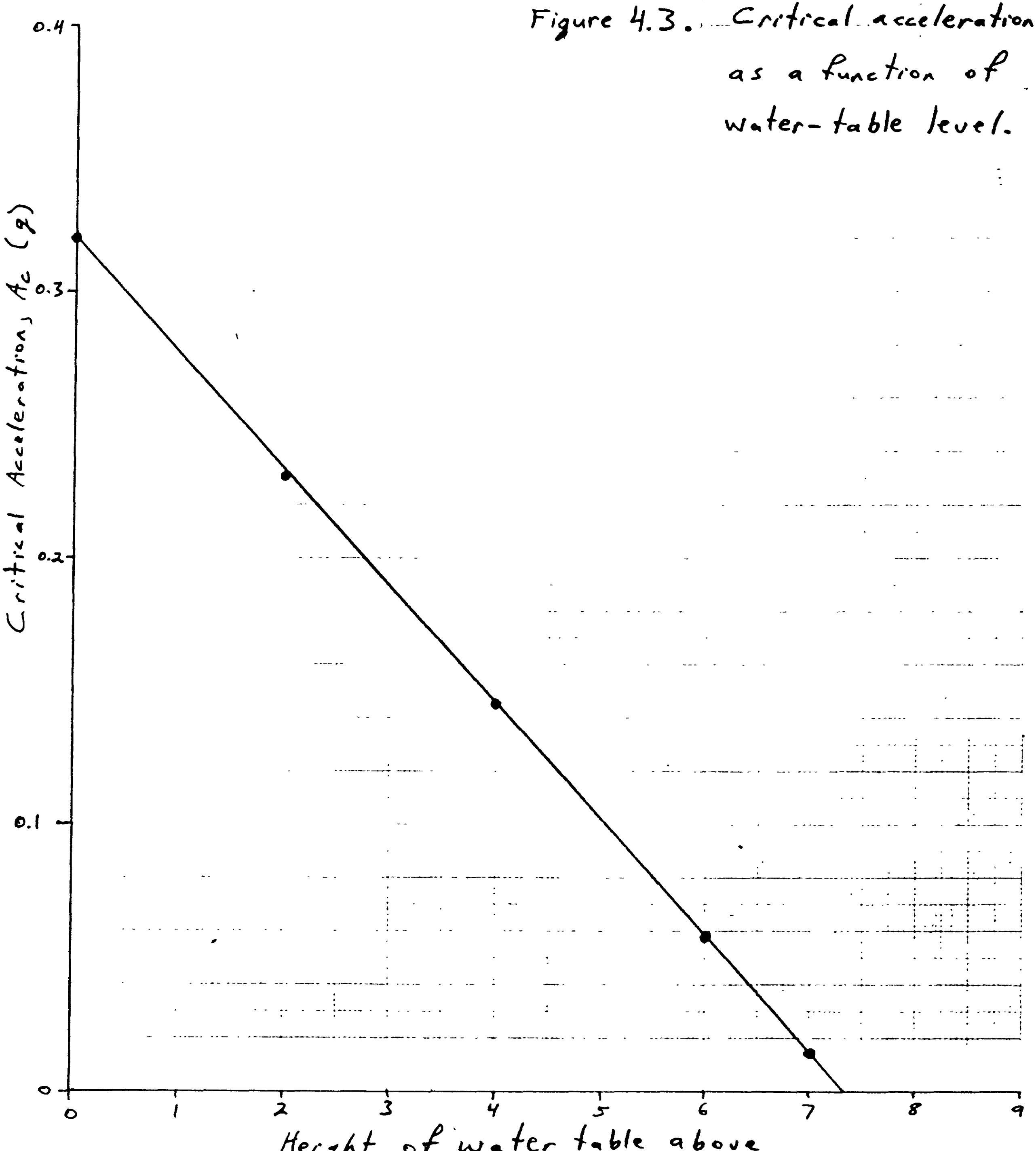

Figure 4.3. Critical acceleration as a function of water-table level.

Figure 4.4. Relationship between critical acceleration (A_c), slope angle (α), and water-table level (h) for the Ontake slide.

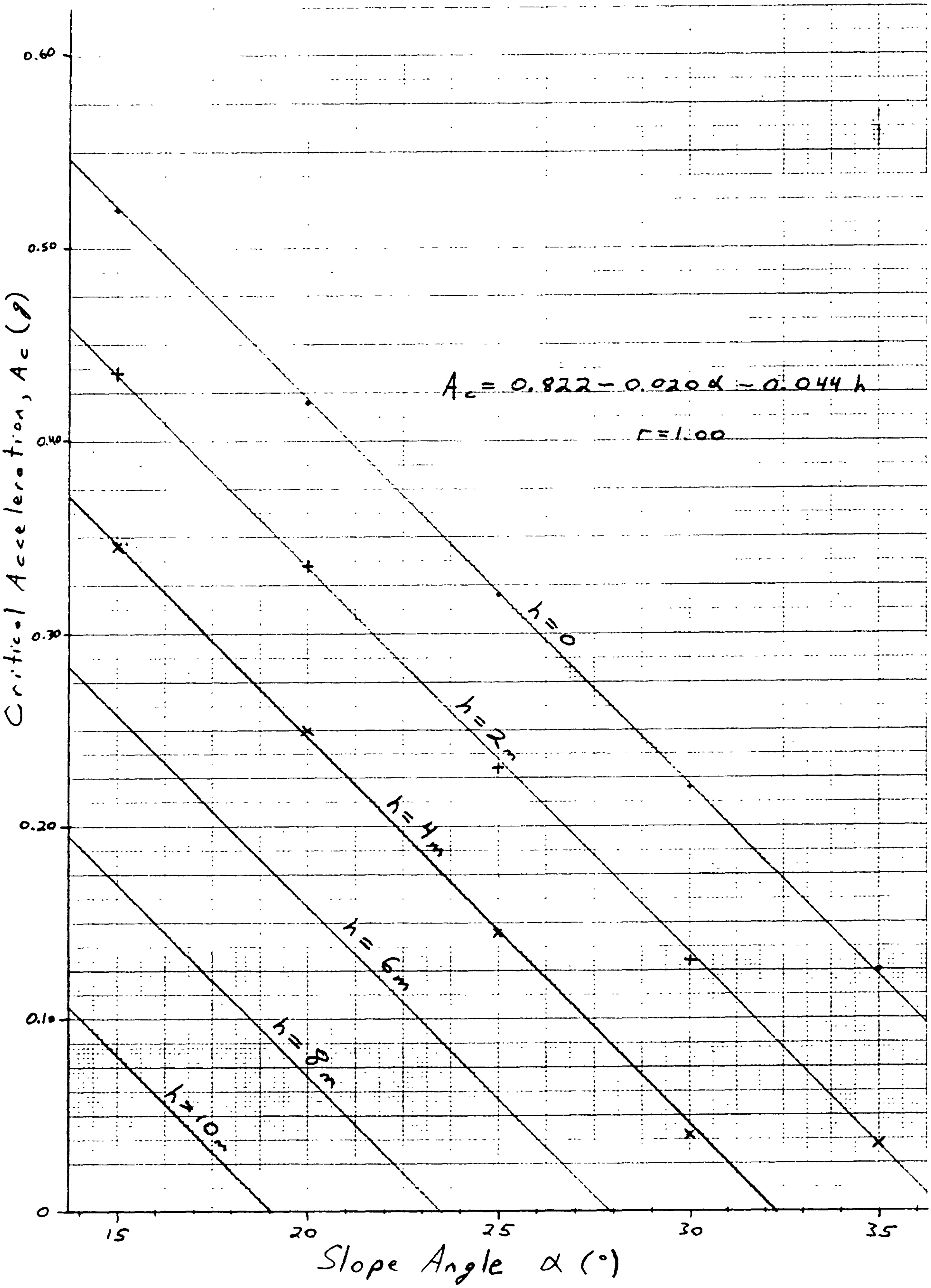

Figure 4.5. Histograms of Newmark displacement.

No water table (h=0)

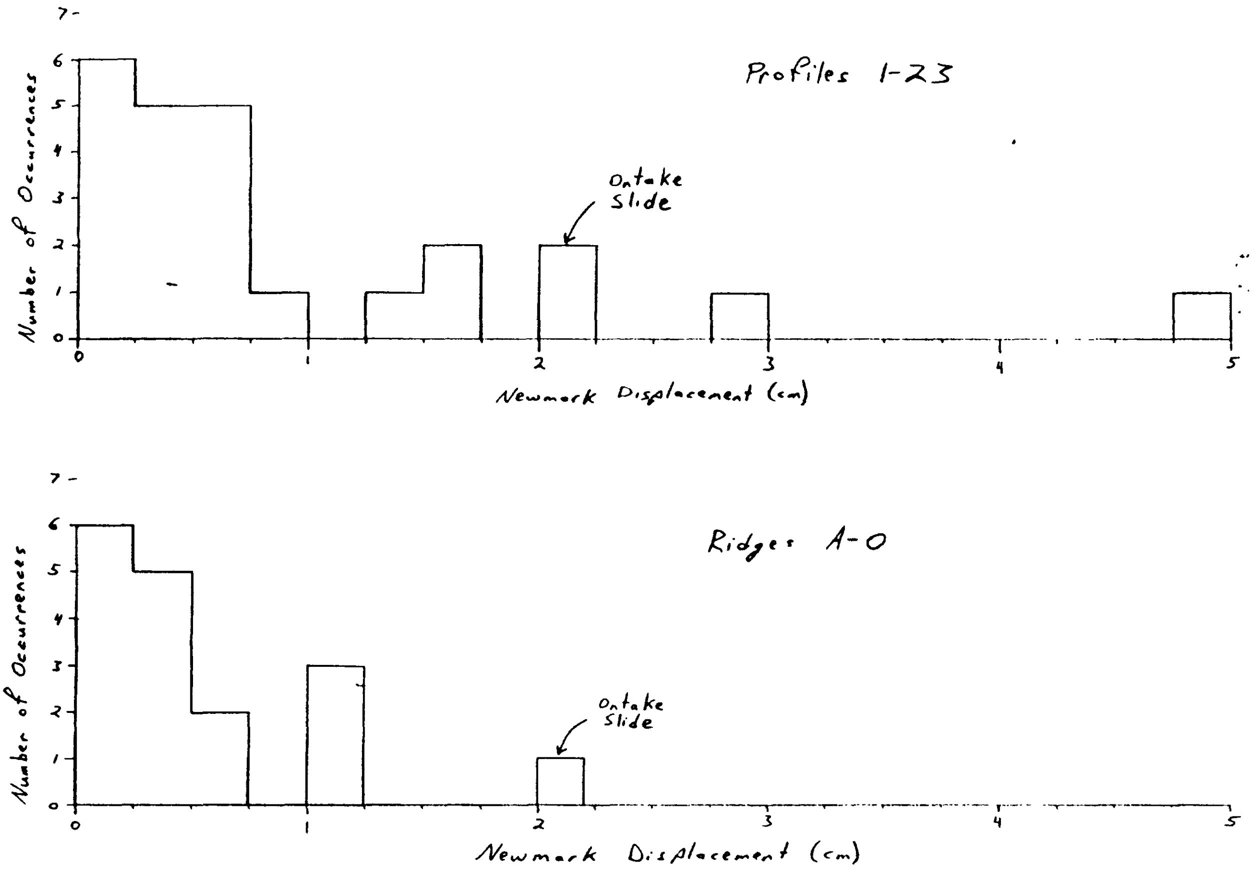

Water table 2m above slip surface (h=2m)

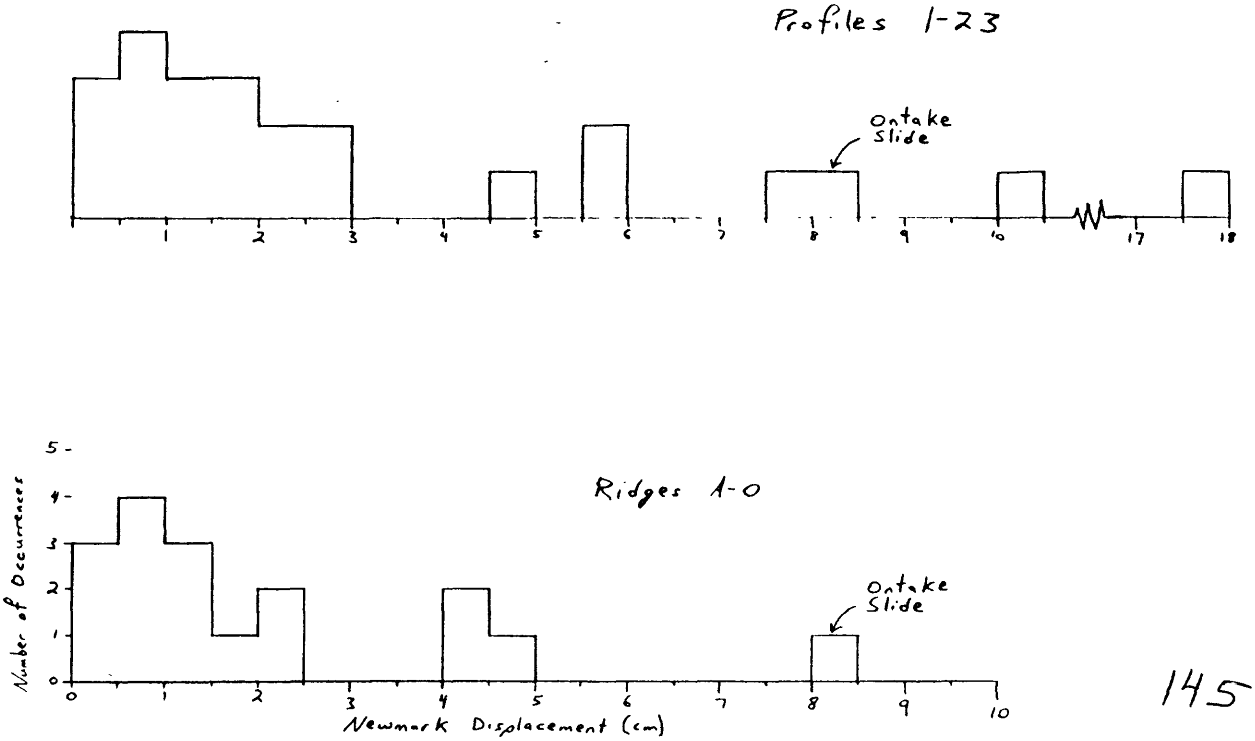

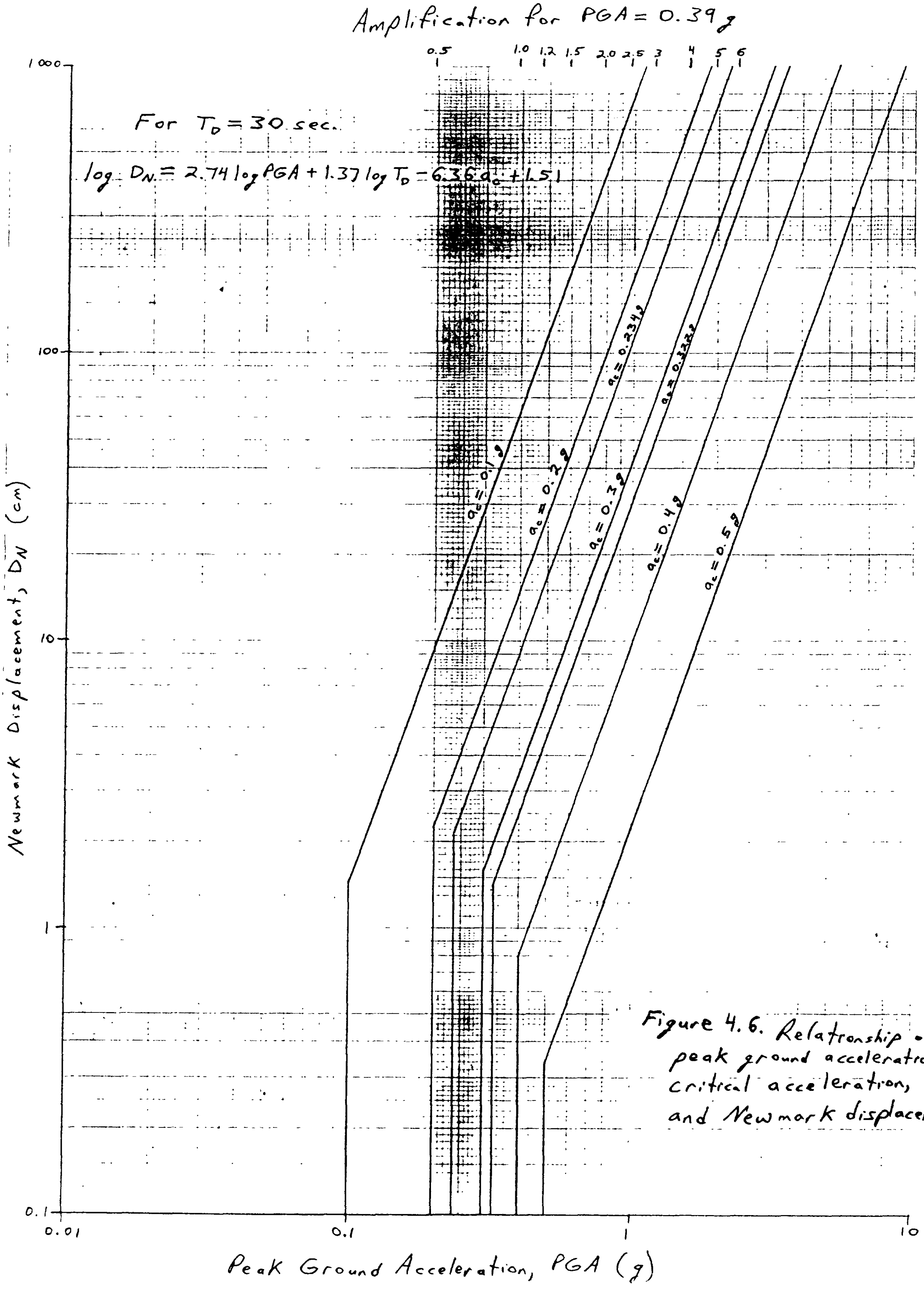

Figure 4.6. Relationship of peak ground acceleration, critical acceleration, and Newmark displacement

References

References

Arias, A., 1970, A measure of earthquake intensity, *in* Hansen, R. J., ed., Seismic design for nuclear power plants: Cambridge, Massachusetts Institute of Technology Press, p. 438-483.

Boore, D. M., 1972, A note on the effect of simple topography on seismic *SH* waves: Seismological Society of America Bulletin, v. 62, no. 1, p. 275-284.

Boore, D. M., 1973, The effect of simple topography on seismic waves: implications for the accelerations recorded at Pacoima Dam, San Fernando Valley, California: Seismological Society of America Bulletin, v. 63, no. 5, p. 1603-1609.

Bouchon, Michel, 1973, Effect of topography on surface motion: Seismological Society of America Bulletin, v. 63, no. 3, p. 615-632.

Brune, J. N., 1984, Preliminary results on topographic seismic amplification effect on a foam rubber model of the topography near Pacoima Dam: Proceedings of the Eighth World Conference on Earthquake Engineering, San Francisco, v. 2, p. 663-669.

Celebi, M., ed., 1986, Seismic site-response experiments following the March 3, 1985 central Chile earthquake: U. S. Geological Survey Open-File Report 86-90, 208 p.

Celebi, M., in press, Topographical and geological amplification determined from strong-motion and aftershock records of the 3 March 1985 Chile earthquake: Seismological Society of America Bulletin.

Davis, L. L., and West, L. R., 1973, Observed effects of topography on ground motion: Seismological Society of America Bulletin, v. 63, no. 1, p. 283-298.

Dobry, R., Idriss, I. M., Ng, E., 1978, Duration characteristics of horizontal components of strong-motion earthquake records: Seismological Society of America Bulletin, v. 68, p. 1487-1520.

Griffiths, D. W., and Bollinger, G. A., 1979, The effect of Appalachian Mountain topography on seismic waves: Seismological Society of America Bulletin, v. 69, no. 4, p. 1081-1105.

Hanks, T. C., and Kanamori, H., 1979, A moment magnitude scale: Journal of Geophysical Research, v. 84, no. B5, p. 2348-2350.

Ishihara, K., and Hsu, H. L., 1986, Considerations for landslides in natural slopes triggered by earthquakes: Proceedings of the Japan Society of Civil Engineers, no. 376/III-6 1986-12, 16 p.

Ishihara, K., Hsu, H. L., Nakazumi, I., Sata, K., 1986, Analysis of landslides during the 1984 Naganoken-Seibu earthquake: Proceedings of the International Symposium on Engineering Geology Problems in Seismic Areas, Bari, Italy, v. 2, p. 175-215.

Janbu, N., 1955, Application of composite slip surface for stability analysis: Proceedings of the European Conference on Stability of Earth Slopes, Stockholm, v. 3, p. 43-49.

Janbu, N., 1973, Slope stability computations, *in* Hirschfeld, R. C., and Poulos, S. J., eds., Embankment-Dam Engineering: New York, Wiley, p. 47-86.

Jibson, R. W., 1985, Landslides caused by the 1811-12 New Madrid earthquakes: Stanford University, Ph. D. dissertation, 237 p.

Jibson, R. W., and Keefer, D. K., in press, Landslides triggered by earthquakes in the central Mississippi Valley, Tennessee and Kentucky: U. S. Geological Survey Professional Paper 1336-C.

Kawashima, K., Arizawa, K., and Takahashi, K., 1984, Attenuation of peak ground motion and absolute acceleration response spectra: Proceedings of the Eighth World Conference on Earthquake Engineering, San Francisco, v. 2, p. 257-264.

Newmark, N. M., 1965, Effects of earthquakes on dams and embankments: Geotechnique, v. 15, no. 2, p. 139-160.

Okusa, S., Anma, S., and Maikama, H., 1985, A gigantic avalanche of earth and rocks in the 1984 Naganoken-Seibu earthquake, Central Japan: Proceedings of the First International Conference on Geomorphology, Manchester, U. K., 41 p.

Rogers, A. M., Katz, L. J., and Bennett, T. J., 1974, Topographic effects on ground motion for incident P waves--a model study: Seismological Society of America Bulletin, v. 64, no. 2, p. 437-456.

Sasaki, Y., and Kuwabara, T., 1986, Estimated earthquake motion affecting large landslide slopes: Japan Society of Civil Engineers, Proceedings of November 1986 Annual Meeting, 4 p. (in Japanese).

Tanaka, K., Oyagi, N., Inokuchi, T., Uehara, S., and Takahashi, H., 1985, Rock avalanche and slope failures induced by the Naganoken-Seibu earthquake, 1984: Proceedings of the Seventeenth Joint Meeting of the U. S. - Japan Panel on Wind and Seismic Effects, Tsukuba, Japan, 14 p.

Wilson, R. C., in press, Quantitative prediction of seismic intensity as a function of magnitude and distance: Seismological Society of America Bulletin.

Wilson, R. C., and Keefer, D. K., 1983, Dynamic analysis of a slope failure from 6 August 1979 Coyote Lake, California, earthquake: Seismological Society of America Bulletin, v. 73, no. 3, p. 863-877.

Wilson, R. C., and Keefer, D. K., 1986, Predicting areal limits of earthquake-induced landsliding, *in* Ziony, J. I., ed., Earthquake Hazards in the Los Angeles Metropolitan Area: U. S. Geological Survey Professional Paper 1360, p. 317-345.

Wong, H. L., and Jennings, P. C., 1975, Effects of canyon topography on strong ground motion: Seismological Society of America Bulletin, v. 65, no. 5, p. 1239-1257.

APPENDIX

Activity Report Submitted to the Public Works Research Institute

ACTIVITY REPORT

Submitted to

PUBLIC WORKS RESEARCH INSTITUTE
MINISTRY OF CONSTRUCTION

by

Randall W. Jibson
United States Department of Interior
Geological Survey
Geologic Division
Office of Earthquakes, Volcanoes, and Engineering
Branch of Geologic Risk Assessment
Reston, Virginia 22092 USA

March 31, 1987

1. PREFACE

As a recipient of the JAPANESE GOVERNMENT RESEARCH FOR FOREIGN SPECIALISTS grant, I visited the PUBLIC WORKS RESEARCH INSTITUTE, MINISTRY CONSTRUCTION, from January 12 through March 31, 1987.

I am grateful for the opportunity to work at the Public Works Research Institute. During my visit, everyone showed the greatest kindness and worked to make my stay comfortable and productive. Special thanks to the headquarters office of the Ministry of Construction for supporting my research and for making opportunities for exchange of ideas between scientists from different countries possible.

Many individuals at the hosting agency, the Public Works Research Institute, Ministry of Construction, worked to make my visit possible and to insure that it was productive. I extend my thanks to Director General Kamijo and to Deputy Director Narita and Assistant Director Fukui. I am particularly grateful for the efforts of Dr. Iwasaki, Director of the Earthquake Disaster Prevention Department, and Dr. Sasaki, Head of the Ground Vibration Division, who extended the invitation for this trip and who provided excellent working conditions and a stimulating research project. The entire staff of the Ground Vibration Division was most helpful and made my stay very enjoyable.

2. RESEARCH OBJECTIVES AND ACTIVITIES

2. 1 OBJECTIVE

The objective of this research was to determine the effects of topographic amplification of earthquake shaking on the dynamic stability of slopes, particularly in the case of large, deep-seated landslides. The massive debris avalanche from the south flank of Mt. Ontake triggered by the 1984 Naganoken-Seibu earthquake was investigated in detail as a possible case of slope instability caused by topographic amplification.

The research was executed as a series of discreet studies related to this objective:

1. A method was developed to estimate the relative dynamic performance of slopes having different stabilities in different levels of ground shaking. This required relating an index of dynamic slope performance, Newmark displacement, to seismic slope stability and earthquake magnitude and proximity.

2. Data from a previous field study of topographic amplification of earthquake shaking, conducted by the United States Geological Survey after the 1985 Central Chile earthquake, were analyzed for comparison with the Mt. Ontake landslide and with results from model tests described below. Also, data from the Matsuzaki dense seismic observation array, operated by the Public Works Research Institute, were analyzed for comparison.

3. Shaking-table tests on silicon ridge models were designed and conducted by the Public Works Research Institute. Results from these tests were analyzed and compared to results from the Chile earthquake experiment, the Matsuzaki dense seismic array, and stability studies of the Mt. Ontake landslide.

4. The dynamic performance of the ridge that failed as the Mt. Ontake landslide was analyzed, and the performances of several nearby intact ridges on Mt. Ontake were also analyzed using the method described above in #1. Results of this analysis were used to determine the likelihood that topographic amplification of earthquake shaking caused the Mt. Ontake landslide.

2. 2 ACTIVITIES

Activities during my visit to the Public Works Research Institute (PWRI) are summarized below:

January 12	Arrive in Japan
January 13-31	Research at PWRI on dynamic slope performance
February 1-4	Research at PWRI on seismic shaking intensity
February 5-8	Consultation with Dr. Ishihara at Tokyo University, Drs. Kobayashi and Sassa at Kyoto University, and Dr. Harp of the U. S. Geological Survey
February 9-18	Research at PWRI on Chile earthquake experiment
February 19-21	Visit dense seismic observation arrays at Matsuzaki, Numazu, and Shizuoka
February 22- March 16	Research at PWRI on results of shaking-table tests
March 17-19	Visit Nagano Prefecture to observe landsides triggered by the 1984 Naganoken-Seibu earthquake
March 20-26	Research at PWRI on stability of Mt. Ontake ridges
March 27	Tour of National Center for Research on Disaster Prevention
March 28-30	Preparation of final report at PWRI
March 31	Departure from PWRI

3. 0 PRESENTATION OF FINDINGS

A draft report summarizing my research activities and findings was presented to the Public Works Research Institute. The conclusions of the report are summarized below:

1. A method was developed to estimate relative dynamic slope performance of slopes having different stabilities subjected to different levels of ground shaking. The following equation can be applied in a variety of ways to the problem of dynamic slope performance:

$$\log(D_n) = 1.34\,(\mathbf{M}) - 1.85\log(R) - 6.36\,(A_c) - 5.14$$

where D_n is the Newmark displacement in centimeters, **M** is the moment magnitude of the earthquake, R is the earthquake source distance in kilometers, and A_c is the critical acceleration of the landslide block in g's. The Newmark displacement is an index of relative dynamic slope performance.

2. Results from the seismic site-response experiment conducted after the 1985 Central Chile earthquake illustrated the differences in ground shaking on ridges and intervening valleys (figure 1). Figure 2 shows average horizontal amplification ratios of ridge stations to a valley station, and significant amplifications (ratios greater than 2) occur for all ridge stations in a broad peak

around 2-4 Hz and in a narrower peak around 8 Hz. These resonant frequency ranges may relate to some elements of the ridge geometry, such as ridge height or width, that are about the same lengths as the incident seismic waves.

3. Results from analysis of the data from the Matsuzaki dense seismic array show that amplification of about a factor of 3 occurs at stations over the thickest parts of the ridge and near the midpoint of the crestline at the top of the steepest part of the ridge as compared to stations at the base of the ridge.

4. Shaking table tests of silicon slope models (figure 3) showed that the resonant frequency, about 14-16 Hz for all models, is independent of the overall height, length, width, crestline angle, and side-slope angle (figure 3, dimensions H, L, W, α, and β, respectively). The aspects of the model geometries held constant for the models included slope length and maximum ridge thickness (figure 3, dimensions S and T) and the 45° angle of the rigid model base; therefore, the resonant frequency must be controlled by one or more of these constant factors.

The spatial distribution of acceleration ratios along the model crestlines and vertically along the maximum cross sections (figure 4-6) shows the inertial effects of amplification. For the fundamental resonance frequency (peak 1), amplification is greatest near the midpoints of the crestlines; for higher frequency responses (peaks 2 and 3), amplification maxima are near the one-third points along the crestlines. Maximum amplification ratios are about 6 for peak 1; in higher frequency modes the ratios are less. In the maximum vertical cross section (figure 6), amplifications range from 1 (no amplification) at the base of the ridge to more than 6 at the ridge surface; amplifications in the fundamental mode are greater than those of higher frequency modes.

The first derivative of the acceleration distribution curves is an index of the shear stress (Shear-Stress Index) induced by differential amplification within a ridge. This Index is plotted in figures 7-9 for the curves shown in figures 4-6, respectively. Figures 7 and 8 show the Shear-Stress Index along the ridge crestlines, and maximum values are randomly scattered along the central 80 percent of the crestlines. Figure 9 likewise shows a rather random distribution of induced shear stress along the maximum vertical cross section; the Shear-Stress Index is much less within the ridge than along the crestline.

5. The estimated peak ground acceleration at the Ontake slide with no amplification effects is 0.39 g, sufficient to cause catastrophic failure in all but the most favorable ground-water conditions. The maximum amplification required to cause failure in the most favorable ground-water condition is only 1.1. Therefore, it appears unlikely that amplification was required for failure.

Comparison of the dynamic performances of 38 ridges and profiles on Mt. Ontake revealed that only two had Newmark displacements greater than the ridge that failed (figure 10). Thus, it appears that the ridge that failed did so because it was the most susceptible to failure in the conditions present during the 1984 earthquake, and no extraordinary effects such as topographic amplification would have been necessary to cause failure.

6. All of the evidence presented here indicates that (1) inertial effects and shear stresses induced by topographic amplification are greatest along ridge crests and are much less significant deep within and near the bases of ridges, and (2) no amplification of ground shaking was necessary to cause failure of the Mt. Ontake debris avalanche. Thus, topographic amplification may have little effect on deep-seated landslides. This is consistent with my observations and with published reports that ridges experiencing amplification in past earthquakes displayed primarily surficial effects--churned earth and shallow, disrupted landsliding--located along their crests. Much information regarding the Mt. Ontake landslide is unavailable, however, and new data could indicate some effect of amplification.

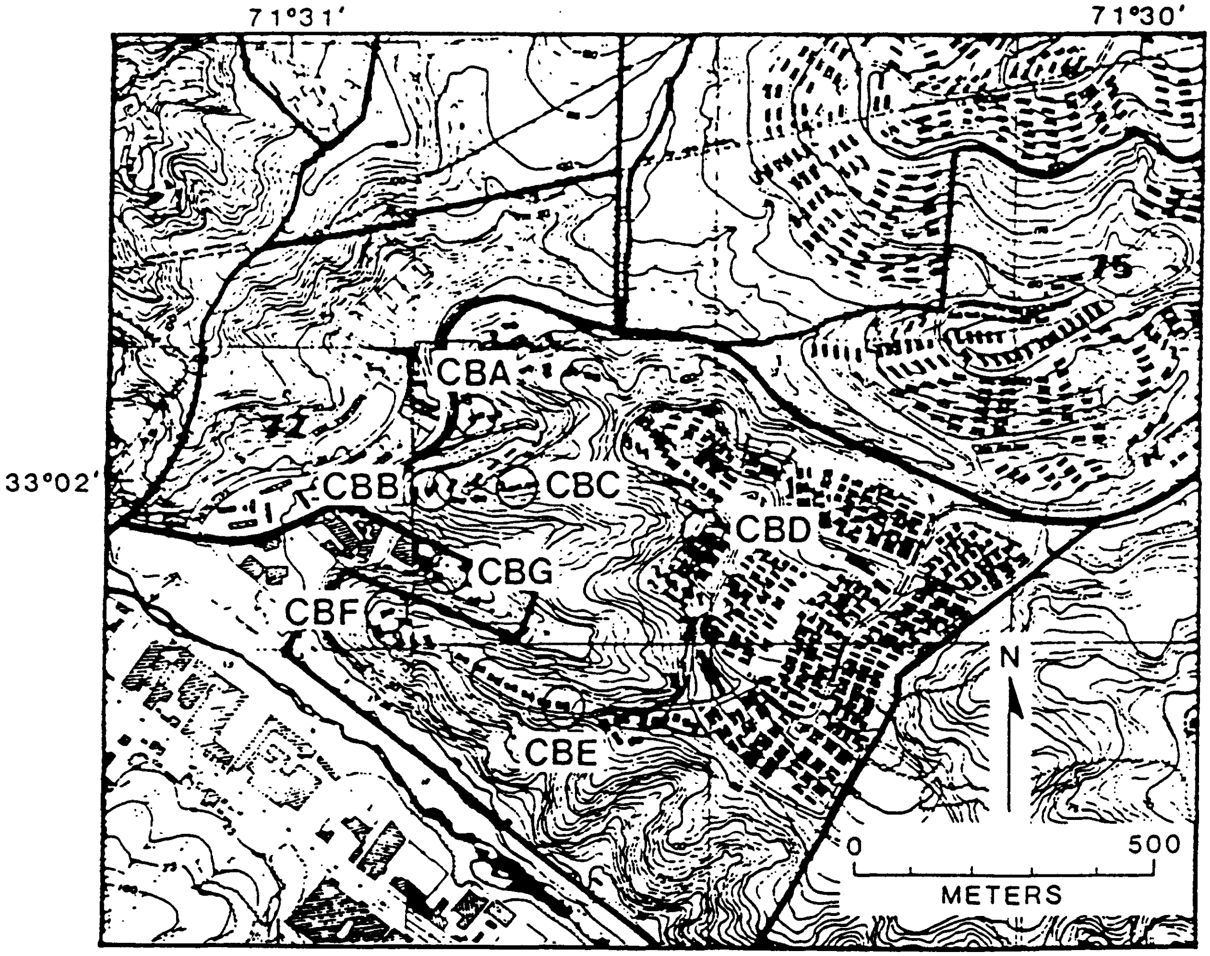

Figure 1 Detailed topography of Canal Beagle. The stations of the Canal Beagle site are indicated. Also a general scale and the latitudes and longitudes are shown. (from Celebi, 1986)

Figure 2

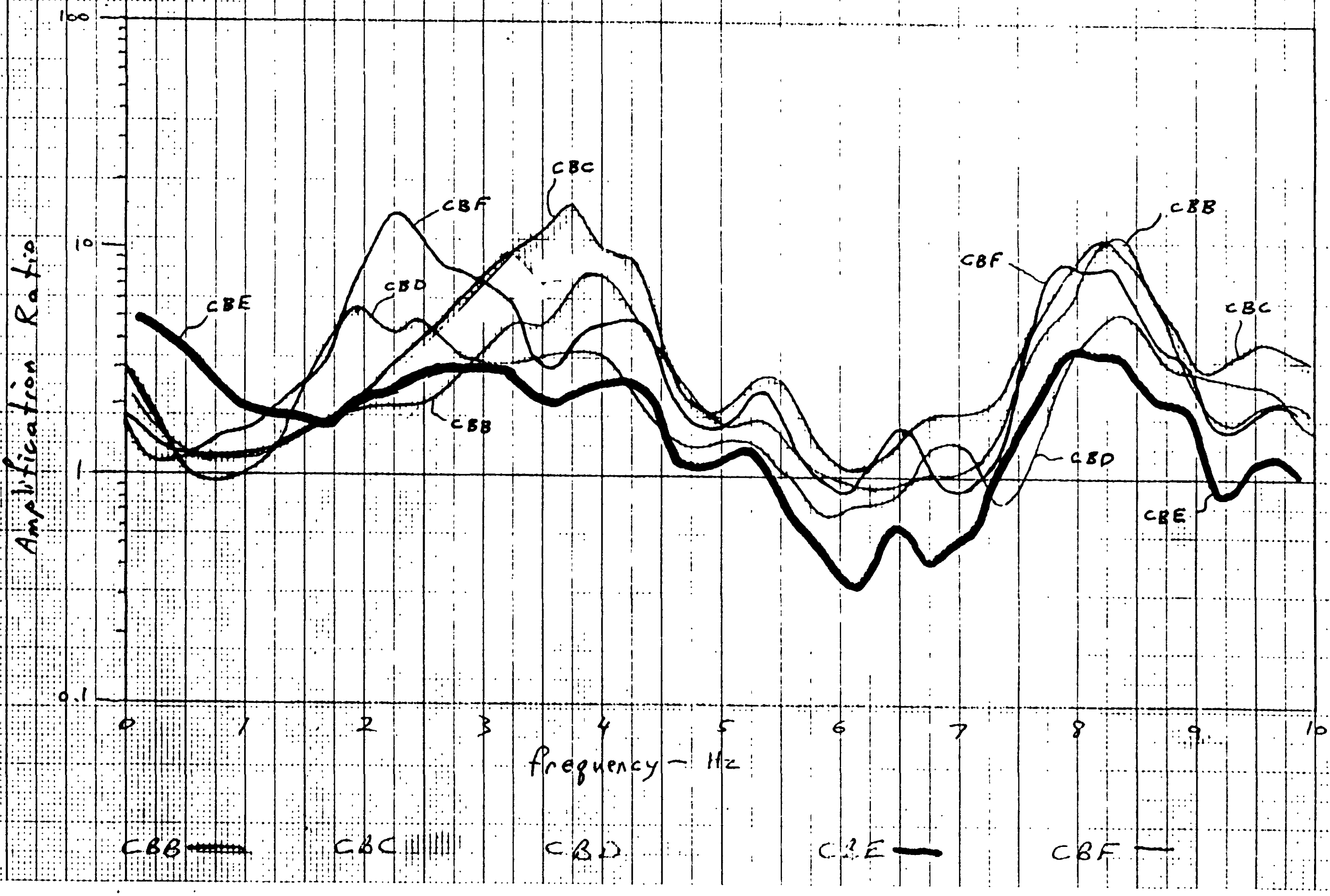

Average Horizontal

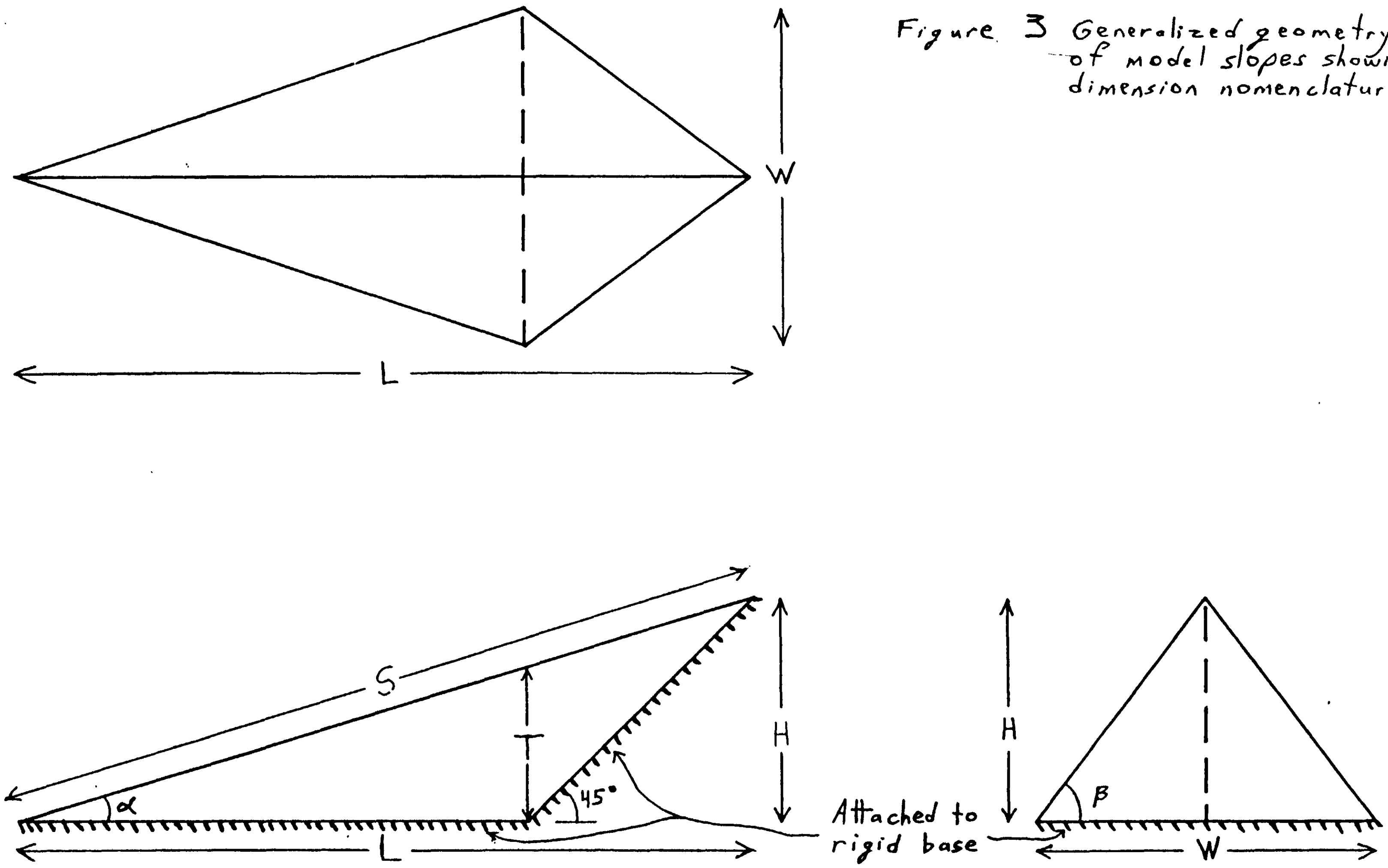

Figure 3 Generalized geometry of model slopes showing dimension nomenclature.

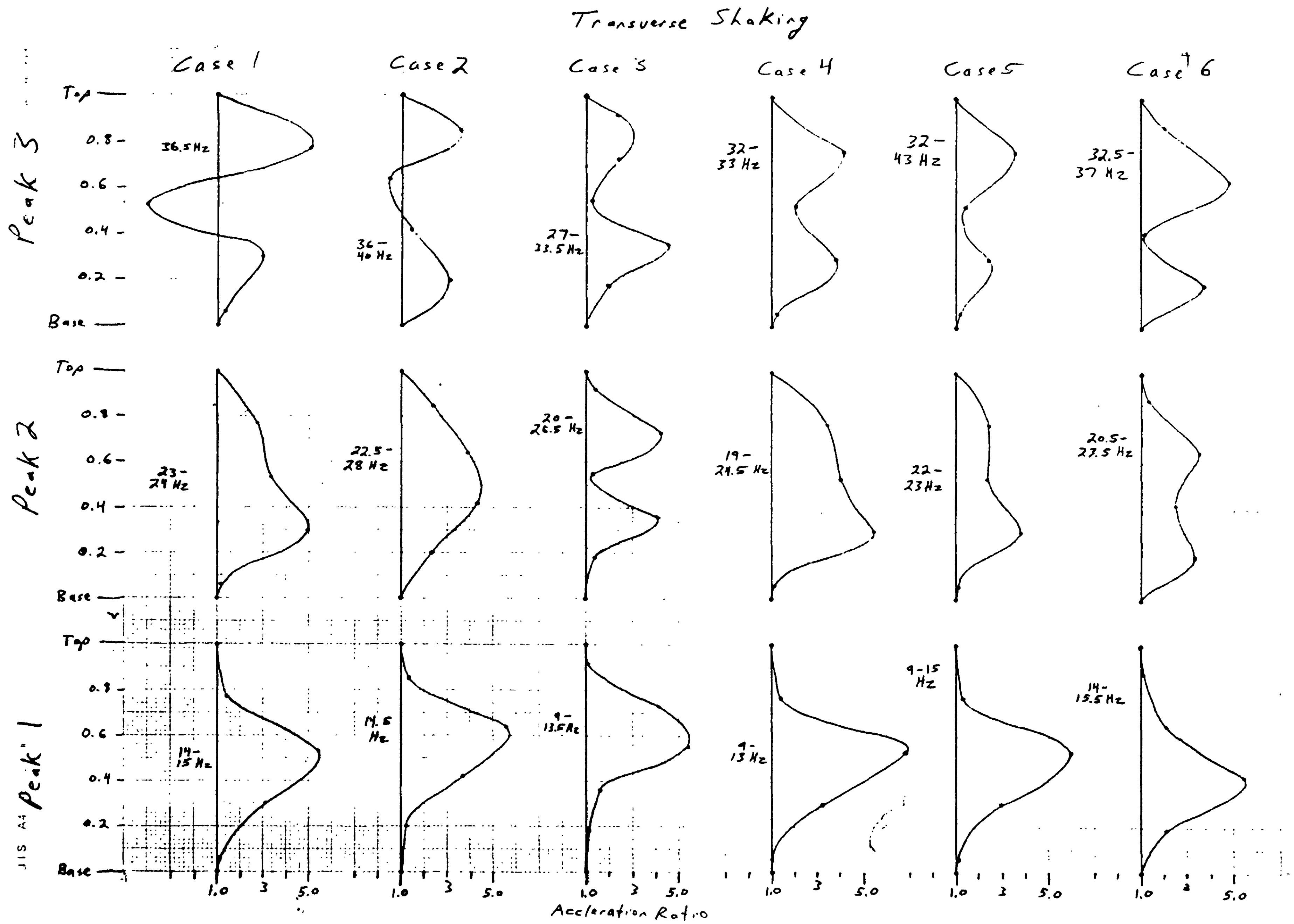

Figure 4. Acceleration ratio plotted along ridge crestline for three major response peaks, transverse shaking.

Transverse Shaking

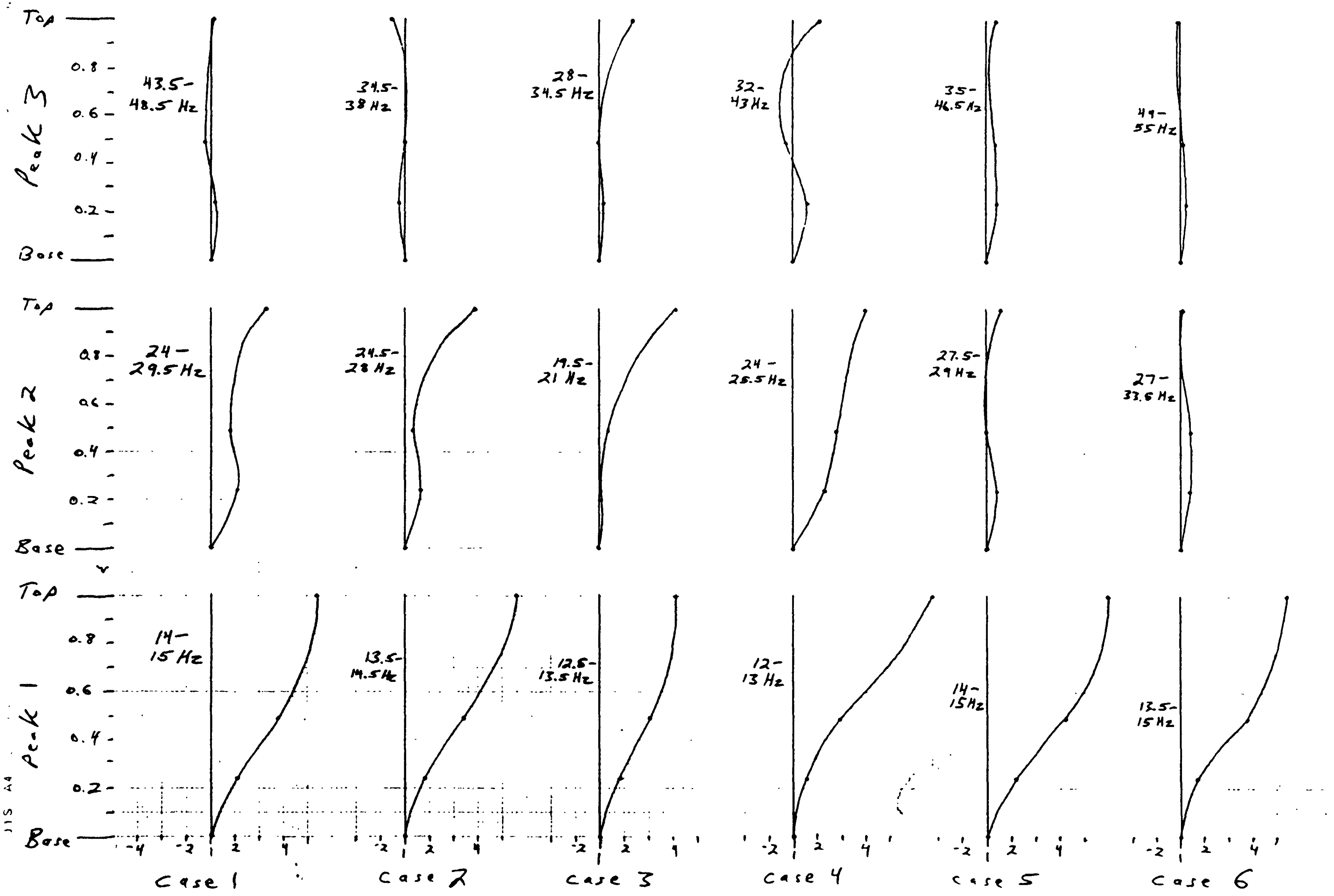

Figure 6 Acceleration ratio plotted along maximum vertical cross section for three major response peaks, transverse shaking.

Longitudinal Shaking

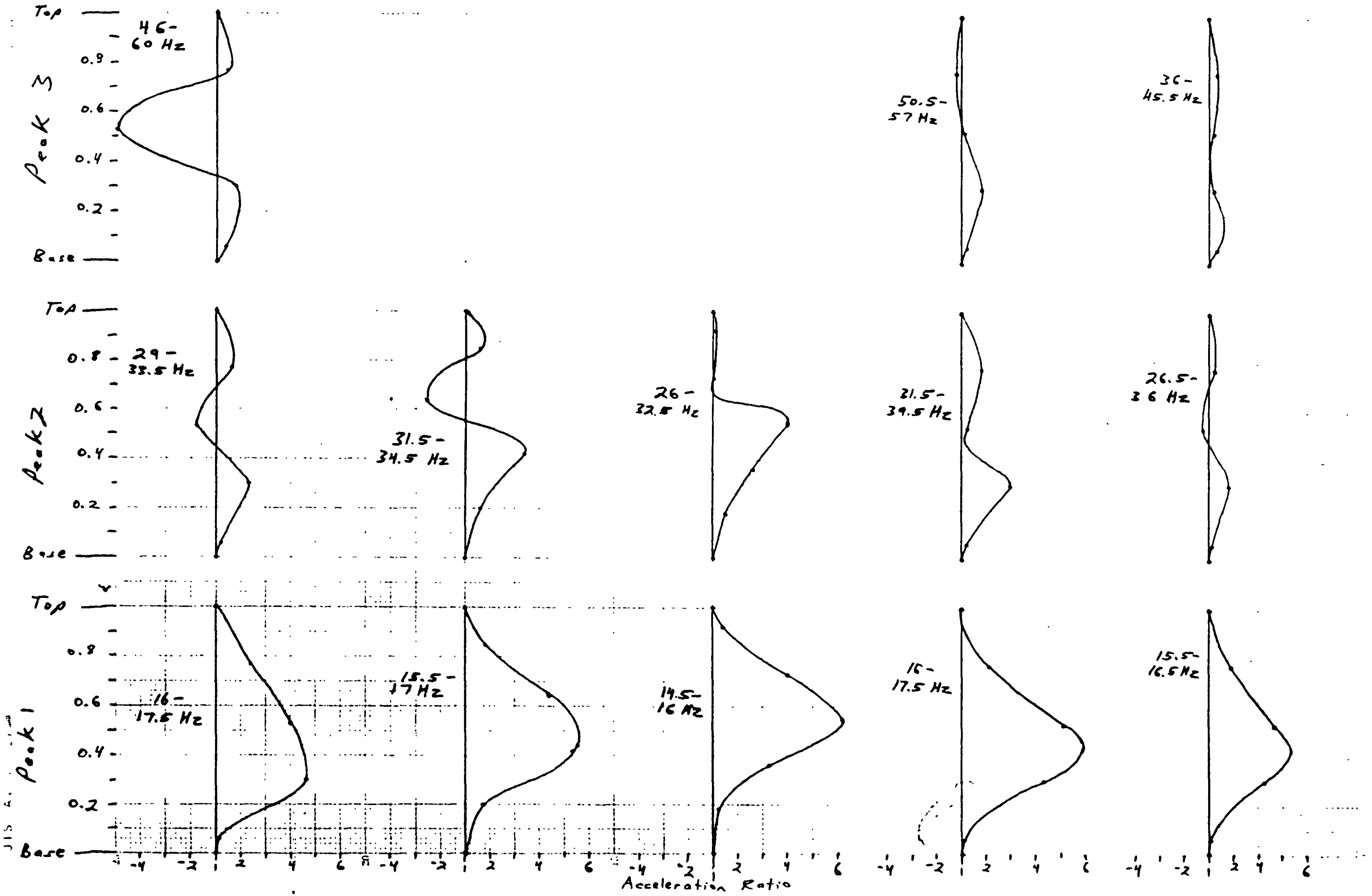

Figure 5. Acceleration ratio plotted along ridge crestline for three major response peaks, longitudinal shaking.

Transverse Shaking

Figure 7. Shear-stress Index plotted along ridge crestline, transverse shaking.

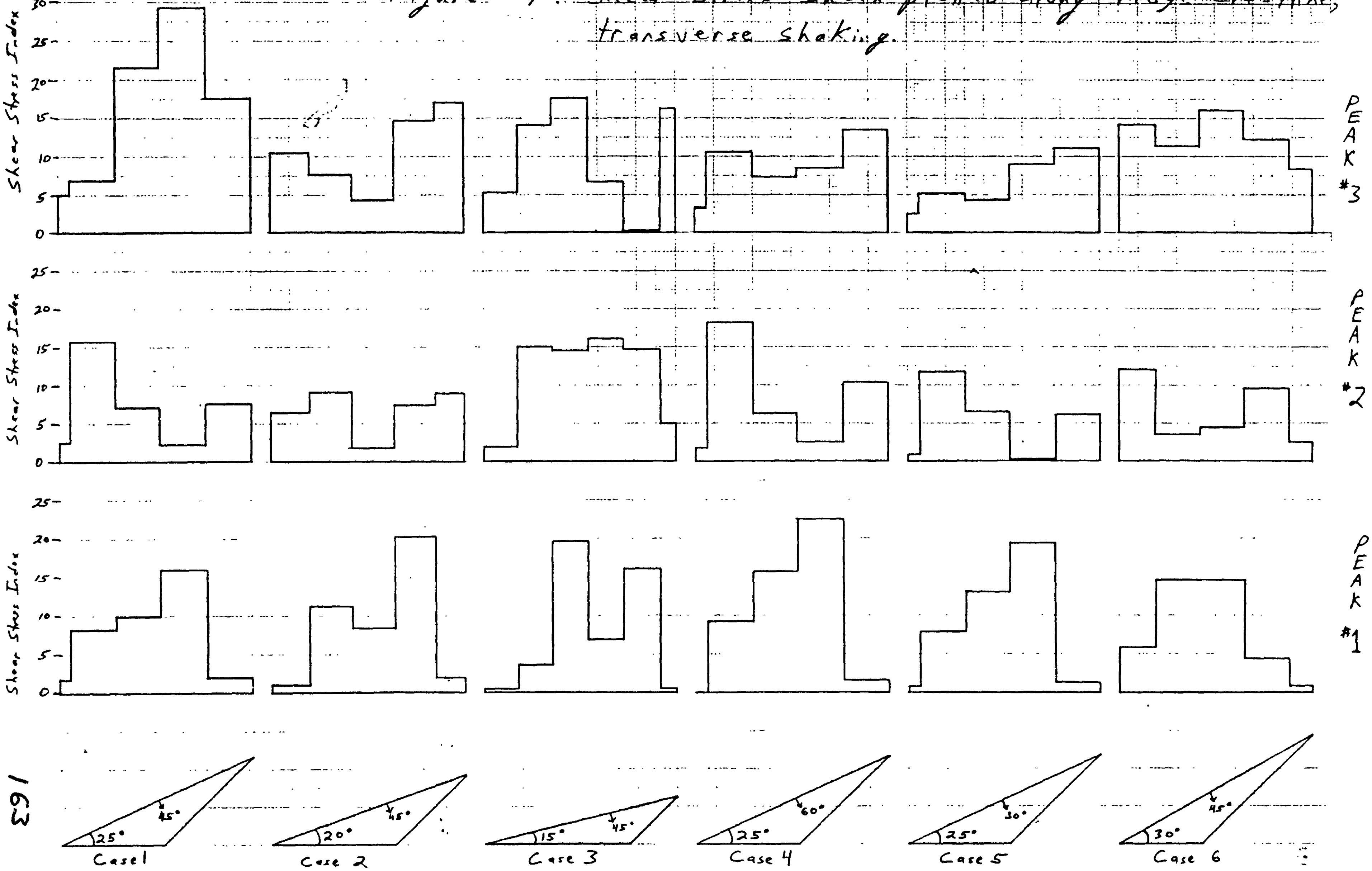

Longitudinal Shaking

Figure 8. Shear-Stress Index plotted along ridge crestline, longitudinal shaking.

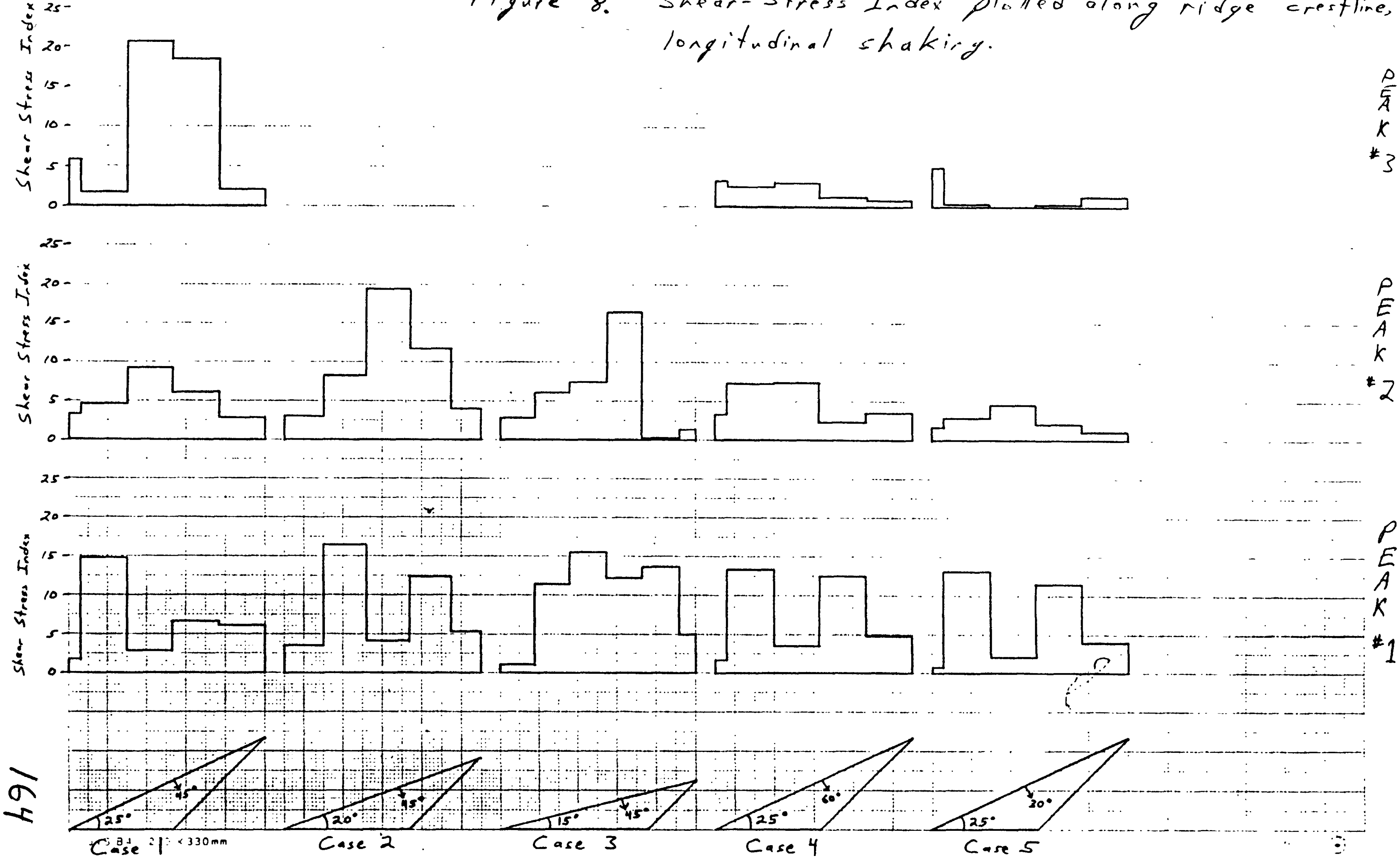

Figure 9. Shear-Stress Index plotted along maximum vertical cross section, transverse shaking.

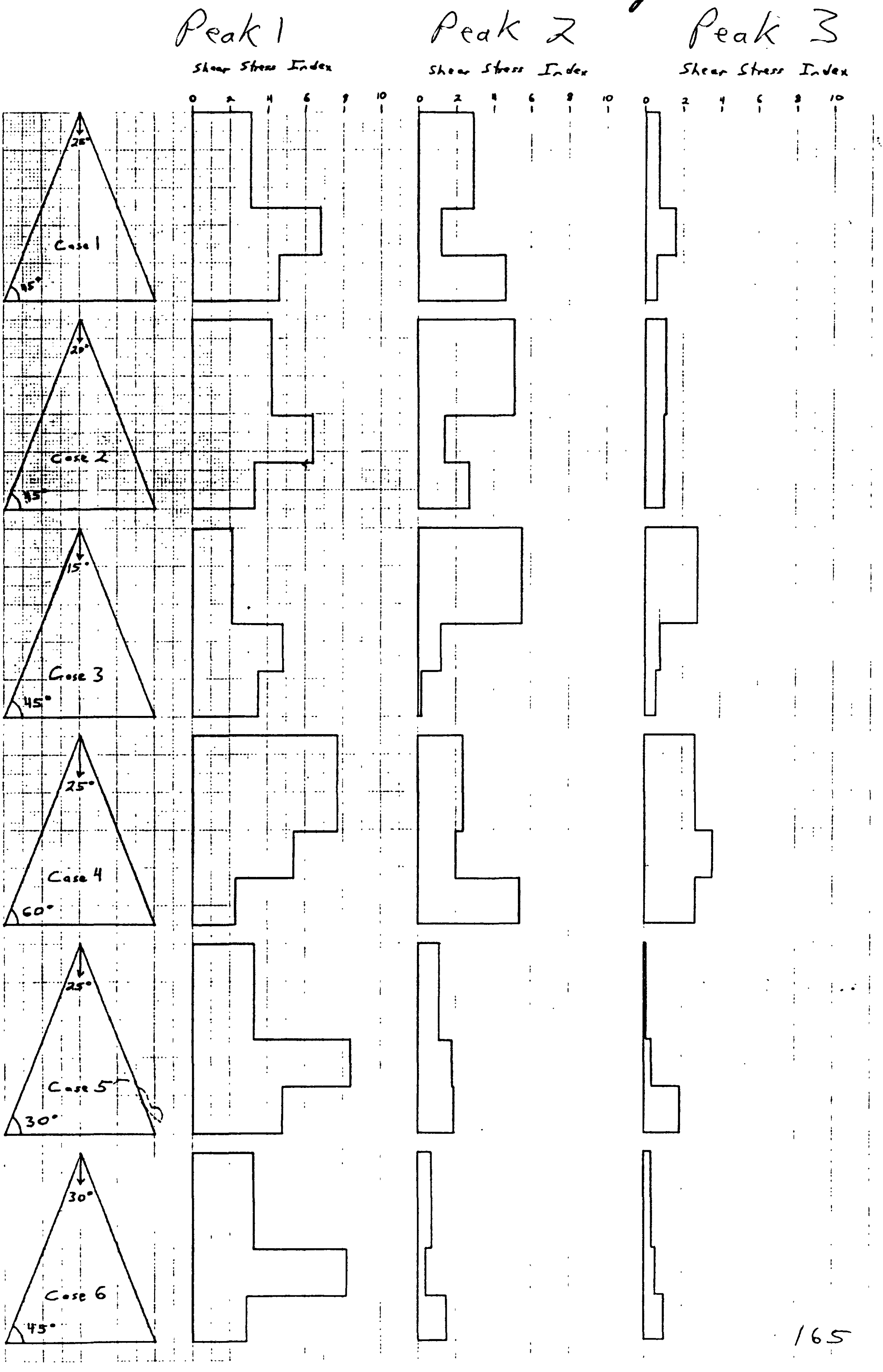

Figure 10. Histograms of Newmark displacement.

No water table (h=0)

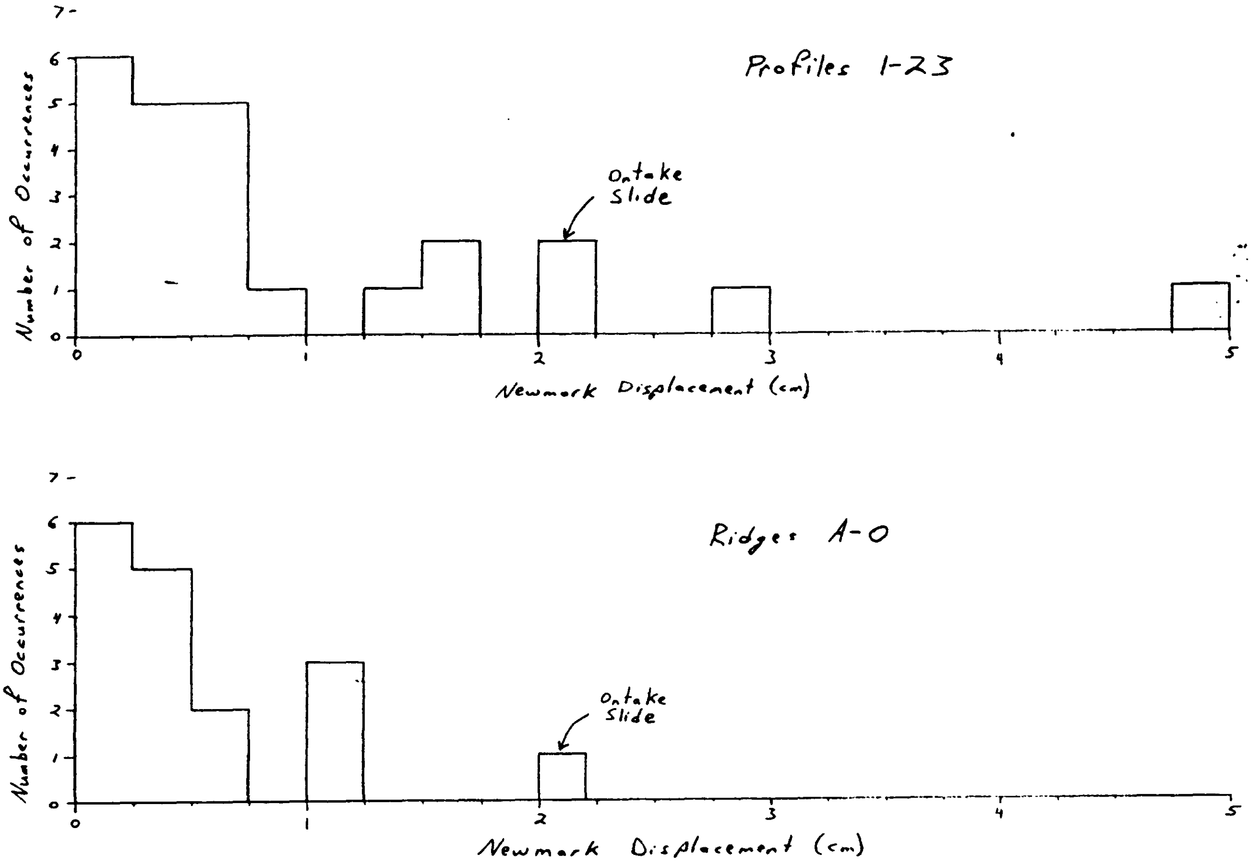

Water table 2m above slip surface (h=2m)